Disks and Jets in the Formation of Multiple Stellar Systems

Ana Karla Díaz Rodríguez

Programa de Doctorado en Física y Matemáticas
UGR/IAA-CSIC

INSTITUTO de ASTROFISICA de ANDALUCIA
CSIC
I·A·A

UNIVERSITAS · GRANATENSIS · 1531
PLUS ULTRA
UNIVERSIDAD DE GRANADA

UNIVERSIDAD DE GRANADA

Disks and Jets in the Formation of Multiple Stellar Systems

Ph.D. dissertation by

Ana Karla Díaz Rodríguez

Programa de Doctorado de Física y Matemáticas

Supervisor: Dr. Guillem Anglada Pons

Instituto de Astrofísica de Andalucía - CSIC

A Ruby y Arnol, mis abuelos

To boldly go where no man has gone before!

- James T. Kirk

Agradecimientos

A mi familia, dispersa geográficamente, que se regocija al unísono de este momento. Especialmente a mi madre, por sostenerme. Especialmente a Víctor, por impulsarme. A mis amigas de siempre, que también son familia.

A mi tutor Guillem Anglada, del que he aprendido muchísimo, como científico y como persona. A mis compañeros Mayra Osorio, José Francisco Gómez, Enrique Macías y Juan Manuel Guijón. A nuestros colaboradores del equipo HOPS.

A Itziar de Gregorio, Carlos Carrasco y Luis Felipe Rodríguez, por recibirme con los brazos abiertos y compartir conmigo su conocimiento.

A todos los que han entrado y salido de mi vida en estos (largos) años. A los que se han quedado.

This research has been funded by FEDER/MCIU through the AEI/AYA2017-84390-C2-1-R grant.

I acknowledge an FPU fellowship (FPU12/03181) from the Spanish Ministry of Education, Culture and Sport. I also acknowledge support from the State Agency for Research of the Spanish MCIU through the "Center of Excellence Severo Ochoa" award to the Instituto de Astrofísica de Andalucía (SEV-2017-0709).

This work uses VLA data from the following projects: 15A-260, 15A-369, 14B-296, 16B-417. VLA is a telescope of the NRAO, a facility of the NSF (USA) operated under cooperative agreement by Associated Universities, Inc.

This work uses the following ALMA data: ADS/JAO.ALMA#2015.1.01229.S, ADS/JAO.ALMA#2016.1.01305.S. ALMA is a partnership of ESO (representing its member states), NSF (USA) and NINS (Japan), together with NRC (Canada), MOST and ASIAA (Taiwan), and KASI (Republic of Korea), in cooperation with the Republic of Chile. The Joint ALMA Observatory is operated by ESO, AUI/NRAO and NAOJ.

Resumen

El objetivo general de esta tesis es estudiar las primeras etapas del proceso de formación estelar en sistemas múltiples. Para ello analizamos dos aspectos complementarios de la formación múltiple de estrellas: la formación simultánea de protoestrellas en un cúmulo, y la formación de un sistema binario individual. Utilizamos observaciones sensitivas, de alta resolución y de multifrecuencia obtenidas con los instrumentos *Very Large Array* (VLA) y *Atacama Large Millimeter/Submillimeter Array* (ALMA), en modo de continuo y de línea. Las observaciones centimétricas de continuo con el VLA nos permiten detectar la emisión libre-libre térmica de jets ionizados y discos fotoevaporados, mientras que la emisión continua milimétrica detectada con ALMA traza el polvo en el plano medio de los discos circunestelares, y la emisión de línea nos proporciona los medios para estudiar su cinemática. Además, la alta resolución angular y la sensibilidad de nuestras observaciones nos permiten detectar componentes de varios potenciales sistemas múltiples.

En primer lugar, presentamos observaciones del VLA en múltiples longitudes de onda (0.7 - 5 cm) y en varias épocas (1994 - 2015) hacia la región que contiene las fuentes de IR lejano FIR 3 (HOPS 370) y FIR 4 (HOPS 108) en la Nube Molecular de Orión 2 (OMC-2, por sus siglas en inglés). Reportamos la detección de 10 fuentes de radio, siete de ellas identificadas como objetos estelares jóvenes (YSO, por sus siglas en inglés). Obtenemos la imagen del radio jet muy bien colimado (VLA 11) con emisión térmica libre-libre en su núcleo, asociado con la protoestrella de Clase I HOPS 370, de masa intermedia. El jet presenta varios nudos (VLA 12N, 12C, 12S) de emisión de no térmica (probablemente sincrotrón debido al choque de electrones relativistas) a distancias de $\sim$ 7500 - 12500 unidades astronómicas (au) de la protoestrella, en una región donde otros trazadores de choque han sido previamente identificados. Mostramos que estos nudos se están alejando de la protoestrella HOPS 370 a $\sim$100 km s^{-1}. La protoestrella de Clase 0 HOPS 108, que detectamos como una fuente de radio independiente, cinemáticamente desacoplada del jet, cae en el camino de estos nudos no térmicos. Estos resultados favorecen el escenario propuesto anteriormente donde la formación de HOPS 108 ha sido desencadenada por el impacto del jet de HOPS 370 con el material denso a su alrededor. Sin embargo, HOPS 108 presenta una velocidad de movimiento propia aparente de $\sim$ 30 km s^{-1}, similar a la de otras estrellas "fugitivas" en Orión, cuyo origen es desconcertante.

Más adelante, ampliamos nuestro estudio a todo el campo de visión de esas observaciones, una porción de 12′.5 de longitud del Filamento con Forma de Integral (ISF, por sus siglas en inglés) que contiene a toda la región OMC-2 y los 2′.5 más al sur de la región OMC-3. Reportamos 47 fuentes de radio adicionales, 23 de las cuales se presentan aquí por primera vez. Para estas 47 fuentes de radio, reportamos sus posiciones, densidades de flujo e índices espectrales. Discutimos sobre la naturaleza de estas 47 fuentes de radio analizando su índice espectral de radio, morfología, emisión en otros rangos de longitud de onda, posición relativa al ISF y asociación con condensaciones de polvo. Concluimos que, del total de 57 fuentes de radio en el campo de visión, 41 (72 %) están muy probablemente asociadas con la región de formación estelar, 6 son fuentes de fondo extragalácticas, y no estamos seguros de la asociación con la región de las 10 fuentes restantes. De las 41 fuentes asociadas con la región de formación estelar, 36 están trazando la posición de YSOs, 3 están trazando la emisión no térmica de los nudos de un jet, una está trazando la pared ionizada por choques de una cavidad, y una podría ser un YSO o un nudo de un jet. Identificamos de forma clara la emisión de radio continuo de las fuentes impulsoras de los 9 chorros moleculares previamente reportados en nuestro campo de visión. Para cuatro de estas fuentes resolvemos claramente su morfología alargada característica de los radio jets. Detectamos emisión térmica libre-libre proveniente de dos YSOs de Clase III que podría estar trazando sus discos fotoevaporados asociados. Encontramos signos de variabilidad en 13 fuentes de radio, siete de las cuales también son variables en longitudes de onda más cortas (infrarrojo cercano/óptico/rayos X). Encontramos 7 pares de fuentes de radio con una separación proyectada < 3000 au, que constituyen potenciales sistemas binarios; teniendo en cuenta fuentes adicionales que se han detectado a otras longitudes de onda, identificamos un total de 17 potenciales sistemas múltiples en nuestro campo de visión en ese rango de separación.

Finalmente, estudiamos el sistema binario cerrado SVS 13, con componentes separadas 90 au. Detectamos al menos dos discos circunestelares de polvo y gas, y un disco circumbinario con prominentes brazos espirales, que parece estar en las primeras etapas de formación, asociado con este sistema protoestelar. La emisión de polvo parece más intensa y compacta hacia la componente VLA 4B, mientras que la VLA 4A parece estar asociada con una mayor cantidad de polvo y con transiciones moleculares más intensas. Somos capaces de estimar temperaturas rotacionales y densidades de columnas moleculares, indicando altas temperaturas y una rica química. Las transiciones moleculares típicas de los *corinos* calientes se

detectan hacia las dos componentes VLA 4A y VLA 4B. A partir de la emisión de polvo observada y la información cinemática estimamos la orientación del sistema, las masas estelares y las de sus discos asociados. Nuestro análisis de los movimientos propios y la cinemática de los discos sugieren que hasta cuatro objetos estelares, uno de ellos una estrella visible, podrían estar presentes dentro de una región de tamaño < 100 au. En resumen, SVS 13 parece ser un excelente caso de estudio con el que contrastar simulaciones numéricas de las primeras etapas de la formación de sistemas binarios y múltiples.

Summary

The general goal of this thesis is to study the first stages of the star formation process in multiple systems. For that, we analyze two complementary aspects of multiple star formation: the simultaneous formation of protostars in a cluster, and the formation of an individual binary system. We use sensitive, high-resolution, and multifrequency continuum and line observations obtained with the Very Large Array (VLA) and the Atacama Large Millimeter/Submillimeter Array (ALMA). The centimeter VLA continuum observations allow us to detect the thermal free-free emission from ionized jets and photoevaporating disks, while the millimeter ALMA continuum emission traces the dust in the mid-plane of the disks and the line emission provides us means to study its kinematics. Additionally, the high angular resolution and sensitivity of our observations allow us to detect components of several possible multiple systems.

In the first place, we present multiwavelength (0.7 - 5 cm), multiepoch (1994 - 2015) VLA observations toward the region enclosing the bright far-IR sources FIR 3 (HOPS 370) and FIR 4 (HOPS 108) in the Orion Molecular Cloud (OMC) 2, in Orion. We report the detection of 10 radio sources, seven of them identified as young stellar objects (YSOs). We image a well-collimated radio jet with a thermal free-free core (VLA 11) associated with the Class I intermediate-mass protostar HOPS 370. The jet presents several knots (VLA 12N, 12C, 12S) of non-thermal radio emission (likely synchrotron from shock-accelerated relativistic electrons) at distances of $\sim$ 7500 - 12500 au from the protostar, in a region where other shock tracers have been previously identified. We show that these knots are moving away from the HOPS 370 protostar at $\sim$ 100 km s^{-1}. The Class 0 protostar HOPS 108, which we detect as an independent, kinematically decoupled radio source, falls in the path of these non-thermal radio knots. These results favor the previously proposed scenario where the formation of HOPS 108 has been triggered by the impact of the HOPS 370 outflow with a dense clump. However, HOPS 108 presents an apparent proper motion velocity of $\sim$30 km s^{-1}, similar to that of other runaway stars in Orion, whose origin is puzzling.

Later, we extend our study to the whole field of view of those observations, a 12$'$.5-long portion of the Integral Shaped Filament (ISF) which contains the whole OMC-2 region and the southernmost 2$'$.5 of the OMC-3 region. We report 47 additional radio sources, 23 of which are presented here for the first time. For these 47 radio sources, we report the positions, flux densities, and spectral indices.

We discuss the nature of the 47 reported radio sources by analyzing their radio spectral index, morphology, emission at other wavelength ranges, position relative to the ISF, and association with dust clumps. We conclude that, out of the 57 total radio sources in the field of view, 41 (72%) are very likely associated with the star-forming region, 6 are extragalactic background sources, and we are unsure about the association with the star-forming region of the remaining 10 sources. Of the 41 sources associated with the star-forming region, 36 are tracing the position of YSOs, 3 are tracing non-thermal emission from jet knots, one is tracing the shock-ionized wall of an outflow cavity, and one could be either a YSO or a jet knot. We unambiguously identify the radio continuum emission of the driving sources of the 9 previously reported molecular outflows in our field of view. In four of these sources, we clearly resolve the elongated morphology characteristic of radio jets. We detect thermal free-free emission from two Class III YSOs that may be tracing their associated photoevaporating disks. We find signs of variability in 13 radio sources, seven of which are also variable at shorter wavelengths (near-IR/optical/X-ray). We find 7 pairs of radio sources with a projected separation < 3000 au, that are potential binary systems; taking into account the additional sources detected at other wavelengths, we then identify a total of 17 potential multiple systems in our field of view within this separation range.

Finally, we study the close binary system SVS 13, with components separated 90 au. We detect at least two circumstellar disks of dust and gas, and one circumbinary disk with prominent spiral arms, that appears to be in the earliest stages of formation, associated with this protostellar system. Dust emission appears more intense and compact toward component VLA 4B, while VLA 4A seems to be associated with a larger amount of dust and with stronger molecular transitions. We are able to estimate rotational temperatures and molecular column densities, indicating warm temperatures and rich chemistry. Molecular transitions typical of hot corinos are detected toward both VLA 4A and VLA 4B. From the observed dust emission and the kinematical information, we estimate the orientation of the system, the stellar masses and the mass of their associated disks. Our analysis of the proper motions and the kinematics of the disks suggest that up to four stellar objects, one of them a visible star, could be present within a region of size <100 au. In summary, SVS 13 seems to be an excellent test-bed to test numerical simulations of the earliest stages in the formation of binary and multiple systems.

Granada, 19 de noviembre de 2020

La doctoranda Ana Karla Díaz Rodríguez y el director de la tesis Guillem Anglada Pons, garantizamos, al firmar esta tesis doctoral, que el trabajo ha sido realizado por la doctoranda bajo la dirección del director de la tesis y, hasta donde nuestro conocimiento alcanza, en la realización del trabajo, se han respetado los derechos de otros autores a ser citados, cuando se han utilizado sus resultados o publicaciones.

The doctoral candidate Ana Karla Díaz Rodríguez and the thesis supervisor Guillem Anglada Pons, guarantee, by signing this doctoral thesis, that the work has been done by the doctoral candidate under the direction of the thesis supervisor and, as far as our knowledge reaches, in the performance of the work, the rights of other authors to be cited, when their results or publications have been used, have been respected.

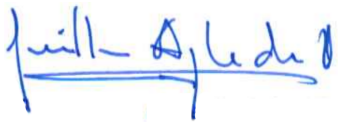

Director de la Tesis

Doctoranda

Index

List of Figures

List of Tables

Chapter 1

Introduction

1.1 Overview on Star Formation

1.1.1 Sites of Star Formation: Molecular Clouds, Filaments and Dense Cores

Molecular clouds are regions of the interstellar medium of high density ($n \simeq 10^2$ - 10^5 cm^{-3}) and low temperature ($T \simeq 10$ - 30 K) where the gas is mainly in molecular form. The mass of the molecular clouds is composed of $\sim 99\%$ of gas and $\sim 1\%$ of dust grains. The molecular gas is mostly H_2, with traces of other molecules such as CO, H_2O, NH_3, CS, and HCN. The other molecules are much less abundant than H_2, down by a factor $> 10^4$ (Wakelam et al. 2010).

Nearly all molecular gas in the interstellar medium is distributed in giant molecular clouds, with individual masses of 10^5 - 10^6 $M_\odot$, sizes up to 50 pc, and average densities of $n \sim 10^2$ cm^{-3} (Williams et al. 2000). Molecular clouds are not homogeneous but have a hierarchical structure (Blitz 1993; Williams et al. 2000; Heyer, & Dame 2015). They contain intermediate-size clumps with larger column and volume densities than the parent molecular cloud, and within these, smaller (< 0.1 pc), higher density ($n > 10^4$ cm^{-3}) cores. Massive clumps can form stellar clusters, while dense cores can form individual stars or multiple systems with few components (McKee, & Ostriker 2007).

In the last decades, filamentary overdense structures have been observed inside molecular clouds, regardless of whether they are actively forming stars or not (André et al. 2010, 2014, and references therein). These filaments have a wide range of lengths (0.1 - 100 pc), masses (~ 1 - 10^5 $M_\odot$), and line-masses (≤ 4000 $M_\odot$ pc^{-1})

(Bally et al. 1987; Kainulainen et al. 2017; Hacar et al. 2018). Their formation seems to be governed by large-scale turbulent motions inside the molecular clouds (Padoan et al. 2001; Arzoumanian et al. 2011; Xu et al. 2019).

Filaments are thought to play an important role in the evolution of molecular clouds and star formation. Young stellar groups and massive protostellar candidates have been observed in "hubs" or intersections of filaments (Myers 2009; Hill et al. 2011; Hennemann et al. 2012). On the other hand, the subsequent fragmentation of super-critical filaments (line-masses $> 16\ M_{\odot}\ \mathrm{pc}^{-1}$) via gravitational instability could give place to dense cores (André et al. 2010; Offner et al. 2014). Results of the *Herschel* Gould Belt survey (HGBS; see André et al. 2010), covering the entire spatial extent of nearby molecular clouds ($d \leq 0.5$ kpc), showed that more than 75% of the prestellar cores (self-gravitating dense cores that have not yet formed a protostar) identified in this survey are located within super-critical filaments (André et al. 2019, and references therein).

The $\sim$ 8 pc-long Integral Shaped Filament (ISF, Bally et al. 1987; Chini et al. 1997; Peterson & Megeath 2008) is the closest highly super-critical filament, at $\sim$400 pc, in Orion. Its proximity allows the high-resolution mapping over a large area (e.g. Polychroni et al. 2013, Kainulainen et al. 2017). Furthermore, its protostellar population has been well characterized by means of *Spitzer* (Megeath et al. 2012) and *Herschel* (Furlan et al. 2016) observations. These two ingredients make the ISF a unique place to study the fragmentation of super-critical filamentary gas into (high- and low-mass) protostars (e.g., Takahashi et al. 2013; Stutz & Kainulainen 2015; Teixeira et al. 2016; Kainulainen et al. 2017).

Although infrared observations are helpful to detect star-formation sites and to characterize the evolutive stage of the young stellar objects (YSOs; see Section 1.1.4), they cannot directly trace the most embedded protostars. The dusty envelope absorbs and re-emits the emission from the protostar with a peak in the far-IR, while at shorter wavelengths the cloud becomes completely opaque. Therefore, the observation of these embedded objects in the near-IR range is impossible, and at mid and far-IR only the envelope can be observed.

However, the molecular cloud is transparent at radio wavelengths and we can detect with high angular resolution thermal centimeter continuum emission from a region very close to the protostar (see Section 1.1.3). This is the most accurate way to obtain the position of embedded protostars. Additionally, radiointerferometric observations have a high angular resolution, that allows us to separate the emission from individual protostars in crowded star-forming regions (e.g. NGC

2071: Carrasco-González et al. 2012; ONC: Forbrich et al. 2016), and even to resolve close binary systems (e.g. NGC1333 SVS 13: Anglada et al. 2000; L723 VLA 2: Carrasco-González et al. 2008a) and, in some cases, track their orbital motions over a certain period of time (e.g. L1551 IRS5: Lim & Takakuwa 2006).

1.1.2 Gravitational Collapse of a Dense Core

Molecular clouds are generally gravitationally bound, with forces such as thermal pressure, magnetic field, and turbulence counteracting the effect of gravity. When this equilibrium of forces is locally broken, the gravitational collapse of a dense core can occur, leading to the formation of a central object, the protostar, which accretes material from the envelope until it reaches its final mass (Larson 1969, 1972; Shu 1977; Larson 2003).

We can briefly summarize the gravitational collapse in a simplified, spherically symmetric scenario, as follows (see Figure 1.1; see Estalella & Anglada 2008 for a detailed description). The optically thin dense core collapses under its own gravity from the inside-out in a non-homologous way (i.e., the density increases more rapidly at the center of the core). This collapse is initially isothermal since the energy generated from the contraction is easily released as thermal emission from the dust grains. When the central density is high enough, the material becomes optically thick so that no radiation can escape anymore. The temperature and pressure increase gradually inside the optically thick region since the gas now contracts adiabatically, eventually halting the accretion and creating the first "hydrostatic core". Outside the first hydrostatic core, the material continues to free-fall onto it, creating a shock front on its surface that elevates its temperature. When the temperature reaches ~ 2000 K, the dissociation of the H_2 inside the core begins. This process is highly endothermic. Therefore, gravity wins over pressure and the first hydrostatic core collapses rapidly, faster than the infalling envelope due to its higher density. A second hydrostatic core then forms inside the first one and these coexist for a brief time, each one with a shock front on its surface. Finally, the outermost (first) core disappears when all its mass has fallen onto the inner (second) one, which constitutes the protostar. The material of the envelope continues to free-fall onto the protostar. For a collapsing dense core of 1 $M_\odot$, the material at the center becomes opaque when the central density is $\sim 10^{-13}$ g cm^{-3}, the first hydrostatic core forms in about 10^4 yr, when the central density reaches $\sim 10^{-10}$ g cm^{-3}, while the second hydrostatic core forms ~ 1 yr later, with an

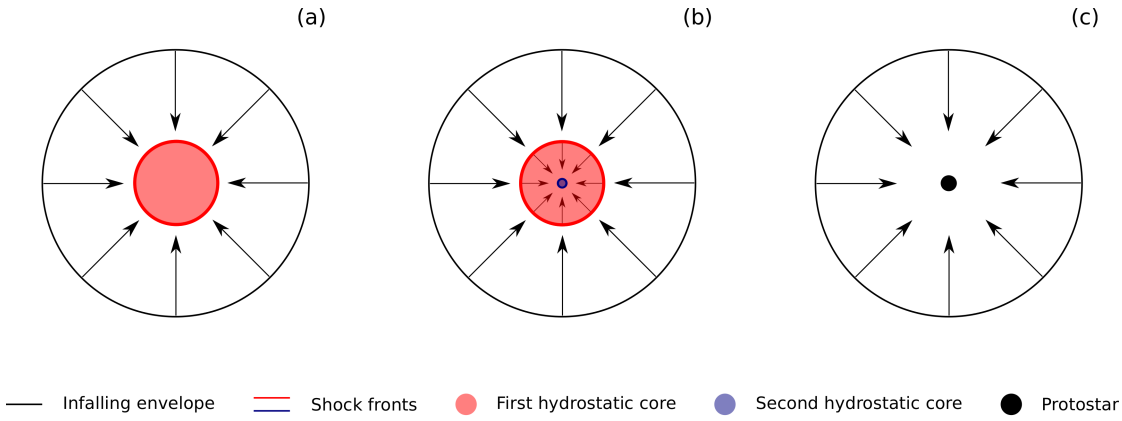

Figure 1.1 Schematic view of the gravitational collapse of a dense core. (a) Isothermal collapse and formation of the first hydrostatic core. (b) Collapse of the first hydrostatic core and formation of the second hydrostatic core. (c) The first hydrostatic core disappears and the envelope continues to free-fall onto the second hydrostatic core, the protostar.

initial density of $\sim 10^{-3}$ g cm^{-3}. In this case, the two cores coexist for about 10 yr.

The identification of collapsing cores can be difficult, since rotation, infall, and outflow motions (all present in the earliest stages of star formation, see next Section) may produce similar observational features. A hallmark of infall that can be detected through radio observations is the so-called central-blue-spot (Anglada et al. 1987, 1991; Mayen-Gijon et al. 2014; Mayen-Gijon 2015), which is expected to appear in the first-order moment map of angularly resolved, optically thick line emission, due to an asymmetry in the blue- and red-wing line profiles. Recently, Estalella et al. (2019), building on the previous works, derived an analytical expression for this infall hallmark, and apply it to observational data of several dense cores (G31, B335, and L1287). They were able to successfully fit the first-order moment maps and to obtain values for the central masses onto which the collapse is occurring, showing that the central-blue-spot appears to be a robust and reliable observational indicator of infall.

On the other hand, the observations of the first hydrostatic cores are challenging due to their small spatial extent (only a few au), the high opacities involved, and their short life. Only a few candidates have been identified in the last two decades (e.g. Belloche et al. 2006; Chen et al. 2010; Gerin et al. 2015; Maureira et al. 2020a, and references therein). Fortunately, the improvement of the observation capabilities of the modern radiointerferometers allows now to survey hundreds of protostars, increasing the probability of detecting a first hydrostatic core. Taking

advantage of this, Karnath et al. (2020) identified the potentially youngest protostars (four objects) in a sample of ∼330 protostars in Orion (Tobin et al. 2020) and proposed one of them as a first hydrostatic core candidate.

1.1.3 Disks and Jets in Young Stellar Objects

The development of a rotating circumstellar disk is a natural outcome of the gravitational collapse of a rotating core since a centrifugal barrier forms in a plane perpendicular to the rotation axis and the infalling material tends to be deposited on this plane (Terebey et al. 1984; Adams & Shu 1986; Shu et al. 1987; Saigo & Hanawa 1998). The accretion of mass from the envelope to the protostar proceeds mainly via this disk, therefore it is also called "accretion disk" in the literature. On the other hand, high velocity, bipolar collimated ejections of material (usually called jets) take place in the direction perpendicular to the disk, removing at least 60% of the excess of angular momentum in the disk (Bacciotti 2004) and, therefore, allowing the protostar to accrete matter up to its final mass. These jets blow away material from the disk and envelope, generating molecular outflows that move at lower velocities and in a less-collimated way, opening cavities in the material surrounding the protostar.

Jets and outflows are signposts of stellar formation. They are observed from radio to X-ray wavelengths (see reviews of Bally 2016 and Anglada et al. 2018) and are associated with YSOs of a wide range of masses, from embedded proto-brown dwarfs (Bourke et al. 2005; Palau et al. 2014; Kim et al. 2019) to massive protostars (Beuther et al. 2002; Garay et al. 2003; Navarete et al. 2015; Rosero et al. 2019). Since the mass loss rate in the flow is proportional to the disk accretion rate (Pudritz et al. 2007, and references therein), jets and outflows are generally more powerful in the youngest YSOs, in which the accretion is more important, than in more evolved ones (Bally 2016). The youngest outflows are relatively small and best traced by molecules such as CO, SiO, H_2O, and H_2, while older outflows can extend to parsec scales and are best traced by shock-excited atoms and ions such as hydrogen-recombination lines, [SII], and [OII] (Bally 2016).

Although the exact mechanism for jet ejection is not fully understood, it is believed to be closely related to the circumstellar disks. Magneto-hydrodynamical simulations (Ouyed, & Pudritz 1997a,b; Shu et al. 2000; Pudritz et al. 2007) show that a rotating disk threaded by a large-scale magnetic field generates a hydromagnetic wind (the jet) perpendicular to the disk, which efficiently carries away

angular momentum from the disk. This mechanism was first proposed by Blandford, & Payne (1982) to explain the launching of jets from accretion disks around black holes, and was soon after proposed as the mechanism for protostellar jets (Pudritz, & Norman 1983, 1986). The magnetic field of the YSO is thought to play a fundamental role in the collimation of the jet, which takes place close to the protostar, within a few tenths of an au (Frank et al. 2014, and references therein).

Observations at centimeter wavelengths trace thermal free-free emission from the ionized gas at the base of the jets, in a region very close to the protostar that is inaccessible at other wavelengths. When observed with enough angular resolution, this emission appears elongated in the direction of the large-scale outflow and is therefore commonly called "radio jet" (Fig. 1.2; see Anglada et al. 2018 for a comprehensive review of radio jets from YSOs). It has been empirically well established that the centimeter luminosity of radio jets correlates with both the bolometric luminosity of the protostar ($L_{\rm bol}$) and the outflow force (Anglada et al. 1992; Anglada 1995, 1996; Anglada et al. 2015, 2018). The correlation with the outflow force has been interpreted as evidence that shocks are responsible for the ionization of jets; while the correlation with the bolometric luminosity relates the mass accretion (traced by $L_{\rm bol}$, dominated by the accretion luminosity) and outflow (traced by radio emission from the ionized jet) processes in YSOs. These correlations are sometimes referred to as the "Anglada correlations". In Fig. 1.3 we show the most up-to-date Anglada correlations, derived from a sample of 81 YSOs with $10^{-2} L_\odot \lesssim L_{\rm bol} \lesssim 10^6 L_\odot$ in Anglada et al. (2018). In Chapter 3 we discuss in more depth these correlations.

On the other hand, as the protostar evolves, there are several mechanisms at play responsible for the settling, growth, and radial transport of dust in the accretion disk (for a review see Testi et al. 2014). For example, dust particles can grow through collisions from the μm-sizes characteristic of the dense cores from which the protostar form, to planetesimal sizes. However, the outcome of the collision depends on the size and the velocity of the impacting particles (see Fig. 2 of Testi et al. 2014), leading to a rapid growth to $\sim$mm-sizes, but to a less effective growth to planetesimal sizes. On the other hand, larger particles settle in the mid-plane of the disk and are transported radially to the inner parts of the disk, while smaller particles are mixed vertically up to the surface of the disk and are transported radially to the outer parts of the disk. In the mid-plane of the accretion disk, the particle density is higher, favoring the collision and therefore

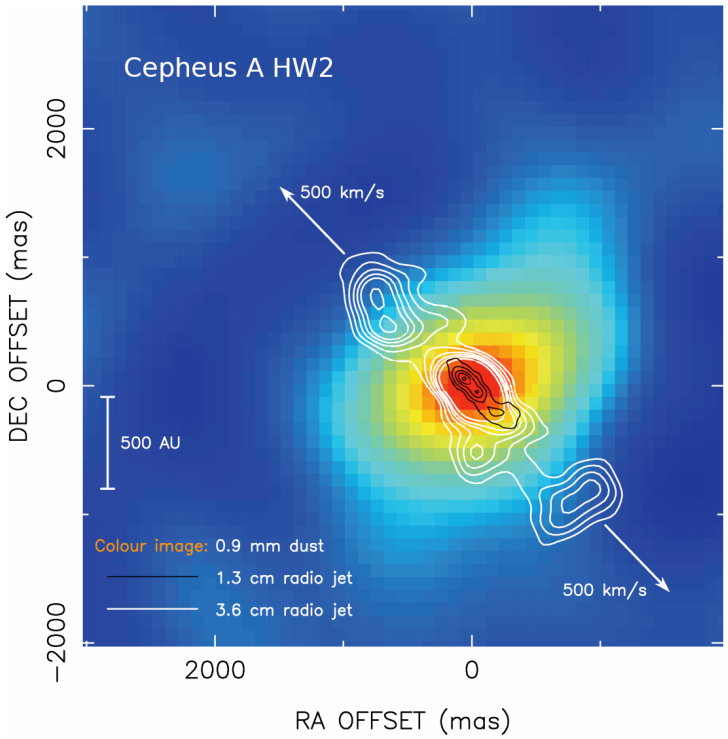

Figure 1.2 Cepheus A HW2 radio jet, tracing the emission of the ionized gas in a region very close to the protostar (adapted from Torrelles et al. 1996).

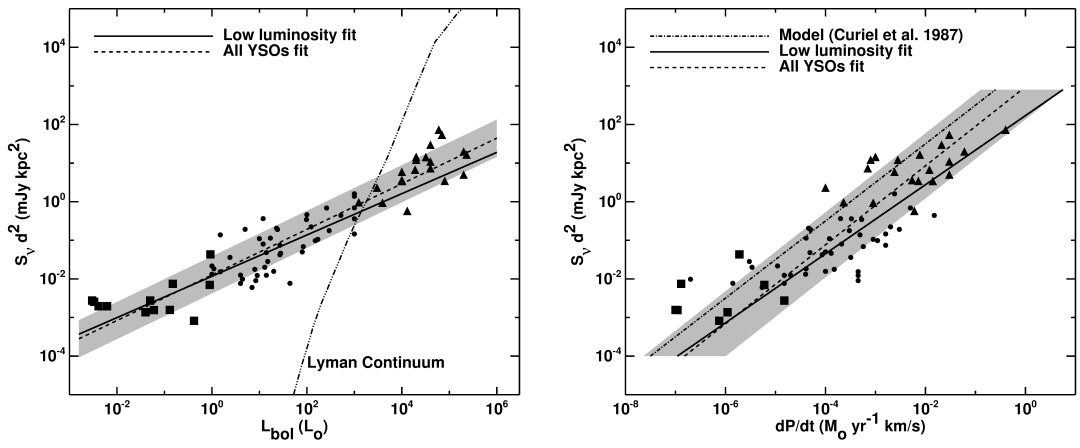

Figure 1.3 Anglada correlations showing the connection between the accretion and the outflow processes in YSOs. Triangles are high luminosity objects ($L_{\rm bol} > 1000$ $L_\odot$), the dots are low luminosity objects ($1 \leq L_{\rm bol} \leq 1000$ $L_\odot$), and squares are very low luminosity objects ($L_{\rm bol} < 1$ $L_\odot$); the gray area indicates the residual standard deviation of the fit (from Anglada et al. 2018).

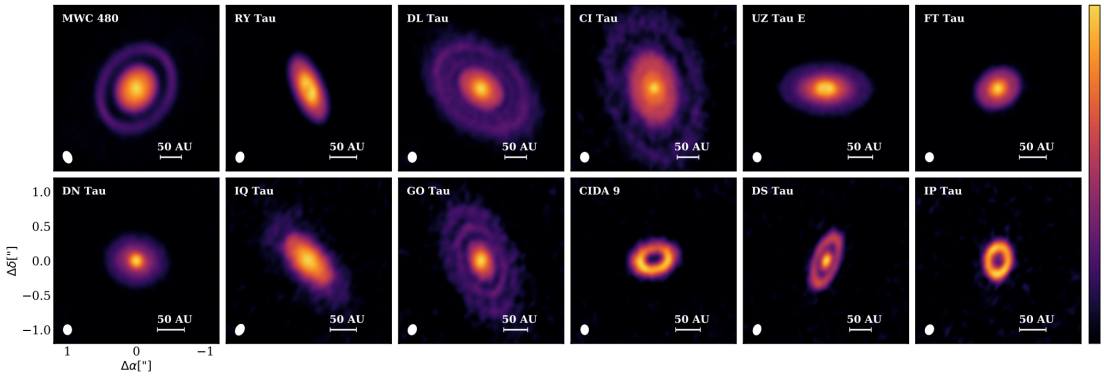

Figure 1.4 Protoplanetary disks with cavities and rings detected at 1.33 mm continuum emission toward the Tauros star-forming region (from Long et al. 2018).

the grain growth; this region contains the bulk of the material for planet formation. Accretion disks in the phases of grain grow before the formation of planetary-size bodies that are directly observable, are usually called "protoplanetary disks" (Testi et al. 2014).

The opacity of the dust grains change as they grow in size (D'Alessio 1996), therefore different regions of the disks (with grains of different sizes) can be probed with observations at different wavelengths. While infrared observations are sensitive to small grains in the surface of the disk, millimeter and sub-mm observations are sensitive to ∼mm-size dust particles in the mid-plane, where planetary formation is expected to occur. In fact, several protoplanetary disks imaged so far at these wavelengths show internal structures such as gaps and rings (ALMA Partnership et al. 2015; Isella et al. 2016; Long et al. 2018; Macías et al. 2018; see Fig. 1.4), asymmetries (Osorio et al. 2014; Carrasco-González et al. 2016), and spiral arms (Pérez et al. 2016; Huang et al. 2018; Phuong et al. 2020). The origin of these structures in protoplanetary disks is currently a topic of hot discussion but appears to be related to the presence of protoplanets. In this sense, radio-interferometric millimeter/submillimeter observations could indeed be revealing the onset of planetary formation.

1.1.4 Classification of Young Stellar Objects

The changes a YSO undergoes during its formation are reflected in its broad-band (1 μm to 1 mm) spectral energy distribution (SED). In particular, the slope of the SED between 2.2 and 100 μm, $\alpha_{IR} = d\log(\lambda S_\lambda)/d\log\lambda$, has been used for a long time as a criterion to classify low-mass YSOs into different evolutionary groups

(Lada & Wilking 1984; Adams et al. 1987; Andre et al. 1993). These are (see Fig. 1.5):

- **Class 0:** These objects are surrounded by a large amount of material of the initial envelope, still in the process of accretion and, therefore, they are not detected at near-IR or optical wavelengths. They are characterized by powerful outflows. The observed emission comes mainly from the cold envelope of infalling gas, not from the central protostar. The SED is similar to that of a black body at a very low temperature, with the peak of emission in the far-IR. The youngest known objects, with ages $\lesssim 10^4$ years, belong to this group.

- **Class I:** These objects are still embedded in an envelope but a circumstellar accretion disk has already formed around the central protostar. Their luminosity comes mainly from the accretion process. They also present outflows, although less potent than those from Class 0 YSOs. The SED is much wider than that of a black body, with the peak of emission at shorter wavelengths than in Class 0 YSOs. It has an IR excess due to the presence of a large amount of circumstellar dust that emits at near and mid-IR wavelengths. It is characterized by a positive value of $0 < \alpha_{IR} \leq 3$. The age of these objects is between $\sim 10^4$ and $\sim 10^5$ years.

- **Class II:** These objects have accreted a large fraction of the circumstellar envelope, and therefore, are detectable at optical wavelengths and are called pre-main sequence stars. Their luminosity comes mainly from the stellar contraction. The SED is still considerably wider than that of a black body, but has less IR excess than Class I objects, since they are surrounded by less circumstellar dust, and peaks in the near-IR. It is characterized by negative values of $-2 < \alpha_{IR} \leq 0$. The age of these objects ranges between $\sim 10^5$ and $\sim 10^6$ years. Classical T Tauri stars are in this evolutionary stage.

- **Class III:** These objects have accreted almost all of the surrounding material and their circumstellar disks could harbor recently formed planets. The emission comes from the reddened photosphere of the star. The SED is similar to that of a black body at high temperature, with no or very little IR excess from the circumstellar disk. It is characterized by very negative values of $-3 < \alpha_{IR} \leq -2$. These objects are non-accreting pre-main sequence stars, with ages ranging between $\sim 10^6$ and $\sim 10^7$ years.

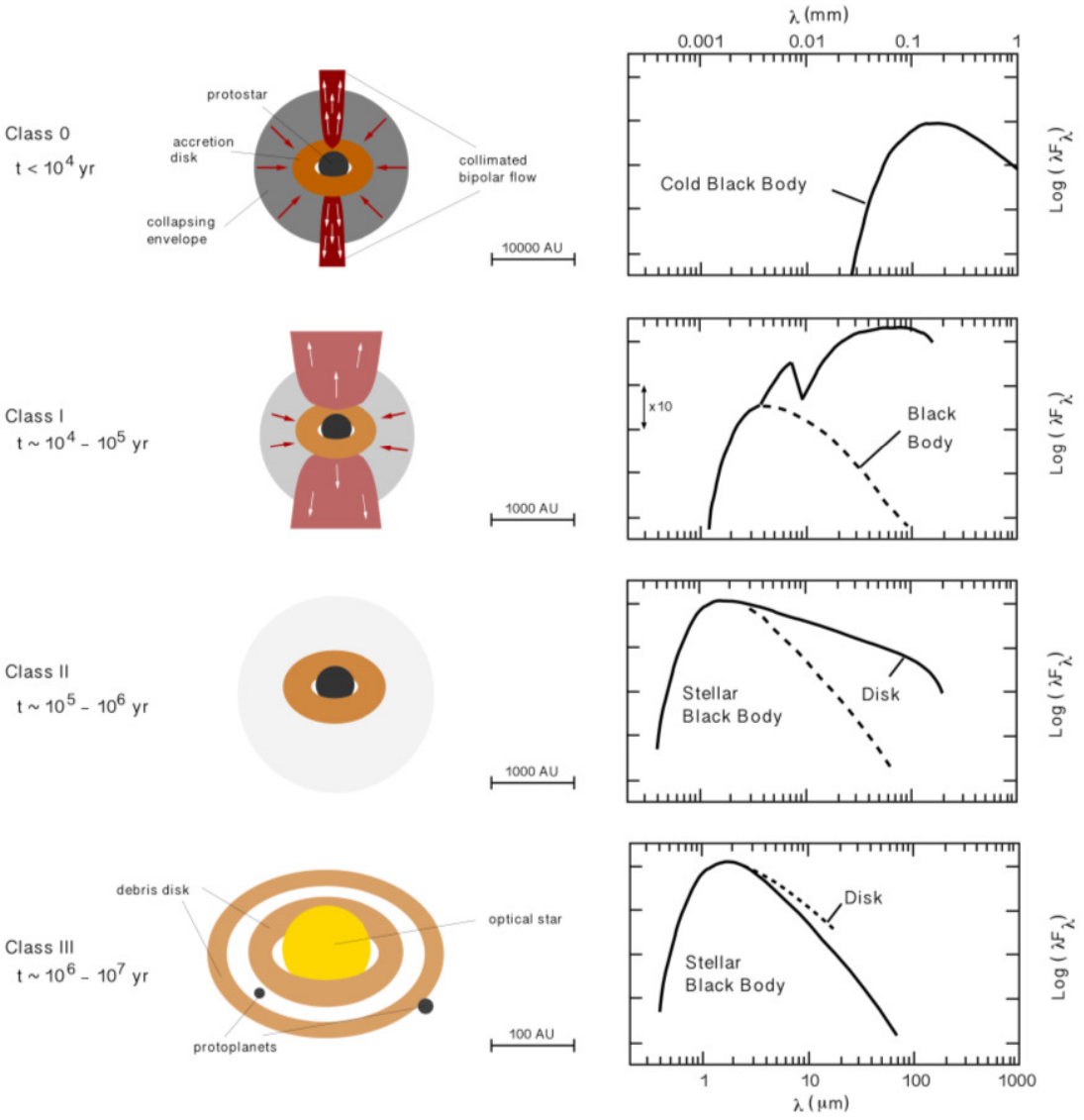

Figure 1.5 Schematic view of the evolutionary classes of low-mass YSOs and their SEDs. The classification is made based on the spectral energy distribution between 2.2 and 100 μm.

1.2 Multiplicity and Feedback in Star Formation

The schematic view of the isolated formation of an individual star presented in the previous Section is an idealistic scenario. It is now well established that most stars belong to multiple systems. Observations have revealed that multiplicity increases with stellar mass, both the number of multiple systems and the number of components of each system (see Duchêne, & Kraus 2013, and references therein). On the other hand, binaries are observed more frequently among pre-main sequence stars than among evolved stars (e.g., Ghez et al. 1993; Reipurth, & Zinnecker 1993), suggesting that some companions are lost as a result of the dynamical evolution of the multiple systems, leading to the ejection of members.

Additionally, massive clumps can form simultaneously groups of stars, such as the embedded Trapezium cluster, in Orion. According to Lada, & Lada (2003), most stars in the Galactic disk may have originated in embedded clusters. An important consequence of the clustered star formation is the stellar feedback, which can favor subsequent star formation (positive feedback) or inhibit it (negative feedback).

It is necessary then to understand how the picture of the isolated formation of an individual star is modified taking into account the effects of possible companions forming simultaneously.

1.2.1 Proposed Mechanisms for Multiple Star Formation

There are two main proposed mechanisms responsible for the formation of multiple stellar systems that appear to operate simultaneously: (1) the fragmentation of a turbulent core (Goodwin et al. 2004; Fisher 2004), which could form both wide and close multiple systems, and (2) the fragmentation of a gravitationally unstable disk (Bonnell 1994; Bonnell, & Bate 1994a,b; Kratter et al. 2010), which mainly forms close multiple systems.

In the first case, turbulent fluctuations within a self-gravitating core can produce multiple non-linear perturbations in density, which collapse faster than the whole core. This would explain the existence of multiple systems with misalignment between the planes of the disks and the binary orbit (Jensen et al. 2004; Scholz et al. 2010; Jensen, & Akeson 2014). According to the simulations of Offner et al. (2014), this process forms binaries with an initial separation $\sim$ 1000 au, that can migrate inward to closer proximity, or outwards and become unbound.

The second case requires a massive ($\gtrsim$ 0.1 $M_{\odot}$) rotationally-supported disk around a protostar, that fragments to form less massive stars. Such disks should be common, but should be sparsely observed because they fragment rapidly (within a few thousand years; Stamatellos, & Whitworth 2009). This process could form binary systems with separations from a few au to a few hundred au. The simulations of Kratter et al. (2010) show that disks fragmentation into binary or multiple systems occurs only when material falls in several times more rapidly than the canonical isothermal limit. They also show that disks with masses lower than half of the total system mass (disk+star) are stable (i.e., do not fragment). A possible example of the fragmentation of a disk was reported by Tobin et al. (2016a). They imaged the dust and molecular gas emission of the triple protostellar system L1448 IRS3B, revealing a disk with a spiral structure surrounding the three protostars. They argued that the disk has likely gone through a recent episode of gravitational instability and fragmentation, based on an analysis of the Toomre parameter (Q) of the system[1].

However, there is a lower limit of $\sim$ 10 - 14 au for the initial separation of a binary system (Bate 2004). This value is determined by the typical radius of the first hydrostatic core, which appears to be $\sim$ 5 - 7 au independently of the initial conditions of the collapsing core (Larson 1969; Vaytet et al. 2012; Vaytet, & Haugbølle 2017). Fragmentation is inhibited inside this first core (Boss 1988; Bate 1998). This limit is called the opacity limit for fragmentation. Since closer binaries do exist, there must be another mechanism for their creation or, at least, for decreasing their separation after their formation.

Close binaries can result from dynamical interactions and orbital decay (Bate 2000). If a flyby-star with enough velocity interacts with a binary system, the latter could be hardened (i.e, decrease its separation) or the 3 stars undergo chaotic interactions (Hut, & Bahcall 1983). These interactions may lead to the ejection of the flyby-star, the formation of an inner binary with a bound tertiary component, or the ejection of the lower mass component of the original system while the flyby-star becomes bound to the other one, with a separation smaller than the original system (Hut, & Bahcall 1983; Bate et al. 2002; Reipurth, & Mikkola 2012). These outcomes are possible if the binding energy of the system is greater than the kinetic energy of the flyby, otherwise, the binary system is destroyed by

[1]For Keplerian disks $Q \approx 2(M_{*}H)/(M_{d}R)$ (Kratter, & Lodato 2016), where M_{*} is the mass of the protostar and M_{d}, R and H are the mass of the disk, its radius, and its scale height, respectively. $Q > 1$ indicates that the disk is stable against gravitational collapse.

the encounter. Thus, successive interactions may create binaries with progressively smaller separations.

Only a few proposed cases of tidal encounters with flybys have been mapped in the millimeter so far (e.g. RW Aurigae: Dai et al. 2015; AS 205: Kurtovic et al. 2018). The most recent being the case of UX Tauri A/C, part of a quadruple system in Taurus (d = 139 pc), imaged in CO by Zapata et al. (2020). According to these authors, UX Tauri C has a close approach of a possible wide, evolving, and eccentric orbit around the disk of UX Tauri A, causing the observed spiral arms in the disk of UX Tauri A and an extended stream of gas connecting this disk to Tauri C disk.

1.2.2 Accretion Disks in Binary Systems

Theoretical work has been done to simulate how the presence of a stellar companion during the accretion process influences the formation and evolution of disks. The simulation by Bate, & Bonnell (1997) has been traditionally regarded as a standard. They modeled the accretion of a protobinary embedded in a gas cloud with initial mass ratio between the primary (more massive) and the secondary component $q = M_s/M_p$ and initial specific angular momentum of the infalling gas j_{inf}. Their simulation showed that circumstellar disks can develop either around a single or both components of the binary and even a circumbinary disk can be formed. A disk will form around a component only if j_{inf} is greater than the specific orbital angular momentum of that component about the center of mass of the binary. Additionally, the size of the circumstellar disk will increase with j_{inf}. For most values of q, they observed a trend with j_{inf} (see Fig. 1.6). If the infall occurs with zero angular momentum (i.e., no rotation), no circumstellar disks are formed. Accretion of material with low j_{inf} results in a circumstellar disk around the primary star, while the secondary remains essentially naked. This would explain the infrared companions (IRCs) found toward some visible T Tauri stars (e.g., HK Tau: Stapelfeldt et al. 1998, T Tau: Koresko 2000). In this scenario, the IRC would be the primary component viewed through its edge-on circumstellar disk, while the visible star would be the secondary. For infall material with higher j_{inf}, the secondary component also develops a circumstellar disk. The value of the specific angular momentum above which the secondary forms a disk depends inversely on q^2. For intermediate values of j_{inf}, two circumstellar disks are formed, and the formation of a circumbinary disk begins. For high enough j_{inf}, the secondary will

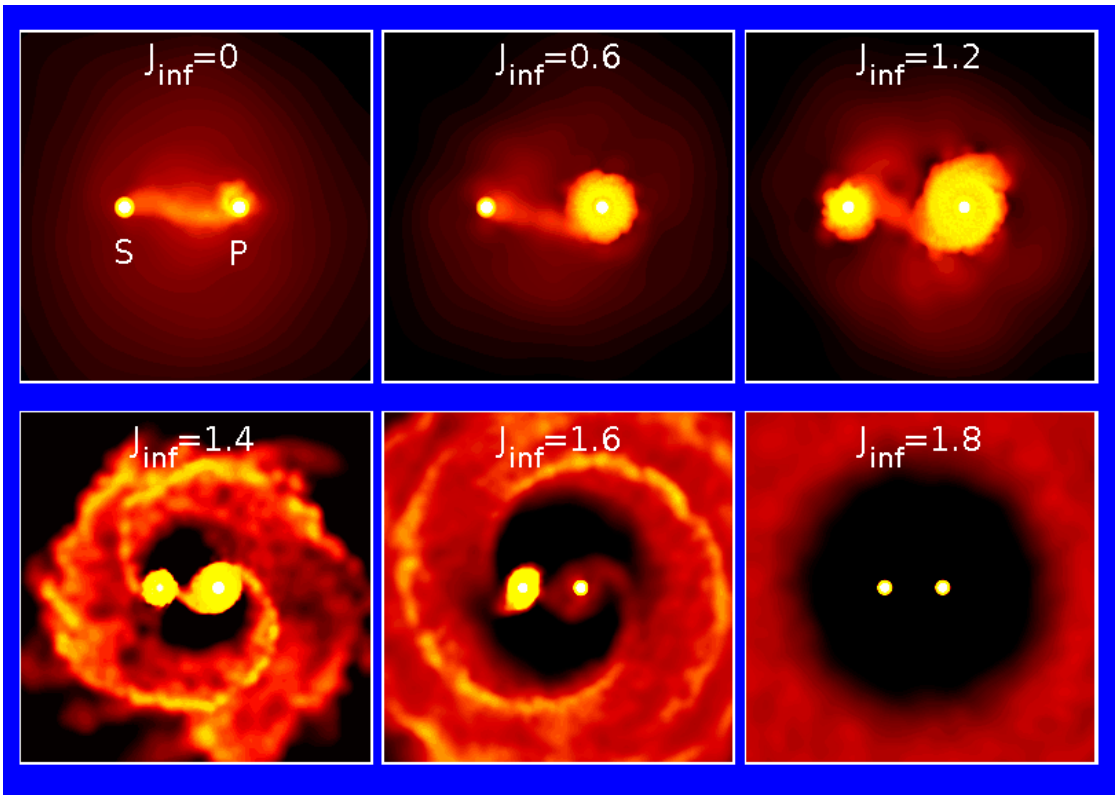

Figure 1.6 Accretion onto a $q = 0.6$ protobinary system (adapted from Bate, & Bonnell 1997). Rotation is anticlockwise. For low values of the specific angular momentum (j_{inf}) most of the infalling material is accreted by the primary (P) protostar, for intermediate values the fraction captured by the primary decreases, and the fraction captured by the secondary (S) increases. For high values, a circumbinary disk begins to form.

accrete more material than the primary. Finally, for material with the highest j_{inf}, all the gas goes into the circumbinary disk, and no circumstellar disks are formed. The circumbinary disk forms with lower j_{inf} for higher q. Also, accretion with low j_{inf} decreases the separation of the binary over time, while accretion of gas with high j_{inf} increases it (Bate 2004).

The role of j_{inf} in the accretion of a binary system has been reexamined by Ochi et al. (2005). In these new simulations, the primary always accretes more than the secondary, even for high values of j_{inf}, contradicting the result of Bate, & Bonnell (1997). They argued that the difference is due to limited spatial resolution and large numerical viscosity in the older simulations. Observations of close binary systems in formation would help to shed light on this issue, but since the components are very embedded they are usually hard to distinguish from each other.

On the other hand, according to Artymowicz & Lubow (1994), the sizes of the circumstellar and circumbinary disks are tidally truncated due to resonant interactions occurring when the period of the binary is proportional to the period of the disk(s) rotation. For nearly circular binaries separated a distance a, the outer edge of the circumprimary and circumsecondary disks are located at $0.5a$ and $0.2a$, respectively, while the inner edge of the circumbinary is truncated approximately at $2a$. The sizes of the circumstellar disks decrease with an increasing eccentricity of the orbit and the circumbinary disk forms at larger distances from the protostars.

Circumstellar disks in multiple systems appear to be smaller than those around single stars and, therefore, will dissipate more rapidly (Bouwman et al. 2006; Kraus et al. 2012). Additionally, radiation from the companion could photoevaporate the circumstellar disk of the other star, truncating its size or even completely destroying it. In fact, several surveys have found a lower fraction of disks in close binary systems (separation $\leq$ 100 au) than in wider binaries and single stars (Bouwman et al. 2006; Cieza et al. 2009; Cheetham et al. 2015; Daemgen et al. 2016; Barenfeld et al. 2019).

An interesting case is the detection of a dwarf (radius $\sim$3 au) circumstellar disk in XZ Tau B (Osorio et al. 2016), the outer component of a hierarchical triple system (Carrasco-González et al. 2009). The disk presents a central cavity (radius $\sim$1 au), which the authors attribute to the presence of a protoplanet. The small size of this disk allows following in real-time its evolution, with observable changes in the order of a few months.

1.2.3 Stellar Feedback: Jets and Outflows

Protostellar jets and outflows are the strongest forms of feedback in low-mass star-forming regions. They shape the structure of the molecular cloud in their vicinity, opening cavities, creating shells or dispersing dense gas essential for star formation. Matzner, & McKee (2000) have shown that outflows can completely disrupt cluster-forming cores. The result of this negative feedback is that star formation is a relatively inefficient process, with only 10 - 30% of the gas in embedded clusters converted into stars (Lada, & Lada 2003).

On the other hand, jets and outflows have been proposed as possible triggers of star cluster formation. As they propagate through their parent molecular cloud, they drive local turbulent compressions that can make dense gas gravitationally unstable, causing its fragmentation and collapse and the subsequent formation of

stars (Li, & Nakamura 2006; Nakamura, & Li 2007). Observationally, is it difficult to discern between dense cores that are spontaneously forming stars, or those in which the collapse has been triggered. The best way is to try to observe the process while it occurs. A few candidates of outflow-triggered star formation have been proposed (Sandell, & Knee 2001; Girart et al. 2001; Yokogawa et al. 2003; Shimajiri et al. 2008, 2009; Nakamura et al. 2019), but none of them have been indisputable confirmed. In some cases, the claim is based only on morphological evidence (i.e. the protostar is located in the tip of an outflow) that could only be a mere projection effect. An important piece of evidence supporting a triggered formation scenario would be the detection of signs of interaction between the outflow and the dense core (e.g. shocks), and the direct imaging of the triggered candidate in the region of the interaction.

1.3 Motivation, Goals, and Methodology of our Work

As we have shown, the presence of a disk-jet system, a consequence of the star formation process, leads to important interactions between the protostar and its environment. However, the first stages in the formation of multiple stars and, in particular, the association with disks and jets is unknown in many aspects, because its study requires observations with very high angular resolution and sensitivity.

In this thesis, we use radiointerferometric observations making it possible to detect emission from very embedded YSOs, with a great angular resolution and sensitivity. Our data have been obtained with the Karl G. Jansky Very Large Array (VLA) of the National Radio Astronomy Observatory (NRAO)[2] and the Atacama Large Millimeter/submillimeter Array (ALMA)[3] at several bands, in continuum and spectral line mode. I have been involved in different aspects of the observing campaigns, from the design of the observation proposals to the reduction (calibration and imaging) of the obtained data. The study at radio wavelengths has been complemented with observational data at other wavelength ranges. We

[2]NRAO is a facility of the National Science Foundation (NSF) operated under cooperative agreement by Associated Universities, Inc.

[3]ALMA is a partnership of ESO (representing its member states), NSF (USA) and NINS (Japan), together with NRC (Canada), MOST and ASIAA (Taiwan), and KASI (Republic of Korea), in cooperation with the Republic of Chile. The Joint ALMA Observatory is operated by ESO, AUI/NRAO and NAOJ.

have used images obtained with *Herschel* and APEX in the far-IR, *Spitzer* in the mid-IR, and the *Hubble* Space Telescope (HST) and NEWFIRM in the near-IR.

In this work, we study two complementary aspects of multiple star formation: the simultaneous formation of protostars in a cluster, and the formation of an individual binary system.

First, we analyze the protostellar content toward the Orion Molecular Cloud 2 (OMC-2), part of the Integral Shaped Filament, in Orion. The Orion Complex constitutes a remarkable laboratory to study the clustered formation of stars and their feedback, such as the triggered star formation, since protostars of low and intermediate mass coexist in different stages of evolution. We complement previous studies of the region made at lower angular resolution in the IR as part of the open-time key program Herschel Orion Protostar Survey (HOPS, e.g. Furlan et al. 2016), and high-resolution submillimeter wavelengths observations of the circumstellar disks in the region (Tobin et al. 2020). Our centimeter observations allow us to detect radio jets that pinpoint the position of YSOs, allowing the identification of embedded multiple systems, and provide an extinction-free census of outflow (and thereby accretion) activity.

Additionally, we study the close binary system SVS 13, in NGC 1333. The components of this system, separated ∼90 au, appear to have different characteristics, since one of them is associated with dust emission, likely from an accretion disk, while the other one is not (Anglada et al. 2000, 2004). Our centimeter observations allow us to detect the two components of the system, while the submillimeter observations allow us to probe the circumstellar material around them at different scales. We make a detailed analysis of the system, investigating how the standard view of star formation has been modified in this particular case.

Our results are presented as follows:

- In Chapter 2 we present multiwavelength (0.7 - 5 cm) and multi-epoch (1994 - 2015) VLA observations toward the region enclosing the bright far-IR sources FIR 3 (HOPS 370) and FIR 4 (HOPS 108) in OMC-2. We report the detection of a non-thermal lobe associated with the HOPS 370 thermal jet. We present strong new evidence supporting the triggered formation of HOPS 108. This chapter has been published entirely in Osorio et al. (2017).

- In Chapter 3 we extend our analysis to our whole field of view (∼ 12.′5) of the observations presented in the previous Chapter, making a census of the young stellar population toward OMC-2/3. This is the most sensitive study

in centimeter wavelengths of the region up to date. We investigate the nature of the 57 radio sources detected, finding that 41 (72%) are associated with the star-forming region. Our high resolution allows us to separate different components of what were previously considered individual objects. With the aid of complementary IR observations, we are able to present a comprehensive picture of several of the detected YSOs and their closest environment.

- In Chapter 4 we present multiwavelength (0.7 - 3 cm) continuum VLA observations, and continuum and line ALMA 0.9 mm observations of the close binary system SVS 13. We detect the circumstellar disks of both components of the system, as well as the circumbinary disk in formation, in which spiral features are detected, and study their kinematics. We are able to estimate physical parameters such as the masses of the stellar components of the system, of their circumstellar disks and of the circumbinary disk/inner envelope of dust and gas. We report the detection of Complex Organic Molecules toward the system, implying it is a hot molecular corino.

- In Chapter 5 we summarize our results and outline the future work.

1.3.1 List of Publications

The work presented in this thesis has originated the following publications:

- *"Star Formation Under the Outflow: The discovery of a Non-Thermal Jet from OMC-2 FIR3 and its Relationship to the Deeply Embedded FIR 4 Protostar"*
  Osorio, M., **Díaz Rodríguez, A. K.**, Anglada, G., Megeath, T., Rodríguez, L. F., Tobin, J. J., Stutz, A. M., Furlan, E., Manoj, P., Gómez, J. F., Laurent, L., 2017, The Astrophysical Journal, 840, 36

- *"Multifrequency deep radio continuum VLA observations toward OMC-2/3"*
  Díaz Rodríguez, A. K., Osorio, M., Anglada, G., Megeath, T., Stutz, A. M., Tobin, J. J., Furlan, E., Gómez, J. F., Rodríguez, L. F., Fischer, W. J., and et al., in preparation.

- *"Exploring the Early Stages of Formation of Disks and Outflows in Uneven Close Binary Systems. The Case of SVS 13"*
  Díaz Rodríguez, A. K., Osorio, M., Anglada, G. et al., in preparation.

Other publications related to this thesis are:

- *"Analysis and test of the central-blue-spot infall hallmark"*
  Estalella, R., Anglada, G., **Díaz-Rodríguez, A. K.** and Mayen-Gijon, J. M., 2019, A&A, 626, A84

- *"Herschel/PACS far-IR spectral imaging of a jet from an intermediate mass protostar in the OMC-2 region"*
  Gonzalez-Garcia, B., Manoj, P., Watson, D. M., Vavrek, R., Megeath, S. T., Stutz, A. M., Osorio, M., Wyrowski, F., Fischer, W., Tobin, J. J., Sanchez-Portal, M., **Díaz Rodríguez, A. K.**, Wilson T. L., 2016, A&A, 596, A26.

- *"Detection of Irregular, Sub-mm Opaque Structures in the Orion Molecular Clouds: Protostars within 10000 years of formation?"*
  Karnath, N., Megeath, S. T., Tobin, J., Stutz, A., Li, Z. Y., Sheehan, P., Reynolds, N., Sadavoy, S., Stephens, I., Osorio, M., Anglada, G., **Díaz-Rodríguez, A. K.** and Cox, E., 2020, ApJ, 890, 129

- *"The VLA/ALMA Nascent Disk and Multiplicity (VANDAM) Survey of Orion Protostars. I. Identifying and Characterizing the Protostellar Content of the OMC2-FIR4 and OMC2-FIR3 Regions"*
  Tobin, J. J., Megeath, S. T., van't Hoff, M., **Díaz-Rodríguez, A. K.**, Reynolds, N., Osorio, M., Anglada, G., Furlan, E., Karnath, N., Offner, S. S. R., Sheehan, P., Sadavoy, S. I., Stutz, A. M., Fischer, W. J., Kama, M., Persson, M., Di Francesco, J., Looney, L. W., Watson, D. M., Li, Z. Y., Stephens, I., Chandler, C. J., Cox, E., Dunham, M. M., Kratter, K., Kounkel, M., Mazur, B., Murillo, N., Patel, L., Perez, L., Segura-Cox, D., Sharma, R., Tychoniec, L., and Wyrowski, F., 2019, ApJ, 886, 6

- *"The VLA/ALMA Nascent Disk and Multiplicity (VANDAM) Survey of Orion Protostars. A Statistical Characterization of Class 0 and I Protostellar Disks"*
  Tobin, J. J., Sheehan, P., Megeath, S. T., **Díaz-Rodríguez, A. K.**, Offner, S. S. R., Murillo, N. M., van't Hoff, M., van Dishoeck, E. F.,Osorio, M., Anglada, G., Furlan, E., Stutz, A. M., Reynolds, N., Karnath, N., Fischer, W. J., Persson, M., Looney, L. W., Li, Z. Y., Stephens, I., Chandler, C. J., Cox, E., Dunham, M. M., Tychoniec, L., Kama, M., Kratter, K., Kounkel, M., Mazur, B., Maud, L., Patel, L., Perez, L., Sadavoy, S. I., Segura-Cox,

D., Sharma, R., Stephenson, B., Watson, D. M. and Wyrowski, F., 2020, ApJ, 890, 130

- *"The VLA/ALMA Nascent Disk and Multiplicity (VANDAM) Survey of Orion Protostars IV. Unveiling the Embedded Intermediate-Mass Protostar and Disk within OMC2-FIR3/HOPS-370"*
  Tobin, J. J.; Sheehan, P.; Reynolds, N.; Megeath, S. T.; Osorio, M.; Anglada, G.; **Diaz-Rodriguez, A. K.**; Furlan, E.; Kratter, K.; Offner, S.; Looney, L.; Kama, M.; Li, Z. Y.; van 't Hoff, M.; Sadavoy, S.; Karnath, N., 2020, Accepted to ApJ.

Chapter 2

The Discovery of a Non-Thermal Jet from OMC-2 FIR 3 and its Relationship to the Deeply Embedded FIR 4 Protostar

2.1 Introduction

OMC-2 is an active star-forming region (e.g., Peterson & Megeath 2008) in the Orion A molecular cloud, located at a distance of 414 ± 7 pc (Menten et al. 2007; Kim et al. 2008; Kounkel et al. 2017). Mezger et al. (1990) identified six bright mm/IR sources (FIR 1-6) within a region of about 6′ in size that have been associated with YSOs through subsequent studies (Adams et al. 2012, Furlan et al. 2014, 2016 and references therein). The region has been imaged at mm and sub-mm wavelengths by Chini et al. (1997) and Lis et al. (1998), and in the near and mid-IR by Tsujimoto et al. (2003a), Nielbock et al. (2003), and Megeath et al. (2012). At mm and sub-mm wavelengths, the brightest source is FIR 4, which has been associated with the HOPS 108 Class 0 protostar (Adams et al. 2012, Furlan et al. 2016)[1]. This source is connected through a filamentary cloud structure to the bright source FIR 3, also known as HOPS 370, an intermediate-mass Class I YSO with an $L_{\rm bol} \sim 360\ L_{\odot}$ (Adams et al. 2012, Furlan et al. 2016) located about 30″ to the NE (see Fig. 2.1 for the positions and nomenclature of the sources). The region was observed with the VLA at 3.6 cm in the D configuration (angular resolution ∼ 8″) by Reipurth et al. (1999). These authors found a weak elongated source (VLA 12) toward FIR 4 (HOPS 108) that was interpreted as a radio jet

[1] In low-resolution observations, FIR 4 probably includes emission from other nearby objects.

originating from this protostar. A stronger, but unresolved source (VLA 11), was detected toward FIR 3 (HOPS 370).

The nature of the source FIR 4 is still uncertain. Shimajiri et al. (2008), through mm and sub-mm observations, proposed that FIR 4 was composed of 11 dusty cores. These authors detected molecular line emission from shock tracers (SiO and CH_3OH) in the proximity of FIR 4 and proposed that the interaction of a powerful molecular outflow driven by FIR 3 (e.g., Williams et al. 2003, Takahashi et al. 2008) with a dense clump could be triggering the formation of a next generation of stars at the position of FIR 4. On the other hand, López-Sepulcre et al. (2013), based on 2 mm observations, proposed that FIR 4 was composed of at least three cores, and suggested that its associated 3.6 cm source VLA 12 traces an HII region photoionized by an early-type (B3 - B4) star with a luminosity of 700 - 1000 $L_\odot$ embedded within one of these cores. A bolometric luminosity $L_{\rm bol} \simeq 1000\ L_\odot$ for FIR 4 was obtained by Crimier et al. (2009) but this estimate, based on low angular resolution IRAS data, is very uncertain because of the difficulties in separating the emission of the protostar from that of the surrounding molecular cloud and other neighboring objects.

In a rigorous analysis of the available photometry of HOPS 108, including Herschel measurements that constrain better the peak of the SED than the IRAS fluxes, Furlan et al. (2014) give $L_{\rm bol} = 37\ L_\odot$. This is much lower than the earlier estimate by Crimier et al. (2009) or the value adopted by López-Sepulcre et al. (2013). Due to uncertainties in the amount of external heating and the inclination of the protostar, Furlan et al. (2014) find that they can fit the SED with models having values for the intrinsic total luminosity[2] ranging from 15 $L_\odot$ to 540 $L_\odot$, although models with luminosities $\leq 100\ L_\odot$ are favored.

Manoj et al. (2013) detected far-IR CO lines indicative of shock-heated gas at high temperatures (> 2000 K) toward both HOPS 108 and HOPS 370. Recently, González-García et al. (2016) imaged in far-IR [OI] lines and in the sub-mm CO (6-5) line, a powerful ($\dot{M} \simeq 2 \times 10^{-6}\ M_\odot\ {\rm yr}^{-1}$, as estimated by these authors) bipolar jet/outflow originating from HOPS 370. The outflow extends to the NE of HOPS 370 (FIR 3) in the direction where a 4.5 μm Spitzer/IRAC image (which traces shock-excited H_2 emission) shows an extended jet that terminates in a bow shock (Megeath et al. 2012). To the SW, the outflow terminates near the location

[2]The intrinsic total luminosity of a source and its bolometric luminosity derived from the observed flux densities can differ in the case of an inhomogeneous surrounding medium (e.g., if outflow cavities are present) resulting in an anisotropic radiation field where the observed flux density depends on inclination angle (see Furlan et al. 2016).

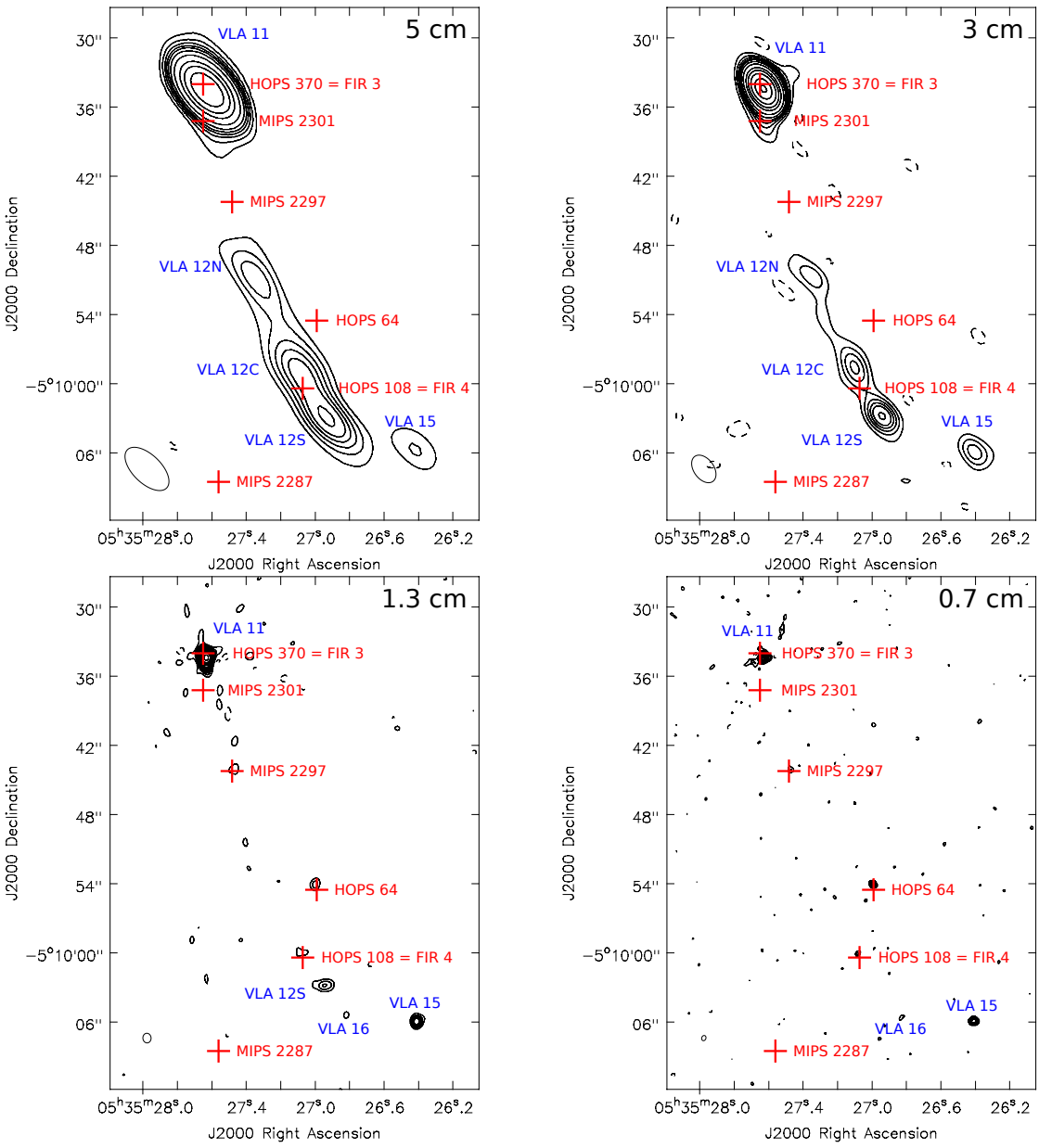

Figure 2.1 VLA C-configuration maps (epoch 2014) of the region around the HOPS 108 protostar. Contour levels are −3, 3, 6, 9, 12, 15, 20, 30, 50, 70, 100, 150, and 200 times the rms noise of each map. The robust weighting parameter (Briggs 1995) was set to 0. The synthesized beam is shown at the bottom left corner of each map. The 10.4 μm positions (Nielbock et al. 2003) are indicated by red plus signs whose size corresponds to the positional uncertainty. For HOPS 108, which is not reported at 10.4 μm, the 24 μm position (Megeath et al. 2012) is given. Top left: C band (5 cm); rms = 11 μJy beam^{-1}; HPBW = 4.″75 × 2.″46, P.A. = 46°. Top right: X band (3 cm); rms = 9 μJy beam^{-1}; HPBW = 2.″68 × 1.″73, P.A. = 36°. Bottom left: K band (1.3 cm); rms = 10 μJy beam^{-1}; HPBW = 0.″84 × 0.″71, P.A. = 5°. Bottom right: Q band (0.7 cm) map; rms = 15 μJy beam^{-1}; HPBW = 0.″46 × 0.″36, P.A. =−20°.

of HOPS 108, with a bright [OI] emission peak that González-García et al. (2016) argue originates in the terminal shock produced by the jet.

In summary, Shimajiri et al. (2008), López-Sepulcre et al. (2013), and González-García et al. (2016) suggest that the protostar HOPS 108 results from the interaction of an outflow driven by HOPS 370 with a dense clump. Within this scenario, López-Sepulcre et al. (2013) assume that a star cluster is being formed, with the radio source VLA 12 tracing an HII region associated with the most massive star; for this star, they adopt a luminosity of $\sim 1000\ L_{\odot}$, similar to earlier estimates of Crimier et al. (2009). On the other hand, Furlan et al. (2014), Reipurth et al. (1999), and Adams et al. (2012) interpret VLA 12 as a radio jet driven by a modest luminosity protostar associated with HOPS 108.

In this Chapter, we analyze new and archive VLA observations that shed new light on the origin of the HOPS 108 protostar, the nature of its radio emission, and its relationship with other nearby sources.

2.2 Observations

The observations were carried out with the VLA in the C configuration in 2014 (Project 14B-296) at C (5 cm), X (3 cm), K (1.3 cm), and Q (0.7 cm) bands, and in the A configuration in 2015 (Project 15A-369) at C band (5 cm). In both cases, the phase center was close to the position of HOPS 108. Further details of the observational setup are given in Table 2.1. The data were edited and calibrated using the Common Astronomy Software Applications (CASA; version 4.2.2) package.

We also analyzed several epochs of VLA archive data at X-band (3.6 cm) obtained with different configurations between 1994 and 2000 (see Table 2.1 for details). These data were edited and calibrated using the Astronomical Image Processing System (AIPS), and then were concatenated using the CASA package.

All the images were made with the CASA task CLEAN using multi-frequency synthesis (Conway et al. 1990) and fitting the frequency dependence of the emission with a Taylor series expansion with nterms = 2 during the deconvolution. There is extended emission of the bright HII region M43 (NGC 1982) $\sim 5'$ to the south of HOPS 108 that makes it difficult the imaging of the archive (X-band) data and the new data at C band. In order to do a proper cleaning of our target sources, we downweighted the extended emission by removing the shortest baselines. For the archive and the 2014 C-band data, we used only baselines > 5 kλ and the multiscale

deconvolution algorithm to make the images. For the 2015 A-configuration data, which are more sensitive, we used only baselines > 25 kλ.

2.3 Results and Discussion

In our new data of epochs 2014 and 2015, we detect the radio sources VLA 11, VLA 12, and VLA 13 previously reported at 3.6 cm by Reipurth et al. (1999), but our observations cover additional bands and are more sensitive, revealing further details. The FWHM of our primary beam, centered near VLA 12, ranges from $\sim 1'$ at Q-band to $\sim 8'$ at C band. Therefore, we detected additional sources, including several of the IR sources in the field. In this Chapter we will discuss only the sources detected in the proximity (within $< 30''$) of HOPS 108. Positions of these sources are given in Table 2.2. The remaining detected sources will be discussed in Chapter 3.

2.3.1 Identification of the Detected Sources

In Figure 2.1 we show the maps of VLA 11 and VLA 12 at different wavelengths obtained in our 2014 VLA C-configuration observations. VLA 12 (in the proximity of FIR 4/HOPS 108) is clearly detected as a very elongated source at 5 and 3 cm, showing three knots that we call VLA 12N, VLA 12C, and VLA 12S, for the northern, central, and southern observed emission peaks, respectively. At first glance, these results appear to confirm VLA 12 as a radio jet, as was first suggested by Reipurth et al. (1999). These knots coincide with the southern, brightest part of the jet/outflow traced by the far-IR [OI] and sub-mm CO (6-5) lines, which is assumed to originate in HOPS 370 (González-García et al. 2016; see Fig. 2.2, left). The IR position of the HOPS 108 protostar (Megeath et al. 2012) falls close to (within $\sim 2''$) the position of knot VLA 12C, apparently favoring HOPS 108 as the driving source of the proposed VLA 12 radio jet.

At shorter wavelengths (1.3 and 0.7 cm; bottom panels in Fig. 2.1) the emission of the VLA 12 knots decreases making them undetectable, indicating that they have a negative spectral index α (where $S_\nu \propto \nu^\alpha$), characteristic of non-thermal emission. This is confirmed by the analysis of the spectra obtained from our full dataset (Table 2.3, Fig. 2.3). Despite the possible time variability both in flux density (that can be more prominent in non-thermal emission) and morphology, as well as the difficulties inherent in the measure of extended emission from data

Table 2.1 Parameters of the VLA Observations

Date	VLA Conf	Band	Central Frequency (GHz)	Bandwidth (GHz)	Project	Phase Center α(J2000)	Phase Center δ(J2000)	Flux Calibrator	Adopted Flux Density (Jy)	Phase Calibrator	Bootstrapped Flux Density (Jy)	On-Source Time (hours)
1994Nov 17	C	X	8.4649	0.100	AR0323S	05 35 25.825	−05 09 51.38	3C286	5.06	J0541-0541	1.240±0.010	0.5
1998 Jan 13	D	X	8.4851	0.100	AR0387	05 35 24.220	−05 10 07.27	3C48	3.15	J0541-0541	0.7420±0.0010	1.0
2000 Jan 14	B	X	8.4851	0.100	AR0411	05 35 26.970	−05 10 01.20	3C48	3.28	J0541-0541	1.2990±0.0030	3.2
2014 Oct 16	C	K	22.000	8.048	AM1313	05 35 27.070	−05 10 00.60	3C147	2.78	J0541-0541	0.7188±0.0010	1.4
2014 Oct 16	C	Q	44.063	8.048	AM1313	05 35 27.070	−05 10 00.60	3C147	0.91	J0541-0541	0.5234±0.0006	0.6
2014 Oct 18	C	C	6.000	4.048	AM1313	05 35 27.070	−05 10 00.60	3C147	7.94	J0541-0541	0.9260±0.0013	0.5
2014 Oct 18	C	X	10.000	4.048	AM1313	05 35 27.070	−05 10 00.60	3C147	4.84	J0541-0541	0.9050±0.0006	0.5
2015 Aug 06	A	C	6.000	4.048	AO0316	05 35 27.080	−05 10 00.30	3C147	7.94	J0541-0541	1.161±0.04	0.5
2015 Sep 11	A	C	6.000	4.048	AO0316	05 35 27.080	−05 10 00.30	3C147	7.94	J0541-0541	1.066±0.04	0.5

Table 2.2 Positions of the Radio Sources

Source	Alternative Names	Nature	Ref.	Position[a] α(J2000)	Position[a] δ(J2000)
VLA 11	FIR 3, HOPS 370, MIPS 2302, MIR 21	Class I YSO	1	05 35 27.6337±0.0007	−05 09 34.368±0.011
MIPS 2301	MIR 22	YSO	2	05 35 27.639±0.008	−05 09 37.09±0.12
MIPS 2297	MIR 23	Class II YSO	2	05 35 27.4711±0.0020	−05 09 44.06±0.03
VLA 12N		Jet knot	3	05 35 27.385±0.011	−05 09 50.68±0.16
HOPS 64	MIPS 2293, MIR 24, FIR 4d/e	Class I YSO	1	05 35 26.9960±0.0023	−05 09 54.060±0.034
VLA 12C		Jet knot	3	05 35 27.111±0.012	−05 09 58.57±0.18
HOPS 108	FIR 4, MIPS 2289	Class 0 YSO	1	05 35 27.086±0.004	−05 09 59.95±0.06
VLA 12S		Jet knot	3	05 35 26.9389±0.0017	−05 10 02.876±0.025
VLA 16		YSO	3	05 35 26.8243±0.0028	−05 10 05.64±0.04
VLA 15	FIR 4j	YSO	3	05 35 26.4091±0.0011	−05 10 05.951±0.016

[a] Positions derived from elliptical Gaussian fits in the A-configuration C-band map of epoch 2015, except for MIPS 2301 and MIPS 2297 that are not detected in this map, and whose positions were derived from the 1994 - 2000 X-band and the 2014 Q-band maps, respectively. Uncertainties correspond to those of absolute positions and are calculated adding in quadrature a systematic error of 0.″01 (Dzib et al. 2017) to the formal error of the fit, $0.5\,\theta/\mathrm{SNR}$ (Reid et al. 1988). The systematic error accounts for uncertainties introduced by the phase calibration process and the error of the fit for those due to the source size and signal-to-noise ratio.

References — (1) Furlan et al. 2016; (2) Megeath et al. 2012; (3) This work.

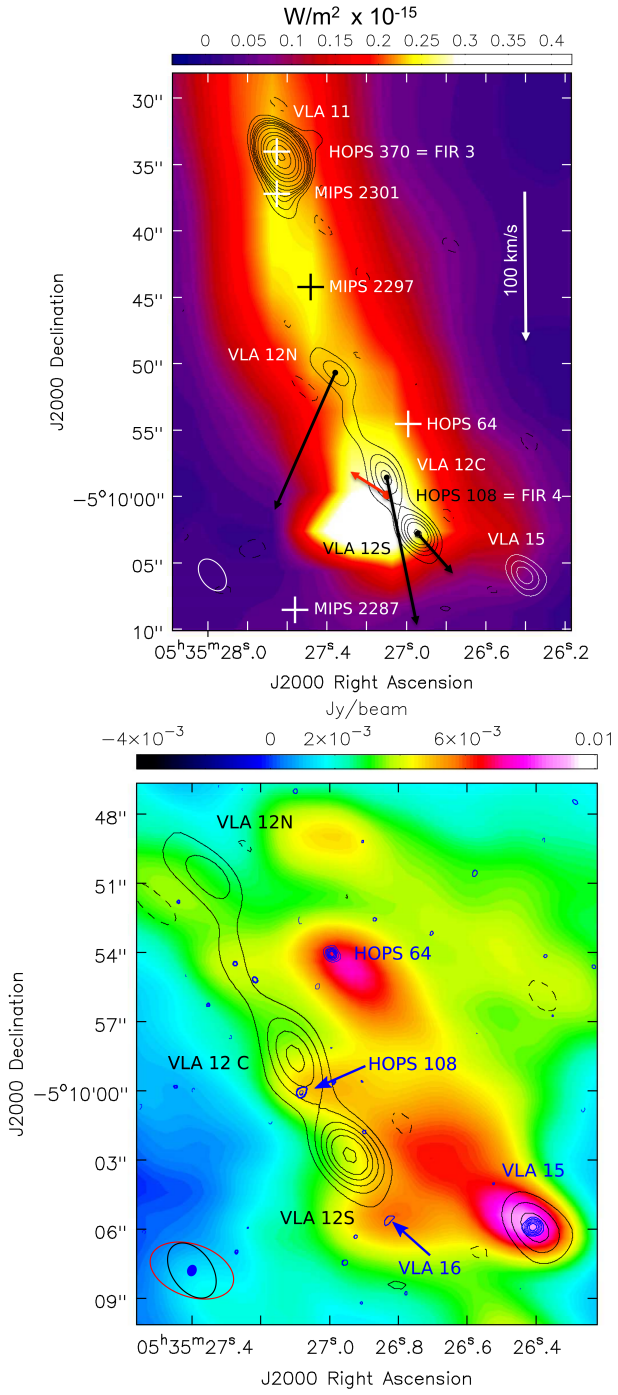

Figure 2.2 *Left panel:* Image of the [OI] 63 μm line emission (color scale, González-García et al. 2016) overlaid on the 3 cm emission VLA map (contours, see Fig. 2.1) with proper motions indicated by arrows. Both images are tracing the jet ejected from HOPS 370. Note that the [OI] 63 μm emission peaks close to the position of HOPS 108, suggesting that this protostar has been formed in a region where a strong shock interaction between the jet and the ambient medium is taking place. Plus signs indicate the positions of IR sources. *Right panel*: ALMA image of the dust emission at 3 mm (color scale, Kainulainen et al. 2017) overlaid on the VLA maps at 3 cm (black contours) and 0.7 cm (blue contours, see Fig. 2.1). Note that the radio jet at 3 cm appears to delineate the eastern edge of the dust clump traced by the ALMA image.

taken with different angular resolutions, the obtained spectral indices in the centimeter range are negative for the three knots of VLA 12, with values of -1.1, -1.3, and -0.6. The behavior is clear even if only the C-configuration data from October 2014, which were taken almost simultaneously, are considered. Also, we have checked in these data that the negative spectral indices obtained are not spurious results of differences in the uv coverage and/or angular resolution, which could make data at shorter wavelengths less sensitive to extended emission. To do that, we obtained pairs of images of contiguous bands using only baselines in the same uvrange. Using these pairs of maps we confirmed that the flux density truly decreases at shorter wavelengths, resulting in negative spectral indices for the VLA 12 knots. These negative spectral indices cannot be explained by thermal emission (see Rodríguez et al. 1993) and should be attributed to non-thermal emission, probably arising from relativistic electrons accelerated in strong shocks (Carrasco-González et al. 2010; see below). This rules out the HII region scenario proposed by López-Sepulcre et al. (2013) for VLA 12.

Although the position of the knot VLA 12C at 6 and 3 cm appears somewhat ($\sim 1\farcs5$) displaced to the NE of the position of HOPS 108 (as obtained from 24 and 8 μm data; Megeath et al. 2012), at 1.3 and 0.7 cm the radio emission appears to be closer to the HOPS 108 IR position (see Fig. 2.1). This shift in the position could indicate either an opacity gradient or that the radio emission observed at shorter wavelengths originates in a different object than the emission observed at longer wavelengths. This last suggestion is confirmed by our data of subarcsecond angular resolution at long wavelengths (Fig. 2.4) that reveal two radio sources spatially separated by $\sim 2''$. We identify the northeasternmost of these two radio sources with the VLA 12C knot and the other source, whose position coincides with the IR source, with the radio counterpart of the HOPS 108 protostar. Recent ALMA observations with an angular resolution of $0\farcs12$ (Tobin et al. 2019) reveal a compact source at 870 μm whose position coincides within $< 0\farcs1$ with the cm position (Table 2.3) confirming the nature of HOPS 108 as a protostar and its association with the cm radio source. Furthermore, the spectral index of HOPS 108 obtained from the cm data that separate its emission from that of VLA 12C shows that HOPS 108 has a positive spectral index ($\alpha = 0.66 \pm 0.29$; Table 2.3 and Fig. 2.3) and, thus, it is associated with thermal (free-free) emission, in contrast to the knots of VLA 12, whose emission is non-thermal. From the empirical correlation between cm flux density and bolometric luminosity for protostellar objects, $(S_\nu\, d^2/\mathrm{mJy\,kpc^2}) = 0.008\,(L_\mathrm{bol}/L_\odot)^{0.6}$ (Anglada et al. 2015), and using

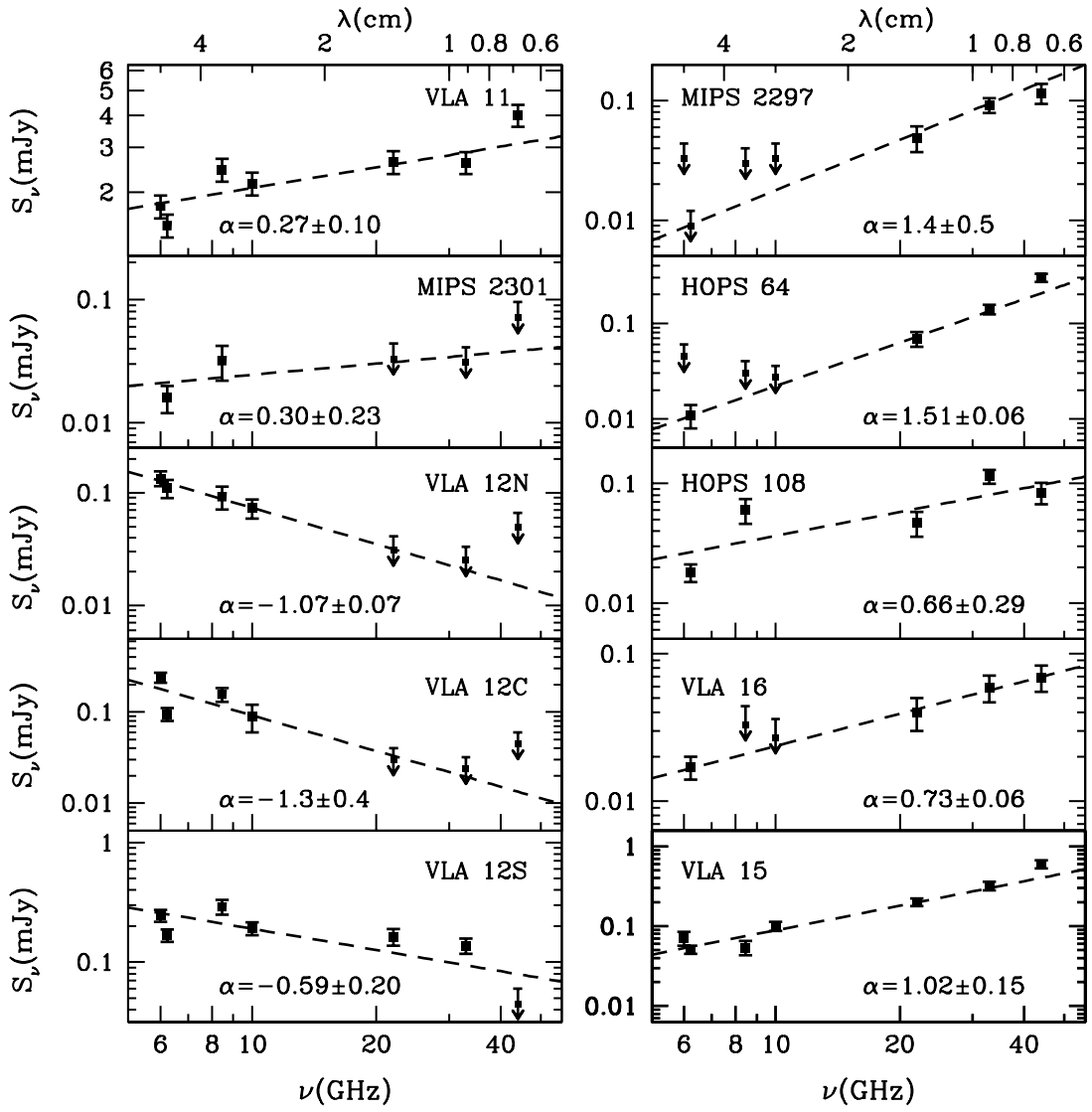

Figure 2.3 Spectra of the detected VLA sources. Error bars are 1σ. Upper limits are represented by arrows where the central symbol is at 3σ. Dashed lines represent least-squares fits. To avoid possible dust contamination the 0.7 cm data point has been excluded in the fitting for the positive spectral index sources. Upper limits have been taken into account only when they constrain the fit.

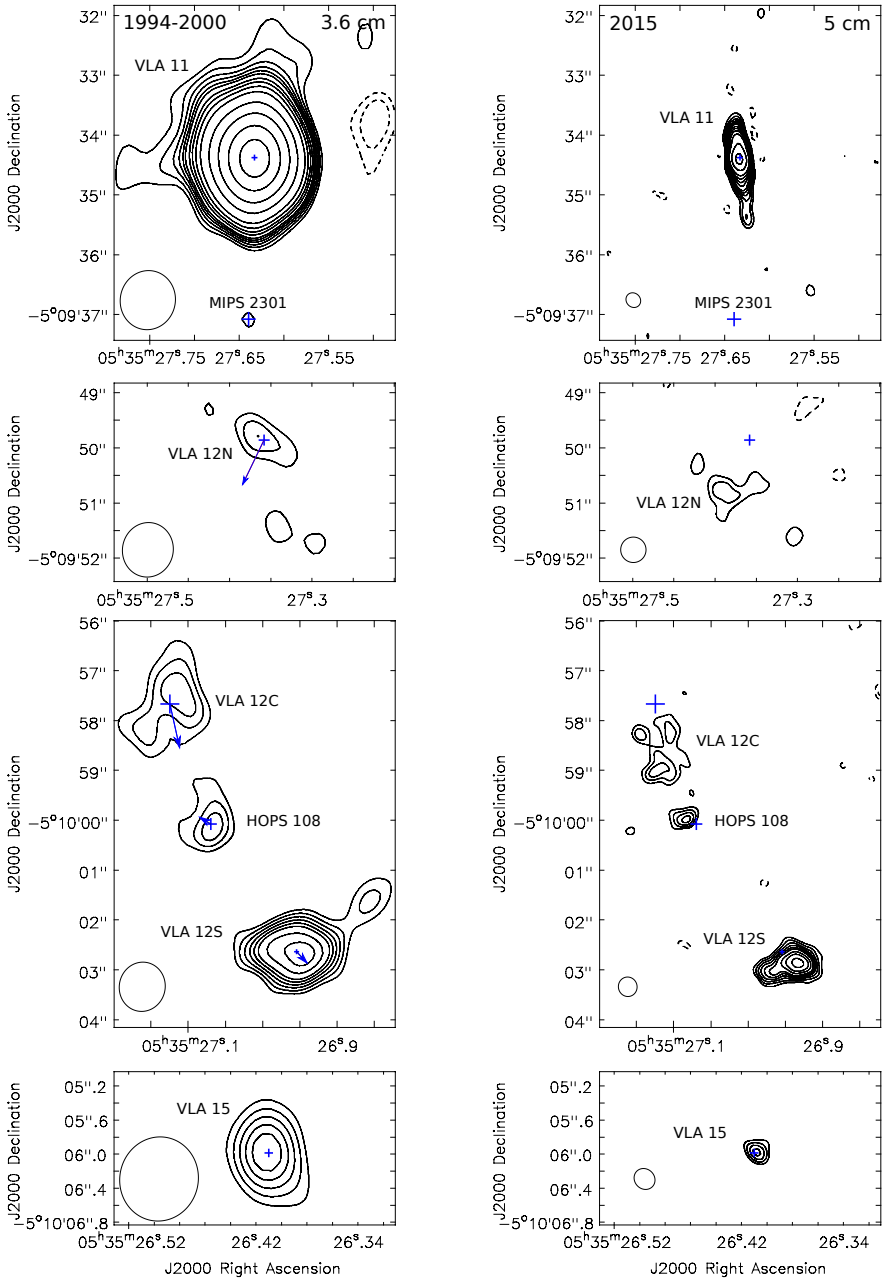

Figure 2.4 Proper motions of the VLA sources. First epoch maps (X band; left panels) were obtained by combining archive data from 1994 to 2000 (Table 2.1). Second epoch maps (C band; right panels) were obtained from the 2015 data. Different weightings have been used to better emphasize the emission of each source. Synthesized beams of $\sim 0\farcs95$ and rms of ~ 10 μJy beam^{-1} were obtained for the first epoch maps, while synthesized beams of $\sim 0\farcs24$ - $0\farcs46$, and rms of 3 - 8 μJy beam^{-1} were obtained for the second epoch maps. Contour levels are -4, -3, 3, 4, 5, 6, 7, 8, 10, 12, 15, 20, 35, 60, 100, and 150 times the rms noise of each map. Positions of the sources derived from elliptical Gaussian fits to the first epoch maps are marked with blue plus signs, whose sizes represent their positional errors. Arrows indicate the displacement between the two epochs.

our measured flux density at 3 cm (Table 2.3), we estimate a bolometric luminosity $L_{\rm bol} \simeq 7\ L_{\odot}$ for HOPS 108. This value of the bolometric luminosity is close to the lowest end of the range considered by Furlan et al. (2016) in the modeling of this object, being much smaller than early estimates ($L_{\rm bol} \simeq 1000\ L_{\odot}$; Crimier et al. 2009; López-Sepulcre et al. 2013) that were based on very low angular resolution data, and significantly smaller than the value obtained if the contribution of the VLA 12 knots is not removed ($L_{\rm bol} \simeq 100\ L_{\odot}$; Furlan et al. 2014). Thus, separating the emission of HOPS 108 from that of the VLA 12 knots confirms HOPS 108 as a low-luminosity object.

The radio source VLA 11, which was associated with FIR 3 (HOPS 370) and reported as unresolved by Reipurth et al. (1999), is clearly resolved as a very elongated bipolar radio jet along a P.A. $\simeq 5^{\circ}$ in our A-configuration data at 5 cm (Fig. 2.4). The radio source is also resolved in the 3.6 cm image obtained by combining archive data from 1994 - 2000. The spectral index is $\alpha = 0.27 \pm 0.10$ (Table 2.3, Fig. 2.3), which is a reasonable value for a thermal free-free radio jet (Anglada 1996). HOPS 370 is known to be associated with an outflow extending along a P.A. similar to that of the radio jet (González-García et al. 2016; see Fig. 2.2, left). The morphology of VLA 11 appears to change in the 0.7 cm image (Fig. 2.1), which shows weak extended emission in a direction perpendicular to the jet, suggesting a noticeable dust contribution at this wavelength. To prevent dust contamination, the 0.7 cm data point has been excluded in the fits to determine the spectral index of this and the remaining thermal sources.

In the lower resolution images at 6 and 3 cm (Fig. 2.1), VLA 11 appears blended with the radio emission of MIPS 2301 (Megeath et al. 2012, an IR source also known as MIR 22, Nielbock et al. 2003) located $\sim 3''$ south of VLA 11. MIPS 2301 is well separated, but only marginally detected, in the higher resolution 3.6 cm image shown in Figure 2.4 and in the A-configuration images at 5 cm obtained with the robust weighting parameter set to values > 1 (not shown in Fig. 2.4). Note that MIPS 2301 is not aligned along the VLA 11 jet axis (P.A. $= 5^{\circ}$). Thus, its radio emission can be distinguished from the knots of the radio jet in the high angular resolution images. With the data currently available, we obtain a positive spectral index, $\alpha = 0.30 \pm 0.23$ (Table 2.3, Fig. 2.3), consistent with thermal free-free emission from a YSO. More sensitive observations are required for a better characterization of the nature of the radio emission of this object.

The source MIPS 2297 (Megeath et al. 2012, also known as MIR 23, Nielbock et al. 2003) is marginally detected at 1.3 cm and 0.7 cm (Fig. 2.1), but clearly detected

in the 0.9 cm observations of Tobin et al. (2019). It shows a positive spectral index ($\alpha = 1.5 \pm 0.5$) in the cm regime (Table 2.3 and Fig. 2.3), confirming its nature as a YSO. So far, MIPS 2297 has not been studied in great detail, but it is classified as a young star with disk (Class II) by Megeath et al. (2012).

We also detect HOPS 64 (Fig. 2.1), a Class I object (Furlan et al. 2016) that in the cm range presents a positive spectral index of $\alpha = 1.51 \pm 0.06$ (Table 2.3, Fig. 2.3), suggesting optically-thick free-free emission from a YSO. The position of the radio source falls in between the FIR 4d and FIR 4e cores imaged by Shimajiri et al. (2008) and is close to, but slightly displaced from, one of the main emission peaks of the dust cloud imaged by ALMA at 3 mm (Kainulainen et al. 2017; see Fig. 2.2, right). Nevertheless, the position of the radio source coincides accurately (within $< 0\farcs1$) with that of a compact 870 μm source recently detected with ALMA (Tobin et al. 2019).

A few arcsec to the SW of the knot VLA 12S we detect a weak source. The source has not been reported previously at other wavelengths and we call it VLA 16. The detection is marginal in the individual bands ($\sim 5\sigma$ at most) but we consider that the source is real because it appears in four of the five observed bands (see Table 2.3). The spectral index is ~ 0.7 (Fig. 2.3), consistent with that of a YSO/jet. The position of the radio source falls near a secondary emission peak in the 3 mm ALMA image (Kainulainen et al. 2017) shown in Figure 2.2 and coincides very well (within $< 0\farcs1$) with the position of a weak 870 μm source recently detected with ALMA observations of higher angular resolution (Tobin et al. 2019). From the empirical correlation between cm emission and bolometric luminosity (Anglada et al. 2015) we infer $L_{\rm bol} \simeq 1\ L_{\odot}$. All these results confirm the reality of the source VLA 16 and its nature as an embedded low-luminosity YSO.

Finally, we report the detection in all the observed bands of a compact source, located $\sim 8.5''$ SW of VLA 12S, and that we call VLA 15 (Tables 2.2, 2.3, Figs. 2.1, 2.3, 2.4). The position of the source coincides with the FIR 4j core imaged by Shimajiri et al. (2008) and falls close to (but slightly offset from) one of the main emission peaks of the dust cloud imaged at 3 mm by ALMA (Kainulainen et al. 2017; see Fig. 2.2, right). No counterparts at other wavelengths had been reported so far, but the source has been recently imaged at 870 μm with ALMA (Tobin et al. 2019). The radio source has a positive spectral index ($\alpha = 1.02 \pm 0.15$) and we suggest that it traces a very young embedded stellar object associated with the OMC-2 star-forming region that deserves further study at other wavelengths.

Table 2.3 Flux Densities and Proper Motions of the Sources

	Flux Density[a]						Proper Motions[d]			
Source	5 cm (mJy)	3 cm (mJy)	1.3 cm (mJy)	0.9 cm[b] (mJy)	0.7 cm (mJy)	Spectral Index[c]	$\mu_\alpha \cos\delta$ (mas yr^{-1})	μ_δ (mas yr^{-1})	V (km s^{-1})	P.A. (deg)
VLA 11	1.76±0.18	2.16±0.22	2.62±0.27	2.61±0.26	4.0±0.4	0.27±0.10	0.7±0.8	0.7±0.8	2±2	47±47
MIPS 2301	0.016±0.004[e]	0.032±0.010[f]	< 0.03	< 0.03	< 0.07	0.30±0.23	... [g]	... [g]	... [g]	... [g]
MIPS 2297	< 0.03	< 0.03	0.049±0.012	0.092±0.013	0.116±0.022	1.4±0.5	... [g]	... [g]	... [g]	... [g]
VLA 12N	0.134±0.020	0.073±0.014	< 0.03	< 0.025	< 0.05	−1.07±0.07	22±11	−46±11	100±21	155±12
HOPS 64	0.011±0.003[e]	< 0.027	0.069±0.012	0.140±0.016	0.30±0.03	1.51±0.06	... [g]	... [g]	... [g]	... [g]
VLA 12C	0.24±0.03[h]	0.09±0.03[h]	< 0.03	< 0.024	< 0.04	−1.3±0.4	−11±14	−50±15	101±29	192±16
HOPS 108	0.018±0.003[e]	0.060±0.014[f]	0.047±0.011	0.115±0.014	0.084±0.017	0.66±0.29	14±7	9±7	32±14	57±25
VLA 12S	0.246±0.028	0.192±0.024	0.163±0.026	0.137±0.020	< 0.04	−0.59±0.20	−13±3	−14±3	37±6	223±10
VLA 16	0.017±0.003[e]	< 0.027	0.040±0.010	0.059±0.012	0.069±0.014	0.73±0.06	... [g]	... [g]	... [g]	... [g]
VLA 15	0.071±0.014	0.100±0.013	0.200±0.022	0.32±0.04	0.60±0.07	1.02±0.15	−0.6±3.0	2±3	4±6	343±88

[a] Measured in the 2014 C-configuration maps, except when noted. Primary beam correction has been applied. Upper limits are 3σ.

[b] From C-configuration observations made on 27 March 2016 (J. Tobin, private communication).

[c] The data point at 0.7 cm has been excluded from the fit in the sources with a positive spectral index to avoid possible contamination from dust emission.

[d] Measured from the X-band map made from 1994 - 2000 data and the C-band map at epoch 2015. Positions were obtained from elliptical Gaussian fits. Positional uncertainties were calculated as explained in the footnote of Table 2.2. Errors in the proper motions were estimated from the uncertainties in the absolute positions using standard propagation error theory. For resolved sources, opacity effects can produce small differences in the positions if obtained from maps at different wavelengths and/or angular resolutions, resulting in additional uncertainty in the proper motion measurements.

[e] Obtained from the C-band 2015 A-configuration map because the source is not detected or appears blended with nearby sources in the C-band 2014 C-configuration map.

[f] Obtained from the 1994 - 2000 multiconfiguration map at 3.6 cm because the source appears blended with nearby sources in the X-band 2014 C-configuration map.

[g] Not detected in the first epoch map (1994 - 2000 data) or too weak for a reliable positional fit.

[h] The expected contribution of HOPS 108, estimated from higher resolution data, has been subtracted.

2.3.2 Proper Motions of the Detected Sources

We searched for proper motions by comparing the positions of the radio sources detected in the high-angular resolution maps obtained from archive data (epochs 1994 - 2000) and from our last observations (epoch 2015). Unfortunately, the sensitivity of the archive data in a single epoch was insufficient, and we combined in the same map data taken over ∼6 years, which is not optimal to measure accurate proper motions, because of motions and changes in the morphology of the sources over this period. Also, the archive data were observed in X band (8.4 - 8.5 GHz) while the new data have been obtained in C band (4 - 8 GHz) (Table 2.1). Although the frequency ranges of the two bands are almost contiguous, the differences in frequency could result in apparent motions due to variations of opacity with frequency, particularly in extended sources. Despite all these factors that contribute to the uncertainty in our measurements, the relatively high velocity of the jet and long time (∼ 18 yr) elapsed between the two maps, make the proper motions clearly detectable. Our results show that, while VLA 11 and VLA 15 remain static within the uncertainties, the VLA 12N, VLA 12C, and VLA 12S knots present measurable proper motions of ∼ 40 - 100 km s^{-1} roughly in the S-SW direction (Table 2.3 and Fig. 2.4; see also left panel in Fig. 2.2). HOPS 108 shows a measurable proper motion (32 ± 14 km s^{-1}), but in the NE direction, whose nature is uncertain (see below). The proper motion velocity of VLA 11, the source with the best signal-to-noise ratio, is 2 ± 2 km s^{-1} (Table 2.3). Since this velocity is obtained from the absolute positions of the source, its small value indicates that systematic errors are effectively very small and that their possible residual effects on the determination of the proper motions are at a level of ∼ 2 km s^{-1} or smaller.

2.3.2.1 The HOPS 370 Radio Jet

As discussed above, the knots of VLA 12 are characterized by negative spectral indices, indicating non-thermal emission (see Fig. 2.3), but their overall morphology with three aligned knots, suggests that they pertain to a radio jet. Radio jets associated with YSOs are characterized by thermal (free-free) emission (e.g., Anglada 1996), but in a few cases, non-thermal emission has been found in the jet lobes, at relatively large distances from the jet core that shows a positive spectral index and thermal emission (Carrasco-González et al. 2013, Anglada et al. 2015, Rodríguez-Kamenetzky et al. 2016 and references therein). The most spectacular case of this selected sample of non-thermal radio jets is the HH 80 radio jet, where

linearly polarized emission, indicative of synchrotron radiation, was imaged in the jet lobes (Carrasco-González et al. 2010), while the central core of the jet, with a positive (thermal) spectral index, remains unpolarized. As the velocities of protostellar jets are not relativistic (< 1000 km s^{-1}), it is assumed that the synchrotron emitting electrons are accelerated up to relativistic velocities via the diffusive shock acceleration (DSA) mechanism (Drury 1991) working in the strong shocks present in the interaction of the jet with the surrounding medium. Thus, it is expected that the VLA 12 knots are associated with strong shocks, as indeed is suggested by the detection of several shock tracers in the proximity of this source (Shimajiri et al. 2008, Manoj et al. 2013, González-García et al. 2016; see Fig. 2.2, left panel). Actually, the region near HOPS 108 shows the brightest far-IR [OI], CO, H_2O, and OH line emission among the HOPS spectroscopic sample of sources (P. Manoj et al. 2017, in preparation), indicating the presence of strong shocks.

These results are consistent with the VLA 12 knots being part of a non-thermal radio jet either originating from the Class 0 protostar HOPS 108 (FIR 4), which falls in between the VLA 12C and the VLA 12S knots, or from the intermediate-mass Class I YSO HOPS 370 (FIR 3), as the VLA 12 knots are roughly aligned in the direction of the VLA 11 radio jet associated with HOPS 370 (Fig. 2.1) and fall on the SW lobe of the sub-mm and far-IR outflow (Manoj et al. 2013, González-García et al. 2016) driven by this object.

If HOPS 108 was the driving source of the VLA 12 knots, one would expect proper motions of these knots away from HOPS 108. In particular, the VLA 12N and 12C knots would show proper motions with a component pointing to the north. However, as Figure 2.4 shows, the proper motions of the VLA 12 knots point to the south, consistent with an origin from HOPS 370 (VLA 11), and excluding HOPS 108 as the driving source. Thus, we conclude that the VLA 12 non-thermal radio knots belong to a radio jet, driven by the intermediate-mass Class I object HOPS 370, whose central thermal region is traced by the collimated radio source VLA 11. VLA 11 is bipolar, extending $\sim 1''$ both to the NE and to the SW of the position of the protostar (see top right panel in Fig. 2.4). However, only the SW side of the radio jet shows a distant ($\sim 30''$) non-thermal lobe (VLA 12), without a NE counterpart. The absence of a NE non-thermal radio lobe is probably due to the lack of a dense clump along the NE jet path where a strong shock interaction, similar to that observed in the SW lobe, could take place. The jet is also bipolar in the far-IR [OI] lines (González-García et al. 2016), but its SW lobe is more

extended, with the brightest part associated with the non-thermal VLA 12 radio lobe.

Adopting 1997.65 as an average epoch for the archive data map, the resulting plane-of-the-sky velocities of the VLA 12N, 12C, and 12S knots are ∼100, 101, and 37 km s^{-1}, respectively. The velocities of knots 12N and 12C fall in the range of values measured for other protostellar radio jets (Anglada et al. 2015 and references therein); the velocity of VLA 12S is smaller, suggesting that this distant knot could have suffered a significant deceleration, particularly if the jet has interacted strongly with the ambient medium, as indicated by other observations (Manoj et al. 2013, González-García et al. 2016). In this respect, recent proper motion measurements of the radio knots associated with the Herbig-Haro objects HH 80, HH 81, and HH 80N, far away from the central source, have shown that these knots have significantly slower motions than the radio knots located a few arcsec from the central source (Masqué et al. 2015). This result has been interpreted as indicating strong jet interactions with the ambient cloud that significantly slow down the jet material.

2.3.2.2 The Origin of HOPS 108

Since the position of the HOPS 108 protostar falls in the path of the VLA 11-VLA 12 radio jet, but it can be ruled out as its driving source, an appealing alternative possibility is that the jet is related to the origin of HOPS 108. It has been proposed that shocks associated with the interaction of jets with the surrounding medium could compress the gas and induce local instabilities that may trigger star-formation (e.g., Yokogawa et al. 2003; Graves et al. 2010; Duarte-Cabral et al. 2011). In particular, this scenario has been proposed for HOPS 108, as it is associated with strong shocks (Manoj et al. 2013, González-García et al. 2016) and probably interacting with a nearby dense core (Shimajiri et al. 2008). Interestingly, the shape of the jet in the region of the VLA 12 knots appears to follow the eastern edge of a clump of enhanced dust emission, as imaged by ALMA at 3 mm (Kainulainen et al. 2017; see Fig. 2.2, right panel). Thus, it seems plausible that the formation of the HOPS 108 protostar was triggered by the compression of the material in this clump after a strong shock interaction with the VLA 11-VLA 12 jet, driven by HOPS 370.

The evolutionary status of HOPS 370 and HOPS 108 is also fully consistent with the suggestion of the latter being triggered by the former. HOPS 370, with a bolometric temperature $T_{\rm bol} = 72$ K, has been classified as an intermediate-mass

young Class I object (Adams et al. 2012, Furlan et al. 2016) and we would expect an age (time elapsed since the onset of collapse) of a few times 10^5 years for this object. HOPS 108, with a lower bolometric temperature $T_{\rm bol} = 38$ K, is supposed to be younger, and it has been classified as a Class 0 protostar (Adams et al. 2012; Furlan et al. 2016). We can then hypothesize that some 10^5 years ago the jet of HOPS 370 started to impact the molecular clump (see Fig. 2.2, right panel) from which HOPS 108 later formed. After an interaction of a few times 10^4 years, enough time had passed to allow the collapse of the clump and the start of the protostellar stage of HOPS 108. The travel time of the gas from HOPS 370 to HOPS 108 is only 500 years (as derived from our measured proper motions) and the delay in the influence of the first object on the second can be taken to be much shorter than the other timescales. We then have a scenario in which the evolutionary status of the sources is consistent with one of them triggering the formation of the other.

It should be noted that the MIPS 2297 source also falls on the path of the HOPS 370 jet, but closer to the origin. Since MIPS 2297 seems to be older than HOPS 108 one could think that it is the result of an earlier episode of triggered star-formation. If MIPS 2297 is really a Class II object, as proposed by Megeath et al. (2012), it would be even older than HOPS 370, making the possibility of triggered formation inviable. However, MIPS 2297 is not well studied yet, and if it happens to be younger this possibility cannot be fully discarded. On the other hand, Shimajiri et al. (2008) proposed that the formation of HOPS 64 ($\sim 6''$ NW from HOPS 108) could have also been triggered by the outflow from HOPS 370. However, in the recent study by Furlan et al. (2016), both HOPS 370 and HOPS 64 are classified as Class I sources, suggesting a similar evolutionary stage, which would be in conflict with a triggered star-formation scenario for HOPS 64. It is also possible that MIPS 2297 and/or HOPS 64, which are both visible at shorter wavelengths, lie in front of the plane where HOPS 370 and HOPS 108 are located; so, they could be close to HOPS 370 and its jet just in projection, but in reality be farther away and have formed in OMC-2 independently of this source. Finally, the new source VLA 16 also falls on the path of the jet, very close to the southernmost detected knot, VLA 12S. There are four young stars that could be triggered or affected by the HOPS 370 jet, but only for HOPS 108 there is further evidence of ongoing shock-interaction, although it may have occurred in the past.

A puzzling issue in the triggered-formation scenario for HOPS 108 is its large proper motion velocity (~ 32 km s^{-1}; Table 2.3). Such a large velocity implies that

it should have been acquired very recently (< 200 yr) in order for the star to be formed in the proximity (within a few arcsec) of its current position, in the region where the shock emission has been identified (Manoj et al. 2013; González-García et al. 2016). Otherwise, if this velocity was maintained during a longer time interval, it would imply that the HOPS 108 protostar originated at a distant position from its current location, making inviable the triggering hypothesis. Relatively low velocities are expected if the protostars are mechanically linked to the molecular gas reservoir and thus obtain their velocities directly from the gas they are forming in, as proposed by Stutz & Gould (2016), who found typical radial velocities with respect to the ambient cloud of ~ 0.6 km s^{-1} for protostars and ~ 1.8 km s^{-1} for pre-main sequence stars in the Integral Shaped Filament (ISF) region in Orion. These authors propose a slingshot-like ejection mechanism to account for the increase in velocity of pre-main sequence stars relative to protostars. However, this mechanism cannot explain velocities above a few km s^{-1}.

In contrast, HOPS 108 presents a much larger proper motion velocity, similar to the ~ 27 km s^{-1} of the BN object in the nearby Orion BN/KL stellar system (Goddi et al. 2011; Rodríguez et al. 2017). Another runaway star, V 1326 Ori, with a peculiar large proper motion velocity of about 28 km s^{-1} has been recently identified in a radio survey of proper motions in the core of the Orion Nebula Cluster (Dzib et al. 2017). For the BN/KL system, in order to explain both the uncollimated explosive molecular outflow (Zapata et al. 2009) and the stellar velocities, violent (proto-)stellar interactions and the subsequent dynamical ejection of said (proto-)stars have been invoked (Bally & Zinnecker 2005; Gómez et al. 2008; Bally et al. 2017). This acceleration mechanism would require the presence of a binary or multiple stellar system near FIR 4/HOPS 108 to make it compatible with the triggering scenario. Shimajiri et al. (2008) imaged 11 potential cores within a region of $\sim 20'' \times 20''$ in the proximity of FIR 4 and interpreted them as tracing a young stellar cluster whose formation was triggered by the impact of the jet with the ambient cloud. If this was the case, interactions within this multiple system could have resulted in the recent ejection of HOPS 108. We identify the region imaged by Shimajiri et al. (2008) with the clump of dust imaged by ALMA at 3 mm (Kainulainen et al. 2017; Fig. 2.2, right panel), where the sources HOPS 108, HOPS 64, VLA 15, and VLA 16 appear to be embedded. Since HOPS 108 moves toward the NE, we do not find a suitable candidate that might be receding from a close enough common position and that could be responsible for a past interaction with HOPS 108, casting doubt on this possibility.

There are other detected radio sources in the region that could have dynamically interacted with HOPS 108 in the past (e.g., VLA 13, also know as HOPS 368, located $\sim 40''$ to the SW; see Chapter 3). However, the location of a potential encounter would fall at a large distance from the current position of HOPS 108 and, as noted above, would make the origin of this object incompatible with a scenario of (local) triggered star-formation. On the other hand, if HOPS 108 was accelerated in a distant encounter it seems unlikely that our observation occurs just at the moment when it crosses the VLA 12 knots of the HOPS 370 jet, at the point of its maximum interaction with the ambient cloud.

Another possibility to explain the observed large proper motion of HOPS 108 is to assume that it is due to a change in the shape of its radio emission because of blending with the emission of the nearby VLA 12 knots. Since these knots move toward the SW, with VLA 12C approaching HOPS 108 and VLA 12S going away, a partial blending with these knots can result in an apparent motion of HOPS 108 toward the NE. Also, a one-sided ejecta of a high-velocity cloud of ionized plasma by the protostar could produce a change in the shape of its radio emission and an apparent proper motion. One-sided high-velocity ejecta from young stars have been observed in several other sources (e.g., Rodríguez et al. 2017 and references therein). Such ejecta with a velocity of the order of hundreds of km s^{-1} in a poorly resolved source would result in a one-sided distortion in the source shape and thus a change in the centroid position that could mimic a motion of several tens of km s^{-1}. Wavelength-dependent opacity effects in an extended source could emphasize these changes in the position of the centroid of the emission. Indeed, we found that the precise position of the HOPS 108 radio source changes with wavelength. Additional, sensitive high-angular resolution observations could provide a more precise measure of the HOPS 108 proper motions and reveal the possible presence of either a high-velocity ejecta from this source or a nearby binary/multiple system whose past interaction with HOPS 108 had been responsible for its current high proper motions.

2.4 Conclusions

We analyzed new (2014 - 2015) multiwavelength (0.7 - 5 cm), multiconfiguration VLA observations together with archive (1994 - 2000) data at 3.6 cm that allowed us to obtain spectral indices and proper motions of radio sources in the region

enclosing FIR 3 (HOPS 370) and FIR 4 (HOPS 108) in OMC-2. Our main conclusions can be summarized as follows:

1. We detect radio emission from the far-IR sources HOPS 370, HOPS 108, and HOPS 64, as well as from the mid-IR sources MIPS 2297 and MIPS 2301. We also detect two new sources, both associated with dust cores, that we call VLA 15 and VLA 16. For all these sources we obtain positive spectral indices in the centimeter wavelength range, consistent with thermal free-free emission from young stellar objects.

2. The radio source VLA 11, associated with HOPS 370, presents a clearly elongated bipolar morphology in the NE-SW direction. Because of this morphology and its positive spectral index ($\alpha \simeq 0.3$) we interpret VLA 11 as the thermal region closest to the origin of a well collimated bipolar radio jet driven by the HOPS 370 intermediate-mass protostar. We detect several knots of emission (VLA 12N, 12C, and 12S) at $\sim$ 7500 - 12500 au to the SW of HOPS 370 with negative spectral indices and showing proper motions of $\sim$ 40 - 100 km s^{-1} away from the HOPS 370 protostar. We interpret these knots as a non-thermal lobe of the HOPS 370 jet. The VLA 12 knots are found in a region where previous observations have detected several tracers of strong shocks, suggesting that their non-thermal emission is likely synchrotron emission from relativistic electrons accelerated in shocks, as has been proposed for other non-thermal jet lobes. Although VLA 11 is bipolar, a similar non-thermal radio lobe is not found to the NE of HOPS 370, probably because there is not a dense clump where the jet interaction could take place.

3. HOPS 108 is identified as a compact radio source independent and kinematically separated from the radio emission of the VLA 12 knots of the HOPS 370 jet. Its position along the path of the VLA 12 knots and coincidence with different shock tracers suggest a scenario where the formation of HOPS 108 has been triggered by the interaction of the HOPS 370 jet with the surrounding medium, as was already proposed by Shimajiri et al. (2008). The more advanced evolutionary stage of HOPS 370 relative to HOPS 108 and the short dynamical timescale of the jet, are consistent with this scenario. However, HOPS 108 presents a large proper motion velocity of about 30 km s^{-1} toward the NE whose nature is uncertain. This velocity is similar to the proper motion velocities found in runaway stellar sources in Orion (Rodríguez et al.

2017; Dzib et al. 2017). Such a large velocity in HOPS 108 would be inconsistent with the triggered scenario unless the source had been accelerated to this high velocity very recently. Alternatively, an apparent proper motion could result because of a change in the position of the centroid of the source due to a partial blending with the emission of the nearby VLA 12 knots or to a one-sided ejecta of ionized plasma, rather than by the actual motion of the protostar itself. Deep high-angular resolution observations at several epochs are required to clarify this issue.

4. Sources HOPS 370 and VLA 15 do not show detectable proper motions ($V < 2$ - 4 km s^{-1}), as expected for embedded protostars.

Chapter 3

Multifrequency deep radio continuum VLA observations toward OMC-2/3

3.1 Introduction

The Orion Molecular Cloud complex, with distances ranging from 380 to 450 pc (Menten et al. 2007; Kim et al. 2008; Stutz & Gould 2016; Kounkel et al. 2017, 2018; Großschedl et al. 2018), is one of the nearest active star-forming regions, where young stellar objects (YSOs) of both low and high luminosity coexist. The complex is composed of two elongated giant molecular clouds, Orion A and B, with a total mass exceeding $2 \times 10^5 M_\odot$ (Wilson et al. 2005), roughly aligned in the north-south direction (see Fig. 1 of Megeath et al. 2012). Toward the northern end of the Orion A cloud, Mezger et al. (1988, 1990) and Chini et al. (1997) identified several bright millimeter sources, aligned along an Integral Shaped Filament (ISF, Bally et al. 1987; Peterson & Megeath 2008; Stutz & Gould 2016; Kainulainen et al. 2017). Most of these sources were later associated with YSOs (e.g., Adams et al. 2012, Furlan et al. 2014, 2016, and references therein). Outstanding among them are the bright FIR 3 and FIR 4 sources, which are associated with the Class I HOPS 370 and the Class 0 HOPS 108 YSOs, respectively. In this Chapter, we analyze the protostellar content toward the Orion Molecular Clouds 2 and 3 (OMC-2/3), two of the richest molecular clouds in protostars and prestellar cores, located in the northern part of the ISF.

The Orion complex has been intensively observed in the infrared spectral range with surveys carried out with the *Spitzer* Space Telescope (Megeath et al. 2012, 2016) and the *Herschel* Space Observatory. In particular, 330 protostars have

been studied in great detail as part of the open-time key program Herschel Orion Protostar Survey (HOPS, e.g., Stanke et al. 2010; Fischer et al. 2010, 2017; Manoj et al. 2013; Stutz et al. 2013; Furlan et al. 2014, 2016; González-García et al. 2016, Fischer et al. 2021, in preparation). For these objects, identified with HOPS numbers, Furlan et al. (2016) modeled their spectral energy distributions (SEDs) from near-IR to sub-millimeter wavelengths allowing the determination of fundamental properties such as their luminosity and the envelope mass, as well as their classification in terms of evolutionary stage. However, in some cases, the SED was contaminated by emission from nearby sources, due to the relatively low angular resolution of those observations. Therefore, observations at other wavelength ranges and with higher angular resolution can help to better understand the nature of these sources. In this sense, the VLA/ALMA Nascent Disk and Multiplicity (VANDAM) survey of Orion (Tobin et al. 2020), targeting 328 protostars with ALMA at 870 μm and 102 of them with the VLA at 9 mm, will help to identify at high angular resolution ($\sim 0\farcs1$, much higher than the data used to construct the SED) possible disks associated with the sources, and clarify their nature and multiplicity.

In particular, radio observations at cm wavelengths can detect the most embedded, youngest YSOs, even those of very low luminosity. These radio sources trace the base of collimated outflows of partially ionized gas (radio jets), providing not only an extinction-free census of outflow (and thereby accretion) activity but also a tool to pinpoint the position of YSOs and identify embedded multiple systems (Anglada et al. 2018).

The OMC-2/3 region has been observed by different programs at radio wavelengths with the Very Large Array (VLA). Reipurth et al. (1999) observed it at 3.6 cm in the VLA D-configuration (angular resolution of $\sim 8''$ and rms of 30 - 40 μJy beam^{-1}) to investigate its protostellar content, detecting 14 radio sources toward the ISF, 11 of which are likely related to the star-forming region according to these authors. As part of a study of several star-forming regions with outflow activity, Reipurth et al. (2004) observed a small fraction of OMC-3 (a region of $\sim 3' \times 3'$ around the bipolar reflection nebula Haro 5a/6a), using the VLA A configuration at 3.6 cm (angular resolution of $\sim 0\farcs3$ and rms of 7 μJy beam^{-1}), with the detection of two additional YSOs[1]. Kounkel et al. (2014) surveyed the whole Orion

[1]Reipurth et al. (2004) reported originally four sources from their observations, but sources VLA 15 and 17 in that paper correspond to sources VLA 5 and 6, respectively, from Reipurth et al. (1999). On the other hand, source VLA 15 from Reipurth et al. (2004) is a different radio source than source VLA 15 reported in Chapter 2.

complex at 5 cm in A configuration (sub-arcsecond angular resolution and rms of 60 μJy beam^{-1}) looking for non-thermal emitters in order to measure the distance to the region. They increased by 25 the known radio sources in the OMC-2/3 region, 17 of which are likely YSOs according to these authors. In summary, these three papers report a total of 41 radio sources toward the region OMC-2/3, and propose 30 of them as likely YSOs.

The vicinity of FIR 3/FIR 4 has also been studied recently by Tobin et al. (2019) through VLA continuum observations at 9 mm and ALMA continuum and line observations at 870 μm. They characterized the continuum sources in the region on $\sim$ 40 au scales, and found emission from high-excitation transitions of complex organic molecules (COMs) associated with both HOPS 108 (FIR 4) and HOPS 370 (FIR 3).

In Chapter 2 (published in Osorio et al. 2017) we presented VLA multifrequency observations of OMC-2 in the C configuration from 0.7 to 5 cm (with angular resolution from $\sim 0\farcs4$ to $\sim 4''$), as well as very sensitive (rms = 3 μJy beam^{-1}) observations at 5 cm in the A configuration, more than 10 times deeper than previous surveys. A $\sim 40'' \times 30''$ region around FIR 4, the brightest sub-millimeter source in OMC-2 (Furlan et al. 2014), was analyzed with the aim of clarifying the nature of this object. One of the main results was the detection of a non-thermal lobe in the radio jet driven by the Class I YSO HOPS 370 (associated with FIR 3), suggesting that the interaction of this jet with the ambient could trigger the formation of the Class 0 YSO HOPS 108 (associated with FIR 4), which is located in projection toward the non-thermal jet lobe. In this study, 10 radio sources were reported, 7 of them tracing YSOs, and 3 showing large proper motions and tracing non-thermal knots of the HOPS 370 radio jet.

In this Chapter, we extend the analysis done in Chapter 2 to the entire field of view of those observations, a region of $12\farcm5$ in diameter, comprising the southernmost $2\farcm5$ of the OMC-3 region and the whole OMC-2 region. We note that in this Chapter we adopt the updated distance to OMC-2/3 of 386 $\pm$ 3 pc (Kounkel et al. 2018), slightly different than the one (414 $\pm$ 7 pc, Menten et al. 2007) used in Chapter 2. The use of this updated value for the distance would decrease the luminosities derived by Furlan et al. (2016), who used 420 pc, by 16%.

3.2 Observations

The observations were carried out with the Karl G. Jansky VLA in the C configuration in October 2014 (Project 14B-296) at C (5 cm), X (3 cm), K (1.3 cm), and Q (0.7 cm) bands, and in the A configuration in August-September 2015 (Project 15A-369) at C band (5 cm), with angular resolutions ranging from $\sim 0\farcs4$ to $\sim 4''$ (see Table 3.1). The observed bandwidth was 4 GHz at C and X bands, and 8 GHz at K and Q bands. The phase center was similar in both projects, with coordinates $\alpha(\mathrm{J2000}) = 05^{\mathrm{h}}35^{\mathrm{m}}27\fs070$, $\delta(\mathrm{J2000}) = -05°10'00\farcs60$ for the 2014 runs and $\alpha(\mathrm{J2000}) = 05^{\mathrm{h}}35^{\mathrm{m}}27\fs080$, $\delta(\mathrm{J2000}) = -05°10'00\farcs30$ for the 2015 ones. The data were edited and calibrated using the Common Astronomy Software Applications package (CASA; version 4.2.2). For further details of the observational setup and calibration see Table 2.1.

All the images were made with the CASA (version 4.2.2 for the 2014 data, and versions 5.0.0 and 5.1.1 for the 2015 data) task CLEAN using multi-frequency synthesis (Conway et al. 1990). For the A-configuration map, the wide-field algorithm w-projection (with the number of w-projection planes for convolution automatically determined by CLEAN) was used to correct for the curvature of the sky plane, as noted in the CASA User Reference & Cookbook[2]. Not using this correction results in a shift of the positions of the sources away from the phase center, which reaches $\sim 0\farcs01$ for the farthest ones. The extended emission from the nearby bright HII region M43 (also known as NGC 1982), $\sim 5'$ to the south of the phase center, makes the imaging at C band difficult. As in Chapter 2, to properly clean the radio sources in our field of view, we downweighted the effects of the extended emission from M43, by using only baselines > 5 kλ (suppressing extended emission at scales larger than $\sim 40''$) for the C-configuration maps and > 25 kλ (suppressing extended emission at scales larger than $\sim 8''$) for the A-configuration map. To obtain the C-band image in the C configuration, where the sensitivity to extended structures is higher, we additionally used the multiscale deconvolution algorithm. All the maps presented in this work have been corrected for the primary beam response.

Given the high sensitivity reached, it has been possible to image the region over where the primary beam response is above 10% of that at the field center, where we still have enough sensitivity to detect sources of a few tenths of mJy. The diameter of the imaged region changes with frequency, ranging from $\sim 2'$ at 0.7 cm

[2]Release 4.7.2, available at `https://casa.nrao.edu/casa_cookbook.pdf`.

Table 3.1 Characteristics of the Maps

VLA Conf.	VLA Band	Central wavelength (cm)	Frequency range (GHz)	FoV[a] (′)	Weighting[b]	Synthesized beam Size (″×″)	Synthesized beam P.A. (°)	rms[c] (μJy beam^{-1})
A	C	5	4.162 - 8.160	12.5	Natural	0.42×0.40	14.85	3
C	C	5	3.912 - 7.960	12.5	Robust 0	4.76×2.48	46.28	10
C	X	3	7.912 - 11.960	7.6	Robust 0	2.68×1.73	36.11	9
C	K	1.3	17.976 - 25.960	3.4	Robust 0	0.84×0.71	5.21	10
C	Q	0.7	40.039 - 48.023	1.7	Robust 0	0.46×0.36	−20.49	15

[a] Diameter of the field of view where radio sources have been searched for, corresponding to the region where the primary beam response is above 10% of that at the field center. At C band, the 13 arcsec^2 region where extended emission from M43 dominates (shown in Fig. 3.1) is excluded from the analysis.

[b] The robust parameter (Briggs 1995) is defined as implemented in CASA, taking values between −2.0 (close to uniform weighting) to 2.0 (close to natural).

[c] At the center of the map; the rms at the border of the map is 10 times higher.

to $\sim 13'$ at 5 cm. The largest of these fields covers the ISF in the southernmost 2.′5 of OMC-3 and in the whole OMC-2 region. The four concentric circles in Figure 3.1 mark the size of the imaged region in each band. At C band (5 cm), the extended emission from M43 could be masking the emission from individual radio sources in the S-SE edge of the field, making it difficult the analysis of the maps. Therefore, we excluded from our analysis the 13 arcmin^2 annulus sector shown in Figure 3.1, where the extended emission from M43 dominates. Table 3.1 summarizes the characteristics of the maps obtained.

3.3 Results

In Chapter 2 (Osorio et al. 2017) we discussed 10 radio sources detected in a $\sim 40'' \times 30''$ region around FIR 3/4 (see Table 2.2). There are 47 additional radio sources detected in the whole field of view of our observations, of $\sim 12.'5$ in diameter (Table 3.1), whose positions, deconvolved sizes, and flux densities at the observed bands are listed in Tables 3.2 and 3.3. We indexed the sources according to their declination, from north to south. We consider as detected those sources with peak intensity above a 3σ level in more than one band or epoch, or above a 6σ level if only detected in one band and epoch.

In Figure 3.1 we show the positions of the radio sources detected in our observations of the region, overlaid on a column density map derived from *Herschel* dust emission data at 160 μm, 250 μm, 350 μm, and 500 μm (adapted from Stutz 2018). For the additional 47 radio sources presented in this Chapter, we show in Figure

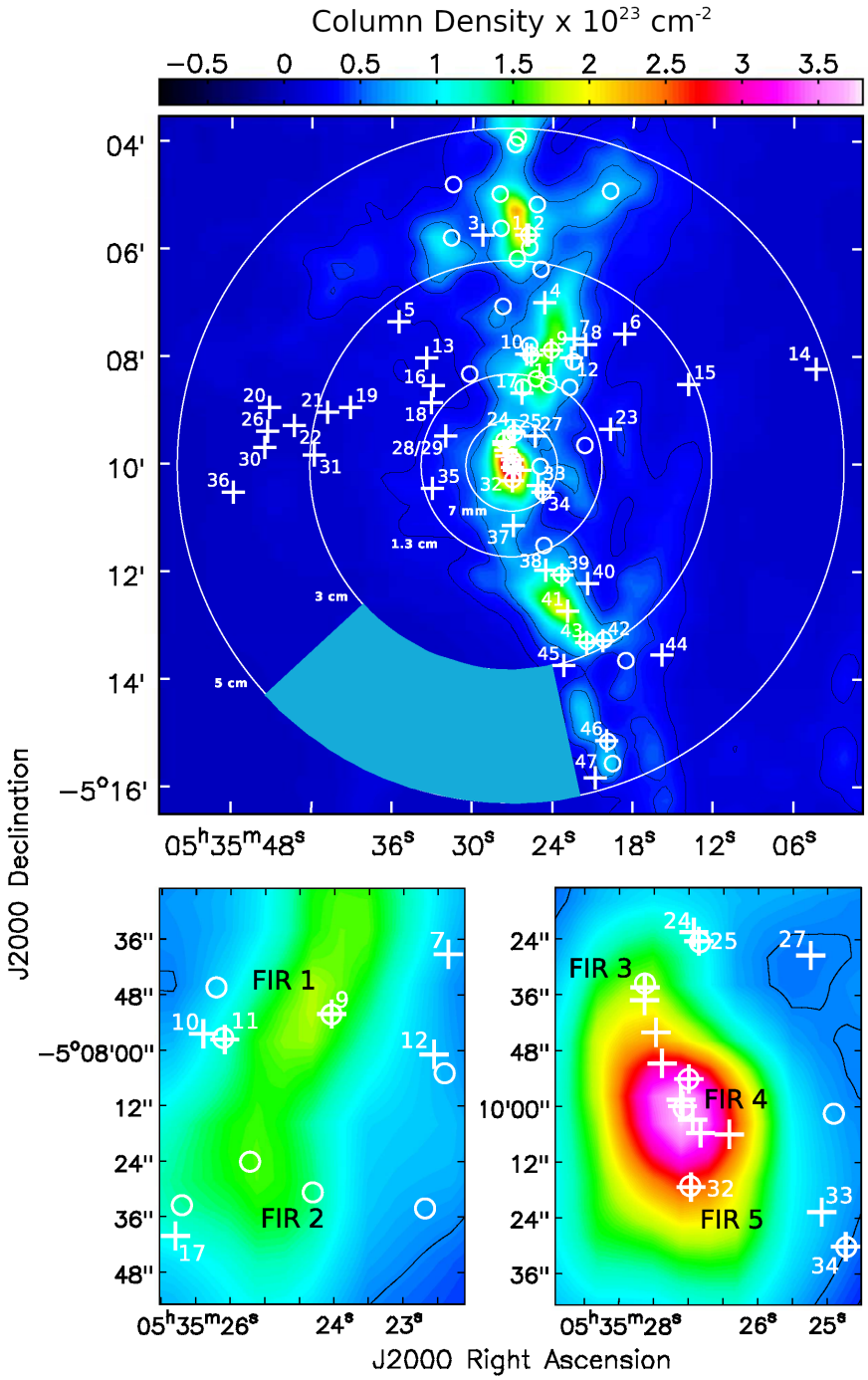

Figure 3.1 Location of the detected radio sources. The background is the column density map of the ISF obtained by Stutz (2018) from *Herschel* dust emission data (160 - 500 μm); contour levels are 2.3, 4, and 6 times 10^{22} cm^{-2} (Hacar et al. 2018, see their Appendix A). Plus signs mark the positions of the radio sources detected with our observations. Numbered sources are reported in this Chapter, while unnumbered were reported in Chapter 2. Open circles mark the position of HOPS sources (Furlan et al. 2016; Stutz et al. 2013; Tobin et al. 2015). Concentric circles mark the region where the primary beam response is $> 10\%$ of that at the field center for each frequency. The light blue annulus sector to the south in the main panel marks the region where extended emission from the bright HII region M43 (NGC 1982) is detected, which is not analyzed in this work. The panels on the bottom are zooms in on crowded regions.

3.2 our highest angular resolution (A-configuration 5 cm) maps. In Figure 3.3 we present the spectra in the cm wavelength range, constructed using all the available data (Reipurth et al. 1999, 2004; Kounkel et al. 2014, this work) for 41 of these sources (for 6 of them we only have data at a single frequency). Spectral indices are listed in Table 3.3 (see details in Section 3.3.2) and additional properties of the sources, compiled from the literature, are presented in Table 3.4.

We point out that there are five previously reported radio sources that fall within our field of view, but are not discussed here. The sources GBS-VLA J053529.00-050909.0, J053517.06-051423.7 and J053525.65-050757.2 (Kounkel et al. 2014) are not detected in our observations of higher sensitivity, which suggests they are variable; the first two sources were reported as probably extragalactic, and the third one as a Class I YSO. At the edge of our field of view, there is a hint of C-band emission toward the position of the proposed radio jet OMC-2/3 VLA 4 (Reipurth et al. 1999, 2004) but the detection is not clear enough to include it in our sample. Finally, we note that Reipurth et al. (1999) reported a source (VLA 14, that they associate with the star-forming region) at a position located $\sim 5\farcs5$ from our Source 40, and we cannot discard the possibility that both are the same object given the poor angular resolution ($8''$) of those observations.

3.3.1 Distribution of the Detected Radio Sources and their Association with the Star-Forming Region

As a first step, we analyze the association of the detected radio sources with the star-forming region. In our maps, we expect a number of extragalactic sources that increases with the wavelength of the observation and the field size (Anglada et al. 1998, see their Appendix A). Therefore, in our set of maps, the largest contamination of extragalactic sources is expected to occur in the A-configuration C-band map since it is the most sensitive, at the longest wavelength, and with the largest field of view. Using equation A11 of Anglada et al. (1998) for a field of view of $12\farcm5$ in diameter decreased by the solid angle of the excluded annulus, we estimate that 13±4 of the 54 sources detected in this C-band map above a 6σ threshold could be extragalactic. Thus, we expect that 41 ± 4 of the sources detected in this map are galactic and likely associated with the star-forming region. On the other hand, in the X-band map we report a total of 31 sources, and we expect that only 2 ± 1 ($\sim 6\%$) are extragalactic, strongly suggesting that the three

Table 3.2 Positions and Sizes of the Radio Sources

Source Index	Position[a] α(J2000)	Position[a] δ(J2000)	Deconvolved size[a] ($''\times''$)	P.A.[b] (°)	Column density[c]	Previous cm detections	Ref.	Notes[d]
			OMC-3					
1	05 35 25.9655±0.0011	-05 05 43.369±0.016	0.50(3)×0.23(7)	99±5	High	VLA 5[e], VLA 15[f], GBS[g]	1, 2, 3	
2	05 35 25.775±0.003	-05 05 43.84±0.05	unresolved	···	High	VLA 5[e]	1	
3	05 35 29.2214±0.0007	-05 05 44.150±0.011	0.23(3)[h]	156±11	Medium	VLA 6, VLA 17, GBS[g]	1, 2, 3	
			OMC-2					
4	05 35 24.55±0.07	-05 06 58.5±1.0	18(2)×13(1)	···	High	VLA 7	1	E
5	05 35 35.4843±0.0023	-05 07 20.54±0.04	unresolved	···	Low			
6	05 35 18.6135±0.0016	-05 07 33.60±0.03	0.43(6)×0.23(7)	80±11	Low			
7	05 35 22.362±0.003	-05 07 39.10±0.05	unresolved	···	High			
8	05 35 21.4827±0.0012	-05 07 45.824±0.019	0.19(5)×0.11(5)	177±75	Medium			
9	05 35 24.0458±0.0009	-05 07 52.074±0.014	0.35(6)×0.20(6)	16±17	High	VLA 8	1	CE
10	05 35 25.897±0.003	-05 07 56.4±0.4	unresolved	···	High	VLA 9[e]	1	
11	05 35 25.5873±0.0007[i]	-05 07 57.596±0.011[i]	0.45(4)×0.18(5)	24±5	High	VLA 9[e]	1	
12	05 35 22.5628±0.0007	-05 08 00.741±0.011	0.28(4)×0.16(5)	45±17	High	GBS[g]	3	
13	05 35 33.3778±0.0008	-05 08 01.319±0.011	0.24(5)×0.17(6)	152±52	Low	VLA 10	1	CE
14	05 35 04.3023±0.0008	-05 08 12.637±0.012	0.33(3)×0.23(3)	95±8	Low	GBS[g]	3	
15	05 35 13.812±0.003	-05 08 30.16±0.04	unresolved	···	Low			
16	05 35 32.881±0.003	-05 08 31.35±0.04	unresolved	···	Low			
17	05 35 26.2911±0.0016	-05 08 40.037±0.024	0.42(7)[h]	42±8	High			
18	05 35 33.041±0.003	-05 08 50.91±0.04	unresolved	···	Low			
19	05 35 39.079±0.003	-05 08 56.39±0.04	unresolved	···	Low			
20	05 35 45.130±0.016	-05 08 56.88±0.24	4.8(3)×4.1(3)[j]	65±23	Low			BS
21	05 35 40.7757±0.0007	-05 09 01.551±0.011	0.22(1)×0.01(6)	136±5	Low	GBS[g]	3	
22	05 35 43.2516±0.0011	-05 09 16.943±0.016	0.27(3)×0.19(3)	19±20	Low			
23	05 35 19.620±0.006	-05 09 20.36±0.09	unresolved	···	Medium			
24	05 35 26.9293±0.0016	-05 09 22.408±0.024	0.26(9)×0.24(13)	175±86	High			
25	05 35 26.8588±0.0010	-05 09 24.387±0.015	0.36(4)×0.06(8)	106±2	High			
26	05 35 45.2699±0.0015	-05 09 23.485±0.023	0.56(6)×0.26(5)	157±6	Low			
27	05 35 25.2418±0.0010	-05 09 27.393±0.014	0.38(15)[h]	137±33	Medium			
28	05 35 31.9503±0.0017	-05 09 27.79±0.03	0.31(9)[h]	107±17	Medium			
29	05 35 31.971±0.003	-05 09 28.26±0.04	unresolved	···	Medium			
30	05 35 45.417±0.019	-05 09 41.4±0.3	6.7(7)×4.2(4)[j]	90±8	Low			BS
31	05 35 41.7768±0.0015	-05 09 49.776±0.022	0.38(5)×0.22(7)	120±13	Low			
32	05 35 26.9643±0.0023	-05 10 17.33±0.03	unresolved	···	High			
33	05 35 25.148±0.006	-05 10 23.02±0.09	2.1(3)×0.5(5)[k]	161±5	High	VLA 13[e]	1	CE
34	05 35 24.7274±0.0007	-05 10 30.117±0.010	0.10(2)×0.07(5)	24±80	High	VLA 13,[w]GBS[g]	1, 3	
35	05 35 32.923±0.008	-05 10 27.10±0.11	unresolved[k]	···	Medium			E

Source Index	Position[a] α(J2000)	δ(J2000)	Deconvolved size[a] ($''\times''$)	P.A.[b] (°)	Column density[c]	Previous cm detections	Ref.	Notes[d]
36	05 35 47.7962±0.0022	-05 10 30.83±0.03	unresolved	···	Low			
37	05 35 26.866±0.003	-05 11 07.53±0.04	unresolved	···	High			
38	05 35 24.472±0.004	-05 11 58.06±0.06	unresolved	···	High			
39	05 35 23.2891±0.0011	-05 12 03.398±0.017	0.24(4)×0.09(6)	65±17	High			
40	05 35 21.3186±0.0007	-05 12 12.671±0.010	0.30(2)[h]	48±3	Medium	VLA 14?[l]	1	
41	05 35 22.8447±0.0015	-05 12 43.554±0.023	0.19(9)[h]	156±24	High			
42	05 35 20.1534±0.0008	-05 13 15.752±0.012	0.52(8)×0.18(9)	11±7	High			CE
43	05 35 21.3660±0.0008	-05 13 17.795±0.012	unresolved	···	High			
44	05 35 15.7575±0.0011	-05 13 32.305±0.017	0.27(3)×0.18(3)	175±17	Medium			
45	05 35 23.1236±0.0020	-05 13 43.56±0.03	0.39(8)×0.09(9)	24±10	Medium			
46	05 35 19.893±0.003	-05 15 08.16±0.04	unresolved	···	Medium			
47	05 35 20.7530±0.0007	-05 15 49.245±0.010	0.31×0.16	21±5	Medium	GBS[g]	3	

[a] Position and sizes derived from elliptical Gaussian fits in the A-configuration C-band map, except for sources 4, 10, and 27, which are not detected in this map, and for whom the C-configuration C, X and K-band maps were used, respectively. Errors are given in parenthesis. Position uncertainties correspond to those of absolute positions, and are calculated adding in quadrature a systematic error of $0\farcs01$, accounting for uncertainties introduced by the phase calibration process (Dzib et al. 2017), to the formal error of the fit, $0.5\,\theta$/SNR (Reid et al. 1988), where θ is the source size and SNR is the signal-to-noise ratio.

[b] Position angle of the major axis of the source measured from north to east.

[c] Derived from the column density map obtained by Stutz (2018) from *Herschel* dust emission data (160 - 500 μm), shown in Figure 3.1. High: $> 6 \times 10^{22}$ cm^{-2}; Medium: (2.3 - 6) $\times 10^{22}$ cm^{-2}; Low: $< 2.3 \times 10^{22}$ cm^{-2}.

[d] E: Irregular extended source. CE: Source formed of a rather compact core and an extension elongated at a different P.A. The fit has been performed to the core. BS: Source with a bow-shock morphology.

[e] Split into two sources in our observations.

[f] From Reipurth et al. (2004), different than source VLA 15 from Chapter 2.

[g] Full name is GBS-VLA J*hhmmss.ss* − *ddmmss.s*, where J*hhmmss.ss* − *ddmmss.s* is the J2000.0 coordinate of the source.

[h] Source resolved only in one direction. The major axis size is obtained using task imfit of AIPS.

[i] This position is displaced about $0.1''$ from the position of the protostar, see Section 3.4.2.8.

[j] From a map obtained with uvtaper = 50 kλ (beam $\simeq 2''$) to better detect the extended emission.

[k] From a map obtained with uvtaper = 100 kλ (beam $\simeq 1''$) to better detect the extended emission.

[l] Uncertain association. Position of source VLA 14, reported by Reipurth et al. (1999) from $8''$ angular resolution data, differs by $\sim 5\farcs5$ from the position of our Source 40.

References— (1) Reipurth et al. 1999, (2) Reipurth et al. 2004, (3) Kounkel et al. 2014.

sources detected at X band but not detected in the A-configuration C-band map are galactic. In summary, we conclude that 44 ± 4 ($\sim$ 77%) of the 57 radio sources detected in the field are galactic and probably associated with the star-forming region.

As illustrated in Figure 3.1, a total of 42 sources out of 57 (74%) are observed toward the ISF (with a column density $> 2.3 \times 10^{22}$ cm^{-2}, marked as medium and high column density in Table 3.2), and 30 of them (53% of the total) lie in the densest part of the filament (with a column density $> 6 \times 10^{22}$ cm^{-2}, marked as high column density in Table 3.2). Since the ISF contains the phase center, from the ratio between the areas of the ISF and the field of view, we can estimate the number of expected extragalactic sources toward the ISF. Assuming a width of $2'$ for the filament, we obtain that only 3 ± 2 of the 42 sources observed toward the ISF (1 ± 1 of those observed toward the densest part) are expected to be extragalactic.

In order to further investigate the membership to the star-forming region of the 42 radio sources detected toward the ISF, we analyzed their association with continuum clumps in the 3 mm ALMA map obtained by Kainulainen et al. (2017) with an angular resolution of $\sim 3''$, the 870 μm ALMA map obtained by Tobin et al. (2020) with an angular resolution of $\sim 0\farcs11$, and the HOPS sources (Furlan et al. 2016) detected in the far-IR with *Herschel* with an angular resolution of $\sim 5 - 7''$ (see Section 3.3.3). We find that 18 ($\sim$ 43%) of the 42 radio sources detected toward the ISF are associated with compact emission at 870 μm likely tracing a disk and we consider them as "bona fide" YSOs (Table 3.4). Of these 18 sources, 11 fall very close (within $\leq 1''$) to the peak of a 3 mm compact core (nine of them are also associated with HOPS sources) suggesting they are deeply embedded objects (Class 0/I); the remaining seven sources are probably more evolved YSOs[3]. Among the remaining 24 radio sources toward the ISF without a reported association at 870 μm, two (not associated with HOPS sources) fall in the proximity of 3 mm dust emission and we consider them as likely YSOs. In summary, we find that for 20 out of the 42 radio sources detected toward the ISF there is additional evidence of their specific association with dust clumps at arcsec/sub-arcsec scales ($\sim 40 - 2700$ au), as traced by mm/sub-mm emission. Since we estimated only about 3 extragalactic sources toward the ISF, we expect that a large fraction of the remaining 22 radio sources are also YSOs, likely in a

[3]Four of them (all associated with HOPS sources) are detected toward the border of a 3 mm core (within $\lesssim 3''$ of the peak), one (associated with a HOPS source) is close (within $\leq 1''$) to a faint 3 mm peak, and two are not associated with any 3 mm compact core or HOPS source.

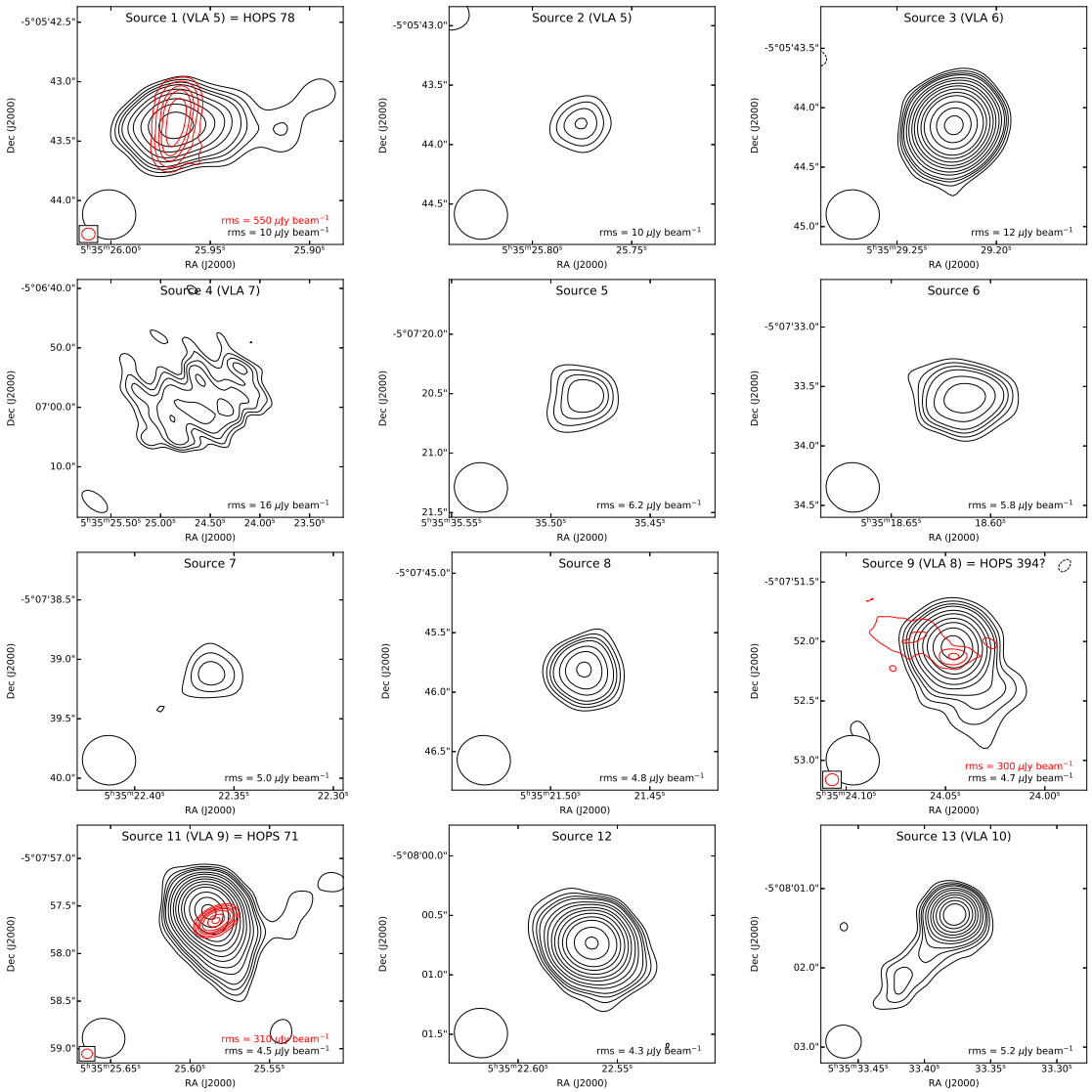

Figure 3.2 VLA A-configuration maps of each radio source with natural weighting at 5 cm (black contours) with ALMA emission at 870 μm overlayed (red contours, adapted from Tobin et al. 2020). For sources 4 and 27, C-configuration robust 0 weighting maps at 5 cm and 1.3 cm, respectively, are presented; for Source 10, see Figure 3.13, top panel. To better detect the extended emission, maps with uvtaper 50 kλ were used for sources 20 and 30, and with 100 kλ for sources 33 and 35. VLA contours (black) are -3, 3, 4, 5, 6, 8, 10, 13, 16, 20, 25, 30, 40, 50, 60, 70, and 80 times the rms of the maps. ALMA contours (red) are 5, 10, 20, 30, 50, 100, and 150 times the rms of the maps. The beam and the rms are shown in the left and bottom right corner, respectively, of each map. Continued on the next page.

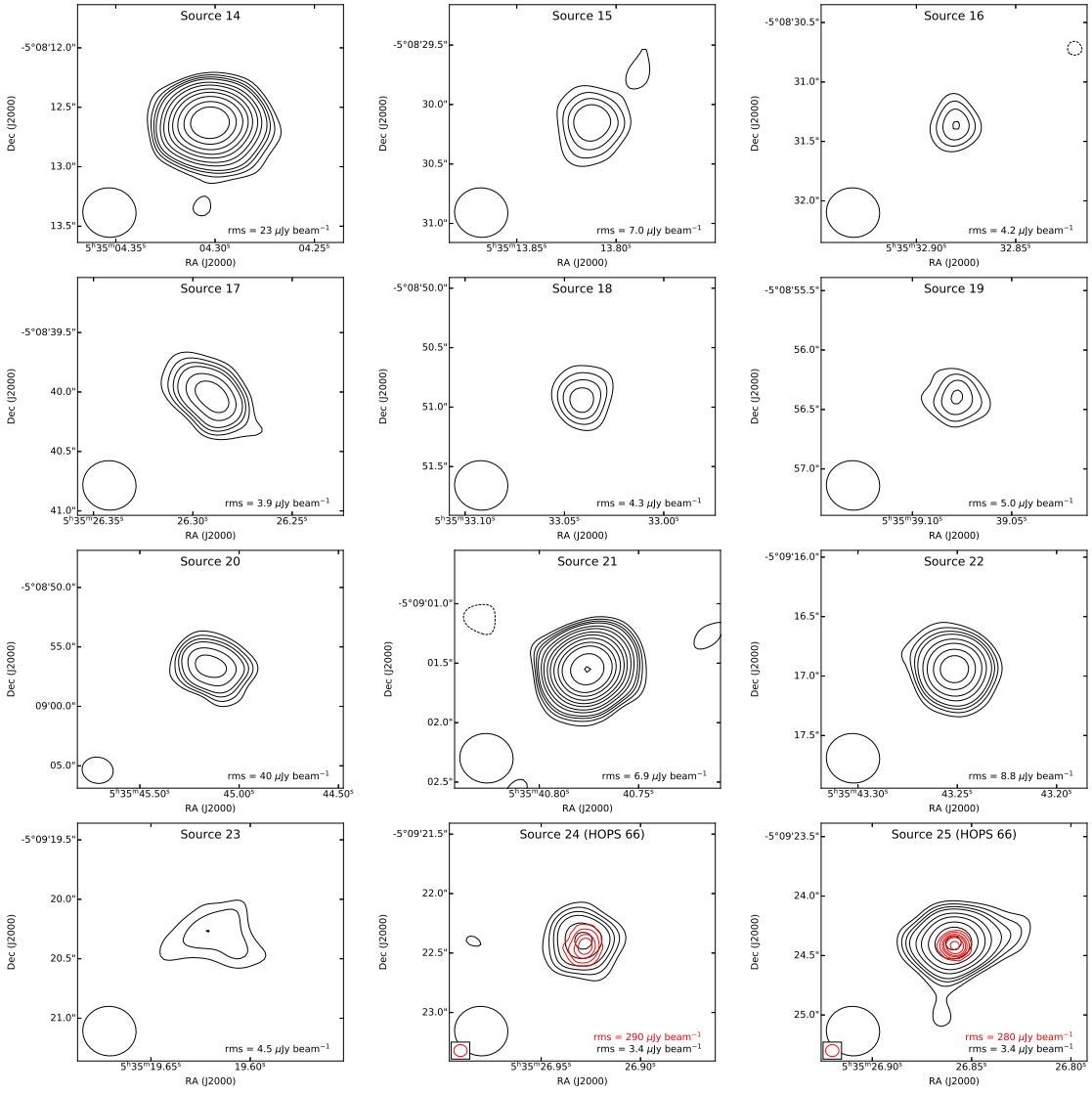

Figure 3.2 Continued on the next page.

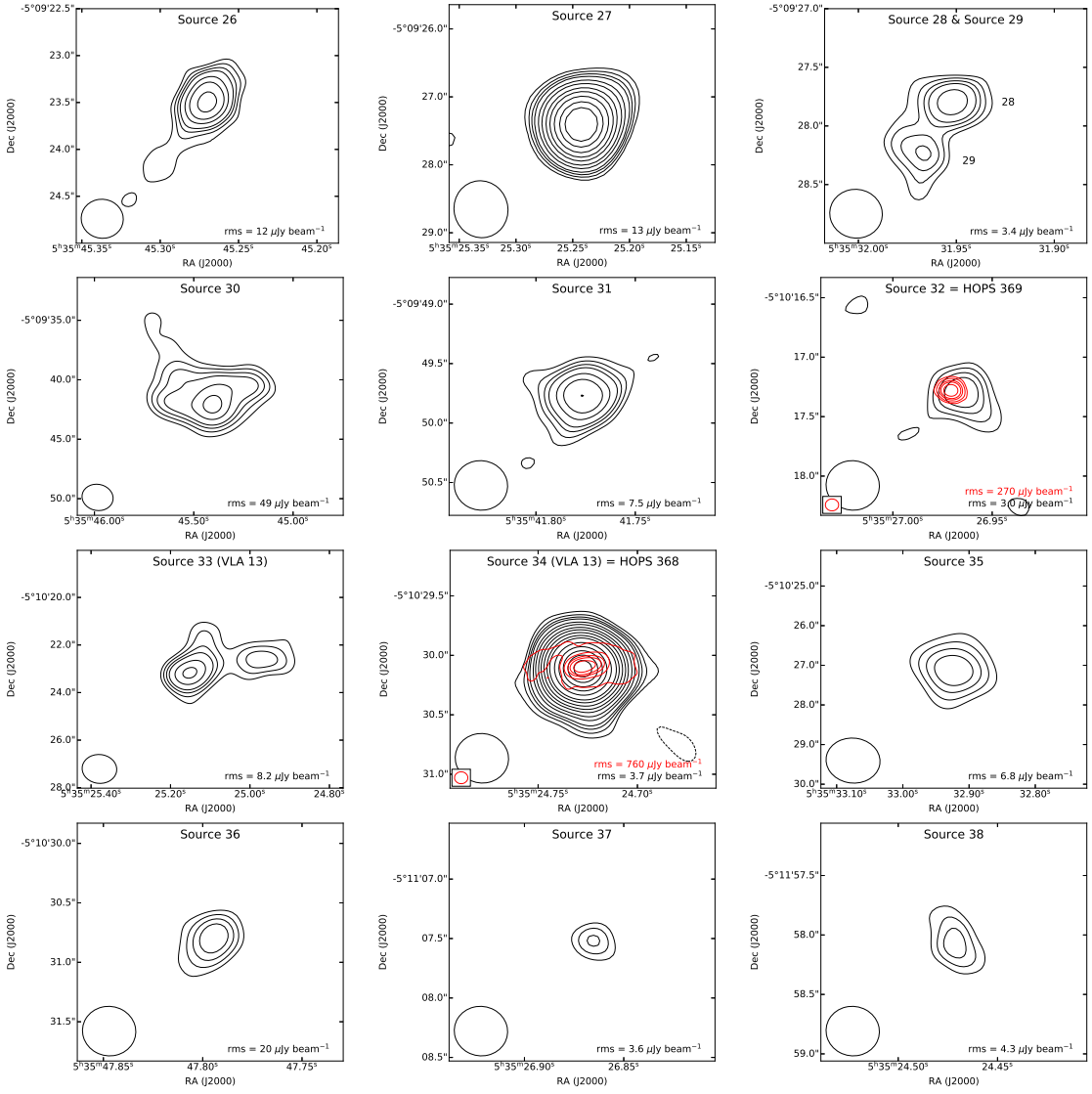

Figure 3.2 Continued on the next page.

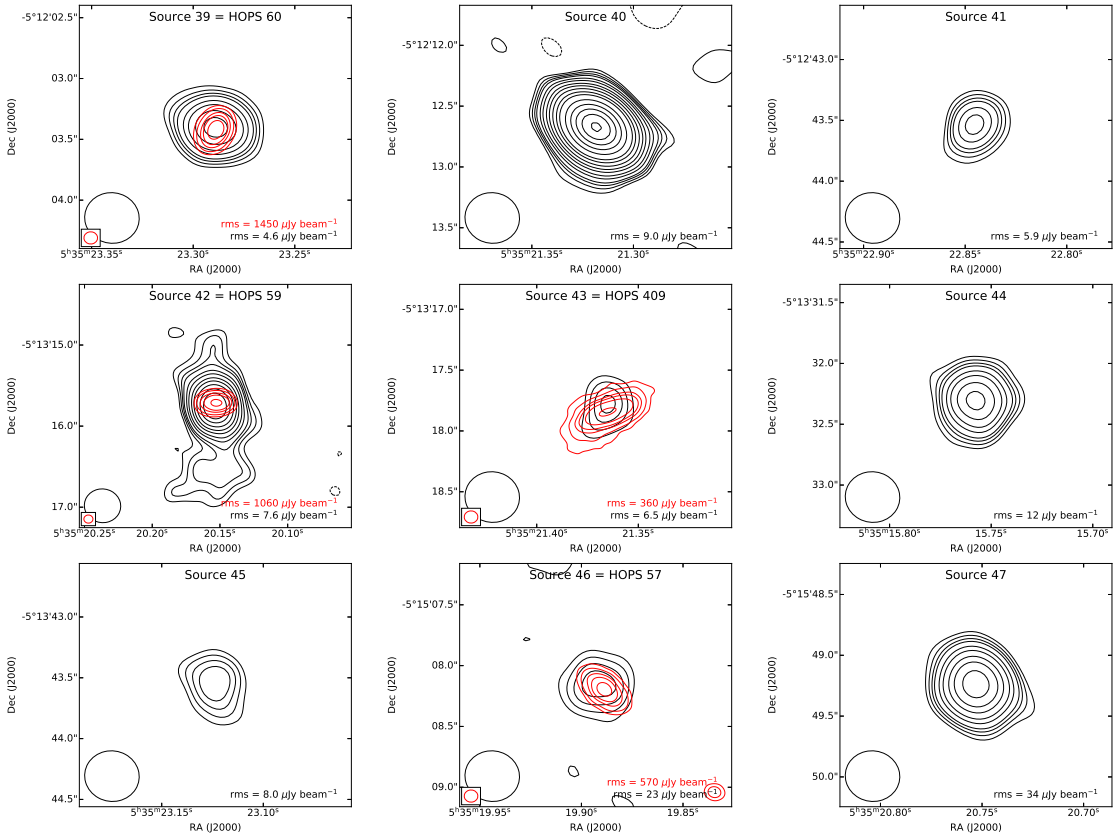

Figure 3.2 Final.

more evolved stage. In Section 3.4.2 we comment on the nature of the individual sources using additional information.

Interestingly, we note that a number of sources appear clustered along an east-west stripe almost perpendicular to the ISF (see Fig. 3.1). This E-W stripe has a width of $\sim 2'$ and extends in right ascension up to the limits of our field of view ($12\farcm5$). The distribution of the sources along the E-W stripe is not uniform, with the eastern side appearing more populated than the western side. This is further illustrated in Figure 3.4, where we plot, for the detected sources, their declination and distance to the ISF ridgeline (formed by finding the right ascension of the pixel with peak emission at each declination in the column density map shown in Fig. 3.1). The sources farther from the ISF are concentrated in a region with a declination between $-05°10'31''$ and $-05°07'20''$ (Fig. 3.4), where the dispersion (σ) of the distances to the ISF ridgeline reaches $114''$. Outside this declination range, the position of the sources fall very close to the ISF ridgeline, with a dispersion of the distances of $\sim 20''$. The two preferred orientations (along the ISF and along the E-W stripe) can be clearly seen in Figure 3.5, where we present the distribution of the position angles of the sources, measured from N to S, positive trough the E and negative trough the W, and taking the origin as the intersection point between the ISF and the E-W stripe (approximately $1\farcm3$ north from the phase center). Most of the sources have a position angle with an absolute value close to 0° or 180° (i.e., along the ISF, which is roughly aligned N-S), but a significant number of sources appear clustered close to a position angle with an absolute value of $\sim 90°$ (i.e., the sources in the E-W stripe roughly perpendicular to the ISF).

The alignment of sources in the E-W stripe suggests that the majority of them are not extragalactic since one would expect unrelated extragalactic sources to be randomly distributed. We may be detecting a cluster of radio-emitting galaxies but as we will see in Section 3.4.2, where we discuss the characteristics of the sources, this possibility can be ruled out. Furthermore, following a similar approach as in the ISF, we estimate that only 2 ± 1 of the ~ 16 sources that fall toward the stripe, but outside the ISF filament, are extragalactic. We consider, then, that most of the sources in the E-W stripe are also probably associated with the star-forming region. We note, however, that there is an apparent scarcity (or, at least, an irregular distribution) of extragalactic sources, since there are no detected sources

Table 3.3 Flux Densities and Spectral Indices of the Radio Sources

Source Index	2014 Flux Density[a] (mJy)				2015 Flux Density[a] (mJy)	Spectral Index[b]	Notes[c]
	5 cm	3 cm	1.3 cm	0.7 cm	5 cm		
1	<0.65[d]	···	···	···	0.37±0.04	-0.3±1.3[e]	V
2	<0.65[d]	···	···	···	0.062±0.012	···	
3	0.67±0.08	···	···	···	0.87±0.09	-0.08±0.50[e]	
4	2.6±0.3	2.2±0.3[f]	···	···	··· [g]	-0.3±0.3	E
5	0.082±0.018	<0.13	···	···	0.057±0.012	≤2.0	
6	0.094±0.018	<0.12	···	···	0.104±0.016	≤0.6	
7	0.055±0.015	<0.07	···	···	0.034±0.009	≤1.8	
8	0.057±0.014	<0.06	···	···	0.066±0.008	≤0.2	
9	0.27±0.03	0.23±0.03	···	···	0.193±0.023	0.0±0.6	
10	0.121±0.016[h]	0.052±0.016	···	···	<0.012	-1.7±0.7[i]	V
11	0.54±0.06[h]	0.58±0.07	···	···	0.44±0.05	0.3±0.4	V
12	0.063±0.013	0.066±0.016	···	···	0.26±0.03	0.1±0.6[i]	V
13	0.36±0.04	0.32±0.05			0.32±0.04	-0.13±0.20	
14	0.81±0.16	···	···	···	1.07±0.12	-0.02±0.19[e]	V
15	<0.06	<0.17	···	···	0.072±0.010	···	
16	<0.04	<0.05	···	···	0.026±0.005	≤2.3	
17	0.049±0.011	<0.03	<0.08	···	0.067±0.010	≤-0.6	
18	0.037±0.012	<0.04	···	···	0.036±0.008	≤0.24	
19	1.36±0.14	2.16±0.23	···	···	0.039±0.012	0.9±0.3[i]	V
20	1.93±0.21	···	···	···	1.72±0.21[j]	···	E
21	1.04±0.11	0.76±0.13	···	···	0.39±0.04	-0.6±0.4[i]	V
22	0.26±0.05	···	···	···	0.19±0.03	···	
23	0.065±0.020	<0.05	···	···	0.075±0.016	≤-0.4	
24	<0.14[d]	<0.25[d]	0.058±0.014	<0.14	0.040±0.007	0.29±0.24	
25	<0.14[d]	<0.25[d]	0.20±0.03	0.26±0.07	0.088±0.011	0.57±0.07	
26	0.29±0.06	···	···	···	0.26±0.04	···	
27	0.121±0.017	0.20±0.03	0.53±0.06	0.96±0.15	<0.009	1.06±0.05	V
28	<0.06[d]	<0.08[d]	<0.17[d]	···	0.033±0.005	0.74±0.03[d]	
29	<0.06[d]	<0.08[d]	<0.17[d]	···	0.022±0.005	0.74±0.03[d]	
30	3.2±0.3	···	···	···	3.2±0.4[j]	···	E
31	0.117±0.021	<0.19	···	···	0.128±0.019	≤1.0	
32	0.032±0.010	<0.04	0.045±0.010	<0.07	0.025±0.004	0.36±0.18	
33	0.49±0.06	0.49±0.06	0.46±0.11[k]	<2.5[l]	0.49±0.07[k]	-0.05±0.01	E
34	0.44±0.05	0.58±0.06	0.99±0.10	0.69±0.14	0.34±0.04	0.73±0.14	V
35	0.19±0.03	0.077±0.016	<0.15	···	0.084±0.017[k]	-1.7±0.5[i]	E, V
36	<0.12	···	···	···	0.16±0.03	1.0±0.4[e]	V
37	<0.04	0.033±0.009	<0.07	···	0.019±0.004	1.2±0.7	
38	<0.05	0.057±0.014	···	···	0.031±0.008	1.3±0.8	

Source Index	2014 Flux Density[a] (mJy)				2015 Flux Density[a] (mJy)	Spectral Index[b]	Notes[c]
	5 cm	3 cm	1.3 cm	0.7 cm	5 cm		
39	0.13±0.03	0.19 ±0.03	···	···	0.089±0.012	1.1±0.7	
40	0.56±0.06	0.53±0.07	···	···	0.84±0.08	-0.1±0.3	V
41	<0.07	<0.11	···	···	0.065±0.009	≤1.9	
42	0.76±0.09	0.59±0.09	···	···	0.58±0.07	-0.3±0.5	
43	0.061±0.016	<0.20	···	···	0.044±0.012	≤3.4	
44	0.20±0.05	···	···	···	0.23±0.03	···	
45	<0.13	···	···	···	0.073±0.016	-0.06±0.69[e]	V
46	<0.20	···	···	···	0.23±0.05	···	
47	1.17±0.11	···	···	···	1.31±0.14	-0.18±0.64[e]	

[a] Flux densities at the representative wavelength of the observing bands, given in Table 3.1. Upper limits are 3σ, except when noted. No data (···) means the source is outside the imaged field of view, except when noted.

[b] The spectral index is obtained from a least-squares fit (in log-log scale) to the 2014 and 2015 data points at the different frequencies where we detected the sources, taking into account upper limits when they are useful to constrain the fit (see Fig. 3.3).

[c] E: Source with extended emission. V: Suspected radio variable; the source present changes by a factor greater than 1.5 (taking into account uncertainties, see Section 3.3.4) in the flux density at a given frequency band (including data from the literature, see Fig. 3.3); in the case of sources 1, 34, and 40, the suspected variability is based on the minimum flux density from the observations of Kounkel et al. (2014), derived indirectly from their Table 2.

[d] The sources are blended. Upper limit corresponds to the total flux density of the two sources.

[e] Adopted from Kounkel et al. (2014).

[f] Measured in a map with uvtaper=20kλ in order to better detect the extended emission.

[g] Emission of this extended source is filtered out by the interferometer in the A configuration.

[h] The sources are blended. The flux density given for each source is obtained from a two-Gaussian fit.

[i] Derived using only 2014-epoch data since the 2015 flux density is significantly different.

[j] Measured in a map with uvtaper = 50 kλ in order to better detect the extended emission.

[k] Measured in a map with uvtaper = 100 kλ in order to better detect the extended emission.

[l] 3σ upper limit, assuming the source is extended with a size $18'' \times 13''$, obtained according to the prescriptions given by Beltrán et al. (2001, Apendix A).

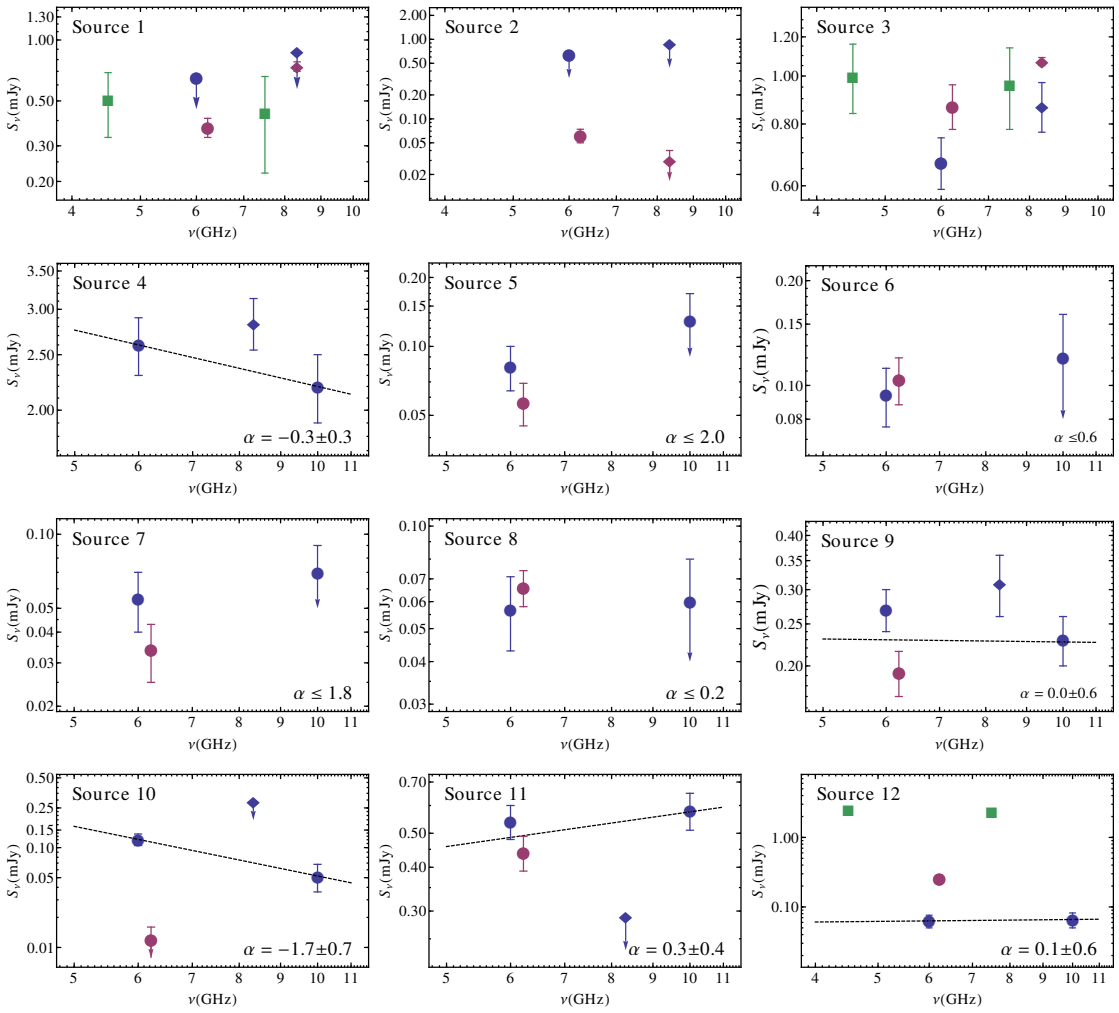

Figure 3.3 Spectra of the radio sources in the centimeter range. Error bars are $\pm 1\sigma$. In general, upper limits are represented by arrows where the central symbols are at 3σ. For sources blended at low-resolution observations (sources 1 and 2, 10 and 11, 24 and 25, 33 and 34) the flux density measured for both sources is given as an upper limit for each one. Least-squared fits (dashed lines) were made using only data from our work (2014 and 2015 epochs), taking into account upper limits when they constrain the fit. In the case of sources 10, 12, 19, 21, and 35, only 2014 data is used since their 2015 flux density is significantly different. The data represented is (see the last panel): red circles, 2015 A-configuration (this work); blue circles, 2014 C-configuration (this work); green squares, 2011 A-configuration (Kounkel et al. 2014); red diamonds, 2002 A-configuration (Reipurth et al. 2004), recalibrated; blue diamonds, 1998 D-configuration (Reipurth et al. 1999). Continued on the next page.

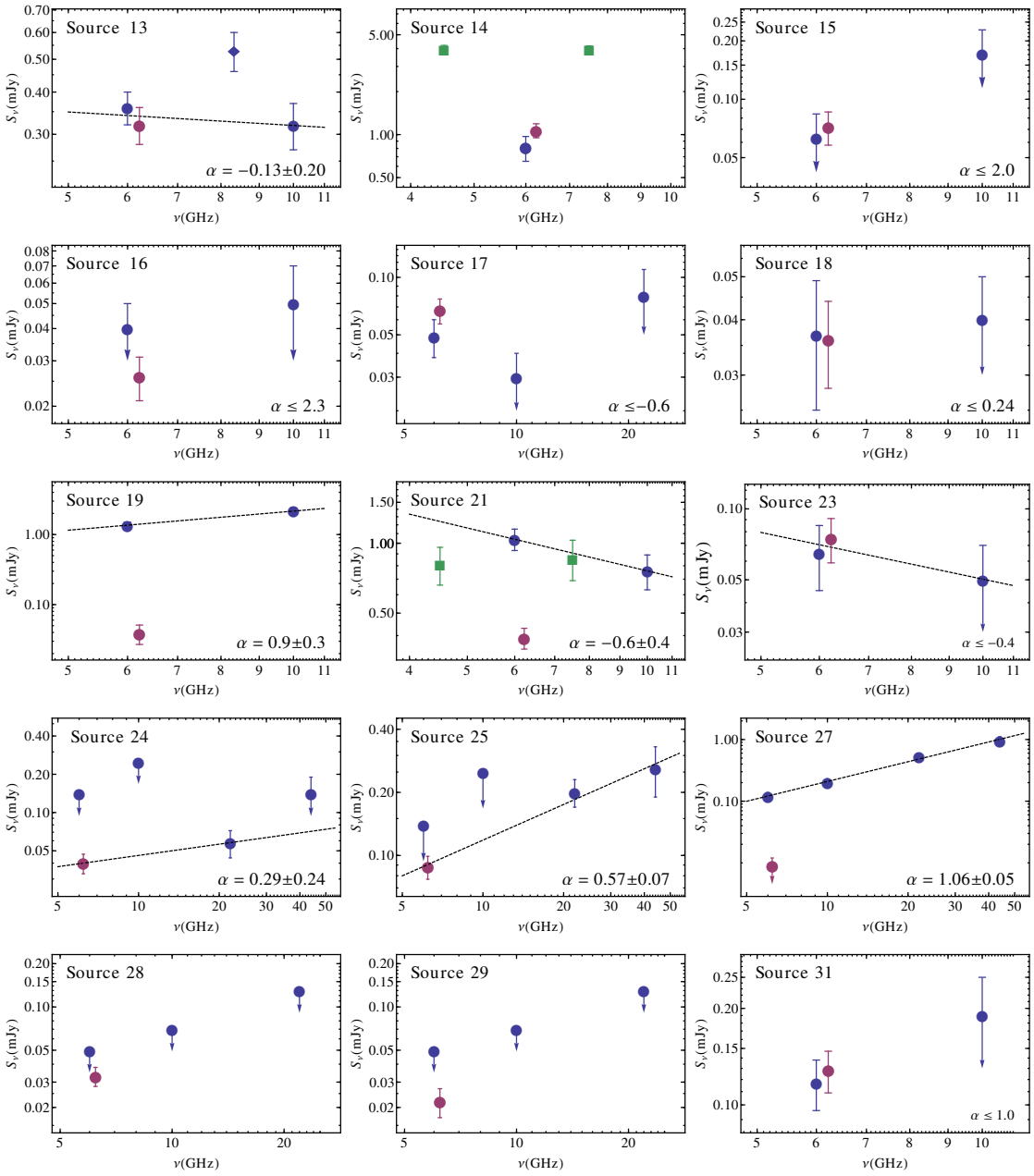

Figure 3.3 Continued on the next page.

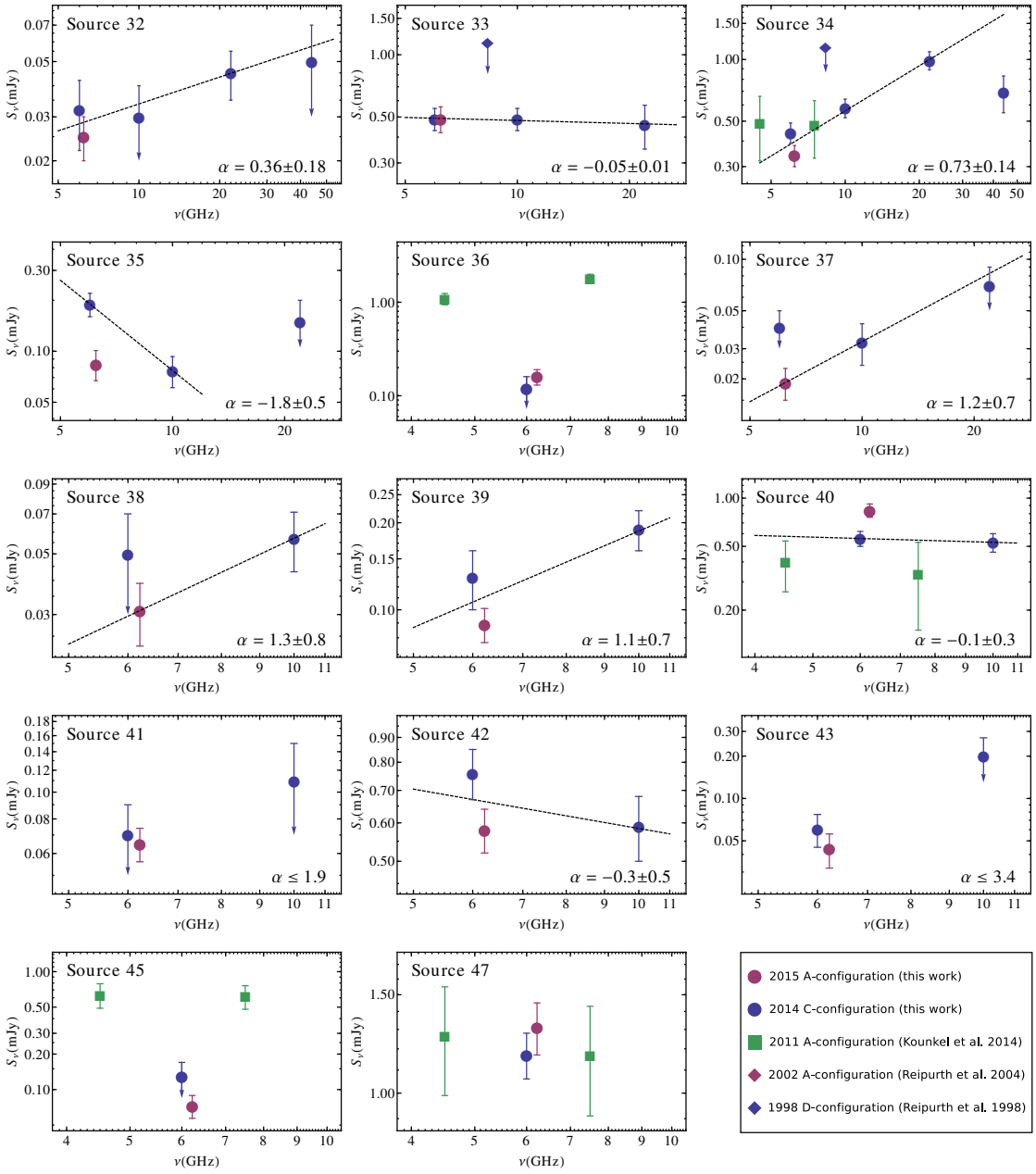

Figure 3.3 Final.

outside the declination range $-05°10'31'' < \delta < -05°07'20''$ at distances $> 50''$ of the ISF ridgeline, where we would expect to detect about ~ 6 extragalactic sources. We do not have an obvious explanation for this apparently anomalous distribution. However, this result deserves a more robust confirmation since we are dealing with relatively small numbers of poor statistical significance.

The column densities toward the E-W stripe, typically $\sim 1 \times 10^{22}$ cm^{-2}, are significantly lower than toward the filament ($\sim$ (2.5 - 40)$\times 10^{22}$ cm^{-2}), suggesting that most of the sources in this stripe could correspond to an older stellar population, in agreement with the fact that most of them have been previously classified as Class III YSOs (see further details in 3.4.2.12). To be consistent with their alignment, these objects should have formed in a structure almost perpendicular to the ISF. Recently, Hacar et al. (2018) found that the ISF is composed of several velocity-coherent fibers, fertile in star formation. While most of the fibers have their axis aligned with the filament, some deviate from this direction, and a few of them are almost perpendicular to it, like the branches of a tree (see their Fig. 4). Therefore, it is conceivable that the radio sources located in the E-W stripe may have previously formed in perpendicular fibers whose material has already been depleted.

In this Section we made, essentially, statistical considerations on the expected number of extragalactic sources, and the association of the detected radio sources to the star-forming region. However, there is additional information on the individual sources (spectral index, emission at other wavelengths, etc), that allows us to ascertain which particular sources belong to the star-forming region. Using these complementary data, in Section 3.4.2 we discuss in detail the nature of the individual sources.

3.3.2 Spectral Indices of the Detected Radio Sources

A useful parameter to investigate the nature of the radio sources is the spectral index α, where $S_\nu \propto \nu^\alpha$. However, the interpretation of spectral indices, especially when they are restricted to a limited range of wavelengths, is not unambiguous. There are uncertainties in the spectral index measurement (due to source variability, differences in angular resolution and/or intrinsic uncertainties in the flux measurements). Additionally, different emission mechanisms (or a combination of

Table 3.4 Association with Emission at other Wavelengths and Nature of the Detected Radio Sources[a]

Source Index	Alternative Names	Compact/unresolved Emission[b]	Outflow/SF Signatures	Nature/ Evol. Stage[c]	Ref.
1	HOPS 78	SMM, FIR, MIR[d]	mm core, H_2 knots, CO outf.	Class 0	1, 2, 3, 4, 5, 6, 7
2		MIR?[d]	mm core?	YSO or Source 1 knot	4, 8, 9
3				EG	10
4		NIR	MIR nebulosity	HII	9, 10, 11
5		MIR, NIR, XR		EG (disk galaxy?)	9, 12, 13
6				?	
7		MIR, NIR, XR*		Class I/II	3, 8, 11, 13
8				?	
9	PBR 019003, HOPS 394, FIR 1a	SMM, FIR?, XR?	mm core?,CO outf.	Class 0, PBR	1, 2, 4, 7, 8, 14
10		SMM, MIR, NIR, OP, XR*		Class II	1, 8, 9, 11, 13, 15
11	HOPS 71	SMM, FIR, MIR, NIR	mm core, CO outf.	Class I	1, 2, 3, 4, 7, 11
12	V0492 Ori	MIR, NIR, OP*, XR	mm core?	Class I/II	3, 4, 8, 11, 13, 15, 16
13		XR		EG	9, 10, 13
14	V1321 Ori	MIR, NIR, OP*, XR		Class III	8, 11, 13, 15, 16
15				?	
16		NIR		?	9
17	NP Ori	MIR, NIR, OP*, XR*		Class III	8, 11, 13, 15, 16
18		NIR		?	9
19	V1576 Ori	MIR, NIR, OP*, XR		Class III	8, 11, 13, 15, 16
20				Source 26 knot?	9
21	V0363 Ori	MIR, NIR, OP*, XR		Class II/III	8, 11, 13, 15, 16
22	V0569 Ori	MIR, NIR, OP*, XR*		Class III	8, 11, 13, 15, 16
23		NIR		EG or Class II/III	9
24	HOPS 66, SOF 1	SMM, FIR[f]	mm core?	YSO	1, 2, 4, 9
25	HOPS 66, SOF 1, V2455 Ori	SMM, FIR[f], MIR, NIR*	mm core, IR cavity	Flat spectrum[g]	1, 2, 3, 4, 11, 16, 17
26		MIR, NIR		Radio galaxy?	9, 12
27	V1344 Ori	MIR, NIR, OP*, XR		Class III	8, 11, 13, 15, 16
28	V0360 Ori	MIR, NIR, OP*, XR*[h]		Class I/II[i]	3, 8, 11, 13, 15, 16
29	V0360 Ori	MIR, NIR, OP*, XR*[h]		Class I/II[i]	3, 8, 11, 13, 15, 16
30				Source 26 knot?	9
31		NIR		?	9
32	HOPS 369, SOF 4	SMM, FIR, MIR, NIR	mm core?	Flat spectrum	1, 2, 3, 4, 11, 17
33				Shock-ionized region	9
34	HOPS 368, SOF 5	SMM, FIR, MIR, NIR	mm core, CO outf., IR cavity	Class I	1, 2, 3, 4, 7, 11, 17
35		MIR, NIR, XR?		EG or Class II/III	8, 9, 12
36	NSV 16575	MIR, NIR, OP*, XR		Class III	8, 11, 13, 15
37	SOF 6, AI Ori	MIR, NIR, OP*, XR	mm core?	Class I/II	3, 4, 8, 11, 13, 15, 16
38		MIR, NIR, OP, XR?		YSO	8, 9, 15, 18

Source Index	Alternative Names	Compact/unresolved Emission[b]	Outflow/SF Signatures	Nature/ Evol. Stage[c]	Ref.
39	HOPS 60, SOF 7, FIR 6b	SMM, FIR, MIR	mm core, CO outf., IR cavity	Class 0	1, 2, 3, 4, 7, 17, 19
40		MIR, NIR, OP, XR		Class III	8, 11, 13, 15
41			mm core?	?	4
42	HOPS 59, SOF 8, FIR 6d, V2364 Ori	SMM, FIR, MIR, NIR*, OP, XR	mm core, CO outf., IR cavity	Flat spectrum	1, 2, 3, 4, 11, 13, 15, 16, 17, 19
43	PBR 135003, HOPS 409, FIR 6c	SMM, FIR	mm core, CO outf.	Class 0, PBR	1, 2, 4, 7, 20, 21
44				?	
45		MIR, NIR, OP, XR		Class II/III	8, 11, 13, 15
46	HOPS 57	SMM, FIR, MIR, NIR, XR	mm core	Flat spectrum	1, 2, 3, 4, 11, 13, 16
47		MIR, NIR, OP, XR*		Class III	8, 11, 13, 15

[a] For sources VLA 11 (HOPS 370), HOPS 108, HOPS 64, MIPS 2301, MIPS 2297, VLA 15, and VLA 16, see Chapter 2.

[b] Point source detected at sub-millimeter (SMM), far-IR, mid-IR, near-IR, optical (OP) or X-ray (XR) wavelengths; the * indicates variability in that wavelength range.

[c] EG: Extragalactic, HII: Ionized region, PBR: PACS Bright Red source, YSO: Young stellar object.

[d] Emission detected as a single source with an intermediate position between our sources 1 and 2. We favor the association with Source 1 (see Section 3.4.2.1).

[e] Note that the source is associated with the mm core #11 of Kainulainen et al. (2017), not with #12 as mistakenly reported in their Table 2.

[f] Emission detected as a single source at far-IR due to insufficient angular resolution.

[g] This classification is based on a SED that probably contains emission from both sources 24 and 25.

[h] Sources 28 and 29 have each one an optical counterpart; emission at mid, near-IR, and X-ray is detected as a single source due to insufficient angular resolution. We favor the association with both sources.

[i] This classification is based on a SED that contains emission from both sources 28 and 29.

References— (1) Tobin et al. 2020, (2) Furlan et al. 2016, (3) Megeath et al. 2012, (4) Kainulainen et al. 2017, (5) Stanke et al. 2002, (6) Williams et al. 2003, (7) Takahashi et al. 2008, (8) Getman et al. 2017, (9) This work, (10) Reipurth et al. 1999, (11) Skrutskie et al. 2006, (12) T. Megeath, private comunication, (13) Tsujimoto et al. 2002, (14) Stutz et al. 2013, (15) Gaia Collaboration et al. 2018, (16) Samus et al. 2017, (17) Habel et al. 2020, (18) Da Rio et al. 2009, (19) Shimajiri et al. 2009, (20) Tobin et al. 2015, (21) Tobin et al. 2016c.

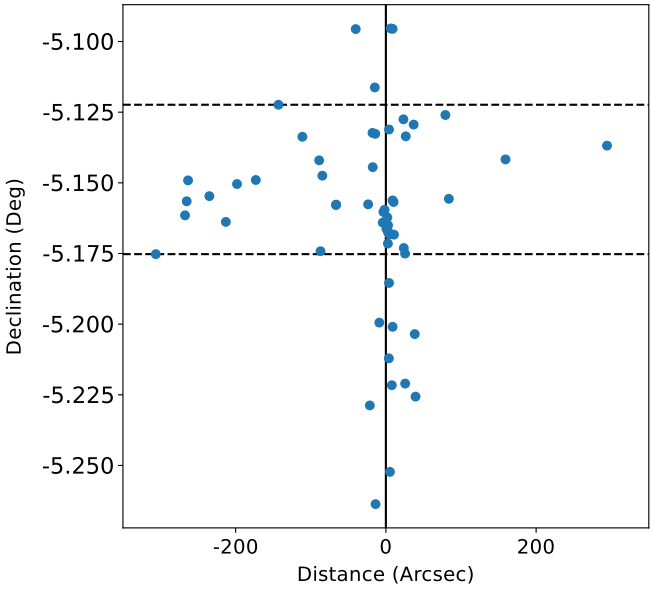

Figure 3.4 Declination of the radio sources versus their distance to the ISF ridgeline. The farthest sources are concentrated in a region with a declination between $-05°10'31''$ and $-05°07'20''$ (the region bounded by dashed lines). The ridgeline of the ISF is formed by finding the α of the pixel with peak emission at each δ in the column density map (Stutz 2018) shown in Figure 3.1.

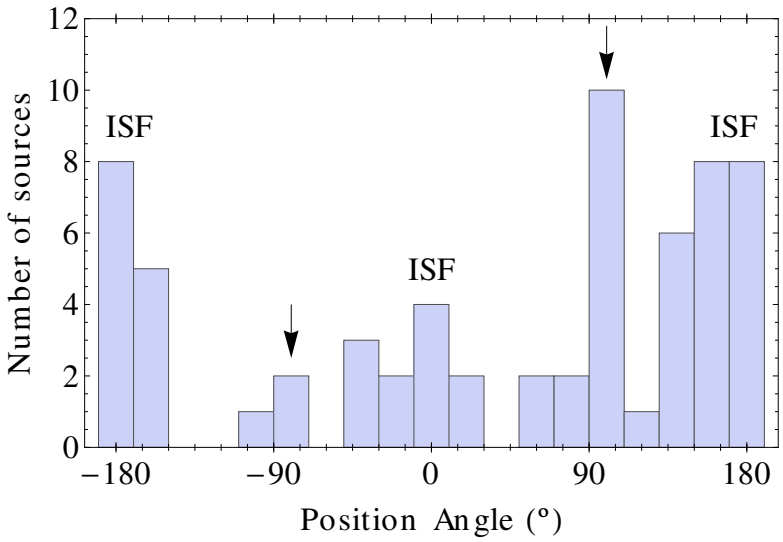

Figure 3.5 Distribution of the position angles of the sources, measured from N to S, positive through the E and negative through the W, taking the origin as the intersection point between the ISF and the E-W stripe. We excluded the only source at a distance $\leq 30''$ from the origin since its position angle is not well determined. Most of the sources have a position angle with an absolute value close to 0° or 180° (i.e., along the ISF, which is roughly aligned N-S), but a significant number of sources appear clustered close to a position angle with an absolute value of $\sim 90°$ (i.e., perpendicular to the ISF), indicated by arrows in the histogram.

them) can produce similar values of the spectral index, while the same emission mechanism can produce different values of the spectral index. Despite these uncertainties, in general, a flat or positive spectral index ($\alpha \geq -0.1$) usually indicates thermal emission, while a negative one ($\alpha < -0.1$) is indicative of non-thermal emission. Below we summarize the possible astrophysical objects that we can detect with our cm observations, and characterize their emission in terms of α.

Massive young stars can photoionize the surrounding gas, creating the so-called photoionized HII regions, with thermal free-free emission. The free-free spectrum of a homogeneous HII region is characterized by optically thick emission at low frequency (with $\alpha \simeq 2$) and optically thin emission at high frequency ($\alpha \simeq -0.1$). The turnover frequency at which the emission becomes optically thin depends on the electronic density n_e of the region. Very young HII regions can be very compact and dense ($n_e > 10^6$ cm^{-3}), in contrast to the more evolved, classical HII regions that can be much more extended, reaching sizes of the order of several pc, and are less dense ($n_e \simeq 10^3$ cm^{-3}). Because of the very high n_e of the youngest HII regions, their turnover frequency occurs at high frequencies, and their cm emission is (moderately) optically thick, with typical spectral indices $\gtrsim 1$.

Thermal radio jets (Anglada 1995, 1996; Anglada et al. 2018) trace the base (a region very close to the exciting source) of the larger ionized jets from YSOs observed at other wavelengths such as infrared and optical. These radio jets are observed through their thermal free-free emission from shock-ionized gas. The emission is expected to be optically thick ($\alpha \simeq 2$) in the region nearest to the star (where densities are higher) and optically thin ($\alpha \simeq -0.1$) at larger distances. The combination of these two components results in a constant spectral index with an intermediate value for the total emission over most of their radio spectrum. For a conical radio jet with constant temperature, velocity, and ionization fraction, $\alpha = 0.6$ is expected (Reynolds 1986). In general, a typical value of spectral indices of observed radio jets is $\alpha \sim 0.4$ (Anglada et al. 2018). Frequently, radio jets appear just as weak compact sources, which, in sensitive sub-arcsec angular resolution observations, can show an elongated morphology in the direction of the large-scale outflow (see Anglada et al. 2018 for a complete review on protostellar radio jets and their properties). They are useful to pinpoint YSOs, particularly those most deeply embedded.

In general, radio emission of photoionized HII regions is expected to be stronger than that of radio jets (which are weakly ionized, likely by shocks, see Anglada et al. 2018). Thus, among the radio sources with $-0.1 \leq \alpha < 2$, we will tend to identify

as radio jets the weak, elongated, or unresolved radio sources, while we will tend to consider as photoionized HII regions the strongest ones, either compact or extended with a cometary or irregular morphology, provided the required photoionization rate to account for the observed cm emission is consistent with the luminosity of the source.

Photoionized disks are also free-free emitters, and thus, they are expected to present radio spectral indices rather similar to those of radio jets (Lugo et al. 2004; Anglada et al. 2018). If angularly resolved, these sources can appear elongated in the direction of the disk plane (Hoare 2006; Macías et al. 2016), making it difficult to distinguish them from the radio jets when no additional information on the orientation of the disk or outflow is available. The mechanism proposed to ionize and heat the disk surface in low-mass YSOs is high-energy radiation (far-UV, extreme-UV, and X-ray) from the stellar chromosphere of the young stars (Class II/III).

Thermal emission from dust, either from a disk or from a dusty envelope, also has a positive spectral index, but steeper than that of free-free (i.e., $\alpha \geq 2$). However, in observations with an insufficient angular resolution, both the dust emission from the disk and the free-free emission from the jet are blended, resulting in an intermediate spectral index between free-free and dust.

Young stars with active magnetospheres (evolved YSOs) can be sources of non-thermal gyrosynchrotron emission. These radio sources are very compact, are expected to present negative spectral indices, and can be circularly polarized (André 1996; Garay et al. 1996; Rodríguez et al. 1999; Kounkel et al. 2014; Ortiz-León et al. 2015). Detection of circular polarization strongly suggests gyrosynchrotron emission, but the lack of detectable polarization does not exclude this kind of emission.

In several cases, negative spectral indices, suggestive of non-thermal emission, have been measured toward the lobes of YSO radio jets, at relatively large distances from the star, while the core of the jet, close to the star, presents a positive spectral index, indicative of thermal emission (e.g., HH 80-81: Marti et al. 1993; Rodríguez et al. 2005, Serpens: Rodríguez-Kamenetzky et al. 2016, HOPS 370: Osorio et al. 2017). The detection of linear polarization in the radio emission of the HH 80-81 jet lobes (Carrasco-González et al. 2010) confirmed its non-thermal synchrotron nature, suggesting that the emission originates from relativistic particles accelerated by strong shocks in the jet. Since the degree of polarization in

YSO jets is low, linear polarization is hard to detect, and, in general, a negative spectral index is considered an indication of a synchrotron jet lobe.

Extragalactic sources also present non-thermal synchrotron emission, typically with a spectral index $\alpha \sim -0.7$ for optically thin emission (Condon 1984). Optically thick synchrotron emission has a positive spectral index and could be confused with thermal emission, but the turnover frequency in extragalactic sources is low (30 MHz - 1 GHz, O'Dea 1998) and falls outside the frequency range of our observations. Extragalactic sources can be highly variable. They are usually very compact but can also show a lobe-core-lobe morphology that can be confused with a YSO jet, but they do not present measurable proper motion.

Thus, radio sources with negative spectral indices are candidates to be either a more evolved YSO, an extragalactic source, or a non-thermal knot of a radio jet. Additional information (e.g., morphology, proper motions, and polarization studies) can help to discern their nature. We will analyze their association with features at other wavelengths (see Section 3.3.3) as an additional piece of information in an attempt to properly classify them.

For all the 47 sources reported here, we measured the flux densities at each observed band (5, 3, 1.3, and 0.7 cm) and constructed their spectra at radio wavelengths using our data, as well as data compiled from the literature (Reipurth et al. 1999, 2004; Kounkel et al. 2014; see Table 3.3 and Fig. 3.3). The spectral index is obtained from a least-squares fit (in log-log scale) to the data points at the different frequencies where we detected the sources, taking into account upper limits when they are useful to constrain the fit. For the spectral index calculations we used only our data, which were obtained within a relatively short time interval, < 1 yr (2014 - 2015), in order to minimize variability problems that would result in spurious values of α. For sources 10, 12, 19, 21, and 35, only the 2014-epoch data is used since their 2015 flux density is significantly different, indicating they could be variable sources (see Section 3.3.4). There are 13 sources that were observed only at 5 cm (see Table 3.3), and a spectral index cannot be obtained. In Table 3.3 we list the values of the spectral indices obtained from our data; for completeness, for a few sources, when our data were insufficient to obtain the spectral index, we list values reported by Kounkel et al. (2014) which were derived using data observed closely in time (3 epochs within 1 month).

As mentioned before, the sign of the spectral index gives information about the nature of the radio emission (flat or positive indicates thermal emission while negative indicates non-thermal emission). Of the whole sample of 57 radio sources,

Table 3.5 Summary of the Spectral Indices and Association with Dust Tracers

Spectral Index[a]	Toward ISF[b]			Outside ISF[b]
	Compact Dust?[c]		Total	
	Yes	No		
≥ -0.1	13	4	17	2
< -0.1	1	6	7	1
?	8	10	18	12

[a] From Table 3.3 and Table 2.3.

[b] We consider that a source is located toward the Integral Shaped Filament (ISF) when the column density at its position, as estimated from Herschel 100 - 500 μm data (Stutz 2018), is $> 2.3 \times 10^{22}$ cm^{-2}, and that it is outside otherwise (see Table 3.2).

[c] Association with compact dust mm/sub-mm emission, either at core (Kainulainen et al. 2017) or disk (Tobin et al. 2020) scales. See Section 3.3.1.

consisting of the 10 radio sources reported in Chapter 2 and the 47 additional sources reported here, we are able to assess the sign of the spectral index for 27 of them (47%): 19 sources with $-0.1 \leq \alpha < 2$ that we identify as likely thermal free-free emission, and 8 sources with $\alpha < -0.1$, suggesting non-thermal emission (values given in Tables 2.3 and 3.3). Most of the sources toward the ISF (17/24) have a positive spectral index, and 76% (13/17) of them are associated with compact mm/sub-mm emission, either at core (Kainulainen et al. 2017) or disk (Tobin et al. 2020) scales (see Section 3.3.1), indicating they are probably YSOs. Notably, all the sources detected toward the peak of a 3 mm core (likely tracing deeply embedded protostars) have positive spectral indices. In Table 3.5 we show a summary of the spectral indices and association with dust of the 57 detected radio sources.

3.3.3 Association of the Radio Sources with other Star Formation Activity Tracers

Emission in other wavelength ranges can give us valuable additional information about our radio sources. For example, protostars (Class 0/I) are usually associated with sub-mm and far-IR thermal dust emission coming from the envelope of infalling gas and dust. Signs of mass ejection such as molecular outflows, collimated jets, and cavities in the envelope are also often observed toward protostars. On the other hand, more evolved YSOs (Class II/III) are generally associated with near-IR and/or optical emission, coming from the accretion disk and the star itself. Class III YSOs are often associated with X-ray emission from magnetic reconnec-

tion flaring near the stellar surface, although a fraction of Class I and II YSOs also present detectable X-ray emission (Getman et al. 2017).

We searched for counterparts of our detected radio sources in point source catalogs in the far-IR (Stutz et al. 2013; Furlan et al. 2016), mid-IR (Megeath et al. 2012, 2016; Getman et al. 2017), near-IR (Skrutskie et al. 2006; Hillenbrand 1997; Hillenbrand et al. 2013; Kounkel et al. 2016), optical (Gaia Collaboration et al. 2018), and X-ray (Tsujimoto et al. 2002, 2003b; Getman et al. 2017). We also searched the literature for signposts and features potentially associated with them, such as mm dust cores (Chini et al. 1997; Kainulainen et al. 2017), outflows (Williams et al. 2003; Takahashi et al. 2008; Shimajiri et al. 2009), and IR outflow cavities (Habel et al. 2020). Additionally, we looked for extended emission associated with our radio sources in images obtained with the following facilities: HST (0.8 - 2.5 μm, Habel et al. 2020), NEWFIRM (1.662 and 2.159 μm, T. Megeath, private communication), *Spitzer* (3.6, 4.5, 5.8, 8, and 24 μm, Megeath et al. 2012), *Herschel* (70 and 160 μm, Stutz et al. 2013), APEX (350 and 870 μm, Stutz et al. 2013). Our results are summarized in Table 3.4, where we report the counterparts and other interesting features observed at other wavelengths potentially associated with our radio sources. Among the IR counterparts, we report seven NEWFIRM and *Spitzer* sources that are identified here for the first time (see further details in Section 3.4.2.4, 3.4.2.13, and 3.4.2.19).

Of the 57 radio sources reported here and in Chapter 2, we find that 45 (79%) have possible counterparts. For better visualization, we show in Figure 3.6 a Venn diagram of the different types of counterparts. As can be seen in the figure, 21 radio sources have X-ray, 36 have near-IR or optical, 35 have mid-IR, and 18 have far-IR or sub-mm proposed counterparts[4]. Out of the 21 radio sources with an X-ray counterpart, only 3 (sources 10, 42, and 46, see Table 3.4) also have a far-IR/sub-mm counterpart, in agreement with the general belief that X-ray emission is probably not associated with the youngest protostars (Getman et al. 2017). Furthermore, Source 42, which is the only one with counterparts at all the wavelengths inspected, is an embedded protostar with an irregular cavity (see further details in Section 3.4.2.23) through which we are probably seeing the short-wavelength emission from the inner envelope and disk. Four radio sources only have FIR/sub-mm counterparts (sources 9, 24, 43 from this Chapter, and VLA 15 from Chapter 2), suggesting they are very young. As expected, the radio sources

[4]We do not include in these statistics the few doubtful identifications marked with "?" in Table 3.4.

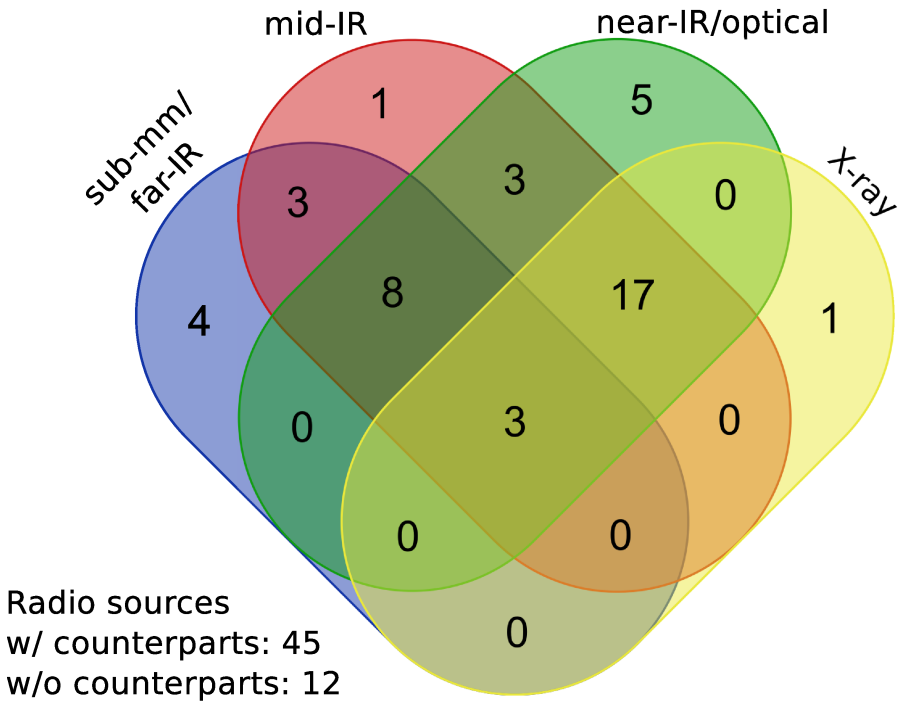

Figure 3.6 Venn diagram of the sub-mm/far-IR (18), mid-IR (35), near-IR/optical (36), and X-ray (21) counterparts of the 57 detected radio sources. The total radio sources with counterparts are 45. The few (5) doubtful identification marked with "?" in Table 3.4 are not included in these statistics. Diagram generated at Bioinformatics & Evolutionary Genomics.

with far-IR/sub-mm counterparts are located in the densest part of the ISF, while radio sources with counterparts at shorter wavelengths are systematically located further away from the ISF (see Table 3.4 and Fig. 3.1). We do not find a trend for the spatial distribution of the radio sources with X-ray counterparts.

Of the same 57 radio sources considered above, we find that 9 (16%) have known outflows and/or cavities associated with them (Table 3.4). These are the sources 1, 9, 11, 25, 34, 39, 42, 43 (discussed in this Chapter) and VLA 11 (discussed in Chapter 2). These sources are also associated with far-IR/sub-mm emission and are observed toward compact dust cores (see Section 3.3.1). They are probably the youngest YSOs in our sample.

In Table 3.4 we include information on the proposed nature of the radio sources, and the evolutionary stage of the YSOs when known (see Section 3.4.2 for further details). We are able to suggest the nature of 46 out of 57 radio sources, with 36 of them probably being YSOs.

3.3.4 Variability of the Radio Sources

We compared our flux density measurements with those of previous works (Reipurth et al. 1999, 2004; Kounkel et al. 2014; see Table 3.3 and Fig. 3.3) in order to search for signs of radio variability. Because the flux values reported by Reipurth et al. (2004) for sources 1 and 3 are systematically higher than values in other works, we recalibrated their data following the more recent recommendations for the VLA calibration process and obtained the more consistent values shown in our spectra (Fig. 3.3). We consider a source as a probable radio variable (Table 3.3) if the flux density at the same band changes by a factor greater than 1.5 between different epochs, taking into account the uncertainties. We exclude from this analysis four sources that do not trace compact emission toward the position of a YSO[5].

We find that 13 out of 53 sources (25%) meet our variability criterion (sources 1, 10, 11, 12, 14, 19, 21, 27, 34, 35, 36, 40, and 45), with changes by a factor up to 30 (the most extreme case is Source 19) in timescales of years. All of these 13 sources seem to be YSOs, mostly evolved ones (Class II/III), except the Class 0 Source 1 and the Class I sources 11 and 34 (see further details in Section 3.4.2); Source 35 could be either an extragalactic source or an evolved YSO.

We searched the literature for variability at X-ray (Tsujimoto et al. 2002, 2003b), near-IR or optical (Samus et al. 2017) wavelengths, finding that 19 out of these 53 sources (36%) are variable at those wavelengths (see Table 3.4 and Chapter 2[6]). All these 19 sources seem to be evolved YSOs (Class II/III, see further details in Section 3.4.2). Interestingly, seven of them are also among the suspected radio variables.

3.3.5 Multiplicity of the Radio Sources

The high angular resolution reached in our observations at 5 cm allows us to separate emission from radio sources as close as 0.″4 (154 au at the adopted distance to Orion), resolving into multiple different sources emission that was previously attributed to a single source in lower angular resolution observations (Reipurth et al. 1999; Furlan et al. 2016; see Tables 3.2 and 3.4). In particular, we resolve the

[5]We excluded sources VLA 12N, VLA 12C, and VLA12S, reported in Chapter 2, since they are knots from the HOPS 370 jet, and Source 33, which we interpreted as a shock-ionized wall of the cavity associated with Source 34 (Section 3.4.2.17).

[6]The sources MIPS 2301 and HOPS 64, variable in the near-IR, and MIPS 2297, variable in the optical, were presented in Chapter 2.

radio sources VLA 5 into sources 1 and 2, VLA 9 into sources 10 and 11, and VLA 13 into sources 33 and 34, and the far-IR source HOPS 66 into sources 24 and 25.

Previous works (e.g., Reipurth, & Zinnecker 1993; Duchêne et al. 2004; Tobin et al. 2016b) have searched for multiple systems with a projected separation $<$ 2000 - 3000 au, which is an order of magnitude smaller than the typical star-to-star separation (between $\sim$ 10000 - 20000 au, depending on the density of the star-forming region, according to Reipurth, & Zinnecker 1993). These authors argued that companions found within these separations are likely to be gravitationally bound. However, using this approach to identify multiple systems has some drawbacks. First, the number of multiple systems identified depends considerably on the adopted range of separations, which is somewhat arbitrary. Secondly, projected separations are smaller than the real distances, and in some cases, unrelated objects may appear as close companions. Finally, unresolved systems, with components closer than the observational resolution limit, will be missed.

Nevertheless, if we consider projected separations between 154 au (our angular resolution limit) and 3000 au ($\sim 8''$), we find 7 possible resolved binary systems[7]. These are the ones formed by sources 1 and 2 (at 1081 au of projected separation), sources 10 and 11 (at 1853 au), sources 24 and 25 (at 849 au), sources 28 and 29 (at 232 au) —reported in this Chapter— and HOPS 370 and MGM 2301 (at 1042 au), HOPS 64 and HOPS 108 (at 2316 au), and VLA 15 and VLA 16 (at 2393 au) —reported in Chapter 2. All of these objects are probable YSOs (see Section 3.4.2 and Chapter 2), except for Source 2 that could be a YSO or a knot of Source 1 (see Section 3.4.2.1). No higher-order multiple systems are found.

Two parameters broadly used to characterize the multiplicity of a sample are the multiplicity frequency or multiplicity fraction (MF), which gives the fraction of non-single systems, and the companion fraction (CF), which gives the average number of companions per system. They are defined as $MF = (B + T + Q + ...)/(S + B + T + Q + ...)$, and $CF = (B + 2 \times T + 3 \times Q + ...)/(S + B + T + Q + ...)$, where S, B, T, Q, ..., are the number of single, binary, triple, and quadruple ..., systems (Reipurth, & Zinnecker 1993). The value of MF is always between 0 and 1, while $CF = MF$ in samples with only single stars or binary systems, or $CF > MF$ in samples with higher-order multiple systems (see Duchêne, & Kraus 2013).

[7]We exclude from this analysis sources VLA 12N, VLA 12C, VLA 12S (reported in Chapter 2), and Source 33 (see Section 3.4.2.17) since they are not tracing YSOs.

For our sample of 53 radio sources, we find $MF = CF = 0.15 \pm 0.05$[8]. This is a "local" result, since our sample represents a small fraction of the more than 300 known protostars in Orion.

Tobin et al. (2016b) explore the multiplicity of their sample of 94 protostars in Perseus for different separation ranges between 20 and 10000 au. In particular, they found $MF = 0.27 \pm 0.05$ and $CF = 0.31 \pm 0.06$ in a separation range from 50 to 2000 au. However, we cannot make a direct comparison. First, there could be intrinsic differences between Perseus and Orion; second, we are analyzing a small portion of Orion, not the whole region; and third, we are probably losing an important fraction of close multiples due to our angular resolution limit (154 au). In fact, Tobin et al. (2016b) found a bi-modal distribution of companion separation for their whole sample, with peaks at $\sim$ 75 au and $\sim$ 3000 au, suggesting that multiple star formation and fragmentation is a multi-scale process. The shorter peak (below our resolution limit) would characterize the proto-binary separation, while the larger peak, the core-to-core separation. A new survey of Orion with $\sim$ 30 au resolution finds a separation distribution similar to that of Perseus (J. Tobin, in preparation).

It is possible that our radio sources have companions wit no detectable radio emission but that have been detected at other wavelengths. In our inspection of the NEWFIRM deep H and K_s images, we find ten near-IR sources at a projected separation $<$ 3000 au from the radio sources 12, 14, 17, 36, 38, 42, and 45, and Kounkel et al. (2016) reported 4 near-IR sources between 100 and 1000 au from sources 7, 11, and 46. Based on the accurate distances reported by Gaia Collaboration et al. (2018) and/or on the analysis of the spatial and velocity structure of the region done by Kounkel et al. (2018), we conclude that sources 14, 36, and 38 probably do not form binary systems with their respective nearby (in projection) near-IR source (see further details in Section 3.4.2.11 and 3.4.2.12) leaving 11 possible near-IR companions. Also, there are six additional sources detected with the VLA at 9 mm and/or ALMA at 870 μm (Tobin et al. 2020) within 3000 au of sources 1 and 2, Source 12, and VLA 15 and VLA 16. On the other hand, sources 19, 22, and 37 are spectroscopic binaries (Tobin et al. 2009), and Source 40 is an astrometric binary with components detected by the NRAO's Very Long Baseline Array (VLBA) observations (Kounkel et al. 2017). If we include these 21 possible companions detected at other wavelengths, we find that three of the previously

[8]We calculate their uncertainties assuming binomial statistics (similar to Tobin et al. 2016b), $\sigma_P = \sqrt{P(1-P)/N_{sys}}$, where P is MF or CF, and N_{sys} is the number of systems.

considered binaries become higher multiple systems (one triple, one quadruple, and one quintuple) and that there are, additionally, seven binary systems, one triple, and two quadruples. We note that in one possible quadruple system probably not all the sources are gravitationally bound (see further information in Section 3.4.2.8). After the inclusion of the 21 additional possible companions, we obtain $MF = 0.37 \pm 0.07$ and $CF = 0.61 \pm 0.07$.

In summary, we are detecting components of 17 potential multiple systems, likely composed of YSOs (see Section 3.4.2). Further analysis, e.g., proper motion studies, will be necessary to determine if these sources are indeed gravitationally bound. For example, if the components of a multiple system candidate present a common proper motion distinguishable from that of the nearby sources, that would mean that they are indeed gravitationally bound since the proper motions in the region have a dispersion of up to ~ 3 km s^{-1} (Dzib et al. 2017; Kounkel et al. 2018). On the other hand, if the relative proper motion of the components of the binary candidate exceeds the escape velocity, they would not be gravitationally bound.

3.4 Discussion

3.4.1 On the Correlation of the Observed Radio Emission with the Bolometric Luminosity and the Outflow Momentum Rate

The existence of empirical correlations between the observed centimeter luminosity ($S_\nu d^2$) of protostars and both the bolometric luminosity ($L_{\rm bol}$) and the outflow momentum rate ($\dot{P}$) is fairly well established. These correlations (sometimes referred to as the 'Anglada correlations') have been inferred from observations of a large sample of sources covering a wide range of bolometric luminosities (Anglada et al. 1992; Anglada 1995, 1996; Anglada et al. 2015, 2018) and have been interpreted as a result of the connection between accretion and outflow processes in star formation. As discussed in the above references (see also, Section 3.3.2), protostars are frequently associated with relatively weak cm continuum emission which is attributed to free-free radiation from partially ionized jets. The mechanism that produces the necessary ionization of these jets is not photoionization by stellar UV photons (as in classical HII regions) but shocks associated with the outflowing gas itself, and a correlation of the radio luminosity and the outflow momentum rate is

expected if this mechanism is at work (Curiel et al. 1987, 1989; Anglada 1996). On the other hand, since the bolometric luminosity of protostars is largely dominated by the accretion luminosity, and because outflows are driven by accretion, the protostars with the higher bolometric luminosities are expected to be associated with the more powerful outflows, and consequently with the stronger (shock-ionized) cm continuum emission; thus, a positive correlation between bolometric and cm radio luminosities is also expected.

These correlations, with recently updated parameters derived from a selected sample of 81 YSOs reliably associated with outflows (with an estimate of $\dot{P}$ for 73 of them) and covering a range of eight orders of magnitude in bolometric luminosity ($10^{-2} L_\odot \lesssim L_{\rm bol} \lesssim 10^{6} L_\odot$), are given by equations (28) and (31) of Anglada et al. (2018):

$$\left(\frac{S_\nu d^2}{\rm mJy\ kpc^2}\right) = 10^{-1.90\pm0.07} \left(\frac{L_{\rm bol}}{L_\odot}\right)^{0.59\pm0.03}, \tag{3.1}$$

$$\left(\frac{S_\nu d^2}{\rm mJy\ kpc^2}\right) = 10^{2.97\pm0.27} \left(\frac{\dot{P}}{M_\odot\ {\rm year}^{-1}\ {\rm km\ s}^{-1}}\right)^{1.02\pm0.08}. \tag{3.2}$$

In these equations, the outflow momentum rate, $\dot{P}$, is the parameter that is most poorly determined by observations. In general, it is estimated from the mass, velocity, and dynamical time of the CO molecular outflow using simple assumptions for the geometry and outflow kinematics, with an important dependence on the assumed CO molecular abundance, opacity effects, and inclination angle. Uncertainties in this parameter are often of an order of magnitude or greater.

The uncertainties in the bolometric luminosity, $L_{\rm bol}$, are mainly due to the poor angular resolution of the FIR observations, where the SED of the youngest objects reaches its maximum, causing it to include the emission of several objects in crowded regions so that these values can only be used as upper limits. Often the structure of the sources is complex (with important asymmetries due to the presence of cavities, etc.) so that the emission is anisotropic and the geometry and orientation of the object strongly influence the observed emission, introducing additional uncertainties in the derived bolometric luminosity, even when this is obtained through detailed modeling.

On the other hand, our knowledge of the distance, d, to star-forming regions has been much improved recently, so this parameter is generally not a substantial

cause of uncertainty. Besides, equation (3.1) is not affected by distance, as long as the same value has been used for radio and bolometric luminosities.

Thus, in general, the parameter that is better determined by the observations is the cm flux density, S_ν; in this case, the main sources of uncertainty are the possible variability in the radio emission and the uncertain behavior of the spectral index when data at different wavelengths are compared. Because of these characteristics of the observational uncertainties, the least-squares fitting has been performed taking $S_\nu d^2$ as the independent variable (i.e., contrary to the way eqs. 3.1 and 3.2 are displayed), and minimizing the errors in $L_{\rm bol}$ and $\dot{P}$. The uncertainties displayed in equations (3.1) and (3.2) correspond to the formal errors of the fits (residual standard deviation) and partially reflect the actual dispersion in these correlations.

Although the general trend traced by these correlations is clear, suggesting the existence of a connection between accretion, outflow, and radio emission, the precise relationship between these three phenomena depends on complex interactions in the outflow ejection through an accretion disk, and in the shock-ionization of the outflow that originates the free-free emission observed at radio wavelengths, which are unlikely described by the simple power-law correlations shown in equations 3.1 and 3.2. For example, as shown by Anglada (1996), a power-law relationship like equation (3.2) is derived from the shock-induced ionization model of Curiel et al. (1987, 1989) under the simplifying assumptions of plane-parallel shocks, optically thin emission, and equaling the momentum rates in the molecular outflow (tracing larger scales and dynamical times) and in the jet (which trace smaller scales and dynamical times). The specific relationship between $S_\nu d^2$, $L_{\rm bol}$, and $\dot{P}$ for a given source will certainly depend in a complex way on many factors, such as the individual properties of the source, environment, and orientation relative to the observer. Consequently, it is expected that in these correlations, in addition to the dispersion of data points due to the observational errors of the measurements, there is an additional intrinsic scatter of the data points due to the particular conditions of each source (Anglada et al. 2018).

Systematic studies focused on individual regions (where distance uncertainties are minimized), performed under uniform conditions, and with accurate determinations of both the bolometric luminosity and outflow parameters, can help to better characterize this intrinsic scatter of the data points. For example, Tychoniec et al. (2018) analyzed the Anglada correlations for a large and homogeneous sample of YSOs consisting of all known protostars in Perseus molecular cloud but covering a

narrow range of luminosities $10^{-1.5} L_{\odot} \lesssim L_{\rm bol} \lesssim 10^{1.5} L_{\odot}$. These authors conclude that, while the general trends are robust when including additional sources with $L_{\rm bol}$ up to $10^4 L_{\odot}$, the correlations are weakened, or even disappear, when data points were restricted to the Perseus sample, revealing the intrinsic scatter of data points.

The field of view covered by our observations includes the positions of 31 far-IR HOPS sources (see Table 3.4 and 3.6), with 14 of them being associated with detected radio sources. The HOPS sources have been observed homogeneously, obtaining their SEDs from near-IR to sub-millimeter wavelengths. Therefore, their $L_{\rm bol}$ have been very well determined in most cases by Furlan et al. (2016) using *Herschel* bands at 70 and 160 μm, which constrain the SED peak, very sensitive to the luminosity. We use this valuable data to investigate the correlation with radio emission.

In Figure 3.7 (top) we plot the 5 cm radio luminosity (S_{ν} d^2) versus $L_{\rm bol}$ (Table 3.6) for the 31 HOPS YSOs with known $L_{\rm bol}$ in our field of view. We show for comparison equation (3.1), extrapolated from 3.6 cm to 5 cm assuming a spectral index $\alpha = 0.4$, which is a typical value for radio jets. The uncertainty interval (residual standard deviation of the fit from which eq. 3.1 was derived) is plotted as a shaded region. We find that most of the HOPS sources in our field of view have bolometric luminosities consistent with the Anglada correlation. There is no source with a radio luminosity significantly higher than expected from equation (3.1), suggesting that shock-induced ionization is the mechanism at work since photoionization by stellar photons for sources in this bolometric luminosity range, 0.1 - 300 $L_{\odot}$, is expected to produce radio luminosities in the range $<10^{-16}$ to $\sim 10^{-2}$ mJy kpc^{-1}, respectively (Fig. 5 in Anglada 1995), well below the observed values. However, although the large majority of 5 cm data points are consistent with the correlation, most of them (18) correspond to non-detections, and only upper limits for the radio luminosity are available. At least, three out of the 14 radio sources detected at 5 cm have radio luminosities clearly lower than expected, namely the ones associated with HOPS 64, HOPS 108, and HOPS 369; HOPS 66 coincides with two radio sources, which are not angularly resolved in the far-IR data (see discussion below).

Table 3.6 Bolometric and Radio Luminosities of the HOPS YSOs in the Field of View

HOPS ID	Radio Source Name	$L_{\rm bol}$[a] ($L_\odot$)	$\dot{P}$[b] ($M_\odot$ km s^{-1} yr^{-1})	$S_\nu d^2$[c] (mJy kpc^2)	Evolutionary Stage[a]
56	-	20	···	<0.05[d]	Class 0
57	46	3	···	0.03[d]	Flat Spectrum
58	-	4	···	<0.019[d]	Flat Spectrum
59	42	42	···	0.11[d]	Flat Spectrum
60	39	19	9.8×10^{-5}	0.019[d]	Class 0
62	-	0.6	···	<0.009	Flat Spectrum
63	-	0.4	···	<0.007	Flat Spectrum
64	HOPS 64	13	···	0.0016[d]	Class I
65	-	0.30	···	<0.008	Class I
66	24	<18[e]	···	0.006[d]	Flat Spectrum
66	25	<18[e]	···	0.013[d]	Flat Spectrum
68	-	5	···	<0.009[d]	Class I
69	-	2	···	<0.009	Flat Spectrum
70	-	6	···	<0.009[d]	Flat Spectrum
71	11	5	4.6×10^{-5}	0.08[d]	Class I
73	-	1.4	···	<0.012[d]	Class 0
74	-	1.0	···	<0.015[d]	Flat Spectrum
75	-	3	···	<0.016[d]	Class 0
76	-	1.6	···	<0.018[d]	Class I
77	-	11	···	<0.021	Flat Spectrum
78	1	8	4.6×10^{-4}	0.06[d]	Class 0
79	-	0.07	···	<0.021	Flat Spectrum
80	-	0.07	···	<0.03	Flat Spectrum
81	-	1.1	···	<0.03[d]	Class 0
82	-	2	···	<0.04	Flat Spectrum
84	-	42	···	<0.06[d]	Class I
108	HOPS 108	33	···	0.003[d]	Class 0
368	34	59	8.4×10^{-5}	0.07[d]	Class I
369	32	30	···	0.005	Flat Spectrum
370	VLA 11	305	···	0.3[d]	Class I
394	9	5	4.8×10^{-6}	0.04[d]	Class 0
409	43	7	1.9×10^{-5}	0.009[d]	Class 0

[a] From Furlan et al. (2016), with the luminosities scaled to our adopted distance of 386 pc.

[b] From Takahashi et al. (2008) and Tobin et al. (2016c).

[c] Radio luminosity obtained from C-configuration 5 cm data (from Table 3.3 and Table 2.3). A-configuration data have been used for HOPS 66, 78, and 108 (blended with nearby sources) and HOPS 57 and 64 (undetected in the C-configuration map). Upper limits are 5σ.

[d] Source detected at Ka band (9 mm) by Tobin et al. (2020).

[e] The far-IR source HOPS 66 includes both radio sources 24 and 25.

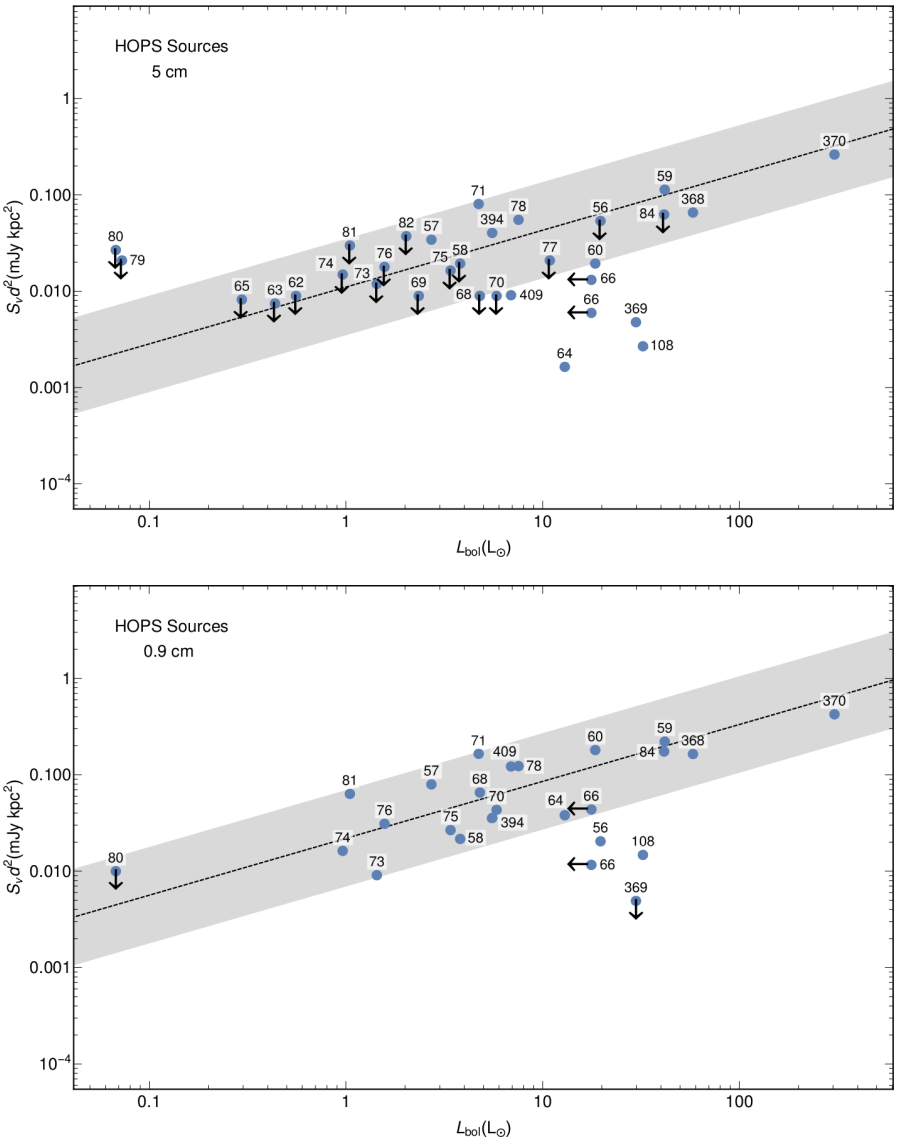

Figure 3.7 Radio luminosity, $S_\nu d^2$, at 5 cm (top panel, Table 3.6) and 0.9 cm (bottom panel, Tobin et al. 2020) versus the bolometric luminosity, $L_{\rm bol}$ (from Furlan et al. 2016, after correction to our adopted distance of 386 pc) for the HOPS YSOs observed in the analyzed field of view. Data points are labeled with their HOPS ID number. The dashed line represents the empirical correlation (and the shadowed area the residual standard deviation of the fit) found at 3.6 cm by Anglada et al. (2018), extrapolated to 5 cm and 0.9 cm, respectively, assuming a spectral index $\alpha = 0.4$. Vertical arrows indicate 5σ upper limits. Horizontal arrows indicate $L_{\rm bol}$ upper limits for radio sources 24 and 25 (both associated with HOPS 66 but unresolved in the far-IR data, see Section 3.4.2.14).

Out of the 18 HOPS sources not detected at 5 cm, 11 were observed at 9 mm by Tobin et al. (2020), detecting 10 of them. In Figure 3.7 (bottom) we plot the observed radio luminosities at 9 mm, together with the Anglada correlation extrapolated to that wavelength. As can be seen in the figure, most of the 9 mm sources appear to follow the correlation. It should be noted that, in some cases, the emission at 9 mm can have a significant contribution of dust thermal emission from the associated disk or envelope; therefore, the actual free-free contribution in some sources can be somewhat lower than the values plotted. However, most of the 9 mm sources appear to follow the correlation, which suggests that the emission at this wavelength is dominated by free-free emission. In any case, it would be interesting to perform still more sensitive observations at 5 cm, a wavelength where the dust contribution should be negligible, to unveil the free-free radio emission from this undetected population of weak radio sources. We estimate that future 5 cm observations reaching an rms sensitivity of ~ 3 μJy beam^{-1} across the whole field of view (similar to the sensitivity reached toward the center of the field in our current observations) should be able to detect the large majority of these sources above a 5-σ level if they have a flux density similar to that expected. This will unambiguously clarify the degree of agreement with the predictions. Nevertheless, we identify three sources, HOPS 56, HOPS 108, and HOPS 369, that have radio luminosities at 9 mm lower than expected.

In summary, we find that most of the HOPS sources in our field of view follow the Anglada correlation of radio emission with $L_{\rm bol}$, and that our non-detections at 5 cm are mostly due to sensitivity issues. However, a few protostars (HOPS 56, HOPS 64, HOPS 108, and HOPS 369; and perhaps HOPS 66) do not follow the correlation and appear as underluminous at radio wavelengths. We note that these sources are located in a crowded region (see Fig. 3.1), where contamination from nearby sources is not unlikely.

The correlation between radio and bolometric luminosities is usually interpreted as a consequence of the connection between outflow (traced by the cm radio emission) and accretion (traced by the bolometric luminosity which, in protostars, is assumed to be dominated by the accretion luminosity). Therefore, for the sources that appear as underluminous in radio (or, equivalently, overluminous in bolometric luminosity), one would expect that either the mechanism of shock-induced ionization is less effective than in the other sources, or that the bolometric luminosity has a significant contribution from mechanisms other than accretion. In more evolved YSOs, where the accretion has decreased significantly, it has been

suggested that the stellar luminosity (which is not expected to be directly related to accretion and outflow) can have an important contribution to the bolometric luminosity, making theses objects to appear radio-underluminous in the Anglada correlation (Rodríguez et al. 2014, 2016). However, our sources are younger and we suggest that the contribution to the bolometric luminosity additional to accretion could be due to external heating. In fact, HOPS 64, HOPS 108, and HOPS 369 fall very close to the non-thermal (likely synchrotron) lobe of the powerful jet driven by HOPS 370 (Osorio et al. 2017; see Chapter 2) where a significant heating due to strong shocks is expected (Shimajiri et al. 2008; Manoj et al. 2013; González-García et al. 2016; Osorio et al. 2017).

In the case of HOPS 66, the low-resolution far-IR emission is associated with two radio sources (sources 24 and 25; see Fig. 3.17) but we do not know which part of the estimated $L_{\rm bol}$ corresponds to each one. However, we note that the bolometric luminosity required to account for the observed 5 cm radio luminosity of Source 24 is of the order of only $\sim 0.3\ L_{\odot}$, which is a very small fraction of the overall bolometric luminosity of HOPS 66 ($18\ L_{\odot}$). Thus, a distribution of luminosities where Source 24 has a bolometric luminosity of the order of $\sim 0.3\ L_{\odot}$ and Source 25 a bolometric luminosity of the order of $\sim 18\ L_{\odot}$ seems a likely possibility, in which both radio sources would follow the Anglada correlation with $L_{\rm bol}$ (see Section 3.4.2.14).

For six of the 14 HOPS sources (HOPS 60, 71, 78, 368, 394, and 409), we also have an estimate of the molecular outflow force (or outflow momentum rate), $\dot{P}$, obtained from the literature (Takahashi et al. 2008; Tobin et al. 2016c; see Table 3.6). All these sources have values of the radio luminosity and outflow momentum rate consistent, within the uncertainties, with the expected correlation described by equation (3.2) (see Fig. 3.8), in agreement with the suggestion that the ionization necessary to account for the observed radio emission is produced by shocks associated with the outflow. Note that the physical parameters of molecular outflows are more scarce than the bolometric luminosities of the YSOs, since they are more difficult to obtain, and here the number of data points is insufficient to trace the trend of the relationship between radio emission and outflow force but just the coincidence in the expected values.

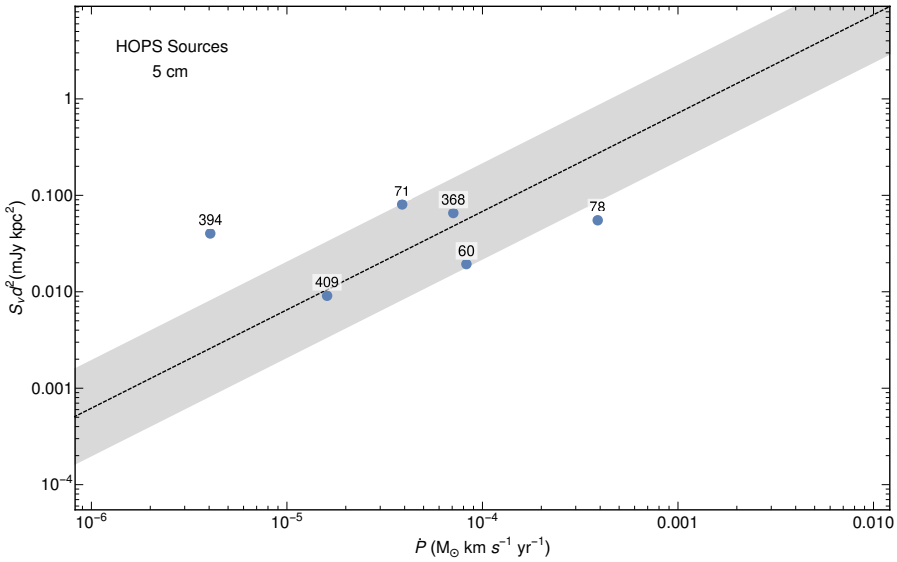

Figure 3.8 Radio luminosity, $S_\nu d^2$, at 5 cm (Table 3.6) versus the outflow momentum rate, $\dot{P}$ (from Takahashi et al. 2008; Tobin et al. 2016c; see Table 3.6) for the six HOPS YSOs in our field of view with known molecular outflow parameters. Data points are labeled with their HOPS ID number. The dashed line represents the empirical correlation (and the shadowed area the residual standard deviation of the fit) found at 3.6 cm by Anglada et al. (2018), extrapolated to 5 cm, assuming an spectral index $\alpha = 0.4$.

3.4.2 Notes on the Nature of the Individual Sources

In this Section we discuss the nature of the 47 reported radio sources by analyzing their radio spectral index, morphology, emission at other wavelength ranges, position relative to the ISF, association with dust clumps, etc. For simplicity, in several cases, we discuss together sources that are close to each other, or those that have similar observational characteristics or evolutionary stages. We are able to determine the nature of 36 of these sources (see Table 3.4).

We conclude that, out of the 57 total radio sources in the field of view, 41 (72%) are very likely associated with the star-forming region, 6 are extragalactic background sources, and we are unsure about the association with the star-forming region of the remaining 10 sources. Of the 41 sources associated with the star-forming region, 36 are tracing the position of YSOs, 3 are tracing non-thermal emission from jet knots (discussed in Chapter 2), one is tracing the shock-ionized wall of an outflow cavity, and one could be either a YSO or a jet knot.

3.4.2.1 Source 1 (VLA 5, HOPS 78) and Source 2

Source 1 is located in the densest part of the ISF (Fig. 3.1), toward the 1.3 mm dust condensation MMS 9 (Chini et al. 1997). The source, also known as VLA 5, was previously detected at 3.6 cm by Reipurth et al. (1999, 2004) and at 5 cm by Kounkel et al. (2014). This source has been proposed as the driving source of a powerful bipolar CO outflow (Williams et al. 2003; Takahashi et al. 2008) that extends almost 1 pc in the E-W direction. The blue lobe of the outflow is associated with a prominent chain of collimated H_2 knots (Yu et al. 1997; Stanke et al. 2002).

In our inspection of the NEWFIRM (T. Megeath, private communication), *Spitzer* (Megeath et al. 2012) and *Herschel* (Stutz et al. 2013) images from 2.2 to 70 μm, we noticed that the peak of the emission shifts from a position compatible with Source 1, to positions farther to the W, as we go from long to short wavelengths. This could be interpreted as emission in an outflow cavity from Source 1 that extends to the W, seeing further down the cavity at shorter wavelengths. Because of its position with respect to Source 1, this cavity would correspond to the blue lobe of the outflow.

Source 1 seems to be very young since it is located toward the peak of a 3 mm compact dust core (Kainulainen et al. 2017, Fig. 3.9), indicating that it is deeply embedded. We associate Source 1 with the far-IR source HOPS 78 (see Table 3.4

for the counterparts), which is tracing a Class 0 YSO (Furlan et al. 2016). The coordinates of HOPS 78 were derived from the *Spitzer* 4.5 μm image and therefore are shifted to the W with respect to our Source 1, which better traces the YSO.

In our 5 cm high-resolution map, Source 1 appears elongated at P.A. $= 99 \pm 5^{\circ}$ (Fig. 3.9), consistent with the direction of the E-W outflow. This source follows the Anglada correlations with $L_{\rm bol}$ and $\dot{\rm P}$ (see Section 3.4.1), suggesting it is a radio jet. Additionally, Tobin et al. (2020) detected with ALMA at 870 μm with $\sim 0\farcs11$ resolution, a structure nearly perpendicular to the radio source that appears to be a circumstellar dust disk (see Fig. 3.2). They also detected the source with the VLA at 9 mm with a flux density of 0.83 ± 0.02 mJy. Although we cannot derive a spectral index only from our observations, using this value together with the flux densities shown in Fig. 3.3 we find a positive spectral index $\alpha = 0.4 \pm 0.3$ for this source, consistent with thermal free-free emission. Therefore, we confirm this source is the driving source of the molecular outflow.

Source 2 is located $\sim 3''$ (~ 1200 au) in projection to the W of Source 1 (Fig. 3.9). It has also been detected with the VLA at 9 mm with a flux density of 0.046 ± 0.017 mJy (Tobin et al. 2020), which, together with our 5 cm flux density (Table 3.3), gives a flat spectral index $\alpha = -0.2 \pm 0.3$, which uncertainty does not allow us to determine the nature of the emission. The source is located toward the border of the 3 mm compact dust core (Kainulainen et al. 2017, Fig. 3.9), suggesting it is more evolved than Source 1, under the assumption that it is an independent object.

Another possibility is that Source 2 were a knot ejected from the Source 1 outflow. This could be hinted at from the VLA maps at 9 mm since the position of the source slightly moves to the W in those observations, taken ~ 1 year after ours. Additionally, in the previous 3.6 cm high-resolution observations of Reipurth et al. (2004) taken in 2002 with an rms of 10 μJy beam^{-1} in the vicinity of these sources, Source 1 is resolved with a prominence to the W side while Source 2 is not detected (unpublished map). A reliable measure of the proper motions of Source 2 should be done to clarify its nature.

Interestingly, Sources 1 and 2 could be members of a quintuple system, since Tobin et al. (2020) detected three additional objects at less than $5''$ (~ 2100 au) from Source 1, with VLA 9 mm and ALMA 870 μm observations.

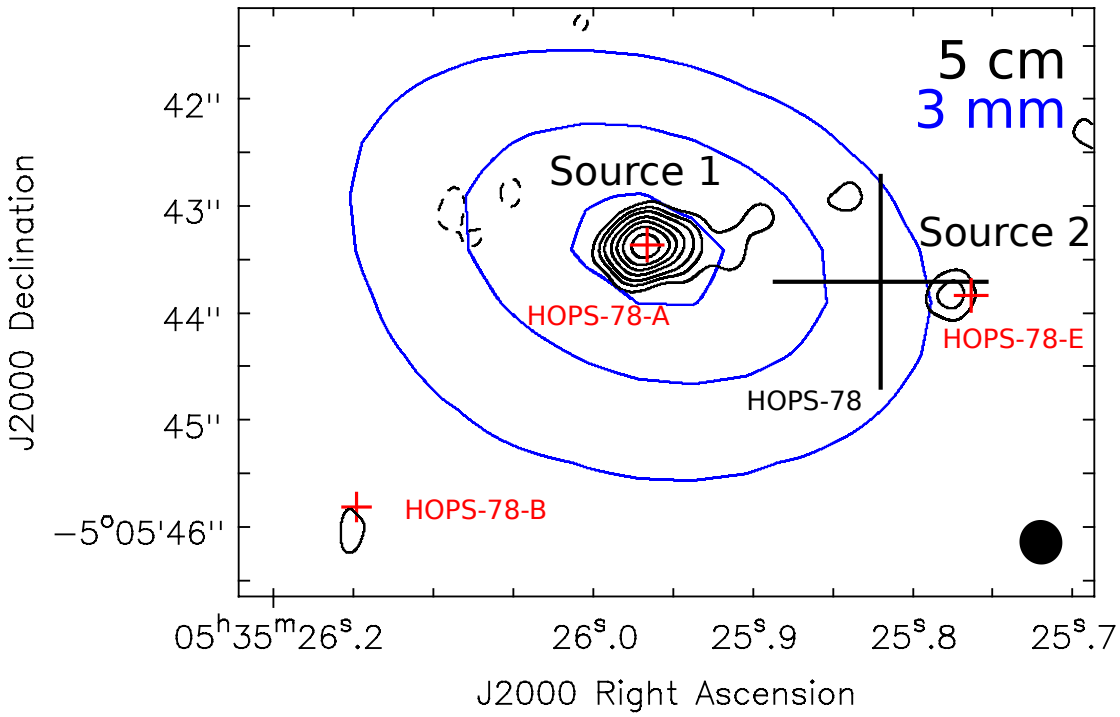

Figure 3.9 Sources 1 and 2. VLA 5 cm A-configuration map with natural weighting (black contours) overlaid on the ALMA 3 mm map (blue contours, adapted from Kainulainen et al. 2017). Plus signs mark the position of the HOPS source (black, Furlan et al. 2016, derived at 4.5 μm) and the 9 mm/870 μm sources (red, Tobin et al. 2020) in the region. Black contour levels are −3, 3, 5, 7, 10, 13, 16, and 20 times 10 μJy beam^{-1}, the rms of the 5 cm map. Blue contour levels are 0.3, 0.6, and 0.9 times 19.6 mJy beam^{-1}, the peak of the 3 mm core. The 5 cm VLA synthesized beam is shown in the bottom right corner of the image. The 3 mm ALMA synthesized beam (HPBW) is $3\farcs8 \times 2\farcs3$, P.A. = 71°.

3.4.2.2 Source 3 (VLA 6)

This source is located toward a tenuous part of the ISF, at $\sim 40''$ from its ridgeline (see Fig. 3.1) and is not associated with any 3 mm compact dust core (Kainulainen et al. 2017). The source, also known as VLA 6, was previously detected with the VLA at 3.6 cm by Reipurth et al. (1999, 2004) and at 5 cm by Kounkel et al. (2014), and does not have any known counterparts at other wavelength ranges.

The source has also been detected at 5 GHz with the VLBA (milli-arcsec angular resolution) with a maximum flux of 1.7 ± 0.5 mJy (Kounkel et al. 2017), indicating that it is very compact and therefore non-thermal. These authors proposed the source as extragalactic, as previously suggested by Reipurth et al. (1999), since it does not have proper motions like those of the YSOs of the region.

3.4.2.3 Source 4 (VLA 7)

This extended source, previously detected at 3.6 cm and named VLA 7 (Reipurth et al. 1999), is located toward the densest part of the ISF, at $\sim 15''$ from its ridgeline (see Fig. 3.1), but is not associated with any 3 mm compact dust core (Kainulainen et al. 2017). The source shows a cometary-like shape at 5 cm (Fig. 3.10), with the SW part (located toward a higher column density, see white contours in Fig. 3.10) being more intense than the NE one. This asymmetry is also observed at 3 cm, although the map has a lower quality because the source is far from the phase center and the primary beam is smaller at this band. There is extended emission at 24 μm tracing heated dust, which shows a morphology similar to that of the radio emission but reaching larger scales (Fig. 3.10).

We obtain a spectral index $\alpha = -0.3 \pm 0.3$ which, although uncertain, is consistent with an optically thin HII region. In the optically thin regime, the flux density at 5 cm could be produced by a B3 zero-age main-sequence star with a luminosity of $L_{\rm bol} \sim 1000\ L_{\odot}$ (Thompson 1984), which is in agreement with Reipurth et al. (1999). These authors proposed IRAS 05329-0508 (V* V415 Ori) as the ionizing source, but this star is located $\sim 40''$ from Source 4, well outside the HII region. We propose instead 2MASS J05352474-0506563, a near-IR point source better centered in the HII region, $\sim 6''$ from the 5 cm emission peak (see Fig. 3.10). According to the Spitzer and Newfirm photometry, this source does

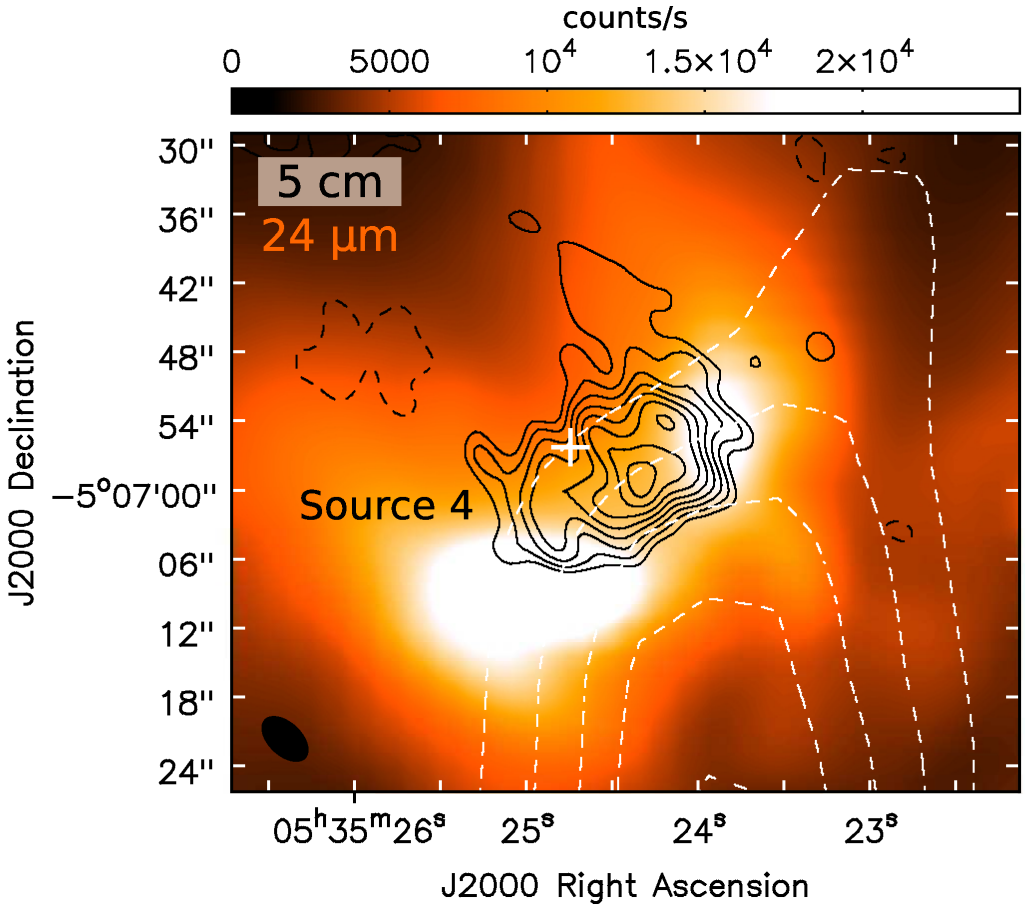

Figure 3.10 Source 4. VLA 5 cm C-configuration map with robust 0 weighting and uvtaper = 50 kλ (black contours) and column density of the ISF (dashed white contours, adapted from Stutz 2018) overlaid on the Spitzer 24 μm image (color scale, adapted from Megeath et al. 2012). The plus sign marks the position of 2MASS J05352474-0506563. Black contour levels are -3,-2, 2, 3, 4, 5, 6, 7, 8, and 9 times 21 μJy beam^{-1}, the rms of the 5 cm map. Dashed white contour levels are 0.5, 0.6, 0.7, 0.8, and 0.9 times 1.77×10^{23} cm^{-2}, the local maximum of the column density. The VLA synthesized beam is shown in the bottom left corner of the image.

not present an IR excess and shows an extinction of $A_K = 10$ mag, with a dereddened absolute magnitude of -4.1, consistent with an O star ($L_{\rm bol} \sim 10000\ L_\odot$), higher than what was inferred from the radio continuum. A possible reason for this discrepancy could be that not all the photons are being used for the photoionization of the gas, e.g., due to the non-homogeneity of the medium, or that the radio continuum emission is being underestimated since the source is very extended, i.e, we are not recovering the whole emission of the source.

3.4.2.4 Sources 5, 16, 18, 23, 31, and 35

These sources are reported here for the first time at radio wavelengths. They are detected toward the border or outside the ISF, more than 1.′4 from its ridgeline (see Fig. 3.1), and are not associated with any 3 mm compact dust core (Kainulainen et al. 2017). We find that all of them are associated with weak (≤ 10 counts/s) emission in the inspected NEWFIRM K_s image (see Fig. 3.11).

In the case of Source 5, its near-IR emission is extended, with morphology and angular size consistent with that of a disk galaxy. The source also has an X-ray counterpart with a hardness ratio suggesting an extragalactic nature according to Tsujimoto et al. (2002) (see Table 3.4 for its counterparts).

We determine a negative spectral index for sources 23 and 35 (see Table 3.3 and Fig. 3.3), suggesting non-thermal emission. Therefore they could be either extragalactic sources or evolved YSOs. On the other hand, the spectral indices of sources 5, 16, 18, and 31 are unconstrained, and the nature of their radio emission is uncertain.

3.4.2.5 Sources 6, 8, 15, and 44

These sources are reported here for the first time at radio wavelengths and do not have any known counterparts at other wavelengths. They are detected toward the border or outside the ISF (see Fig. 3.1), with distances to its ridgeline ranging between 37″ (Source 8) and 2.′7 (Source 15). Their radio spectral indices are unconstrained (see Table 3.3 and Fig. 3.3) and, therefore, their nature is uncertain.

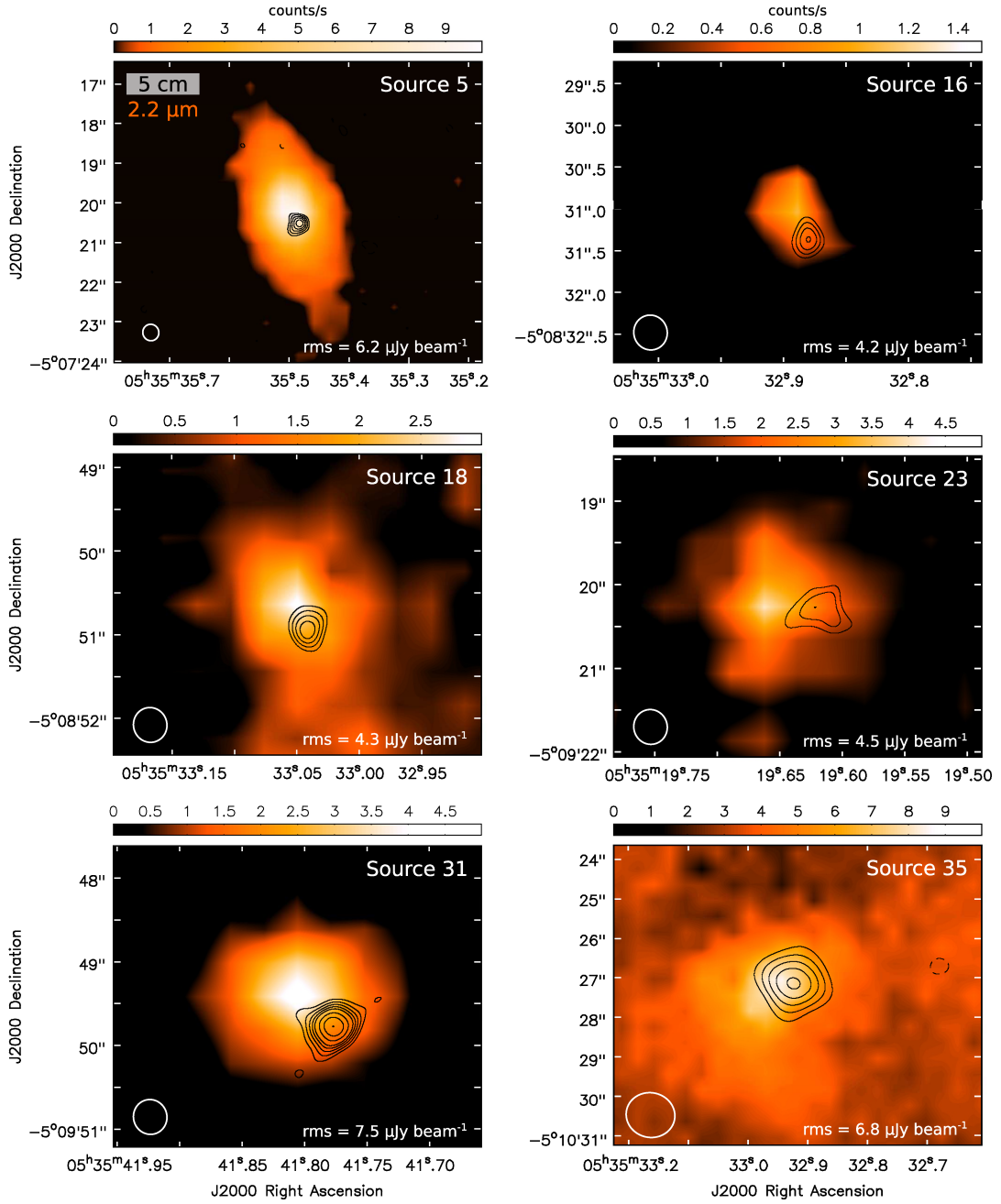

Figure 3.11 Sources 5, 16, 18, 23, 31, and 35. VLA 5 cm A-configuration map with natural weighting (black contours) overlaid on the NEWFIRM 2.2 μm image (color scale, T. Megeath, private communication). In the case of Source 35, uvtaper = 100 kλ was applied to better detect the extended emission. Contour levels are -3, 3, 4, 5, 6, 7, 9, 11, and 13 times the rms of the 5 cm maps, shown at the bottom right corner. The VLA synthesized beam is shown in the bottom left corner of the maps.

3.4.2.6 Source 7

This source is reported here for the first time at radio wavelengths. It is located toward the densest part of the ISF, $\sim 23''$ from its ridgeline (see Fig. 3.1), although is not associated with any 3 mm compact dust core (Kainulainen et al. 2017). Based on IR observations (see Table 3.4 for the counterparts), the source has been previously classified as a YSO with a disk (Megeath et al. 2012; Getman et al. 2017). Interestingly, Source 7 could belong to a binary system since Kounkel et al. (2016) reported two near-IR sources at $\sim 0.5''$ (~ 200 au) of projected separation, one (MGM 2341) coincident with our radio source, and the other one (MGM 2341-b) not detected at radio wavelengths.

3.4.2.7 Source 9 (VLA 8, HOPS 394)

This source, previously detected at 3.6 cm and named VLA 8 (Reipurth et al. 1999), is located in the densest part of the ISF (Fig. 3.1), toward the 1.3 mm dust condensation named FIR 1a (Chini et al. 1997). In this region, the 3 mm ALMA map (Kainulainen et al. 2017) revealed two compact dust cores with peaks separated about $\sim 10''$ in projection, joined by a filamentary structure (see Fig. 3.12, top). The eastern core is associated with a weak source detected at 9 mm and 870 μm (Tobin et al. 2020), and the western core is associated with Source 9. Additionally, the mid-IR source MGM 2334, a YSO with a disk (Megeath et al. 2012), and the far-IR source HOPS 394, an extremely young Class 0 object (source PBR 019003[9] in Stutz et al. 2013; Furlan et al. 2014), have been reported within $2''$ of Source 9 (see Fig. 3.12, top). Although previous works have considered MGM 2334 and HOPS 394 to be the same source, there are hints that suggest they are different objects (see below). On the other hand, there is a proposed bipolar CO outflow at P.A. $\sim 50°$ (Tobin et al. 2016c) in the region that has been associated with HOPS 394.

In our 5 cm high-resolution map, Source 9 is angularly resolved (Fig. 3.12, bottom), showing an extension to the SW at P.A. $\sim 35°$, although the source core appears marginally elongated at a smaller P.A. ($16 \pm 17°$, Table 3.2); at 9 mm, the source is elongated at P.A. $= 27 \pm 10°$ (Tobin et al. 2020). These elongations are

[9]The map used to derive the coordinates of PBR 019003 reported in Table 4 of Stutz et al. (2013) has an offset of $\Delta\alpha = 1\farcs4$, $\Delta\delta = -1\farcs9$ with respect to the 24 μm sources (A. Stutz, private communication), which better trace the position of the YSOs. We use in this work the corrected position of HOPS 394.

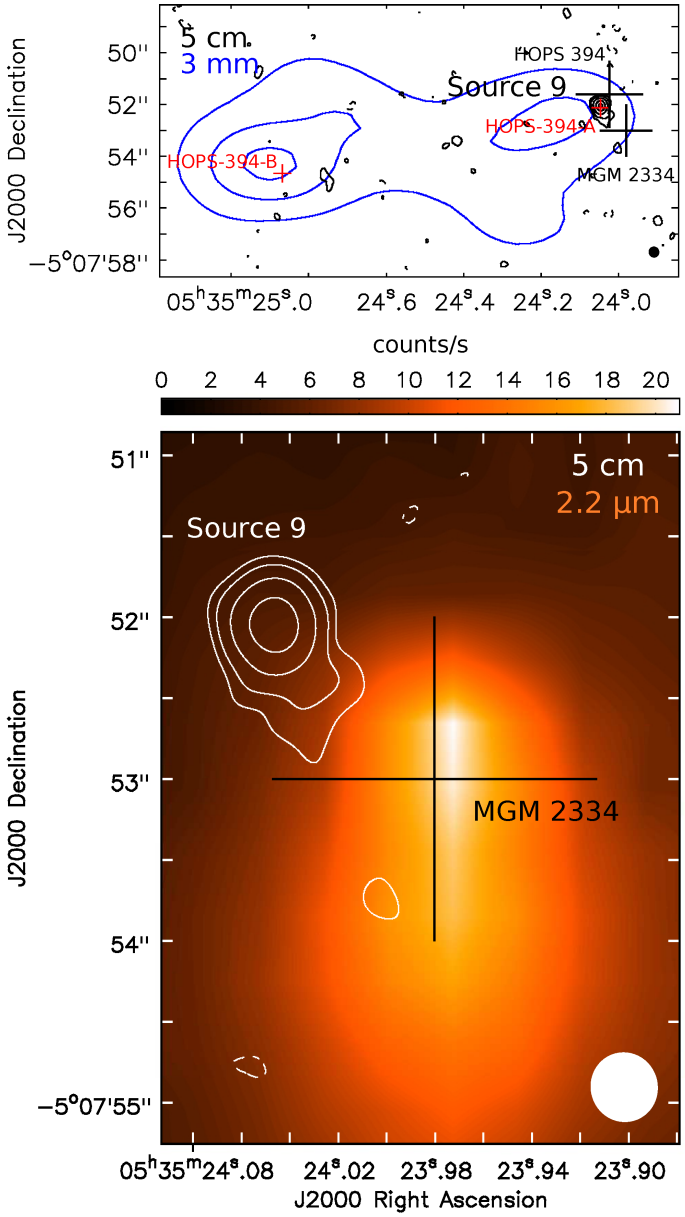

Figure 3.12 Source 9. *Top*: VLA 5 cm A-configuration map with natural weighting (black contours) overlaid on the ALMA 3 mm map (blue contours, adapted from Kainulainen et al. 2017). Plus signs mark the position of the far-IR (black, HOPS 394, derived at 70 μm with an error twice the size of the sign, Stutz et al. 2013, corrected), the mid-IR (black, MGM 2334, derived at 4.5 μm, Megeath et al. 2012), and the 9 mm/870 μm sources (red, Tobin et al. 2020) in the region. *Bottom*: VLA 5 cm A-configuration map with natural weighting (white contours) overlaid on the NEWFIRM 2.2 μm image (color scale, T. Megeath, private communication). The black plus sign marks the position of the MGM 2334 source (Megeath et al. 2012). Black (top) and white (bottom) contour levels are −3, 3, 5, 10, 20, and 30 times 4.7 μJy beam^{-1}, the rms of the 5 cm map. Blue contour (top) levels are 0.3, 0.6, and 0.9 times 12.4 mJy beam^{-1}, the peak of the 3 mm core. The 5 cm VLA synthesized beam is shown in the bottom right corner of the images. The 3 mm ALMA synthesized beam (HPBW) is $3\farcs8 \times 2\farcs3$, P.A. = 71°.

consistent (within the errors) with the direction of the CO outflow. We derive a flat spectral index $\alpha = 0.0 \pm 0.6$ (Table 3.3 and Fig. 3.3) at cm wavelengths, consistent with thermal free-free emission despite the large uncertainty. Additionally, the source follows the Anglada correlation with $L_{\rm bol}$ and $\dot{\rm P}$ (see Section 3.4.1) suggesting it is a radio jet. Thus, we propose that this source is the driving source of the outflow reported in its vicinity. On the other hand, ALMA 870 μm observations detected extended emission in scales of $\sim$ 300 au associated with this source (Tobin et al. 2020), which could be tracing a dust disk or its inner envelope.

The mid-IR source MGM 2334 is located at 1.″4 ($\sim$ 600 au) to the SW of Source 9 (Fig. 3.12, bottom), and appears to be a different object given the IR positional uncertainty (1″ at 4.5 μm). On the other hand, both NEWFIRM (1.7 and 2.2 μm) and HST (0.8 - 2.5 μm) images show a scattered light cone with the vertex at MGM 2334 and extending toward the S, indicating the presence of a cavity associated with this source (Fig. 3.12, bottom). This is inconsistent with the direction of the outflow detected in the vicinity of the sources (P.A. $\sim$ 50°, Tobin et al. 2016c), that we associate with Source 9.

The far-IR source HOPS 394 was detected in observations at 70 and 160 μm (Stutz et al. 2013) with an angular resolution of 5″ and 7.″8, respectively. It is located $\sim$ 0.6″ in projection from Source 9 and could be associated with it, but also with MGM 2334 due to its positional uncertainty (Fig. 3.12, top). Stutz et al. (2013) classified it as an extremely young object due to its strong far-IR emission and faint mid-IR emission, although they warned that it is located in a complex field where the photometry may be strongly contaminated. We favor the association of HOPS 394 with Source 9 since the radio source appears to be younger than MGM 2334. However, we note that extremely young objects (like HOPS 394) are deeply embedded and our accurate position of Source 9 reveals that the radio source appears toward the border of the 3 mm compact dust core (Kainulainen et al. 2017), $\sim$ 2″ ($\sim$ 800 au) from the peak (see Fig. 3.12, top). Additionally, although there is ammonia emission (tracing dense gas) in the surroundings of Source 9, this source is not associated with any peak of emission (D. Li, private communication).

In summary, we propose Source 9 is a radio jet and suggest it as the driving source of the molecular outflow reported in its vicinity. We show that Source 9 is a different object than MGM 2334 and favor the radio source as the counterpart of HOPS 394. New observations of this complex region should be carried out to fully reveal its protostellar content.

3.4.2.8 Sources 10 and 11 (VLA 9, HOPS 71)

Sources 10 and 11, separated $\sim 5''$ ($\sim$ 2100 au) in projection (Fig. 3.13, top), are located toward the densest part of the ISF, $\sim 5''$ ($\sim$ 2100 au) from its ridgeline (see Fig. 3.1). They were previously detected as a single source, VLA 9, in the 3.6 cm lower angular resolution observations of Reipurth et al. (1999). VLA 9 was later associated by Takahashi et al. (2008) with a probable monopolar outflow at P.A. $\sim 40°$.

Source 11 is located toward the peak of a 3 mm compact dust core (Kainulainen et al. 2017), suggesting it is deeply embedded (see Fig. 3.13, bottom). It is also associated with the far-IR source HOPS 71 (Fig. 3.13, top; see Table 3.4 for the counterparts), and is classified as a Class I YSO (Furlan et al. 2016). In our 5 cm high-resolution map, the source is elongated at P.A. = $24 \pm 5°$ (Fig. 3.13, bottom), roughly consistent with the direction of the outflow (P.A. $\sim 40°$) reported in its vicinity (Takahashi et al. 2008). The source has a positive spectral index $\alpha = 0.3 \pm 0.4$ (Table 3.3 and Fig. 3.3) consistent with thermal emission even taking into the account the large uncertainty, and follows the Anglada correlations with $L_{\rm bol}$ and $\dot{\rm P}$ (see Section 3.4.1) suggesting it is a radio jet. All these facts lead us to propose that Source 11 is a thermal radio jet, driving the large scale outflow. We note that the flux densities measured by us for Source 11 are ~ 2 times higher than the one reported by Reipurth et al. (1999) (corresponding to the combination of sources 10 and 11) which could indicate some variability for Source 11 (Fig. 3.3).

Tobin et al. (2020) detected the source (HOPS-71-A in their nomenclature) at 9 mm as a compact core (S = 1.106 $\pm$ 0.024 mJy) with a lobe (S $\sim$ 0.3 mJy) extending to the NW (coincident with the elongation detected at 5 cm by us), and at 870 μm as an elongated structure (S = 130.1 $\pm$ 1.1 mJy) nearly perpendicular to the lobe, consistent with a circumstellar dust disk (see their Fig. 32). The 9 mm and 870 μm peaks coincide very well, while our 5 cm peak is displaced about $\sim 0\farcs1$ to the NW from them, in an intermediate position between the 9 mm compact core and the lobe (see Fig. 3.14). Using the 9 mm and 870 μm observations, we derive a spectral index for the compact core of the source of $\alpha = 2.04 \pm 0.01$,

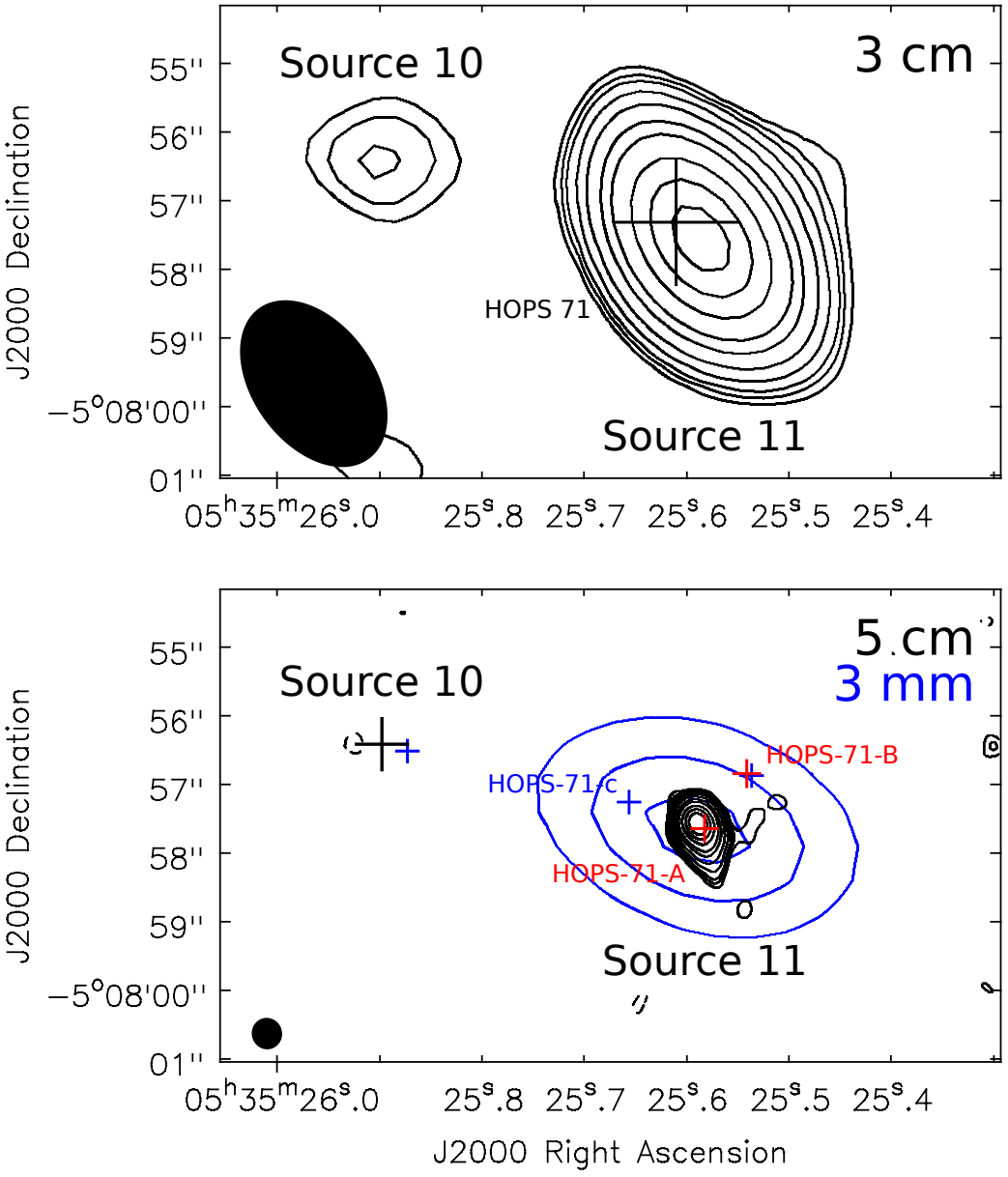

Figure 3.13 Sources 10 and 11. *Top*: VLA 3 cm C-configuration map with robust 0 weighting. Plus sign marks the position of the HOPS source (Furlan et al. 2016, derived at 4.5 μm). *Bottom*: VLA 5 cm A-configuration map with natural weighting (black contours) overlaid on the ALMA 3 mm map (blue contours, adapted from Kainulainen et al. 2017). Plus signs mark the position of the 5 cm Source 10 (black, this work), the 9 mm/870 μm (red, Tobin et al. 2020), and the near-IR/optical objects in the region (blue, Gaia Collaboration et al. 2018). Blue contour levels are 0.3, 0.6, and 0.9 times 8.6 mJy beam^{-1}, the peak of the 3 mm core. In both panels, black contours levels are −3, 3, 4, 5, 7, 10, 15, 20, 30, 40, and 50 times the rms of each map, which are 10 μJy beam^{-1} (top) and 4.5 μJy beam^{-1} (bottom). The VLA synthesized beams are shown in the bottom left corner of the maps. The 3 mm ALMA synthesized beam (HPBW) is $3\farcs8 \times 2\farcs3$, P.A. = 71°.

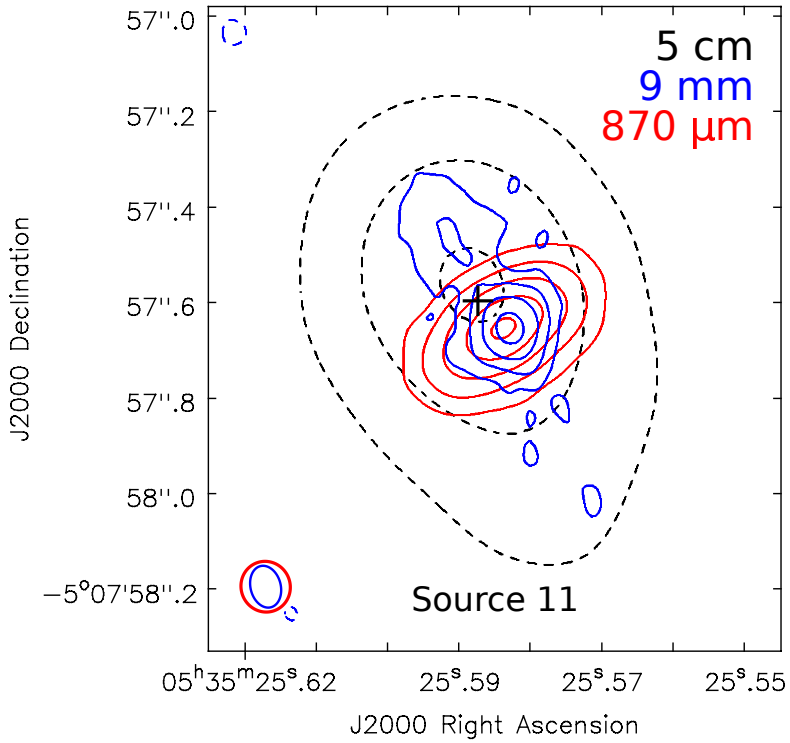

Figure 3.14 Source 11. Emission at 9 mm (blue contours) and 870 μm (red contours), adapted from Tobin et al. 2020, associated with Source 11, which position derived from a Gaussian fit to the 5 cm emission (dashed contours, this work) is marked with a plus sign. The core at 9 mm coincides well with the 870 μm emission tracing the disk, while the 9 mm lobe extends in the direction of the 5 cm elongated source. Red contour levels are 5, 20, 50, 100, and 160 times 310 μJy beam^{-1}, the rms of the 870 μm map. Blue contour levels are -3, 3, 8, 20, and 45 times 9.55 μJy beam^{-1}, the rms of the 9 mm map. Black dashed contour levels are 10, 30, and 60 times 4.5 μJy beam^{-1}, the rms of the 5 cm map. The 9 mm (blue) and 870 μm (red) synthesized beams are shown in the bottom left corner of the map. The 5 cm synthesized beam (HPBW) is $0\farcs42 \times 0\farcs40$, P.A. $= 15°$.

suggesting thermal dust emission with free-free contamination at 9 mm (if not, we would obtain a steeper spectral index $\alpha > 2$). For example, if we consider $\alpha \sim 2.5$ - 3 for the dust thermal emission, then, since we obtain $\alpha = 2$, the free-free contamination at 9 mm would be ~ 0.4 - 0.1 mJy, a value similar to the flux density of the lobe detected at 9 mm.

Our interpretation is that the protostar had a one-sided ejecta of ionized plasma, resulting in a one-sided distortion in the source shape and thus a change in the centroid position in our 5 cm map. This ejecta can be seen at 9 mm, where there is free-free emission (i.e., the lobe) in addition to the thermal dust emis-

sion (i.e., compact core). We note that in this particular case, the position of the protostar is better traced by the circumstellar disk (Tobin et al. 2020).

Source 10 is located close ($\sim 5''$) to the 3 mm compact dust core associated with Source 11 (see Fig. 3.13, bottom). It was classified as a YSO with a disk (Class I/II) by Getman et al. (2017) using the SED in the 1.6 - 8 μm range (see Table 3.4 for the counterparts), but this source has not been detected with ALMA at 870 μm (Tobin et al. 2020). The source has an M spectral type according to Hillenbrand et al. (2013) and is located at a distance of 399 ± 5 pc (Gaia Collaboration et al. 2018). According to Kounkel et al. (2018), the source belongs to the ONC-6 cluster, with a mean age of 0.76 ± 1.01 Myr. We derive a negative spectral index $\alpha = -1.7 \pm 0.7$ (Table 3.3 and Fig. 3.3), indicating non-thermal emission, suggesting it is an evolved YSO (Class II/III).

There are two additional objects close to sources 10 and 11 that we do not detect with our observations (Fig. 3.13, bottom). Kounkel et al. (2016) detected them at near-IR wavelengths and called them HOPS 71-b (coincident with HOPS-71-B from Tobin et al. 2020) and HOPS 71-c. These possible companions appear more evolved than Source 11 according to these authors. HOPS 71-c has also been detected as a variable source in radio (at 5 cm, Kounkel et al. 2014). Gaia Collaboration et al. (2018) reported distances of 361 ± 18 pc for HOPS 71-b, and 374 ± 17 pc for HOPS 71-c, confirming their association with the star-forming region. Kounkel et al. (2018) report, based on their 3D velocities, that Source 10 and HOPS 71-c belong to different ONC clusters (ONC-6 and ONC-12, respectively). Therefore, the possibility of a quadruple system composed of sources 10, 11, HOPS 71-b, and HOPS 71-c does not seem plausible. A triple system composed of Source 11, HOPS 71-b, and either Source 10 or HOPS 71-c could be possible.

In summary, we are resolving VLA 9 into two radio sources called sources 10 and 11 in this work, both YSOs. Source 10 is more evolved than Source 11, and we suggest it is a Class II/III based on its observed properties. Source 11, which could be a member of a triple system, is a radio jet and we propose it is the driving source of the molecular outflow reported in its vicinity.

3.4.2.9 Source 12

Source 12 is located toward the densest part of the ISF (see Fig. 3.1), close ($\sim 0\farcs6$) to a faint 3 mm peak (see Fig. 3.15). It has mid-IR, near-IR, X-ray, and variable optical counterparts (Table 3.4). It was classified as a YSO with a disk based on

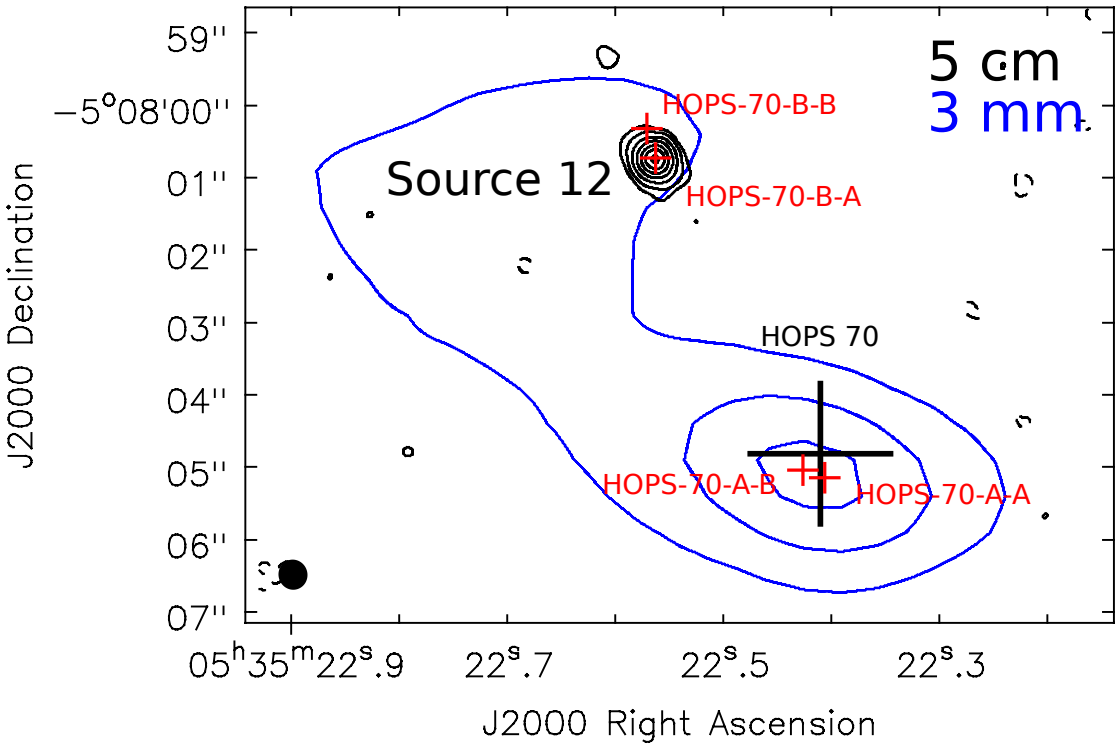

Figure 3.15 VLA 5 cm A-configuration map with natural weighting (black contours) overlaid on the ALMA 3 mm map (blue contours, adapted from Kainulainen et al. 2017). Plus signs mark the position of the HOPS source (black, Furlan et al. 2016, derived at 4.5 μm), and the 9 mm/870 μm sources (red, Tobin et al. 2020) in the region. Black contour levels are −3, 3, 6, 12, 20, 30, 40, and 50 times 4.3 μJy beam^{-1}, the rms of the 5 cm map. Blue contour levels are 0.3, 0.6, and 0.9 times 3.1 mJy beam^{-1}, the peak of the 3 mm core. The VLA synthesized beam is shown in the bottom left corner of the map. The 3 mm ALMA synthesized beam (HPBW) is $3\farcs8 \times 2\farcs3$, P.A. = 71°.

IR emission (Megeath et al. 2012; Getman et al. 2017), and its spectral type is K according to Hillenbrand et al. (2013).

This source, previously detected at 5 cm by Kounkel et al. (2014), presents signs of high radio variability (see Fig. 3.3 and Section 3.3.4). It was also detected with the VLBA (milli-arcsec angular resolution) at 5 GHz with a flux density of 0.80 ± 0.06 mJy (Kounkel et al. 2017), indicating that it is very compact and therefore non-thermal.

Source 12 could have a close companion since there is a source (detected at 9 mm and 870 μm, Tobin et al. 2020) at $\sim 0\farcs4$ ($\sim$ 200 au) of projected separation[10]. In our 5 cm high-resolution map Source 12 is marginally resolved in a direction

[10]Source 12 corresponds to source HOPS-70-B-A in Tobin et al. 2020.

consistent with the P.A. of the potential binary (Table 3.2 and Fig. 3.2), suggesting that we are marginally resolving the two components. Due to the proximity of these two sources we do not know if the IR emission is associated with all, some, or only one of them, and therefore the previous classification of Source 12 as YSO with a disk should be taken with caution. The fact that it is detected with the VLBA suggests that it is a more evolved YSO (Class II/III).

Additionally, HOPS 70, which Tobin et al. (2020) resolved into two sources, is located at $\sim 5''$ ($\sim$ 2100 au) of projected separation from Source 12. Therefore, this source could be a member of a quadruple system. According to Kounkel et al. (2018), Source 12 belongs to the ONC-12 cluster, with a mean age of 0.7 ± 1.6 Myr, and is located at a distance of 294 ± 23 pc (Gaia Collaboration et al. 2018).

3.4.2.10 Source 13 (VLA 10)

This source, previously detected at 3.6 cm and named VLA 10 (Reipurth et al. 1999), is located toward the border of the ISF, $\sim 2'$ from its ridgeline (see Fig. 3.1). The source has an X-ray counterpart (Table 3.4) whose hardness ratio, along with the lack of near-IR counterpart, suggests an extragalactic nature according to Tsujimoto et al. (2002). Reipurth et al. (1999) also suggested it is probably a background radio galaxy based on the lack of a clear association with dust.

We cannot constrain with our observations the spectral index of Source 13 (Table 3.3 and Fig. 3.3). However, in our inspection of the 13 cm VLASS map (Lacy et al. 2019), we find that the source is marginally detected at $\sim 2\sigma$ with a flux density of $\sim$ 0.4 mJy. This value (although with large uncertainty) together with our flux densities, suggests a negative spectral index. In our 5 cm high-resolution map, the source is resolved as a compact core with an elongation to the SE (see Fig. 3.2). This morphology suggests that our observations could be resolving the jet of a radio galaxy, which would be in agreement with the previous proposals. Proper motion studies and a reliable determination of the spectral index should be done to clarify the nature of this source.

3.4.2.11 Source 14

Source 14, previously reported at 5 cm by Kounkel et al. (2014), is located $\sim 5'$ from the ISF ridgeline (see Fig. 3.1). This source has been proposed as a runaway star (Neuhaeuser et al. 1998) that appears to have been ejected $\sim 12 \times 10^4$ years ago from the vicinity of the star θ^1 Ori C, in the Orion Trapezium Cluster (Kounkel

et al. 2017). It has been previously classified as a Class III YSO (Tsujimoto et al. 2002; Getman et al. 2017) with a K spectral type (Strassmeier 2009). The radio source is separated $\sim 4\farcs3$ (~ 1800 au) in projection from the K0 star JW 242 (Hillenbrand et al. 2013), which we do not detect in radio. Since Gaia Collaboration et al. (2018) reported a distance of 569 ± 35 pc for JW 242 and 411 ± 6 pc for the optical counterpart of Source 14 (see Table 3.4 for the counterparts), we discard that the two objects constitute a binary system.

This source is one of the strongest in our sample ($\sim$ 1 mJy) and presents signs of high radio variability (see Fig. 3.3 and Section 3.3.4). We cannot derive a spectral index from our observations since the source was observed only at C band. Kounkel et al. (2014) reported a flat spectral index $\alpha = -0.02 \pm 0.19$, unable to constrain the nature of the emission. However, the source was also detected with the VLBA (milli-arcsec angular resolution) at 5 GHz with a flux density of 1.6 mJy (Kounkel et al. 2017), indicating that it is very compact and therefore non-thermal. This is in agreement with the source being a Class III YSO.

3.4.2.12 Sources 17, 19, 21, 22, 28, 29, and 36

We discuss all these sources together since all of them are located toward the E-W stripe (Fig. 3.1), have mid-IR, near-IR, X-rays, and variable optical counterparts (Table 3.4), and appear to be evolved YSOs (Class II or Class III, see below) with late spectral types K-M (Hillenbrand 1997; Strassmeier 2009; Hillenbrand et al. 2013; Daemgen et al. 2012). We suggest that these sources are part of a population older than those of the filament, which may have formed in structures perpendicular to the ridgeline of the ISF, now depleted of material (see Section 3.3.1).

Source 17 is reported at radio wavelengths for the first time here. It is located $\sim 17''$ from the ISF ridgeline (Fig. 3.1) and has been previously classified as a Class III YSO based on IR observations (Tsujimoto et al. 2002; Getman et al. 2017). We derive a negative spectral index $\alpha \leq -0.6$ (Table 3.3 and Fig. 3.3) for the radio source, consistent with non-thermal emission. In our 5 cm high-resolution map, the source is elongated in the NE-SW direction (see Fig. 3.2) which could point to a marginally resolved binary system. We do not favor a non-thermal jet since the source appears to be too evolved to have a jet and, if it had one, the non-thermal lobe would not be that close to the object. It has several possible companions, since it is separated in projection $\sim 4''$ (~ 1700 au) from the spectroscopic binary and variable star JW 785 (Tobin et al. 2009; Samus

et al. 2017), and $\sim 7''$ ($\sim$ 2900 au) from HOPS 349, none of which we detect in radio. Since Gaia Collaboration et al. (2018) reported distances of 391 ± 5 pc for Source 17 and 381 ± 16 pc for JW 785, it is plausible that they belong to a multiple system.

Source 19, located $\sim 3'$ from the ISF ridgeline (see Fig. 3.1), is reported at radio wavelengths for the first time here and presents signs of high radio variability (see Fig. 3.3 and Section 3.3.4). It was previously classified as a Class III YSO (Getman et al. 2017), and is a spectroscopic binary (Tobin et al. 2009). According to Kounkel et al. (2018), Source 19 belongs to the ONC-21 cluster, with a mean age of 0.8 ± 0.8 Myr, and is located at a distance of 393 ± 3 pc (Gaia Collaboration et al. 2018). We derive a positive spectral index $\alpha = 0.9 \pm 0.3$ for this source (Table 3.3 and Fig. 3.3), although it should be taken with caution due to the high variability of the source.

Source 21, previously reported at 5 cm by Kounkel et al. (2014), is located $\sim 3\farcm3$ from the ISF ridgeline (see Fig. 3.1). Tsujimoto et al. (2002) classified the source as a Class II YSO, while Getman et al. (2017) classified it as Class III. According to Kounkel et al. (2018), Source 21 belongs to the ONC-12 cluster with a mean age of 0.7 ± 1.6 Myr, and is located at a distance of 314 ± 18 pc (Gaia Collaboration et al. 2018). We derive a negative spectral index $\alpha = -0.6 \pm 0.4$ (Table 3.3 and Fig. 3.3), consistent with non-thermal emission. This is further supported by the detection of the source at 5 GHz with the VLBA (milli-arcsec angular resolution) with a maximum flux density of 0.47 ± 0.12 mJy (Kounkel et al. 2017). Those authors noted that the source appears to be marginally extended in RA, which could point to a marginally resolved binary system. In our 5 cm high-resolution map, the source is marginally resolved (Table 3.2 and Fig. 3.2), indicating that some extended emission is also present.

Source 22 is reported at radio wavelengths for the first time here. It is located $\sim 4'$ from the ISF ridgeline (see Fig. 3.1). The source has been previously classified as a Class III YSO (Tsujimoto et al. 2002; Getman et al. 2017) and is a spectroscopic binary according to Tobin et al. (2009). According to Kounkel et al. (2018), this source belongs to the ONC-9 cluster, with a mean age of 1.0 ± 1.3 Myr, and a mean distance of 400 ± 26 pc. We cannot derive a spectral index from our observations since the source was only observed at C band. However, in our inspection of the 13 cm VLASS map (Lacy et al. 2019), we find that the source is detected with a flux density of 1.04 ± 0.23 mJy. This value, along with our 5 cm flux densities (Table 3.3), suggests a negative spectral index. The source

is marginally resolved in our 5 cm high-resolution map, which could point to a marginally resolved binary system. We do not favor a non-thermal jet for the same reasons that in Source 17 (see above).

Sources 28 and 29, separated only $0\farcs6$ ($\sim$ 250 au) in projection, are reported at radio wavelengths for the first time here. They are located $\sim 66''$ from the ISF ridgeline (see Fig. 3.1). In our 5 cm high-resolution map, we separate the emission from the two sources (see Fig. 3.2). The two emission peaks in that map —that correspond to our radio sources 28 and 29— coincide within $0\farcs05$ with the position of two optical sources (Gaia Collaboration et al. 2018), which are components of a binary system (Köhler et al. 2006; Daemgen et al. 2012). Using the C-configuration maps, in which the emission from sources 28 and 29 is blended, we derived a positive spectral index $\alpha = 0.74 \pm 0.03$ for the combination of the two components (Table 3.3 and Fig. 3.3). Emission in the IR is detected at low resolution as a single source that has been previously classified as a YSO with a disk (Megeath et al. 2012; Getman et al. 2017). According to Kounkel et al. (2018), Source 28 belongs to the ONC-12 cluster, with a mean age of 0.7 ± 1.6 Myr, and a mean distance of 402 ± 15 pc.

Source 36 was previously reported at 5 cm by Kounkel et al. (2014), who derived a positive spectral index $\alpha = 1.0 \pm 0.4$ (Table 3.3 and Fig. 3.3), consistent with thermal free-free emission. It has been previously classified as a Class III YSO (Tsujimoto et al. 2002; Getman et al. 2017). According to Kounkel et al. (2018), Source 36 belongs to the ONC-12 cluster, with a mean age of 0.7 ± 1.6 Myr, and is located at a distance of 417 ± 5 pc (Gaia Collaboration et al. 2018). The source is separated $\sim 6\farcs2$ ($\sim$ 2600 au) in projection from the optical variable V574 Ori (Samus et al. 2017), which we do not detect in radio. Since according to Kounkel et al. (2018) V574 Ori belongs to a different cluster than Source 36, we discard that they are components of a binary system.

3.4.2.13 Sources 20, 26, and 30

This is the first report at radio wavelengths of sources 20, 26, and 30. These three sources are located outside the ISF, $\sim 4\farcm5$ from its ridgeline (see Fig. 3.1). They are roughly aligned in the NW-SE direction (Fig. 3.16) and we propose that they are in fact a single object. This object would be a central, elongated jet (Source 26) that has two extended lobes (sources 20 and 30) with bow-shock morphology.

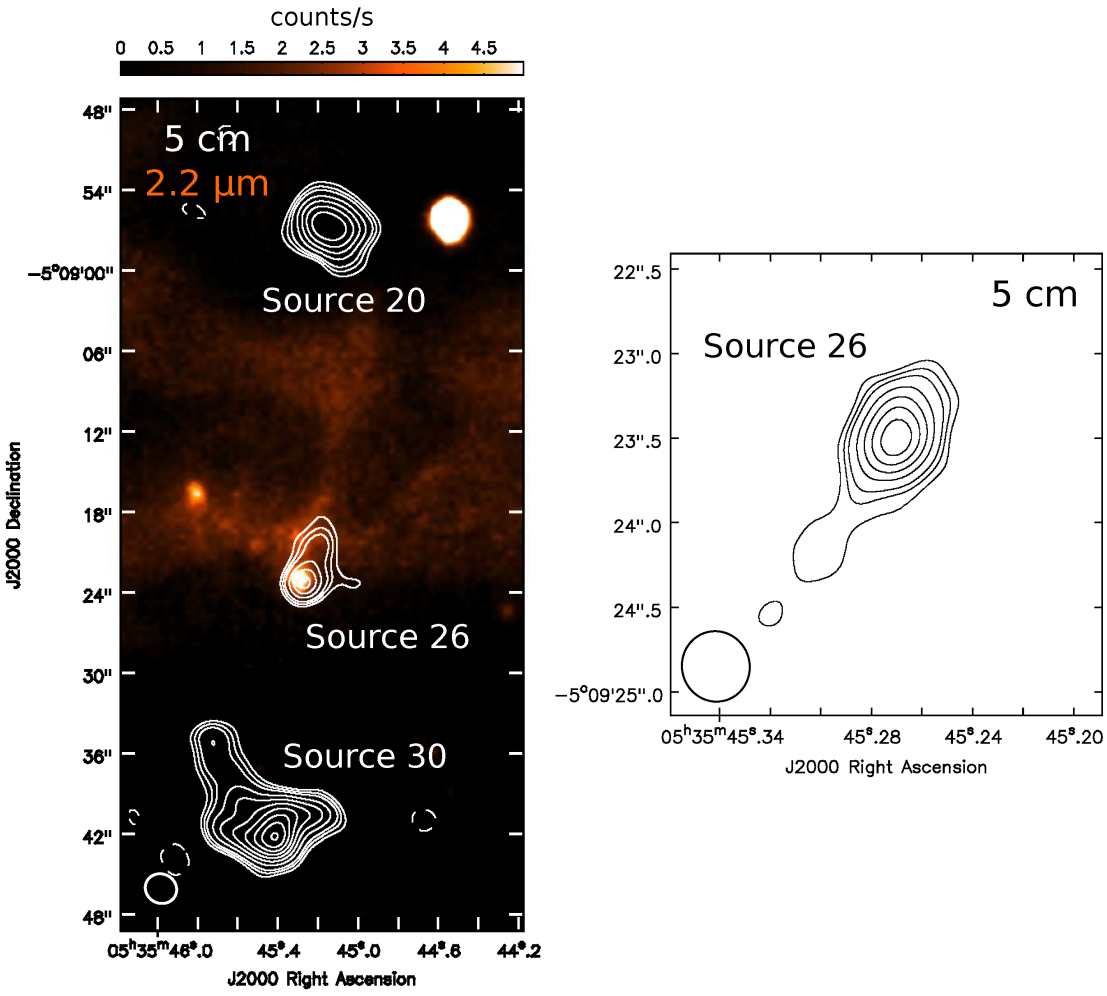

Figure 3.16 Sources 20, 26, and 30. *Left*: VLA 5 cm A-configuration map with natural weighting (contours) overlaid on the NEWFIRM 2.2 μm image (color scale, T. Megeath, private communication). To better detect the extended emission from sources 20 and 30, uvtaper = 50 kλ was applied in the 5 cm data. *Right*: VLA 5 cm A-configuration map with natural weighting of Source 26 with no uvtaper applied. The elongation of the source is clearly appreciated. In both panels, contour levels are -3, 3, 4, 5, 7, 9, 11, 13, 15, 17, 19, 21, and 23 times the rms of the maps, which are 30 μJy beam^{-1} (left) and 12 μJy beam^{-1} (right). The VLA synthesized beams are shown in the bottom left corner of the maps.

In our inspection of the 13 cm VLASS map (Lacy et al. 2019), we find that the lobes are detected with a flux density of 2.3 ± 0.4 mJy (Source 20) and 3.4 ± 0.7 mJy (Source 30). These values, together with our 5 cm flux densities (Table 3.3), suggest a negative spectral index, indicative of non-thermal emission.

We favor that this is an extragalactic object since the central source (Source 26) has associated only weak IR emission shortward of 4.5 μm (Table 3.4), while its possible lobes have no counterparts at all (see Fig. 3.16, left). We propose that we are detecting an extragalactic radio jet (Source 26) and terminal shocks (sources 20 and 30) where the jet impacts the environment. Additional data, including a reliable determination of the spectral indices and proper motion studies, should be obtained in order to confirm this prediction.

3.4.2.14 Sources 24 and 25 (HOPS 66)

Sources 24 and 25, separated $\sim 2''$ ($\sim$ 800 au) in projection, are located toward the densest part of the ISF, associated with the far-IR source HOPS 66 (Adams et al. 2012; Furlan et al. 2016; see Table 3.4 for the counterparts).

The 3 mm ALMA map (Kainulainen et al. 2017) shows a compact dust core associated with both radio sources, suggesting they are embedded in the same parental material (see Fig. 3.17, left). Source 25 is located $\sim 1''$ from the peak of the core, and Source 24 is displaced about $\sim 2''$. We derive positive spectral indices for both sources consistent with thermal free-free emission, $\alpha = 0.29 \pm 0.24$ for Source 24 and $\alpha = 0.57 \pm 0.07$ for Source 25 (Table 3.3 and Fig. 3.3). Both sources are also detected at 9 mm and 870 μm (see Fig. 3.2) with sizes $\sim$ 100 au (Tobin et al. 2019), indicating the presence of circumstellar disks.

In the HST map (Habel et al. 2020), a unipolar cavity opening to the W is clearly associated with Source 25 (Fig. 3.17, left), and, recently, a CO outflow centered on Source 25 has been imaged, with the blue lobe responsible for the IR cavity (Tobin et al., in press). In our 5 cm high-resolution map, the source is elongated at P.A. $= 106 \pm 2^\circ$ (see Fig. 3.17, right), consistent with the direction of the cavity and the outflow. Hence, we confirm this object as the radio jet driving the large scale outflow.

Furlan et al. (2016) classified HOPS 66 as a flat-spectrum and luminous source with a high inclination angle. The latter would be consistent with our detection of Source 25 as an elongated radio jet. On the other hand, the far-IR emission peaks closer to Source 25 and, since both sources appear to be embedded in the

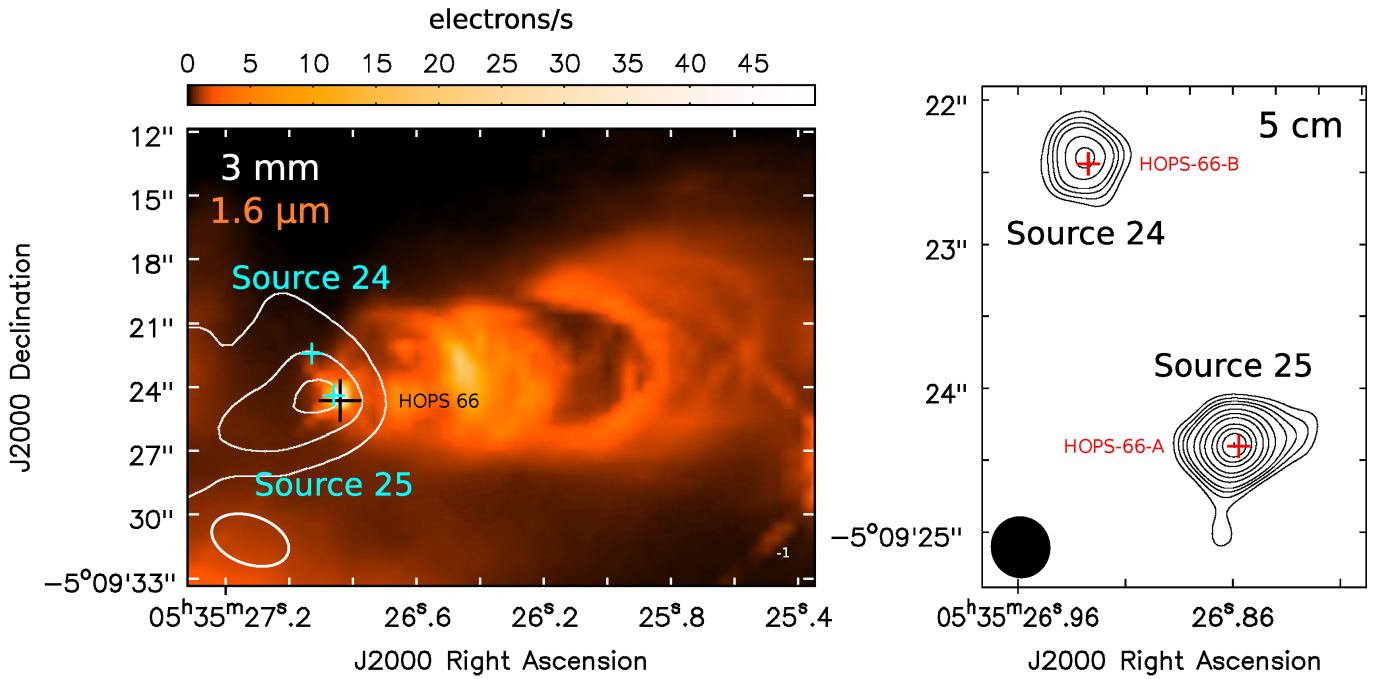

Figure 3.17 Sources 24 and 25. *Left*: ALMA 3 mm map (white contours, Kainulainen et al. 2017) overlaid on the HST 1.6 μm image (color scale, adapted from Habel et al. 2020). Plus signs mark the position of the radio sources (cyan, this work) and the HOPS source (black, Furlan et al. 2016, derived at 4.5 μm) in the region. Contour levels are 0.3, 0.6, and 0.9 times 7.4 mJy beam^{-1}, the peak of the 3 mm core. *Right*: VLA 5 cm A-configuration map with natural weighting. Red plus signs mark the position of the 9 mm/870 μm sources (Tobin et al. 2019). Contour levels are −3, 3, 4, 5, 6, 8, 10, 12, 15, 17, 19, 21, and 23 times 3.4 μJy beam^{-1}, the rms of the map. In both panels, the synthesized beams (VLA: filled, ALMA: outlined) are shown in the bottom left corner. The E-W elongation of Source 25 is consistent with the direction of the monopolar cavity associated with it.

same core, it is possible that the measured (broadband) SED has a contribution also from Source 24. In fact, the observed flattening of the SED could be due to flux coming from both sources, each one with the emission peak at a slightly different frequency.

Furlan et al. (2016) estimated for HOPS 66 an $L_{\rm bol} = 18\ L_{\odot}$ (scaled to our adopted distance of 386 pc). Given the poor angular resolution of the far-IR data, this value probably includes the luminosity of both protostars, and the relative contribution of each one is unknown. However, given that the radio source 25 (likely a radio jet driving the outflow associated with the near-IR cavity) is the one with the higher 5 cm flux density, it seems plausible to attribute essentially all the bolometric luminosity to this radio source, with a much smaller contribution (of the order of a few tenths of $L_{\odot}$) to radio source 24. With this configuration, both sources would follow fairly well the Anglada correlation with $L_{\rm bol}$ (see discussion in Section 3.4.1).

3.4.2.15 Source 27

Source 27 is located toward the ISF, at $\sim 24''$ from its ridgeline, in the region where the ISF and the E-W stripe apparently intersect (Fig. 3.1). The source is not associated with any 3 mm compact dust core (Kainulainen et al. 2017) and has been previously classified based on its near and mid-IR emission (see Table 3.4 for its counterparts) as a Class III YSO (Fűrész et al. 2008; Getman et al. 2017) with M spectral type (Hillenbrand 1997). According to Kounkel et al. (2018), this source belongs to the ONC-16 cluster, with a mean age of 0.4 ± 1.2 Myr, and a mean distance of 386 ± 17 pc.

Source 27 is reported at radio wavelengths for the first time here. We detect the source at the four bands (5, 3.6, 1.3, and 0.7 cm) in our 2014 C-configuration maps, but not in our more sensitive 2015 A-configuration 5 cm map, suggesting it is a radio variable (see Fig. 3.3). Additionally, it has not been detected at 0.9 cm by (Tobin et al. 2020) in their 2016 A-configuration observations with a sensitivity of ~ 8 μJy beam^{-1}. We derive a positive spectral index $\alpha = 1.06 \pm 0.05$ (Table 3.3 and Fig. 3.3), consistent with thermal free-free emission.

To explain the thermal free-free emission of this object, one possibility would be that we are detecting a radio jet, which is expected to be weak for an evolved YSO and more extended at higher wavelengths. Since the source is strong (Table 3.3) and resolved in one direction in our 1.3 cm (Table 3.2 and Fig. 3.2) and 0.7 cm maps, but remains unresolved at higher wavelengths, we can rule out this case.

Another possibility would be that the positive spectral index is not real, but an artifact if we are measuring the combined flux of two components of an unresolved binary. In this case we would expect that, since the source is marginally resolved in one direction at 1.3 cm, the two components would be resolved in the 0.7 cm map with twice the higher resolution, and this does not happen. A viable option given its evolutionary stage would be that we are detecting free-free emission from disk photoevaporation. Further observations, such as the detection of optical and mid-IR forbidden line emission (Font et al. 2004; Alexander et al. 2014), should be carried out to confirm this claim.

3.4.2.16 Source 32 (HOPS 369)

This source is located toward the densest part of the ISF (Fig. 3.1), associated with the far-IR source HOPS 369 (see Table 3.4 for the counterparts) and coincident with a faint 3 mm peak (see Fig. 3.18). The source has been previously classified using its SED as a Class I/II YSO (Fűrész et al. 2008; Getman et al. 2017) and as a flat spectrum source with a high inclination angle (disk close to edge-on, Furlan et al. 2016). On other hand, Habel et al. 2020 report scattered light with an irregular morphology associated with this source.

We derived a positive spectral index $\alpha = 0.36 \pm 0.18$ (Table 3.3 and Fig. 3.3), consistent with thermal free-free emission. The radio source has been detected at 9 mm with a flux density of 0.051 ± 0.007 mJy (Tobin et al. 2019), in good agreement with our spectral index, indicating that at that wavelength almost all the emission is due to free-free emission. It has also been detected at 870 μm by those authors (see Fig. 3.2) as a poorly resolved source that could trace a face-on disk, which would be in conflict with the inclination previously derived from the SED modeling. An elongation of the source is hinted at in our 5 cm high-resolution map (see Fig. 3.18) but we do not resolve the source in any direction. Higher angular resolution observations would be necessary to resolve the radio jet.

3.4.2.17 Sources 33 and 34 (VLA 13, HOPS 368)

The radio source VLA 13, elongated at P.A. $\sim 20°$, was reported by (Reipurth et al. 1999) in their observations with angular resolution $\sim 8''$. Our higher angular resolution allows us to resolve that source into two, sources 33 and 34, separated $\sim 9''$ ($\sim$ 3800 au) in projection (Fig. 3.19). Source 34 was previously reported

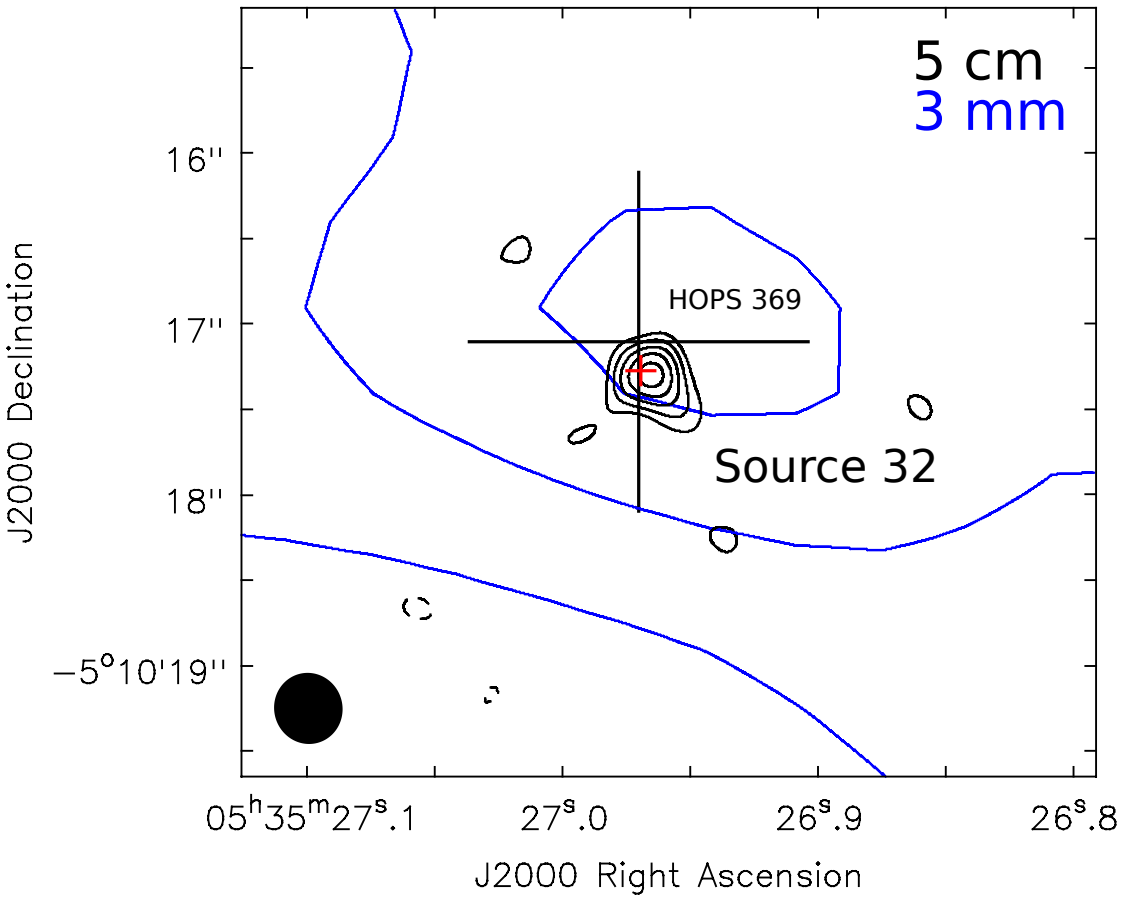

Figure 3.18 Source 32. VLA 5 cm A-configuration map with natural weighting (black contours) overlaid on the ALMA 3 mm map (blue contour, adapted from Kainulainen et al. 2017). Plus signs mark the position of the HOPS (black, Furlan et al. 2016, derived at 4.5 μm) and the 9 mm/870 μm (red, Tobin et al. 2020) sources in the region. Black contour levels are −3, 3, 4, 5, 6, and 7 times the rms of the 5 cm map, 3 μJy beam^{-1}. Blue contour levels are 0.3, 0.6, and 0.9 times 1.8 mJy beam^{-1}, the peak of the 3 mm core. The VLA synthesized beam is shown in the bottom left corner of the image. The 3 mm ALMA synthesized beam (HPBW) is $3\farcs8 \times 2\farcs3$, P.A. = 71°.

at 5 cm by Kounkel et al. (2014), and this is the first report of Source 33 as an independent radio source.

These sources are located toward the densest part of the ISF (Fig. 3.1), in a crowded region where different outflows overlap (see Fig. 8 in Takahashi et al. 2008). There is a bright double cone-shaped reflection nebula seen at K_s and a bipolar CO outflow at P.A. $= 0°$ that have been associated with VLA 13.

Source 34 is located toward the peak of a 3 mm compact dust core (Kainulainen et al. 2017, see Fig. 3.19, left) and is associated with HOPS 368 (Adams et al. 2012; Furlan et al. 2016), a Class I YSO (see Table 3.4 for other counterparts). It was classified as a YSO with a disk by Getman et al. (2017) using the SED in the 1.6 - 8 μm range (see Table 3.4 for the counterparts). Recently, Tobin et al. (2019) imaged with ALMA at 870 μm an elongated structure that can be a dust disk (see Fig. 3.2).

We detect Source 34 toward the center of the CO outflow, between the red and blue lobes (Fig. 3.19, right), and derive a positive spectral index $\alpha = 0.73 \pm 0.14$ for this source (Table 3.3), consistent with thermal free-free emission. The source follows the Anglada correlations with $L_{\rm bol}$ and $\dot{\rm P}$ (see Section 3.4.1) suggesting it is a radio jet. An elongation consistent with the direction of the outflow (and nearly perpendicular to the imaged circumstellar dust disk) is hinted at in our 5 cm high-resolution map (see Fig. 3.2). Higher angular resolution observations would be necessary in order to resolve the radio jet. We note that the flux density of Source 34 at 7 mm is lower than the extrapolated flux density from the fit with lower frequency data points (Fig. 3.3). This flattening of the spectrum could suggest that the radio emission from the jet becomes optically thin at high frequency.

Source 33 is not associated with any 3 mm compact dust core (Kainulainen et al. 2017) (see Fig. 3.19, left). The radio source has an extended morphology and, in the 5 cm high-resolution map, it has two emission peaks, separated $\sim 3''$ in projection (Fig. 3.19, left). We derive a spectral index $\alpha = -0.05 \pm 0.01$ (Table 3.3), consistent with optically thin thermal free-free emission coming from an ionized region. The only star detected toward this radio source is V1343 Ori ($\sim 1''$ to the NW of Source 33 eastern peak), at a distance of 355 ± 33 pc (Gaia Collaboration et al. 2018), but its luminosity of only 0.1 $L_\odot$ (Da Rio et al. 2012) is not enough to yield the observed centimeter density flux. Since Source 33 appears toward the edge of the blue lobe of the Source 34 outflow (see Fig. 3.19, right), we suggest that the ionization of the gas is occurring due to shocks of this outflow in the walls of the cavity.

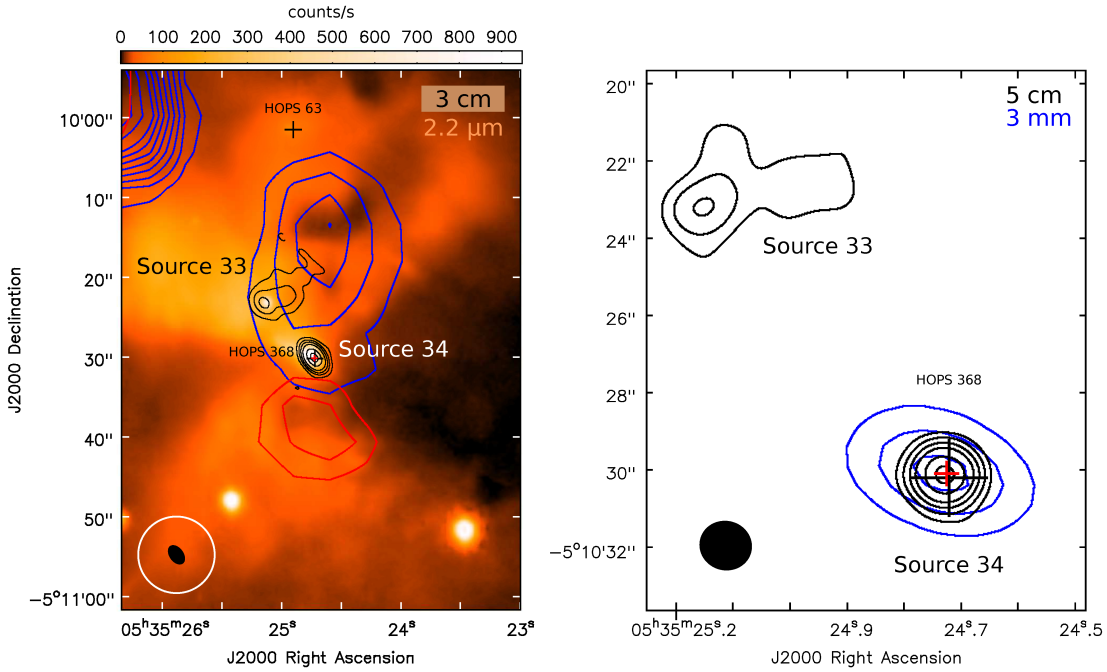

Figure 3.19 Sources 33 and 34. *Left*: APEX CO(6-5) blue- and red-shifted integrated intensity (blue and red contours, respectively, adapted from González-García et al. 2016) and VLA 3 cm C-configuration map with robust 0 weighting (black contours) overlaid on the NEWFIRM 2.2 μm image (T. Megeath, private communication). Contour levels of the CO emission are 3, 4, 5, 6, 7, 8, 9, 10, 12, 14, and 16 times 8000 K, the rms of the map. Black contour levels are −3, 3, 7, 12, 20, 40, and 60 times 9.0 μJy beam^{-1}, the rms of the 3 cm map. *Right*: VLA 5 cm A-configuration map with natural weighting and uvtaper = 100 kλ (black contours) overlaid on the ALMA 3 mm map (blue contours, adapted from Kainulainen et al. 2017). Contour levels are −3, 3, 6, 10, 15, 25, and 35 times 8.2 μJy beam^{-1}, the rms of the 5 cm map. Blue contours are 0.3, 0.6, and 0.9 times 7.6 mJy beam^{-1}, the peak of the 3 mm core. In both maps, plus signs mark the position of the HOPS (black, Furlan et al. 2016, derived at 4.5 μm) and the 9 mm/870 μm (red, Tobin et al. 2020) sources in the region. The VLA (filled) and APEX (outlined) synthesized beams are shown in the bottom left corner of the maps. The 3 mm ALMA synthesized beam (HPBW) is $3\farcs8 \times 2\farcs3$, P.A. = 71°. The N-S outflow driven by Source 34 and the associated double cone-shaped nebula are clearly appreciated in the left panel.

In summary, we propose that Source 34 is the driving source of the outflow detected in its vicinity and that Source 33 is tracing ionized gas in the associated cavity.

3.4.2.18 Source 37

Source 37 is located toward the densest part of the ISF (see Fig. 3.1), coincident with a faint 3 mm peak (see Fig. 3.20). It has mid-IR, near-IR, X-ray, and variable optical counterparts (Table 3.4) and was classified as a YSO with disk based on IR emission (Megeath et al. 2012; Getman et al. 2017). Its spectral type is G according to Penston et al. (1975) and is a spectroscopic binary according to Tobin et al. (2009).

This is the first report at radio wavelengths of Source 37, for which we determine a positive spectral index $\alpha = 1.2 \pm 0.7$ (Table 3.3 and Fig. 3.3), consistent with thermal free-free emission. Gaia Collaboration et al. (2018) reported a distance of 394 ± 5 pc, confirming its membership to the star-forming region.

3.4.2.19 Source 38

Source 38 is reported at radio wavelengths for the first time here. It is located toward the densest part of the ISF but is not associated with any 3 mm compact dust core (Kainulainen et al. 2017), suggesting it is not deeply embedded YSO.

The source has been detected in the optical and the near-IR (see Table 3.4 for the counterparts) and classified with a spectral type M (Da Rio et al. 2009). We report here emission associated with the radio source also at 3.6 and 4.5 μm in the inspected *Spitzer* maps (Fig. 3.21).

We determine a positive spectral index of $\alpha = 1.3 \pm 0.8$ (Table 3.3 and Fig. 3.3), consistent with thermal free-free emission. In fact, the source appears as a weak, marginally elongated source in our 5 cm map, which could indicate that we are detecting a weak radio jet from an evolved YSO (Class II/III). Another option would be that we are detecting an unresolved binary.

Source 38 is located at $\sim 2\farcs5$ ($\sim$ 1000 au) of projected separation from the mid-IR source MGM 2256 (Megeath et al. 2012), which we do not detect at radio wavelengths (Fig. 3.21). Gaia Collaboration et al. (2018) reported a distance of 582 ± 61 pc for MGM 2256 and 366 ± 10 pc for Source 38, suggesting that they do not belong to a binary system since they are actually separated by more than 100 pc.

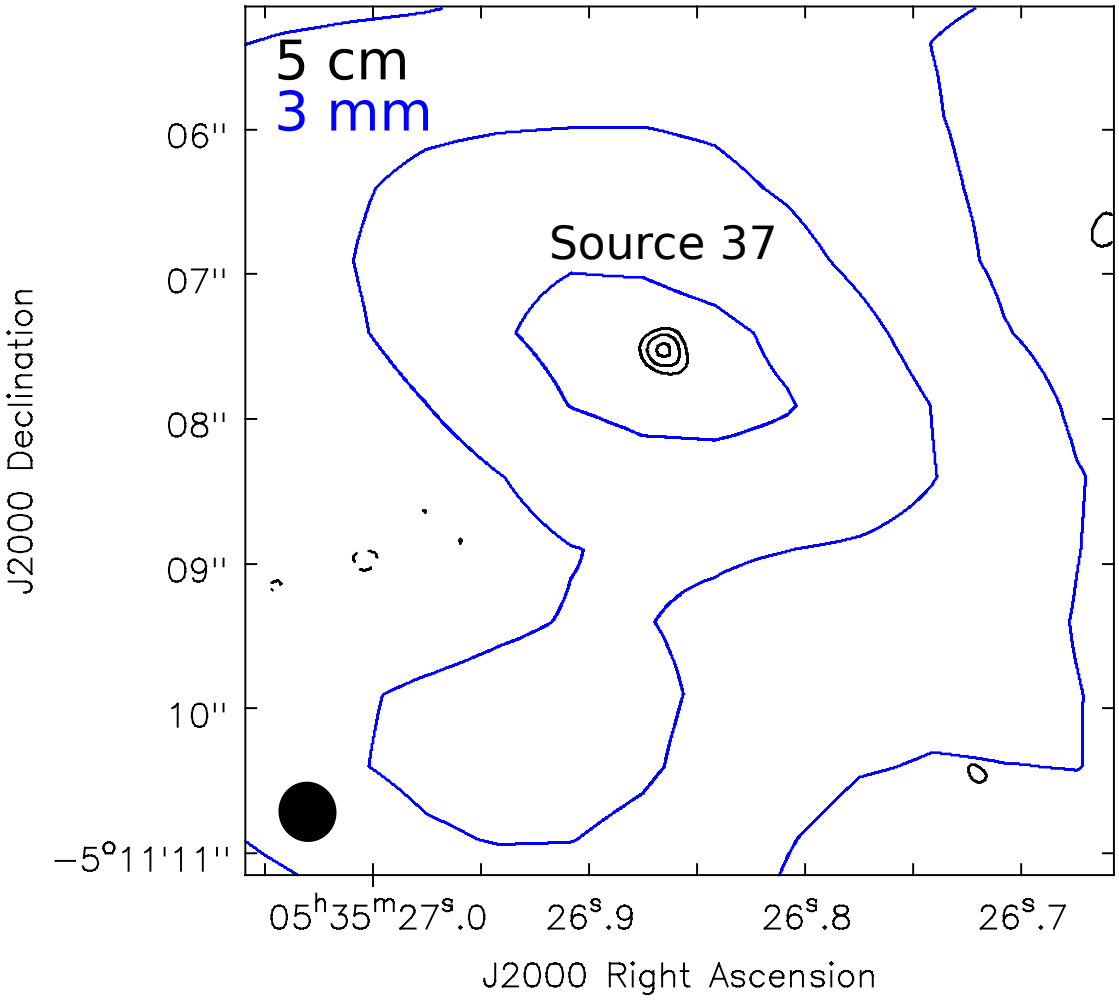

Figure 3.20 Source 37. VLA 5 cm A-configuration map with natural weighting (black contours) overlaid on the ALMA 3 mm map (blue contours, adapted from Kainulainen et al. 2017). Black contour levels are −3, 3, 4, and 5 times 3.6 μJy beam^{-1}, the rms of the 5 cm map. Blue contour levels are 0.3, 0.6, and 0.9 times 1.2 mJy beam^{-1}, the peak of the 3 mm core. The VLA synthesized beam is shown in the bottom left corner of the map. The 3 mm ALMA synthesized beam (HPBW) is $3\farcs8 \times 2\farcs3$, P.A. = 71°.

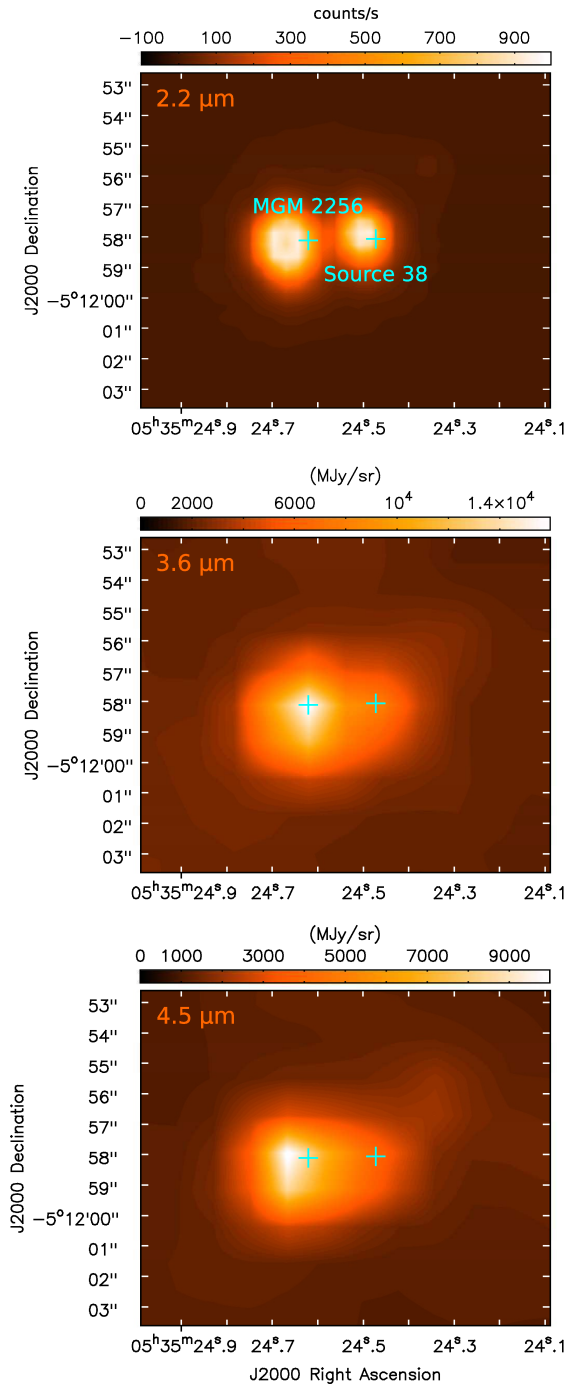

Figure 3.21 Source 38. Near-IR (NEWFIRM 2.2 μm; T. Megeath, private communication) and mid-IR emission (Megeath et al. 2012, Spitzer 3.6 and 4.5 μm). Plus signs mark the position of the radio source (this work) and the mid-IR source MGM 2256 (Megeath et al. 2012, derived at 4.5 μm). Emission toward Source 38 is clearly observed in all panels.

3.4.2.20 Source 39 (HOPS 60)

This source, located in the densest part of the ISF (Fig. 3.1), is associated with the far-IR source HOPS 60 (Adams et al. 2012) and the 1.3 mm dust condensation named FIR 6b (Chini et al. 1997). The source is located toward the center of a bipolar CO outflow at P.A. = 65° (Takahashi et al. 2008; Shimajiri et al. 2009), whose red lobe has opened a cavity to the NW seen in scattered light (Habel et al. 2020, T. Megeath, private communication, see Fig. 3.22).

The radio source is located toward the peak of a compact dust core in the 3 mm ALMA image (Kainulainen et al. 2017, Fig. 3.22), indicating it is deeply embedded. In our 5 cm high-resolution map, the source appears slightly elongated at P.A. = $65 \pm 17°$ (see Fig. 3.2), consistent with the direction of the cavity and the outflow (P.A. = 65°) detected in its vicinity. Additionally, Tobin et al. (2020) detected with ALMA at 870 μm a structure nearly perpendicular to the direction of the outflow that could be a circumstellar dust disk (see Fig. 3.2). We derive a positive spectral index $\alpha = 1.1 \pm 0.7$ (Table 3.3 and Fig. 3.3), indicative of thermal free-free emission. Also, the source follows the Anglada correlations with $L_{\rm bol}$ and $\dot{\rm P}$ (see Section 3.4.1) suggesting it is a radio jet. Therefore, we propose that Source 39 is the driving source of the outflow seen at larger scales.

3.4.2.21 Source 40

Source 40 is located toward the border of the ISF, $\sim 38''$ from its ridgeline (Fig. 3.1), and is not associated with any 3 mm compact dust core (Kainulainen et al. 2017). The source was previously detected at 5 cm by Kounkel et al. (2014) and classified as a Class III YSO (Tsujimoto et al. 2002; Getman et al. 2017, see Table 3.4 for the counterparts). It has a G spectral type according to Hillenbrand (1997) and is located at a distance of 369 ± 10 pc (Kounkel et al. 2017).

The source is a close binary (separation ~ 4 au) with both components detected at 5 GHz in VLBA observations (milli-arcsec angular resolution, Kounkel et al. 2017), indicating they are very compact and therefore non-thermal. We cannot constrain the spectral index from our data (see Table 3.3 and Fig. 3.3) nor taking into account 9 mm data (0.28 ± 0.02 mJy, Tobin et al. 2020).

In our 5 cm high-resolution map, the source exhibits a marginal elongation at P.A. = 48° (Fig. 3.2 and Table 3.2) which is not related to the unresolved binary since we do not have enough angular resolution. This elongation could be

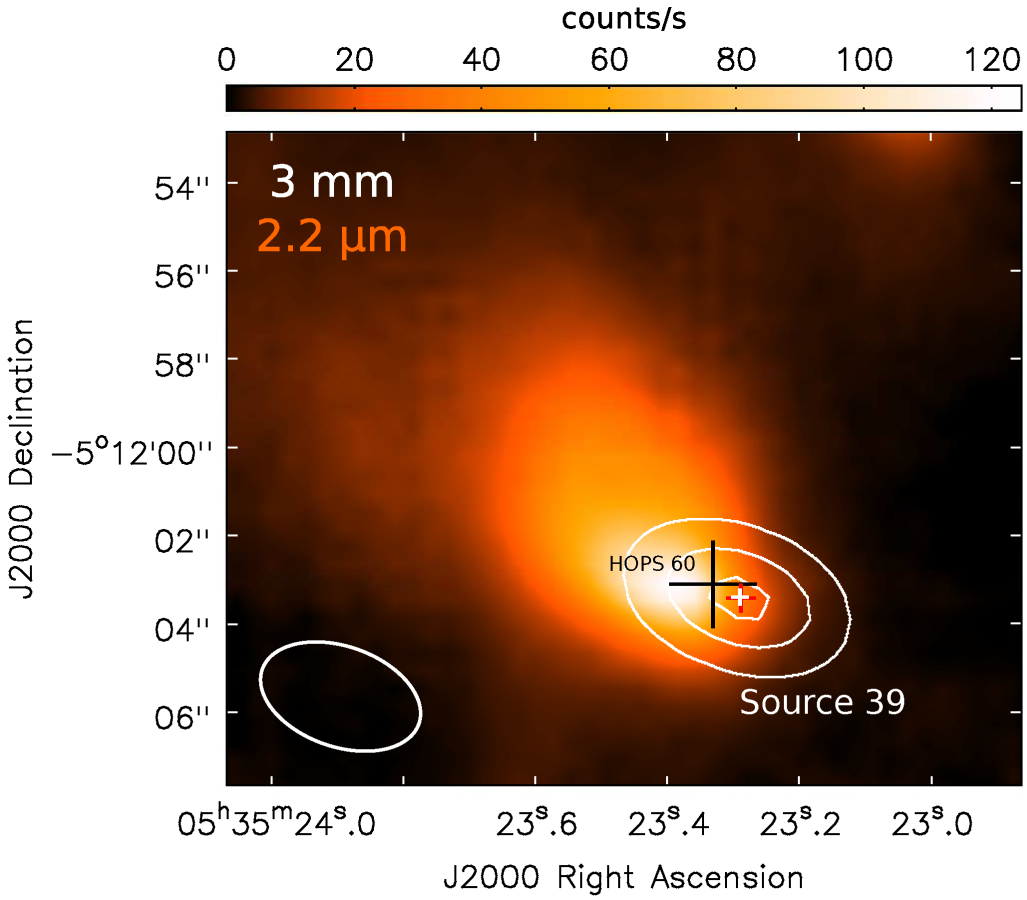

Figure 3.22 Source 39. ALMA 3 mm map (contours, Kainulainen et al. 2017) overlaid on the NEWFIRM 2.2 μm image (color scale, T. Megeath, private communication), in which the monopolar cavity associated with Source 39 is appreciated. Plus signs mark the position of the radio source (cyan, this work), the HOPS source (black, Furlan et al. 2016, derived at 4.5 μm), and the 9 mm/870 μm source (red, Tobin et al. 2020). Contour levels are 0.3, 0.6, and 0.9 times 18.9 mJy beam^{-1}, the peak of the 3 mm core. The ALMA synthesized beam is shown in the bottom left corner.

caused by another component in the system with thermal emission and therefore not detected with the VLBA.

The source VLA 14, reported at 3.6 cm by (Reipurth et al. 1999), but undetected in our observations and those of Kounkel et al. (2014), is located at a projected distance of $\sim$ 5.″5 ($\sim$ 2300 au) from Source 40. Since VLA 14 was detected with an angular resolution of 8″, we cannot discard that VLA 14 and Source 40 are the same source.

3.4.2.22 Sources 41 and 43 (HOPS 409)

These sources are located toward the densest part of the ISF (Fig. 3.1). Source 43 is associated with the 1.3 mm dust condensation named FIR 6c (Chini et al. 1997) and with the extremely young Class 0 object HOPS 409 (source PBR 135003 in Tobin et al. 2015; Furlan et al. 2016). The source is located toward the peak of a compact dust core at 3 mm (Kainulainen et al. 2017, see Fig. 3.23), consistent with it being deeply embedded. A bipolar CO outflow at P.A. $\sim 20^{\circ}$ is associated with this source (Takahashi et al. 2008; Shimajiri et al. 2009; Tobin et al. 2016c). Additionally, Tobin et al. (2020) detected with ALMA at 870 μm a structure nearly perpendicular to the direction of the outflow that could be a circumstellar dust disk (see Fig. 3.2). Although we do not resolve the radio source (Fig. 3.2), nor constrain its spectral index (Table 3.3), we propose that we are detecting the radio jet associated with the large scale outflow. We make this statement based on the facts that the outflow is centered on Source 43 and that this radio source follows the Anglada correlations with $L_{\rm bol}$ and $\dot{\rm P}$ (see Section 3.4.1) suggesting it is a radio jet.

This is the first report at radio wavelengths of Source 41. It is located toward the border of a weak dust clump located $\sim 40''$ NE of Source 43 (see Fig. 3.23). It does not have known counterparts at other wavelengths and its spectral index is unconstrained (Table 3.3). We note that Source 41 seems to fall in projection very close to the path of the blue-shifted lobe of the outflow driven by Source 43, which extends toward a 1.3 mm dust condensation named FIR 6a (Chini et al. 1997) (see Fig. 3.23). Shimajiri et al. (2009) detected collimated SiO emission, a tracer of shocked gas, along this lobe (see their Fig. 5) and argued that interaction between the SiO jet and FIR 6a is probably taking place. The position of Source 41 in a region of strong shocks suggests its association with the outflow. It could be either a knot produced by the shocks or, if the source were indeed associated with the ISF, a possible case of induced star-formation. Further studies toward Source 41, such as proper motions or a reliable determination of its spectral index, should be carried out to address this question.

3.4.2.23 Source 42 (HOPS 59)

Source 42, located toward the densest part of the ISF (Fig. 3.1), is associated with the 1.3 mm dust condensation named FIR 6d (Chini et al. 1997) and the far-IR

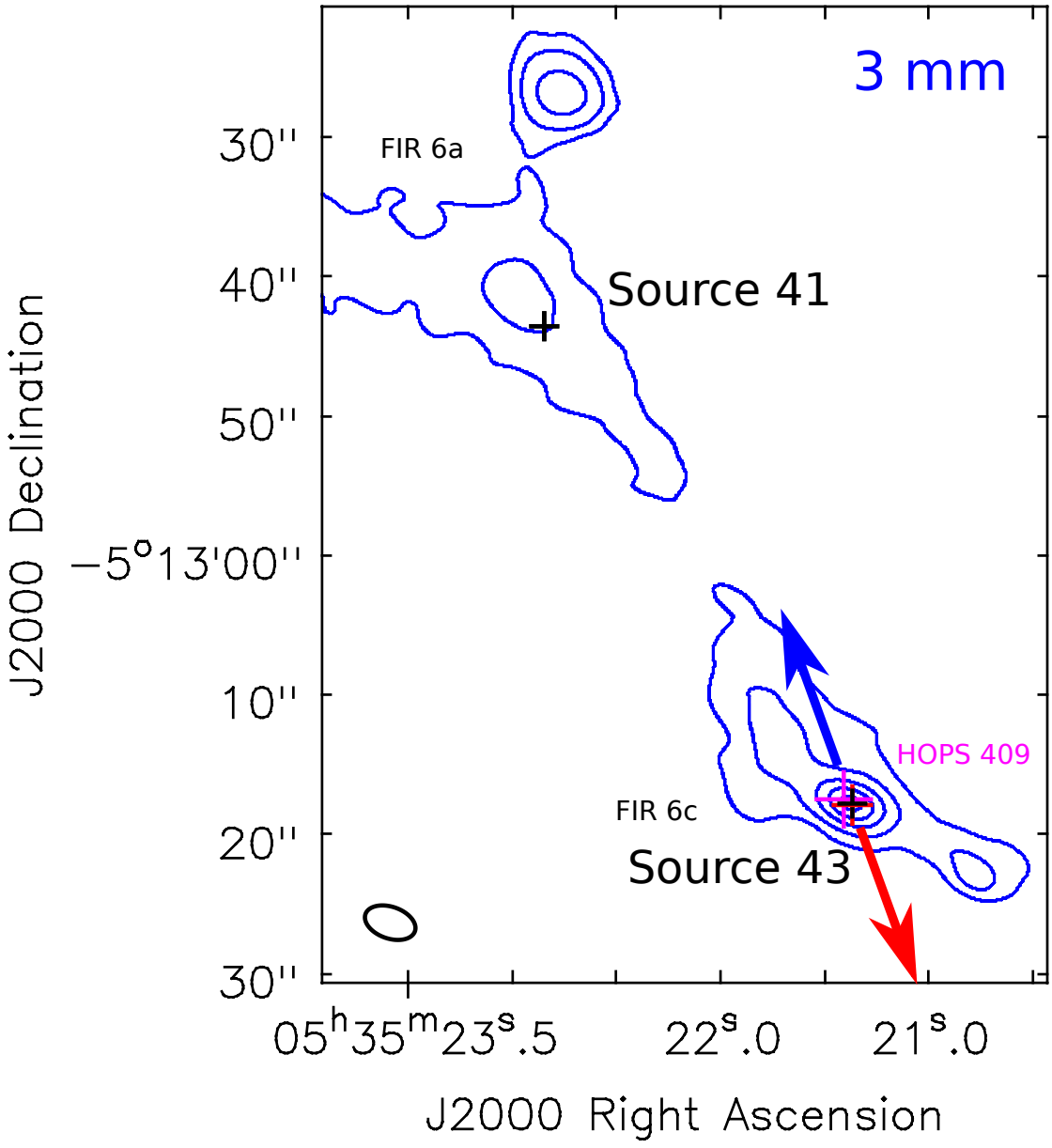

Figure 3.23 Sources 41 and 43. ALMA 3 mm map (contours, adapted from Kainulainen et al. 2017). Plus signs mark the radio sources (black, this work), the HOPS source (magenta, Furlan et al. 2016, derived at 4.5 μm), and the 9 mm/870 μm source (red, Tobin et al. 2020) in the region. FIR names are the millimeter peaks from Chini et al. (1997). Contour levels are 0.1, 0.2, 0.4, 0.65, and 0.9 times 12.0 mJy beam^{-1}, the peak of the FIR 6c 3 mm core. The synthesized beam is shown in the bottom left corner of the image. Source 41 seems to fall in projection very close to the path of the blue-shifted lobe of Source 43 outflow, whose direction is indicated by arrows (Shimajiri et al. 2008; Tobin et al. 2016c).

source HOPS 59 (Adams et al. 2012; Furlan et al. 2016), to which a CO outflow in the N-S direction (Shimajiri et al. 2009) and scattered light with an irregular morphology (Habel et al. 2020) have been previously associated. The 3 mm ALMA map shows that Source 42 is located toward the peak of a compact dust core (Kainulainen et al. 2017, see white contours in Fig. 3.24, left), indicating it is deeply embedded.

The source has a late K-M spectral type according to Hillenbrand (1997). Based on IR observations, Source 42 was classified as a YSO with a disk (Tsujimoto et al. 2002; Getman et al. 2017). This has been recently confirmed by Tobin et al. (2020), who imaged with ALMA at 870 μm a $\sim$ 100 au elongated structure that can be a dust disk (source HOPS-59-A in their nomenclature; see Fig. 3.2).

Our 5 cm high-resolution map shows a clearly elongated source at P.A. = 11$\pm$7° (see Fig. 3.24, right), consistent with the direction of the outflow and nearly perpendicular to the proposed dust disk (Tobin et al. 2020). We find a spectral index $\alpha = -0.3 \pm 0.5$ (Table 3.3). Although with large uncertainty, it could be consistent with thermal free-free emission. Also, the source follows the Anglada correlation with $L_{\rm bol}$ (see Section 3.4.1) suggesting that it is a radio jet. Therefore, we propose that Source 42 is the driving source of the outflow seen at larger scales.

The SED of the source has been modeled as a binary by Adams et al. (2012) and as a single object with a flat-spectrum by Furlan et al. (2016). There is observational evidence supporting that Source 42 belongs to a binary system since it is located $\sim 2\farcs5$ from the optical variable NSV 16490, which we do not detect at cm wavelengths (see Fig. 3.24, left). Furthermore, Gaia Collaboration et al. (2018) reported consistent distances of 421 ± 23 pc for NSV 16490 and 387 ± 18 pc for Source 42.

The star NSV 16490 has been detected from optical to mm wavelengths (Gaia Collaboration et al. 2018; Hillenbrand 1997; Nielbock et al. 2003; source HOPS-59-B in Tobin et al. 2020), being always less bright than Source 42. Therefore, the greater contribution to the observed SED (Adams et al. 2012; Furlan et al. 2016), probably measuring the flux from both components, would be from Source 42.

3.4.2.24 Source 45

Source 45, previously reported at 5 cm by Kounkel et al. (2014), is located toward the border of the ISF, $\sim 21''$ from its ridgeline (see Fig. 3.1), and is not associated with any 3 mm compact dust core (Kainulainen et al. 2017). We detect this source

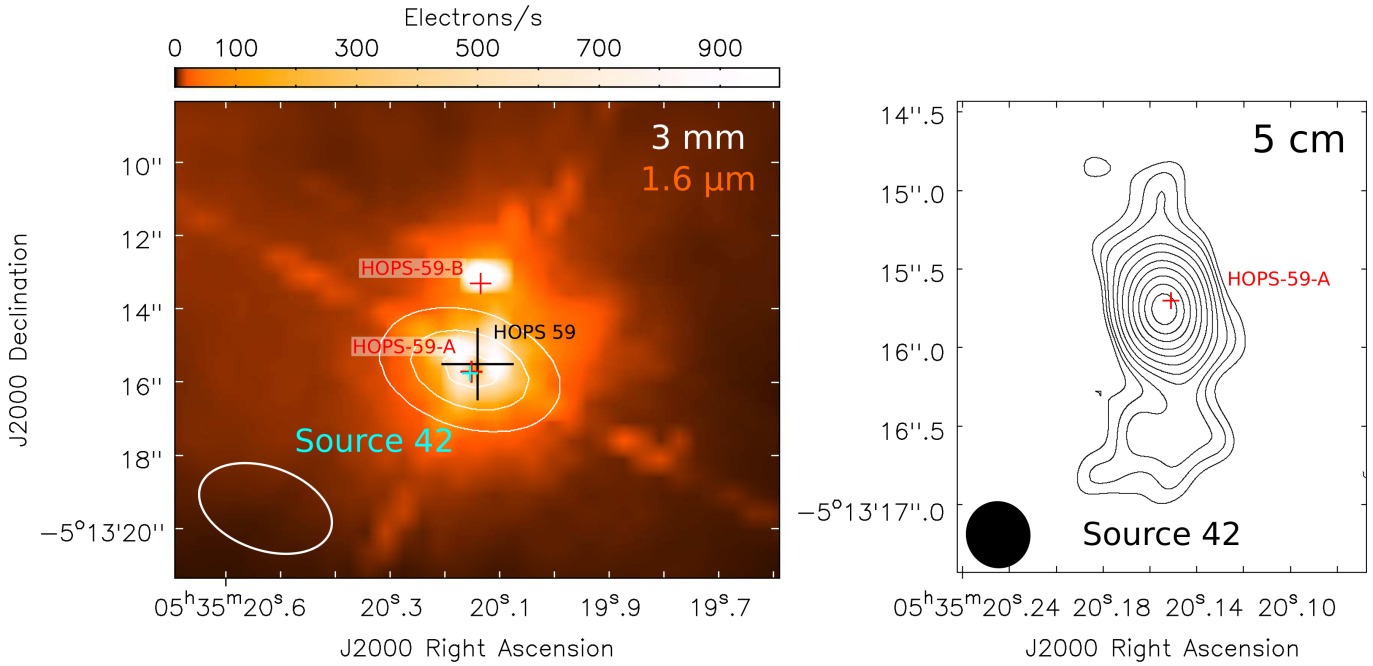

Figure 3.24 Source 42. *Left*: ALMA 3 mm map (contours, Kainulainen et al. 2017) overlaid on the HST 1.6 μm image (color scale, Habel et al. 2020). Plus signs mark the radio source (cyan, this work), the HOPS source (black, Furlan et al. 2016, derived at 4.5 μm), and the 9 mm/870 μm sources (red, Tobin et al. 2020) in the region. Contour levels are 0.3, 0.6, and 0.9 times 22.6 mJy beam^{-1}, the peak of the 3 mm map. *Right*: VLA 5 cm A-configuration map with natural weighting. Contour levels are −3, 3, 4, 5, 7, 9, 12, 16, 20, 25, 30, and 35 times 7.6 μJy beam^{-1}, the rms of the map. In both panels, the synthesized beams (VLA: filled, ALMA: outlined) are shown in the bottom left corner. The elongation of Source 42 is consistent with the N-S outflow associated with it (Shimajiri et al. 2009).

at 5 cm with a slight NE-SW elongation and, comparing our flux density with the one reported by Kounkel et al. (2014), we see signs of radio variability (see Table 3.3 and Fig. 3.3).

Based on its near and mid-IR emission (see Table 3.4 for the counterparts), Tsujimoto et al. (2002) classified this source as a Class II YSO, while Getman et al. (2017) as a Class III. The source has an M spectral type according to Hillenbrand et al. (2013) and could be a member of a multiple system since the brown dwarf TKK 738 and the IR variable V2401 Ori (none of them detected in our observations) lie $\sim 5''$ (~ 2100 au) in projection from the radio source. Gaia Collaboration et al. (2018) reported a distance of 348 ± 36 pc for this source, which is slightly closer than the reported distance to this part of Orion (386 ± 3 pc, Kounkel et al. 2018). Additionally, Kounkel et al. (2018) classified the source as a field star that does not belong to any of the clusters identified by them in Orion A. Therefore, there is a possibility that this source could be a foreground star.

3.4.2.25 Source 46 (HOPS 57)

This source is located toward the densest part of the ISF (Fig. 3.1) and is associated with the far-IR and flat spectrum source HOPS 57 (Furlan et al. 2016; see Table 3.4 for the counterparts) and with scattered light with an irregular morphology (Habel et al. 2020). Furthermore, the source coincides with the peak of a 3 mm compact dust core (Kainulainen et al. 2017, Fig. 3.25), suggesting it is deeply embedded. Additionally, Tobin et al. (2020) detected with ALMA at 870 μm with $\sim 0\farcs11$ resolution, an elongated structure that appears to be a circumstellar dust disk (see Fig. 3.2). They also detected 9 mm emission with VLA (0.53 ± 0.02 mJy), which, together with our flux density at 5 cm (Table 3.3), allow us to derive a positive spectral index $\alpha = 0.5 \pm 0.1$ for this source, consistent with thermal free-free emission. Source 46 could have a companion since it is separated $\sim 1''$ (~ 400 au) in projection from the near-IR variable and optical star V2359 Ori (Kounkel et al. 2016; Samus et al. 2017; Gaia Collaboration et al. 2018; Tobin et al. 2020), which we do not detect in our observations.

3.4.2.26 Source 47

Source 47, previously reported at 5 cm by Kounkel et al. (2014), is located toward the border of the ISF, $\sim 14''$ from its ridgeline (see Fig. 3.1), and is not associated with any 3 mm compact dust core (Kainulainen et al. 2017). Based on its near and

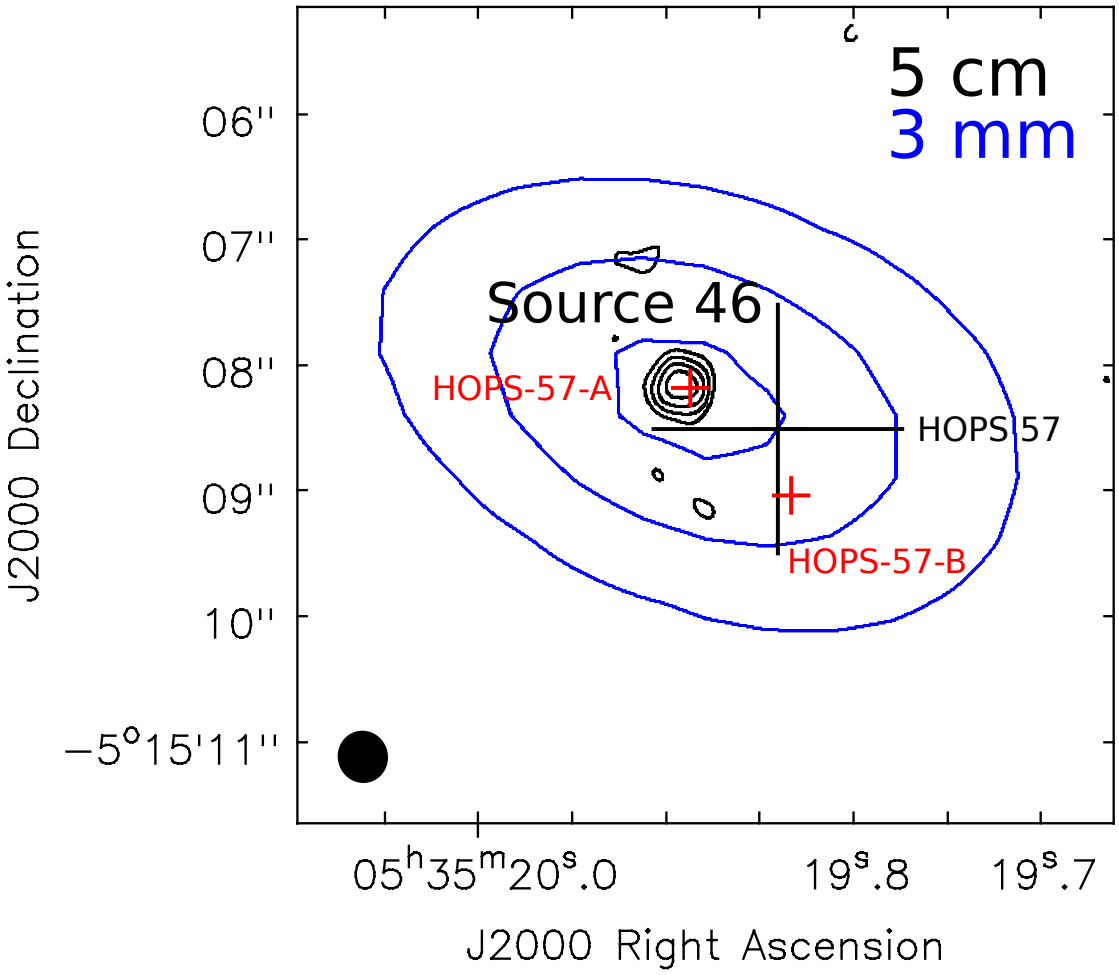

Figure 3.25 Source 46. VLA 5 cm A-configuration map with natural weighting (black contours) overlaid on the ALMA 3 mm map (blue contours, adapted from Kainulainen et al. 2017). Plus signs mark the HOPS source (black, Furlan et al. 2016, derived at 4.5 μm) and the 9 mm/870 μm sources (red, Tobin et al. 2020) in the region. Black contour levels are -3, 3, 4, 5, and 6 times 23 μJy beam^{-1}, the rms of the 5 cm map. Blue contour levels are 0.3, 0.6, and 0.9 times 9.2 mJy beam^{-1}, the peak of the 3 mm core. The VLA synthesized beam is shown in the bottom left corner of the map. The 3 mm ALMA synthesized beam (HPBW) is $3\farcs8 \times 2\farcs3$, P.A. = 71°.

mid-IR emission (see Table 3.4 for the counterparts), the source has been classified as a Class III YSO (Getman et al. 2017) with a spectral type K (Hillenbrand 1997). Gaia Collaboration et al. (2018) reported a distance of 378 ± 9 pc, confirming its association with the star-forming region.

We cannot constrain the spectral index from the 5 cm observations. However, the source was recently detected at 9 mm with a flux density of 1.13 ± 0.12 mJy (Tobin et al. 2020). Using this value, together with the flux densities shown in Fig.

3.3, we derive a spectral index $\alpha = -0.05 \pm 0.03$, which is consistent with optically thin thermal emission. On the other hand, the source is marginally resolved in our high-resolution 5 cm map, with an elongation in the NE-SW direction (Fig. 3.2). This elongation could be caused by the detection of an unresolved binary system and higher angular resolution observations would be needed in order to resolve the components. Assuming that the elongation is real, we rule out the case that we are detecting a radio jet since the source is strong and those are expected to be weak in evolved YSOs. Instead, we suggest that we are detecting free-free emission coming from disk photoevaporation. Further observations, such as the detection of optical and mid-IR forbidden line emission (Font et al. 2004; Alexander et al. 2014), should be carried out to confirm this claim.

3.5 Summary and conclusions

In this Chapter we extended the study carried out in Chapter 2 to the whole field of view of those observations, a region of 12.′5 of diameter, comprising the southernmost 2.′5 of the OMC-3 region and the whole OMC-2 region.

We detect 47 radio sources, 23 of them for the first time, in addition to the 10 radio sources already reported in Chapter 2. For these 47 radio sources, we report the positions, flux densities, and spectral indices, and discuss their nature by analyzing complementary information (i.e their radio spectral index, morphology, emission at other wavelength ranges, position relative to the ISF, association with dust clumps). Out of the 47 radio sources discussed in this Chapter, 12 have previous high-resolution detections of thermal emission from dust attributed to the presence of a circumstellar disk (Tobin et al. 2020). For these cases, our high-resolution detection of free-free emission allows us to establish a complete picture of these potential jet/disk systems.

Our main conclusions are:

1. Out of the 57 total radio sources in the field of view, 41 (72%) are very likely associated with the star-forming region, and 6 are extragalactic background sources. We are unsure about the association with the star-forming region of the remaining 10 sources. Of the 41 sources associated with the star-forming region, 36 are tracing the position of YSOs, 3 are tracing non-thermal emission from jet knots, one is tracing the shock-ionized wall of an outflow cavity, and one could be either a YSO or a jet knot.

2. Most of the radio continuum sources are detected toward the Integral Shaped Filament (ISF), as expected if they were associated with YSOs. In general, the radio sources associated with YSOs previously classified as the youngest objects (Class 0/I) are located toward the densest part of the ISF, while the ones associated with more evolved YSOs (Class II/III) are located toward the border or outside the ISF.

3. Interestingly, there are several radio sources distributed in a stripe nearly perpendicular to the ISF. Most of them have known counterparts at other wavelengths and approximately half of them have been previously classified as Class II/III objects. Since the ISF has been observed to be composed of velocity-coherent fibers, some of which deviate from the large-scale alignment, we suggest that the YSOs observed in this stripe have formed in perpendicular fibers whose material has already been depleted.

4. Through their continuum emission, we have unambiguously identified the position of the driving source of all the previously reported molecular outflows in our field of view (namely sources 1, 9, 11, 25, 34, 39, 42, and 43, in addition to VLA 11, discussed in Chapter 2). We propose these sources as radio jets, and in the case of Source 1, Source 11, Source 25, and Source 42, we indeed see their well-collimated morphology.

5. Using our radio data, complemented with other data from the literature, we verified that the observed radio emission of all but four of the 31 HOPS far-IR sources located within our field of view is consistent with the previously known empirical correlation between radio and bolometric luminosities. This correlation is usually interpreted as a consequence of the connection between accretion (traced by the bolometric luminosity) and outflow (traced by the radio continuum). For the four sources that are radio-underluminous with respect to this correlation, we suggest that either the ionization mechanism is less efficient or that they have important contributions to the bolometric luminosity other than accretion. Since three of these sources (HOPS 64, 108, and 369) are located in the proximity of the shocked region near the edge of the blue lobe of the HOPS 370 outflow, we suggest that external heating from this shocked region could have an important contribution to the bolometric luminosity of these objects.

6. Only six of the HOPS sources within our field of view (HOPS 60, 71, 78, 368, 394, and 409) are associated with molecular outflows for which the momentum rate has been estimated. For all of these sources, the radio luminosity is roughly consistent with the established correlation between these two parameters.

7. Although, in general, the nature of the radio emission from evolved YSOs (Class II/III) is non-thermal, we find two Class III YSOs (Source 27 and Source 47) where we favor a free-free nature for the observed radio emission. We suggest that this emission could result from disk photoevaporation.

8. We find signs of radio variability for 13 out of 53 radio sources, and most of them are evolved YSOs (Class II/III). Remarkably, sources 1, 11, and 34, which are very young (Class 0/I), show high variability in radio, which deserves further investigation. Interestingly, seven of these radio variables are also variables at shorter wavelengths (near-IR/optical/X-ray).

9. We investigate the multiplicity of our sample in a range of projected distances between 154 (our angular resolution) and 3000 au. If we consider only our detected radio sources, we identify 7 possible binary systems and none higher-order system. Taking into account additional known objects in the field of view detected at other wavelengths, then we detect radio components of 17 potential multiple systems: 11 binary systems, two triple systems, three quadruple systems, and one quintuple system. Further analysis, e.g., proper motion studies, will be necessary to determine if these are indeed gravitationally bound systems.

10. We believe our study to be the most sensitive carried out until now in a significant fraction of Orion at wavelengths of a few centimeters, where free-free emission dominates. It shows the potential of this type of study at μJy sensitivity, which will be routine for the next generation of radiointerferometers, such as the ngVLA and SKA. In this sense, this work can be considered a pathfinder for the upcoming surveys, which will have even more sensitivity and angular resolution, further revealing the complexity of crowded star-forming regions.

Chapter 4

Disks in the Young Close Binary System SVS 13

4.1 Introduction

Although most stars belong to binary systems (Leinert et al. 1993; Raghavan et al. 2010; Duchêne, & Kraus 2013), the way in which such systems form still remains poorly known, especially in the first stages of the process. Two main different mechanisms have been suggested for binary formation, namely disk fragmentation (e.g., Bonnell 1994; Bonnell, & Bate 1994a,b; Kratter et al. 2010) and the large-scale fragmentation of cores and filaments, either without turbulence (Matsumoto & Hanawa 2003), with turbulent fragmentation (e.g., Padoan & Nordlund 1999; Offner et al. 2010), or the formation of binaries in a cluster (Bate 2012). Although several observational studies have investigated which mechanism is dominant (e.g., Tobin et al. 2018), the debate is not yet settled.

Besides the investigation of the fragmentation mechanism, a fundamental issue is to investigate the evolution of the binary during the formation process, as this process determines not only the final stellar masses, but also the formation of disks and, consequently, the formation of planets (e.g., Bate & Keto 2015; Bate 2018). Key issues are to study the evolution of the separation between components and the evolution of the mass ratio. The specific angular momentum of the system and its evolution during the process of binary formation determines whether circumstellar disks will form preferentially around the primary, the secondary, or both (Bate, & Bonnell 1997). A large angular momentum is also decisive for the formation of a circumbinary disk. In this respect, recent work suggests that if

planet formation takes place in circumbinary disks, it can favor the formation of large-gaseous planets.

In order to shed light on all these issues, it is fundamental to carry out in-depth studies of the earliest stages of this process, i.e., to study protobinary/multiple systems. Binaries with separations $\sim$ 1000 au are called wide binaries and are attributed to core fragmentation, while those with separations of $\sim$ 100 au are in the boundary between wide and close binaries. In the latter, the interaction between the two stars affects their evolution. This is particularly relevant when the two stars have different initial properties. Thus, protobinaries with separations of the order of 100 au or less, whose observation is currently achievable with the resolution of the large radio interferometers, are excellent targets to study their properties and to compare them with those predicted by numerical simulations. So far, only for a few of these systems there is available (but partial) information about their physical properties, such as temperatures, kinematics (from radial velocities and proper motions), presence of circumbinary disks, stellar and disk masses (from dust and molecular emission and from dynamics), chemical properties, interaction with the surrounding medium (e.g., outflows and interaction with the ambient molecular cloud, flyby encounters and tidal interaction with nearby young stars). Among them, L1551 IRS5 (Rodríguez et al. 1998), L1151 NE (Takakuwa et al. 2017), GG Tau (Phuong et al. 2020), BHB2007 (Alves et al. 2019), UX Tau (Zapata et al. 2020), IRAS 16293−2422 (Maureira et al. 2020a) have been partially studied.

A particularly remarkable case is SVS 13, the proposed exciting source of the HH 7-11 system (Strom et al. 1976). SVS 13 is a nearby (d = 300 pc) optically visible star (e.g., Eisloeffel et al. 1991) but also a strong mm source (e.g., Looney et al. 2000). VLA 3.6 cm observations (Anglada et al. 2000) revealed that SVS 13 is a close binary system, with the two components (VLA 4A and VLA 4B) separated in projection by 0$''$.3 (90 au). Further observations (Anglada et al. 2004) revealed that only one of the components, VLA 4B, presents a strong 7 mm emission, that was attributed to dust. These results were interpreted as that the development of a protoplanetary disk occurs preferentially in one of the components, with the disk being much weaker in the other component. In this Chapter, we present new VLA and ALMA results that, combined with recent GAIA DR2 astrometry, shed new light on this system.

4.2 Observations and Data Reduction

We present continuum observations in the 0.7 - 3 cm (10 - 43 GHz) range carried out with the Karl G. Jansky Very Large Array (VLA) of the National Radio Astronomy Observatory (NRAO), as well as continuum and line observations at 0.9 mm (333 GHz) taken with the Atacama Large Millimeter/submillimeter Array (ALMA). All the maps presented in this work have been corrected by the primary beam response.

4.2.1 VLA Continuum Observations

The VLA observations were carried out as part of Project 15A-260 in the B configuration at Ka (0.9 cm) and Q (0.7 cm) bands on 2015 February 14 and March 7, respectively, and in the A configuration at X (3 cm), K (1.3 cm), Ka, and Q bands on 2015 June 28, June 27, July 7, and June 20, respectively. Data at X band had poor quality, and the observations at this band were repeated in the A configuration on 2016 November 22 as part of DDT 16B-417. The results presented in this paper at X band are obtained using only the DDT 16B-417 data.

The bandwidth was 4 GHz at X band, and 8 GHz at K, Ka, and Q bands. The phase center was at coordinates α(J2000) = $03^{\rm h}29^{\rm m}3\overset{\rm s}{.}75$, δ(J2000)=+31°16′3″.90 in all observations. Calibrators used were J0137+3309 (3C48) for absolute flux and bandpass in X band, and for absolute flux in K and Ka bands, J0542+4951 (3C147) for absolute flux in Q band, J0319+4130 for bandpass in K, Ka, and Q bands, and J336+3218 for complex gain in all bands. The time expended on source in A configuration was 16.48 min at Q band, 23.58 min at Ka band, 39.72 min at K band, and 39.23 min at X band, while in B configuration was 20.43 min at Q band and 21.68 min at Ka band.

The data were edited and calibrated using the Common Astronomy Software Applications package (CASA) version 4.3.1. Images were made with the task CLEAN of CASA version 4.6.0. The synthesized beams range from $\sim 0\overset{''}{.}20$ (X band) to $\sim 0\overset{''}{.}06$ (Q band) and the rms noise from 6 μJy beam^{-1} to 23 μJy beam^{-1}, respectively (see Fig. 4.1). A Ka-band map made by combining A and B configuration data (beam $\simeq \sim 0\overset{''}{.}14$ and rms = 10 μJy beam^{-1}) is shown in Figure 4.3.

4.2.2 ALMA Continuum and Line Observations

The ALMA observations were carried out in Band 7 (0.9 mm) as part of the projects 2015.1.01229.S (Cycle 3) and 2016.1.01305.S (Cycle 4), with a requested angular resolution of $\sim 0''.1$ and $\sim 0''.3$, respectively. Data from Cycle 3 were obtained during two identical runs on 2016 September 9 and 10, with 36 antennas operating with baselines ranging from 15 m to 3247 m. The total time spent on source was 1.6 h. The precipitable water vapor was 0.44 mm and 0.41 mm, during the first and second day of observations, respectively. Data from Cycle 4 were obtained on 2016 November 24, with 40 antennas operating with baselines ranging from 15 m to 704 m. The time on source was 4.15 min and the precipitable water vapor was 0.63 mm. In all cases, the calibrators J237+2848, J238+1636, and J336+3218 were used for bandpass, absolute flux, and complex gain calibration, respectively.

In the Cycle 3 observations, the correlator was configured with one baseband set to low spectral resolution continuum mode, and three basebands set to high spectral resolution line mode. Each line baseband was subdivided into two equal spectral windows of 0.234 GHz bandwidth. The continuum baseband was centered at 333 GHz and had 1.875 GHz of bandwidth. The line spectral windows were centered on ^{13}CO (3-2) at 330.587965 GHz, SO_2 (11-12) at 331.580244 GHz, CS (7-6) at 342.882857 GHz, HC^{15}N (4-3) at 344.200109 GHz, H^{13}CN (4-3) at 345.339756 GHz, and ^{12}CO (3-2) at 345.795990 GHz. The channel width was 0.1058 km s^{-1} (0.122 MHz) for the CO spectral windows, 0.212 km s^{-1} (0.244 MHz) for H^{13}CN, CS, and SO_2, and 0.426 km s^{-1} (0.488 MHz) for the HC^{15}N spectral window. The line free-channels of the line spectral windows (totaling ~ 0.3 GHz) were aggregated to the continuum bandwidth.

In the Cycle 4 observations, the correlator was configured with three basebands set to low spectral resolution continuum mode and one set to high spectral resolution line mode. Continuum basebands had 1.875 GHz of bandwidth each and were centered at 331.5, 333.5, and 344.0 GHz. The high spectral resolution baseband was centered on ^{12}CO (3-2) at 345.795990 GHz, with a channel width of 0.426 km s^{-1} (0.488 MHz) and 0.9375 GHz bandwidth.

After the standard calibration, the highest angular resolution continuum data from Cycle 3 were phase-only self-calibrated to increase the signal to noise ratio. We used two rounds in which the solutions were found in intervals that spanned the entire scan length (first round) and 6.05 s, which is the length of a single integration (second round). The self-calibration solutions were applied to the

spectral line data and the continuum emission was subtracted. Natural weighting maps were obtained with a synthesized beam of $0\farcs17 \times 0\farcs08$, P.A. $= -2.29°$, and rms of 0.9 mJy beam^{-1} for the continuum, and 2 - 3.5 mJy beam^{-1} per channel (depending on the spectral window) for the line maps (cubes). Self-calibrated Cycle 3 data were concatenated with standard-calibrated Cycle 4 data, and we followed the same steps to self-calibrate the whole measurement continuum data set. A continuum natural weighting map was obtained with a synthesized beam of $0\farcs18 \times 0\farcs09$, P.A. $= -1.98°$ and rms of 0.15 mJy beam^{-1}. In our discussion, we use the map obtained with only the Cycle 3 data which has a similar rms and a slightly better angular resolution. For both self-calibration and imaging, CASA version 4.5.2 was used. The images were made using the CLEAN task of CASA.

4.3 Results and Discussion

4.3.1 VLA Results: Binary Protostars Traced by the Ionized Gas

Figure 4.1 shows the VLA A-configuration maps obtained in 2015 - 2016 of the continuum emission toward SVS 13, at 3, 1.3, 0.9, and 0.7 cm. The two compact sources previously identified as VLA 4A (the western one) and VLA 4B (the eastern one) by Anglada et al. (2000, 2004) and by Tobin et al. (2016b) are detected at all the observed wavelengths. The two sources are separated by $\sim 0\farcs30$ (90 au in projection at a distance of 300 pc). The sources appear compact, although there is a hint of weak emission, which is more evident at X and Ka bands, connecting the two sources. As noted previously by Anglada et al. (2004), source VLA 4B is significantly stronger than VLA 4A at 7 mm, while at longer wavelengths the difference in the observed intensities of the two sources is less significant (see further discussion in Section 4.3.3).

In the figures, we plot the optical position of the star SVS 13 as obtained from GAIA DR2 (Gaia Collaboration et al. 2018), corrected by the reported GAIA proper motions to the epoch of the VLA observations (a small correction of, at most, only $0\farcs023$) and converted to J2000 coordinates with the task ICRSToJ2000 of the CASA Extensions AnalysisUtils Python package. As can be seen in the figure, the optical position falls closer to VLA 4B than to VLA 4A. This is in agreement with the association of VLA 4B with the optically visible star SVS 13 made by Hodapp & Chini (2014) and Lefèvre et al. (2017) from the 2MASS astrome-

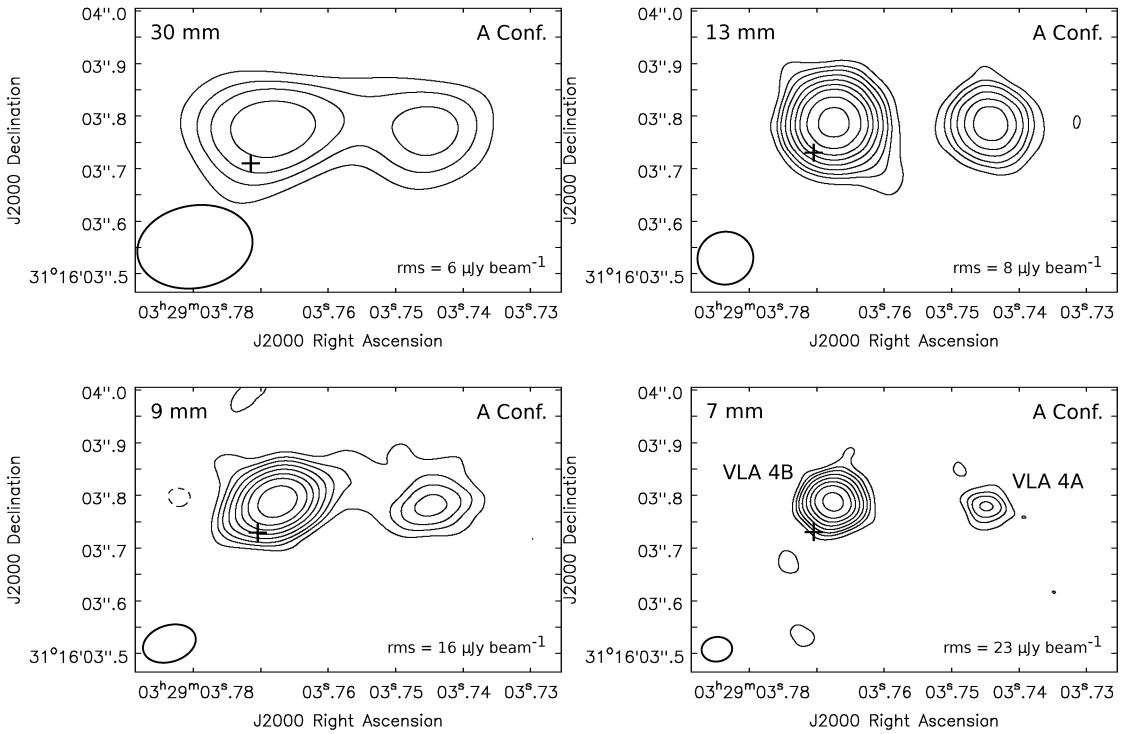

Figure 4.1 VLA images of SVS 13 at X (30 mm), K (13 mm), Ka (9 mm), and Q (7 mm) bands obtained with the A configuration. The plus sign marks the optical position of the star SVS 13 from GAIA DR2 (Gaia Collaboration et al. 2018) extrapolated to the epoch of the VLA observations (see Section 4.3.1). Contour levels are −3, 3, 5, 7, 10, 14, 19, 25, 35, 50, 70, and 95 times the rms of each map. The synthesized beams and the rms are shown in the bottom left and right corners, respectively, of the images. We used natural weighting for maps at K, Ka, and Q bands, and Briggs weighting with the robust parameter set to 0 for the map at X band. The synthesized beams are $0\farcs22 \times 0\farcs16$, P.A. $= -80.27°$ at X band; $0\farcs11 \times 0\farcs10$, P.A. $= -80.65°$ at K band; $0\farcs10 \times 0\farcs07$, P.A. $= -72.89°$ at Ka band; and $0\farcs06 \times 0\farcs05$, P.A. $= -83.40°$ at Q band.

try ($0\farcs1$ accuracy) and is in disagreement with the association of the optical star with VLA 4A made by Anglada et al. (2000) from the data of limited astrometric precision ($\sim 0\farcs3$) available at that time.

Source VLA 4A is closer to the densest part of the ambient cloud, as traced by the moderately angular resolution ($\sim 4''$) VLA ammonia images (Rudolph et al. 2001, Diaz-Rodriguez et al. in prep.; see Fig. 4.2). These images show that the ammonia emission extends preferentially toward the west, suggesting that the VLA 4A component of the binary could be a more deeply embedded object than VLA 4B, in agreement with the association of VLA 4B with the optical star.

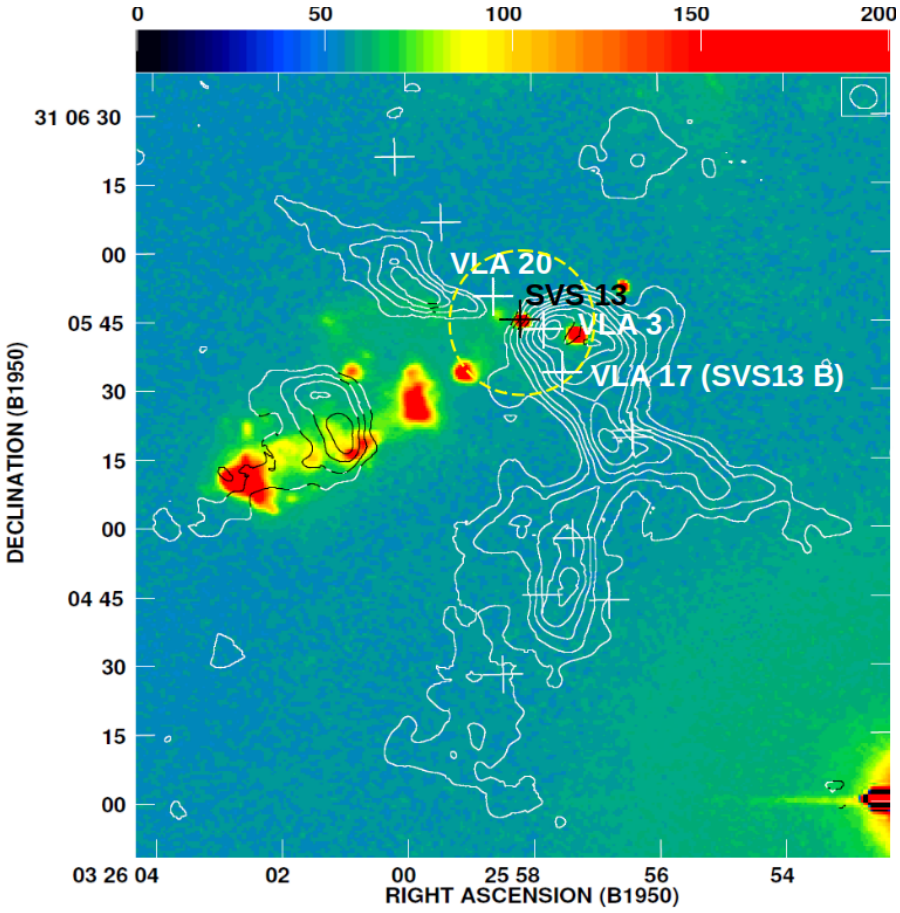

Figure 4.2 VLA map of the integrated ammonia (1,1) line emission (contours; Diaz-Rodriguez et al., in preparation), overlaid on an optical [S II] image of the HH 7-11 region (color scale) from Bally et al. (1996). The synthesized VLA beam is shown in the top right corner. The positions of the cm radio sources detected by Rodríguez et al. (1999) are marked with plus signs. The field of view of our ALMA observations is shown with a dashed-line yellow circle.

Nevertheless, we note that the coincidence between the optical and the radio position is not perfect (see Fig. 4.1 and Table 4.1). The discrepancy is $\sim 0\farcs07$, larger than the estimated astrometric uncertainty, which is $\sim 0\farcs01$ (see discussion in Section 4.3.1.1). Therefore, we should consider the possibility that the optically visible star SVS 13 and the radio source VLA 4B are indeed different objects. If this possibility were confirmed, the SVS 13 system would be a multiple system with at least three stellar objects. Further proper motion studies should be able to clarify this issue.

The VLA Ka-band image in Figure 4.1 also shows a hint of a SE elongation of the source VLA 4B, which is difficult to confirm since the beam is elongated in

Table 4.1 Position of the Radio Sources

Epoch	Wavelength	VLA 4A		VLA 4B		
(yr)	(mm)	RA(J2000)[a]	Dec(J2000)[a]	AR(J2000)[a]	Dec(J2000)[a]	Ref.
1989.04	36	03 29 03.730±0.002	31 16 04.02±0.02	03 29 03.751±0.002	31 16 04.08±0.02	1
1994.31	36	03 29 03.730±0.002	31 16 03.95±0.02	03 29 03.758±0.004	31 16 04.01±0.02	1
1996.98	36	03 29 03.731±0.002	31 16 03.94±0.02	03 29 03.757±0.002	31 16 04.01±0.02	1
1998.32[b]	36	03 29 03.7376±0.0017	31 16 03.957±0.026	03 29 03.7575±0.0015	31 16 03.968±0.023	1, 6
1999.50	36	03 29 03.734±0.002	31 16 03.96±0.02	03 29 03.757±0.001	31 16 03.91±0.02	1
2001.34	7	03 29 03.7405±0.0020	31 16 03.95±0.03	03 29 03.7594±0.0008	31 16 03.937±0.012	2[c]
2002.29	13	03 29 03.7357±0.0015	31 16 03.935±0.022	03 29 03.7596±0.0011	31 16 03.914±0.016	3
2003.40	13	03 29 03.7386±0.0011	31 16 03.876±0.017	03 29 03.7609±0.0007	31 16 03.908±0.011	4
2014.56	9	03 29 03.7430±0.0007	31 16 03.790±0.010	03 29 03.7660±0.0007	31 16 03.810±0.010	5
2015.47	7	03 29 03.7448±0.0007	31 16 03.780±0.010	03 29 03.7676±0.0007	31 16 03.788±0.010	6
2015.49	13	03 29 03.7442±0.0007	31 16 03.785±0.010	03 29 03.7674±0.0007	31 16 03.788±0.010	6
2015.52	9	03 29 03.7455±0.0008	31 16 03.794±0.012	03 29 03.7676±0.0007	31 16 03.789±0.011	6
2016.69	0.9	03 29 03.7460±0.0007	31 16 03.769±0.010	03 29 03.7691±0.0007	31 16 03.761±0.010	6[d]
2016.89	30	03 29 03.7457±0.0010	31 16 03.771±0.015	03 29 03.7689±0.0008	31 16 03.775±0.012	6

[a] Positions derived from elliptical Gaussian fits. Uncertainties correspond to those of absolute positions, and are calculated by adding in quadrature a systematic error of $0''.01$ (for VLA data, Dzib et al. 2017) or $0''.005$ (for ALMA data, Remijan et al. 2020) to the formal error of the fit, $0.5\,\theta$/SNR (Reid et al. 1988). The systematic error accounts for uncertainties introduced by the phase calibration process and the error of the fit for those due to the source size (θ) and signal-to-noise ratio (SNR).

[b] From a map made concatenating data from epochs 1998.24 and 1998.40 reported in Anglada et al. (2000) and Carrasco-González et al. (2008b).

[c] After recalibration of the originally published data.

[d] From a map made using baselines > 750 kλ, where the extended emission has been filtered out (Figure 4.7, bottom).

References — (1) Carrasco-González et al. (2008b); (2) Anglada et al. (2004); (3) G. Anglada, private communication; (4) C. Carrasco-Gonzalez, private communication; (5) Tobin et al. (2016b); (6) This work.

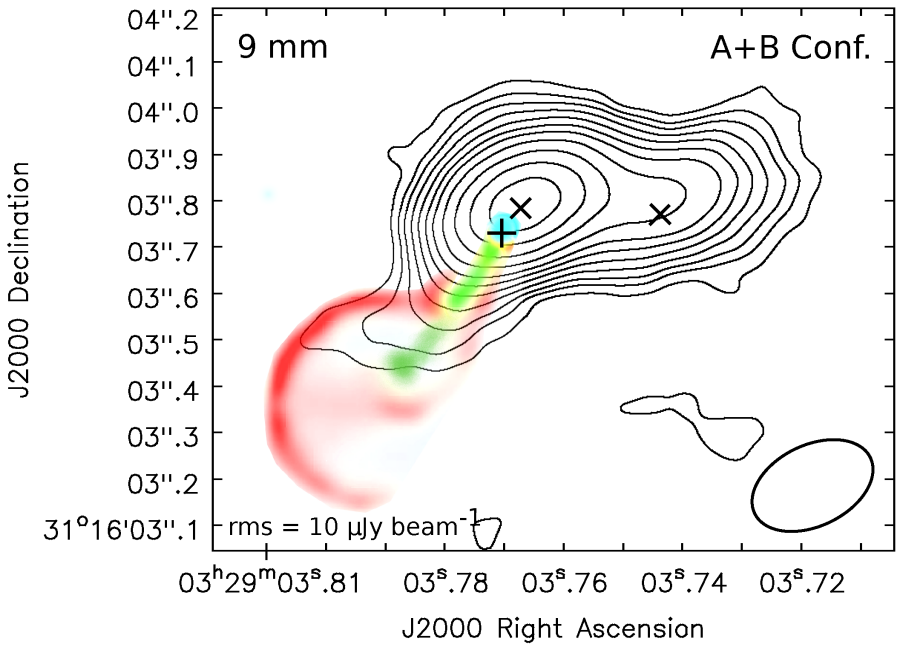

Figure 4.3 VLA image of SVS 13 at Ka band (9 mm) obtained from the concatenated data of the A and B configurations using natural weighting (beam = 0.″28 × 0.″18, P.A. = −64.3°), with an overlaid of Figure 3 (bottom) of Hodapp & Chini 2014, showing the bubble traced by H_2 S(1) (red) and the jet traced by [FeII] (green). The plus sign marks the optical position of the star SVS 13 from GAIA DR2 (Gaia Collaboration et al. 2018) extrapolated to the epoch of the Ka-band observations (see Section 4.3.1). The crosses mark the positions of the two radio sources. Note that the extension to the SE of the (free-free) radio emission traces the direction of the [FeII] jet, and possibly part of the NE wall of the H_2 S(1) bubble. Contour levels are −3, 3, 5, 7, 10, 14, 19, 25, 35, 50, 70, and 95 times the rms of the map. The synthesized beam and the rms are shown in the bottom right and left corners, respectively, of the image.

the same direction. However, in Figure 4.3 we show the Ka-band image obtained from the concatenated A+B configuration data. Although with a lower angular resolution, this image shows quite clearly an extension of the emission from the position of VLA 4B toward the SE. Interestingly, this SE protuberance coincides very well with the axis of the 0.″2 long [FeII] jet imaged by Hodapp & Chini (2014); this microjet pierces inside the first of a series of bubbles and fragments of bubbles traced in the H_2 1–0 S(1) line to the SE of SVS 13. A false-color image of the microjet and its associated bubble is overlaid on the contour map of the 9 mm emission shown in Figure 4.3. The IR and radio images were aligned by matching the IR emission of the SVS 13 star (in light blue in the image) with the GAIA DR2 optical position of SVS 13 corrected to the epoch of our VLA observations

(plus sign). Hodapp & Chini (2014) found evidence of expanding motion of the bubble, with its front end moving at a projected velocity of 20 mas yr^{-1}; since their image was obtained ~ 1.5 yr earlier than our VLA map, the actual size of the bubble at the epoch of our observations could be $\sim 0\farcs05$ larger than what is shown in the figure, which does not affect the accuracy of our comparison. Therefore, it seems that the 9 mm continuum emission of our observations traces the free-free emission of the ionized radio jet associated with the high excitation shock-excited [FeII] jet. Additionally, there is a hint that the 9 mm emission partially traces the NE edge of the bubble observed by Hodapp & Chini (2014) in the lower excitation emission of shock-excited H_2. Unfortunately, our A-configuration data alone are not sensitive enough to trace further details of this jet-bubble system, but additional, more sensitive VLA A-configuration observations could reveal with a high degree of detail the emission of the ionized material associated with this shock interaction, and trace the jet back to its origin to clarify if the optical/IR star SVS 13 is the same object as the radio source VLA 4B. Finally, we point out that there is high-velocity molecular gas associated with this and other bubbles traced by the CO data obtained simultaneously with the ALMA observations reported here and described in Section 4.2.2, which reveal outstanding kinematic information (Blázquez-Calero et al. in prep.).

4.3.1.1 Proper Motions

Proper motions of the radio sources in the region have been measured by Carrasco-González et al. (2008b) and by Lefèvre et al. (2017). There are VLA subarcsecond angular resolution data that separate the two components, VLA 4A and VLA 4B, for about 30 years, from which we can obtain more accurate proper motions and try to measure differences in the relative positions of the two sources that could trace orbital motions (or, at least, to constrain these motions). In Table 4.1 we list the positions of the sources obtained from the literature and from the data presented in this paper. In Figure 4.4 we plot the right ascension and declination coordinates of the two sources as a function of the epoch of observation, from 1989 to 2017. In addition to the cm VLA data we use the ALMA positions at 1.3 mm obtained from an image made using baselines > 750 kλ (Fig. 4.8) in order to minimize the contribution of the extended emission (see Section 4.3.2). Absolute proper motions are 12.3 ± 0.5 mas yr^{-1} at P.A. $= 138.3 \pm 2.4^\circ$ and 13.8 ± 0.4 mas yr^{-1} at P.A. $= 141.5 \pm 1.7^\circ$, for sources VLA 4A and VLA 4B, respectively. These values are in agreement with previous estimates (Carrasco-González et al. 2008b;

Lefèvre et al. 2017) within the uncertainties, but our values are more accurate and allow us to search for evidence of possible orbital motions.

Figure 4.4 shows a hint that the Declination of VLA 4B relative to VLA 4A decreases slightly with time (VLA 4B moving to the south relative to VLA 4A) at a rate of 1.6 ± 0.6 mas yr^{-1} (2.3 ± 0.9 km s^{-1}) with a total displacement of 48 ± 17 mas (14.4 au) in 30 yr, while the total displacement in Right Ascension is considerably smaller (12 ± 22 mas). Small differences in the positions of cm radio sources are difficult to measure because they usually trace free-free jets that can suffer apparent changes in the position because of the ejecta of new ionized knots. In this respect, positions obtained at Q band and shorter wavelengths (tracing the dust contribution of the disk) are more stable and provide more reliable proper motion measurements. This has been noticed, for example, in the well-studied Class 0 A1-A2 close binary of the IRAS 16293−2422 triple system, whose proper motions are affected by the positional changes due to ejecta of ionized knots at cm wavelengths, while data at shorter wavelengths appear more reliable (see discussion in Loinard et al. 2007; Hernández-Gómez et al. 2019; Maureira et al. 2020b). In the case of SVS 13, the plots in Figure 4.4 suggest that such an ejection event may have taken place around epoch 2000, resulting in a reversal of the positions of the two sources in the Declination axis. To partially overcome this problem, in Figure 4.5, we plot the positions of the two sources relative to the average position of VLA 4A as a function of time. Despite this anomaly, we consider that the currently available data show a trend in the relative proper motions, with the declination of VLA 4B moving to the south relative to VLA 4A. This result deserves further investigation and can be easily confirmed by future Q-band VLA and mm/sub-mm ALMA observations at high angular resolution.

If the observed trend in the differences between the proper motions of the two components VLA 4A and VLA 4B (with VLA 4B moving to the south relative to VLA 4A) is real, it would be indicative of counter-clockwise orbital motion in the plane of the sky as seen from Earth. Since the observed blue-shifted jet/outflow lobe points to the south, and assuming that its associated disk is roughly co-planar with the binary orbit, the head of the angular momentum vector points away from the molecular cloud, toward the observer. This is, we are observing the orbital motion from the head of the angular momentum vector. These results are in agreement with what is inferred from the ALMA data (see next sections).

We note that absolute proper motions can, in principle, inform about the relative masses of the two components in the binary, since the center of mass is closer

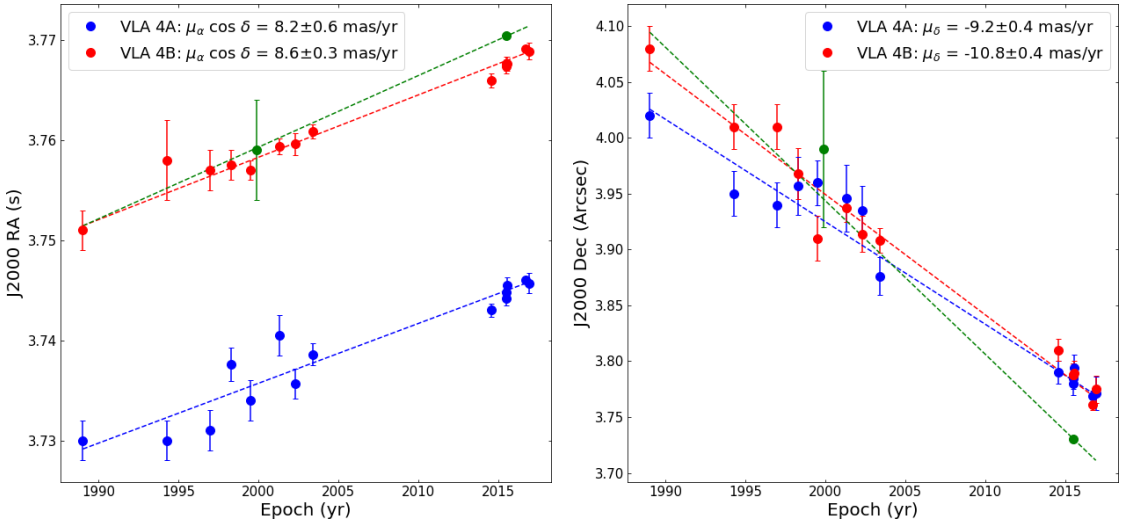

Figure 4.4 J2000 Right Ascension and Declination of the two radio components of SVS 13, VLA 4A (blue) and VLA 4B (red), as a function of the epoch of observation. The positions used in this plot are listed in Table 4.1. Proper motions are obtained through linear least-squares fits (dashed lines) to the radio positions. The near-IR 2MASS position [RA(J2000) = $03^h29^m03.759^s \pm 0.005^s$; Dec(J2000) = $31°16'03''.99 \pm 0''.07$, at epoch J1999.90; Skrutskie et al. 2006] and the optical GAIA DR2 position [RA(J2000) = $03^h29^m3.77040^s \pm 0.00003^s$; Dec(J2000) = $31°16'03''.7304 \pm 0''.0003$, at epoch J2015.5; Gaia Collaboration et al. 2018] are also plotted (green) as a reference. For consistency, the GAIA DR2 coordinates, originally referred to ICRS have been transformed to J2000 using the task ICRSToJ2000 of the AnalysisUtils Python package. The proper motions of the optical star, as reported in the GAIA DR2 catalog have been plotted as green dashed lines.

to the more massive component, and therefore the more massive component is expected to be the one that shows smaller absolute proper motions. However, when the system has a significant (unknown) overall proper motion, as is the case for the SVS 13 system, it is not possible to disentangle which is the component with the smaller proper motion relative to the center of mass, unless the data cover a significant fraction of the orbital period and the curvature of the motion around the center of mass can be directly observed. We note that this criterion was likely erroneously applied to the A1-A2 IRAS 16293−2422 binary to infer the relative masses of the binary components (Maureira et al. 2020b).

In Figure 4.4 we also plot, as a reference, the proper motions of the optical position of the SVS 13 star reported by GAIA (green dotted line), together with the GAIA position (epoch 2015.5) and the 2MASS IR position (epoch 1999.90); this last position is consistent with the GAIA proper motions but the

2MASS positional errors are large and the agreement is not significant enough. Compared with the radio proper motions of VLA 4B [$(\mu_\alpha \cos\delta,\ \mu_\delta) = (8.6 \pm 0.3,\ -10.8 \pm 0.4)$ mas yr^{-1}], we note that the GAIA DR2 proper motions of SVS 13 [$(\mu_\alpha \cos\delta,\ \mu_\delta) = (10.75 \pm 0.75,\ -13.76 \pm 0.63)$ mas yr^{-1}] are quite different, resulting in a significant difference of 2.2 ± 0.8 mas yr^{-1} in RA and 3.0 ± 0.7 mas yr^{-1} in Dec, which is larger than the dispersion in proper motions in the whole NGC 1333 region, 0.92 ± 0.05 mas yr^{-1} in RA and 0.60 ± 0.03 mas yr^{-1} in Dec, as estimated by Ortiz-León et al. (2018). Thus, the observed difference in proper motions between VLA 4B and the optical star SVS 13 is compatible with the two being independent objects belonging to the same molecular cloud. Unless the uncertainties of the proper motions quoted by GAIA are severely underestimated, this suggests that these two sources could be tracing different objects.

In summary, both the positions and the proper motions give support to the possibility that the optical star SVS 13 could be a different object than VLA 4B. If this were the case, this result could account for the observed anomalies in the inferred properties of SVS 13, which has been classified either as a very young Class 0/I object (e.g., Bachiller et al. 2000) to a more evolved PMS star (e.g., Aspin 2003). However, the current uncertainties are still large and this result needs to be confirmed with better data.

4.3.2 ALMA Continuum Results: Circumstellar and Circumbinary Dust

Figure 4.6 illustrates the ALMA field of view (FWHM of the primary beam = 18″, centered on SVS 13), which roughly corresponds to the yellow circle in Figure 4.2. The continuum emission at 0.9 mm is shown in white contours, overlaid on the CO (3-2) line emission (color scale) at $V_{\rm LSR} = +10.2$ km s^{-1}, a velocity slightly red-shifted with respect to the systemic velocity ($V_{\rm sys} \simeq +8.5$ km s^{-1}; e.g., Rudolph et al. 2001), where the extended emission of the ambient molecular cloud impedes a proper imaging. The field of view encloses the continuum emission from the SVS 13 binary, which stands out prominently as the strongest and more extended source near the center of the field, but also dust emission from the nearby YSOs VLA 20, VLA 3, and VLA 17 (MMS 2 = SVS 13B). Although the Class 0 object MMS 2 has been considered in the past a (wide) binary companion of SVS 13 (e.g., Bachiller et al. 2000; hence its alternative name, SVS 13B), at first glance, there is not a direct connection between these two objects in the continuum emission

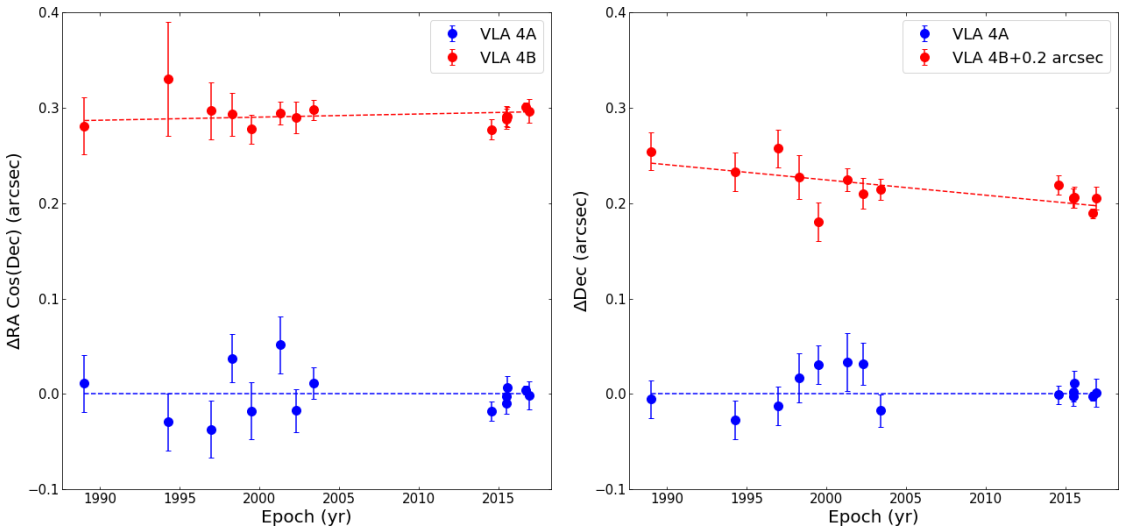

Figure 4.5 J2000 Right Ascension and Declination of the two radio components of SVS 13, VLA 4A (blue) and VLA 4B (red), relative to the average position of VLA 4A, derived from the proper motion fit (Fig. 4.4), as a function of the epoch of observation. An offset of 0.″2 has been added to the difference in declination for improved visualization. The figure is intended to better illustrate the relative motion between the two sources using a co-moving reference system that is reasonably independent of sudden changes in the position of one of them (e.g., produced by possible ejecta events). Sudden positional changes (possibly in source VLA 4A around epoch 2000) in any of the two sources are more easily identifiable with respect to average motions. Most preferably, the center of masses would be used as a reference, but it is not known in this case; the selection of VLA 4A instead of VLA 4B is arbitrary.

map, neither with the remaining objects, which indeed are closer to SVS 13. The CO emission image, instead, is suggestive of a possible connection of SVS 13 with VLA 20 through an arcuate feature, at $V_{\rm LSR} = 10.2$ km s^{-1}, which is reminiscent of a flyby tidal interaction. In this Chapter, we focus our discussion on SVS 13, while the discussion on the remaining sources is mainly deferred to a forthcoming paper (Diaz-Rodriguez et al., in prep.).

Figure 4.7 shows a close-up toward SVS 13 of the 0.9 mm continuum imaged with ALMA. The image shows two strong emission peaks, coincident with the sources VLA 4A and VLA 4B, surrounded by extended emission in the form of spirals that apparently converge mainly toward the position of source VLA 4A. We interpret the two compact emission peaks as tracing circumstellar disks of dust associated with the two protostars, VLA 4A and VLA 4B, at scales $\lesssim$ 0.″2.

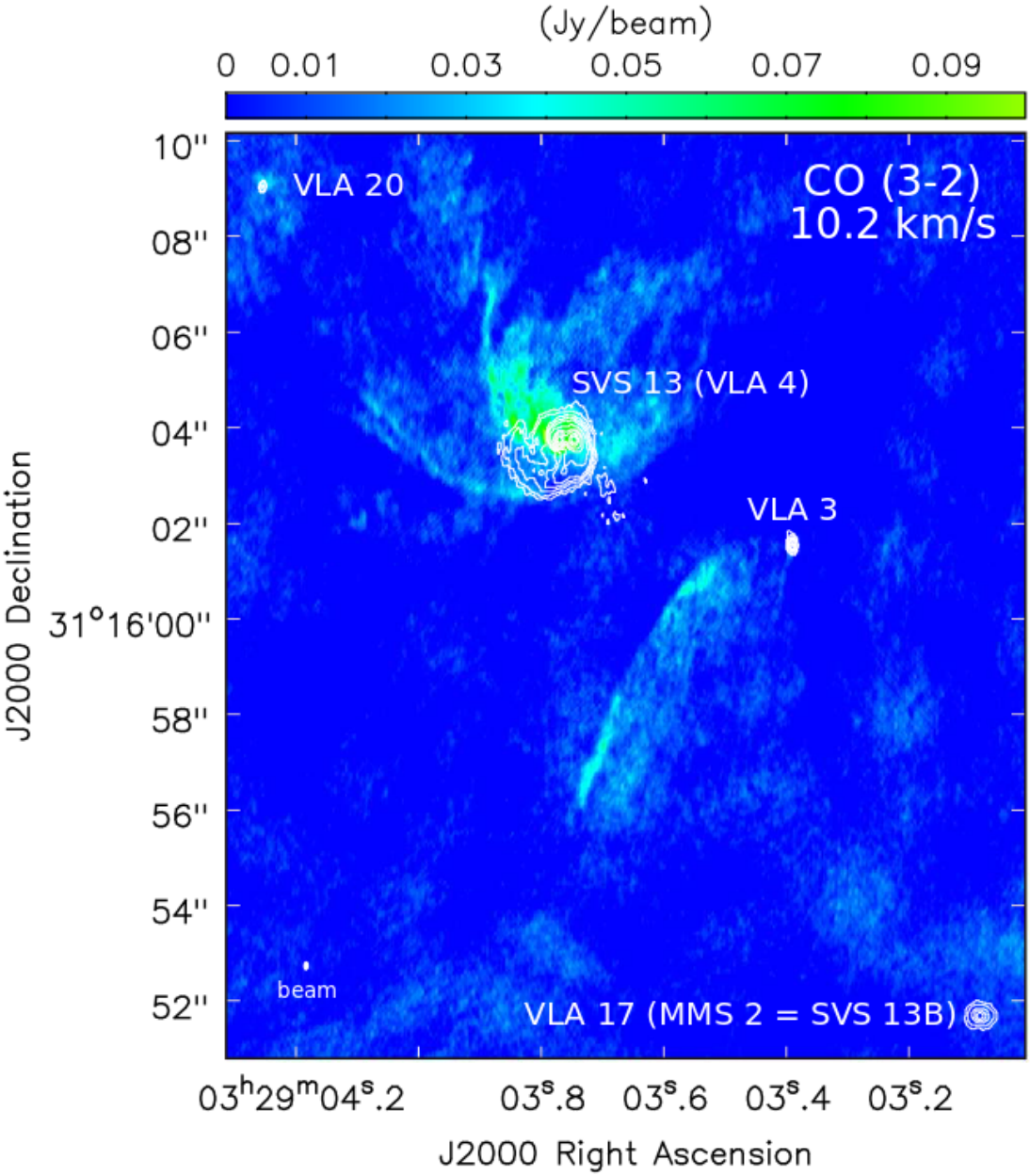

Figure 4.6 ALMA images at 0.9 mm continuum (white contours) and CO (3-2) line at 10.2 km s^{-1} (color scale) of a region $18'' \times 20''$ in size near SVS 13. The region shown corresponds essentially to the ALMA field of view (FWHM of the primary beam = $18''$, centered on SVS 13), and includes the continuum dust emission from the nearby YSOs VLA 20, VLA 3, and VLA 17 (MMS 2 = SVS 13B). The images have not been corrected by the primary beam response.

Most of the continuum emission is distributed at larger scales (within $\lesssim 1\farcs5$ from the stars), tracing dust from a circumbinary disk that is probably still in the process of forming.

If the extended emission is suppressed by restricting the uvrange of the data, we obtain the image shown in Figure 4.8. This image is expected to preferentially trace the circumstellar dust associated with each stellar object. From this image, accurate positions for the two sources are obtained, coincident within ~ 5 mas with the positions inferred from the cm data (see Table 4.1). It is interesting to note that, although in the image using all the baselines (Fig. 4.7) the 0.9 mm emission concentrates toward the western side, apparently mainly associated with VLA 4A, when excluding the extended emission the peak toward VLA 4B is significantly brighter than the peak toward VLA 4A. This suggests that there is a larger amount of emitting dust surrounding source VLA 4A, extending over a larger region than in VLA 4B. The emitting dust associated with VLA 4B appears to be distributed on a more compact scale and, at this scale, the column density is higher and/or the dust is hotter than near VLA 4A.

Specifically, in the 0.9 mm image obtained using only baselines >750 kλ, the peak intensity toward VLA 4A is 44 $\pm$ 1 mJy beam^{-1}, with a flux density of 83 $\pm$ 3 mJy, arising from a compact region with a characteristic size (deconvolved size in the E-W direction, where the synthesized beam is narrower, obtained from a Gaussian fit) of $\sim$ 80 mas ($\sim$ 24 au). The total flux density that is actually associated with this source is difficult to estimate, as there is not a clearly defined boundary, but we estimate it as $\sim$ 220 $\pm$ 25 mJy, from the map obtained using all the baselines. On the other hand, toward VLA 4B the peak intensity is 68 $\pm$ 2 mJy beam^{-1} and the flux density is 109 $\pm$ 4 mJy, coming from a region with a deconvolved size of $\sim$ 60 mas ($\sim$ 18 au); the total flux density of the dust associated with VLA 4B is $\sim$ 160 $\pm$ 16 mJy. In summary, the total amount of dust emission associated with VLA 4B appears to be $\sim$ 30% lower than in VLA 4A, but the column density toward the position of VLA 4B appears to be $\sim$ 50% higher than toward VLA 4A.

From the results described above, we also conclude that the radii of the circumstellar disks of dust associated with VLA 4A and VLA 4B are likely of the order of $\sim$ 12 au and $\sim$ 9 au, respectively. These values of the radii are smaller than those typically found for disks around single stars. In binary systems, tidal truncation to disk radii of about 1/3 of the binary separation is expected (Papaloizou & Pringle 1977; Artymowicz & Lubow 1994), resulting in smaller disks. Since the projected

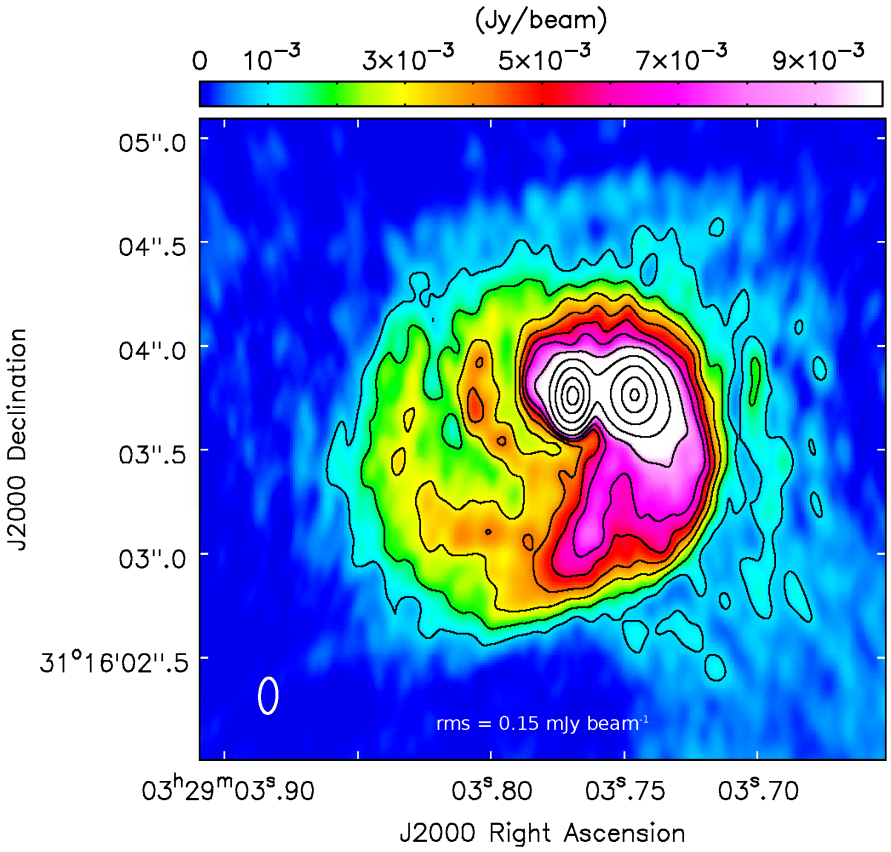

Figure 4.7 ALMA image at 0.9 mm of SVS 13. The two emission peaks are associated with the previously identified cm sources, VLA 4A (the western one) and VLA 4B (the eastern one). The image has been made from the highest angular resolution data (cycle 3) using all the baselines and robust = 0.5 weighting. Contours are −6, 6, 12, 20, 28, 36, 44, 60, 100, 200, 400, and 600 times 0.15 mJy beam^{-1}, the rms of the image. The synthesized beam ($0''.170 \times 0''.084$, P.A. $= -2.3°$) is shown in the bottom left corner of the image. The image has been corrected by the primary beam response.

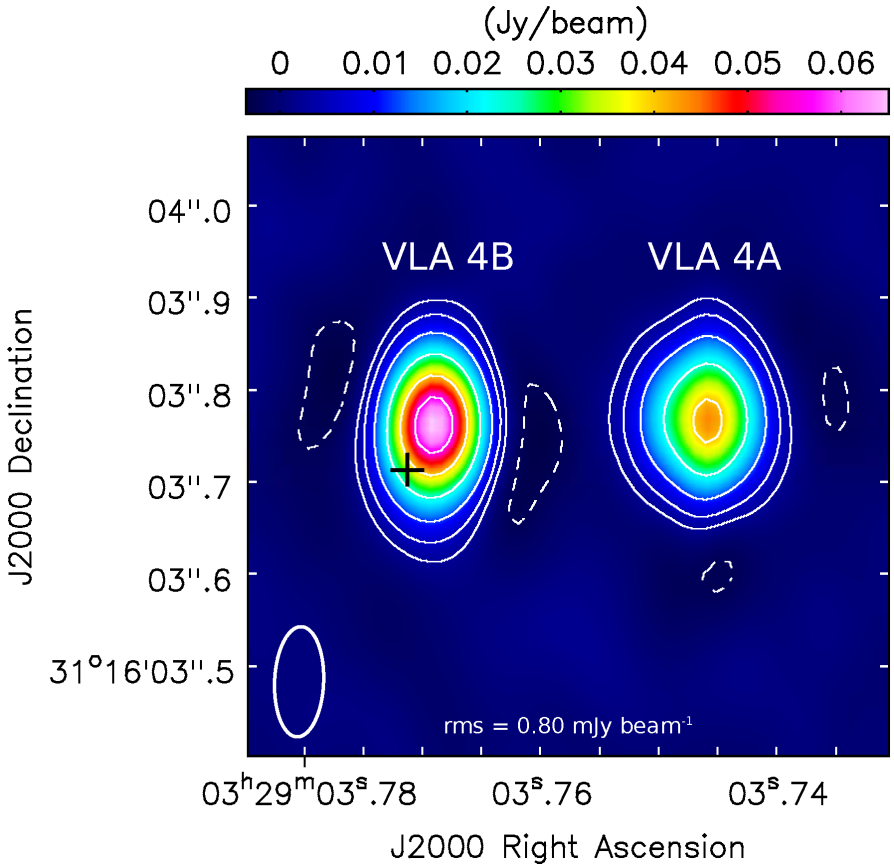

Figure 4.8 Close-up of the 0.9 mm continuum emission near the two components of the SVS 13 protobinary. The image has been obtained from the same data and with the same weighting as in Fig. 4.7, but using only baselines > 750 kλ to filter out the extended emission. The black plus sign marks the J2000 position of the GAIA DR2 (Gaia Collaboration et al. 2018) optical source at the epoch of our observations (see Section 4.3.1). Contours are -7, -3, 3, 7, 15, 30, 50, 70, 90, 120, and 150 times 0.42 mJy beam^{-1}, the rms of the map. The synthesized beam ($0\farcs12 \times 0\farcs05$, P.A. $= -2.4°$) is shown in the bottom left corner of the image.

distance between the components of the SVS 13 binary is 90 au, truncated disks with radii of $\sim$ 30 au would result from tidal truncation. Thus, the circumstellar disks in SVS 13 seem to be smaller than expected, if only tidal truncation is at work (although these are the radii of the dusty disks, while the associated disks of gas may be larger). An extreme case of a still smaller disk of dust was reported by Osorio et al. (2016) in the XZ Tau A/B young system (separation between components of 42 au), where a disk with a radius of only 3 au was imaged.

4.3.2.1 Spirals of Dust

An outstanding feature of the ALMA continuum emission (Fig. 4.7) are the prominent spiral arms associated with the SVS 13 binary. Trailing spiral arms should point away from the direction of rotation, therefore implying an SVS 13 disk counter-clockwise rotation, as seen from Earth. This is in agreement with our conclusion about the sense of the orbital motion inferred from the observed proper motions (Section 4.3.1.1) and with the analysis of radial velocities from the molecular line emission (Section 4.3.4.1 and Fig. 4.12).

To better emphasize the spiral structure, in Figure 4.9 we present the same 0.9 mm ALMA image of Figure 4.7 but normalized by a factor $\propto r^{1.5}$, where r is the distance to the center, to compensate for the decrease in intensity with distance. We identify three spiral arms, S1, S2, S3, in order of apparent intensity (see Fig. 4.9). S1 and, perhaps, S2 seem to originate near the location of VLA 4A, while S3, the weakest one, seems to originate near the location of VLA 4B. Spirals S1 and S2 are quite clearly defined, but for S3 it is unclear whether it is a spiral arm or a feature of the circumbinary disk.

Spirals have been observed in a number of protoplanetary disks and various mechanisms, which can possibly act together, have been suggested to explain their origin, including planet-disk interactions (e.g., Ogilvie & Lubow 2002; Muto et al. 2012; Dong et al. 2015; Phuong et al. 2020), gravitational instabilities (e.g., Lodato & Rice 2005) or shadows (Montesinos et al. 2016). In the simulations of the formation of binary systems, spirals also appear as a natural outcome (e.g., Bate 2018), but there is a debate (e.g., Ochi et al. 2005; Bate, & Bonnell 1997) on the relative accretion rates of the primary and secondary when the specific angular momentum is large. Earlier simulations indicate that the primary accretes more than the secondary only when the accreting gas has a low specific angular momentum, while more recent simulations have refuted this belief. The SVS 13

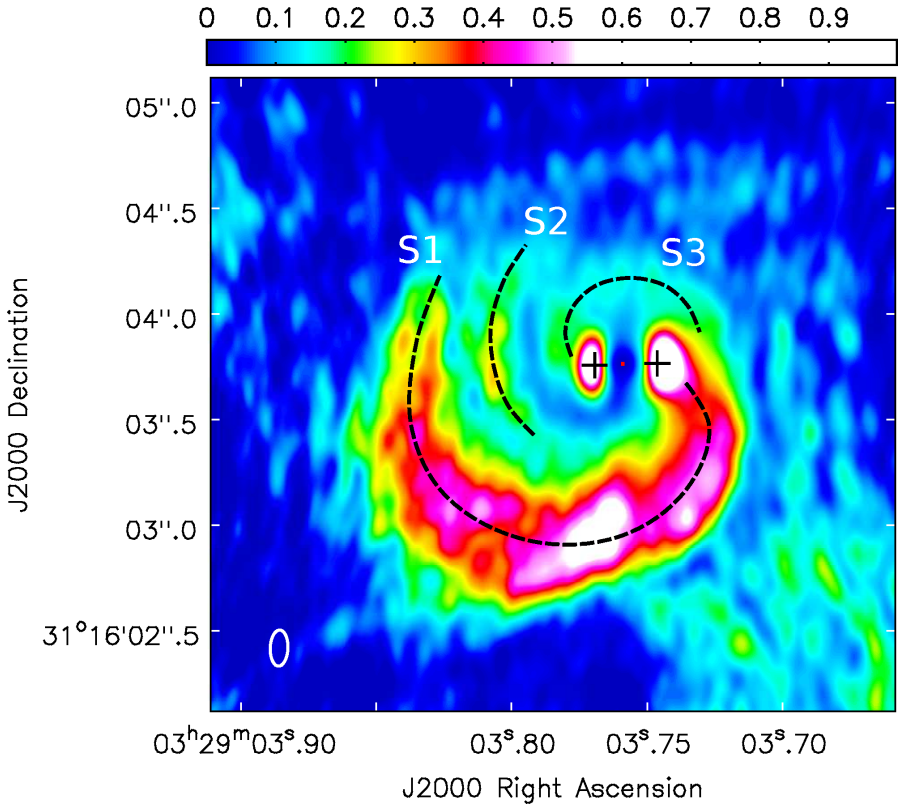

Figure 4.9 Same as in Fig. 4.7 but with the intensity scaled by a factor $\propto r^{1.5}$, where r is the projected distance to the center (red dot) in arbitrary units, to compensate for the decreasing intensity and to enhance the visibility of the spiral features at large distances. The resulting intensity has been normalized to the maximum. No correction has been applied for projection effects. Three tentative spirals (S1, S2, and S3) are identified in the image. The plus signs mark the positions of VLA 4A (western) and VLA 4B (eastern) sources.

binary could be an excellent test-bed of these kinds of simulations. Unfortunately, our current results only provide estimates for the total mass of the stellar system. Future observations of accurate proper motions at mm wavelengths, such as those outlined in Section 4.3.1.1, should be able to shed light on the SVS 13 binary mass ratio and to identify the primary and secondary components to test these alternative possibilities, relevant for the evolution of binary systems with high specific angular momentum, which should be the case for binaries with circumbinary disks.

4.3.3 The Spectral Energy Distribution

Our VLA and ALMA observations angularly resolve the SVS 13 system over a range of wavelengths from 6 cm to 0.9 mm. There are not many observational data on close protobinary systems that angularly separate the emission of the two components. Our data, combined with previous data from the literature allow us to get inside the nature of the emission and the physical properties of this system. In Table 4.2 we list the measured flux densities and in Fig. 4.10 we plot the resulting SED.

Regarding the VLA data, we note that in 2016.9 there was an important decrease of the X-band flux density of VLA 4A, by a factor close to 4, which is atypical for thermal free-free emission, where the flux density variability usually does not exceed $\sim 20\%$ (see Anglada et al. 2018 and Chapter 3); there are, however, other cases reported in the literature of variability at similar levels. This variability is usually attributed to variations in the mass accretion rate but, in general, they imply sudden increases in flux density, sometimes associated with the ejection of new ionized knots, rather than sudden decreases. Further monitoring of the sources with high sensitivity and angular resolution are necessary to improve the previous data and to clarify the origin of the X-band variability. At shorter wavelengths, $\sim$ 7 mm, a smaller increase in flux density, by a factor of $\sim$ 1.5, took place in 2015 in both sources, but only in VLA 4B persisted in the subsequent observations.

Anglada et al. (2004) noticed that the flux density of VLA 4B was much stronger than that of VLA 4A at 7 mm, while the fluxes of the two sources were comparable at longer wavelengths. We confirm this observational result, which can also be seen in the data of Tychoniec et al. (2018) and Tobin et al. (2016b). Since the observed 7 mm flux of VLA 4B coincided with the extrapolation of the mm data available at that time (which did not separate the binary), Anglada et al. (2004) attributed the excess of 7 mm emission to dust and proposed that, while VLA 4B was associated with a circumstellar disk of dust, VLA 4A was not. This observational result was interpreted by Anglada et al. (2004), in terms of the Bate, & Bonnell (1997) theoretical simulations, as suggestive that the formation of the SVS 13 binary system occurred via the accretion of material with low specific angular momentum. In this case, the primary may have a large circumstellar disk, while the secondary is essentially naked; thus, VLA 4B was proposed as the primary, more massive, component and VLA 4A as the secondary. Also,

Table 4.2 Flux Density of the Radio Sources

Frequency	Wavelenght	Flux density (mJy)		Epoch	Resolution	
(GHz)	(mm)	VLA 4A	VLA 4B	(yr)	(″)	Ref.
4.68	64	0.065±0.008	0.059±0.006	2014.2-2014.3	∼0.4	1
7.31	41	0.109±0.006	0.093±0.005	2014.2-2014.3	∼0.4	1
8.33	36	0.17±0.03	0.12±0.03	1994.3-1999.5	∼0.2	2
10.0	30	0.045±0.009	0.084±0.013	2016.9	∼0.2	3
22.1	13	0.24±0.03	0.61±0.06	2015.5	∼0.1	3
30.0	10	0.375±0.026	1.115±0.019	2013.7-2015.9	∼0.1	4
33.0	9	0.46±0.03	1.36±0.14	2015.1-2015.5	∼0.2	3
33.0	9	0.41±0.06	1.22±0.13	2015.5	∼0.1	3
37.5	8	0.51±0.03	1.763±0.022	2013.7-2015.9	∼0.1	4
42.8	7	0.34±0.12	1.29±0.19	2001.3	∼0.1	5[a]
44.0	7	0.61±0.07	1.96±0.20	2015.2-2015.5	∼0.1	3
44.0	7	0.37±0.06	2.08±0.22	2015.5	∼0.05	3
86.8	3.5	26.0±1.0[b]		1998.2	∼3.5	6
94	3.2	21±1[b]		2011.9	∼1.2	7
107.7	2.7	38.0±6.6[b]		1996.3-1998.2	∼0.6	8
230.5	1.3	320±10[b]		1998.2	∼1.5	6
231	1.3	120±7[b]		2011.1	∼0.4	7
232.5	1.3	400±19[b]		2015.7	∼0.2	9
338.2	0.9	83±3[c]	109±4[c]	2016.7	∼0.08	3
338.2	0.9	1102±110[b]		2016.7-2016.9	∼0.1	3

[a] After recalibration of the originally published data.

[b] Extended emission toward both components.

[c] Measured in a map made using baselines >750 kλ, where the extended emission has been filtered out (Figure 4.7, bottom).

References — (1) Tychoniec et al. (2018); (2) Anglada et al. (2000), (3) This work, (4) Tobin et al. (2016b), (5) Anglada et al. (2004), (6) Bachiller et al. (1998), (7) Maury et al. (2019), (8) Looney et al. (2000), (9) Tobin et al. (2018).

according to Bate, & Bonnell (1997) the systems formed by this method should not be developing a significant circumbinary disk.

Our present results clarify the previous conclusions by Anglada et al. (2004) and shed new light on the interpretation of the cm and mm continuum data. Despite SVS 13 being likely a binary system of protostars in a very early stage of the formation process, where it is difficult to separate the different contributions from circumstellar and circumbinary material, we identify three main dust contributions. We see that both VLA 4A and VLA 4B components are associated with circumstellar dust, although with different properties regarding the dust distribution, as discussed in Section 4.3.2. We also clearly see that there is circumstellar dust around the system, with prominent spiral arms that we interpret as constituting a proto-circumbinary disk and we will refer to it as the circumbinary disk (CB).

In Figure 4.10 we plot the SED in the cm/mm regimes, where we identify several contributions, namely: (i) The free-free emission associated with VLA 4A

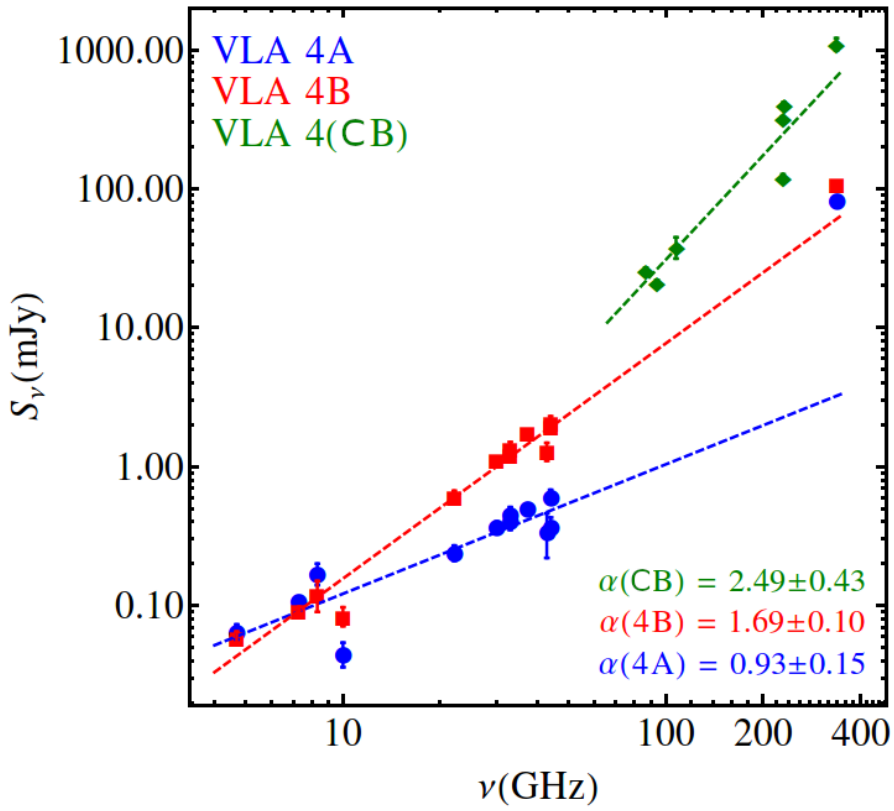

Figure 4.10 Spectral energy distribution (SED) of SVS 13 from cm to mm wavelengths. Data used are reported in Table 4.2; blue and red data points represent the flux density toward the individual components (4A, 4B), while green data points represent extended emission toward the whole system, tracing mainly the circumbinary dust (CB). The spectral indices (α) are obtained from least-squares fits (in log-log scale); for the free-free spectral indices of the individual components, we only used data with a frequency equal or below 44 GHz ($\lambda \geq 7$ mm).

(with a spectral index of 0.93 at wavelengths shorter than ~ 7 mm), likely tracing a thermal radio jet; (ii) The free-free emission associated with VLA 4B (that should be dominant at long wavelengths), also consistent with the presence of a thermal radio jet; (iii) The dust emission of the circumstellar disk associated with VLA 4A (traced by the 0.9 mm blue data point) that implies a change to a steeper spectral index, ~ 2.5, at short wavelengths; (iv) The circumstellar disk around VLA 4B (traced by the 0.9 mm red data point), with a flux density consistent with the extrapolation of the long-wavelength data with a single slope of 1.69, suggesting a mixture of free-free (dominant at long wavelengths) and dust (dominant at short wavelengths) emissions, which are difficult to disentangle with the current data;

(v) The dust emission of the circumbinary disk and its associated spiral arms (green dots with a spectral index of 2.49) which dominates the total emission observed at short wavelengths.

4.3.4 ALMA Line Emission: Circumstellar and Circumbinary Disk Kinematics and Molecular Diversity

4.3.4.1 Distribution of the Molecular Emission

The ALMA observations reveal emission structures from numerous molecular transitions. There are structures at scales of $\sim 10''$ (3000 au) or larger, such as the spiraling molecular structures shown in Figure 4.6 that will be discussed in a forthcoming paper (Diaz-Rodriguez et al., in prep.). We note here, however, that the CO spirals go in the same direction as the dust spiral arms (Section 4.3.2) therefore suggesting a connection between the binary, its associated circumbinary emission, and the larger-scale molecular structures at velocities close to the systemic velocity of the cloud. Additionally, the ALMA cubes show very high-velocity blue-shifted features likely associated with the outflow blue lobe that are discussed in Blázquez-Calero et al. (2020, in prep.). In this Section, we are focusing on the most relevant molecular line emission that appears to be more directly associated with the SVS 13 binary and associated disks, both spatially (within a few arcsec) and in velocity (within a few km s^{-1} of the systemic velocity), and that is most useful to infer the physical properties of the system and its close environment.

Figure 4.11 shows the continuum-subtracted velocity-integrated emission (zeroth-order moment), intensity-weighted mean velocity (first-order moment) and velocity dispersion (second-order moment) of the CS (7-6), $H^{13}CN$ (4-3), and $HC^{15}N$ (4-3) molecular lines. These lines are the centering lines of three of the six observational spectral windows and have been selected as representative of the emission most directly associated with the binary system. As can be seen in the figures, the emission appears distributed surrounding the binary, and we interpret it as mostly tracing circumbinary gas from which the stars are being assembled. The integrated emission clearly peaks toward source VLA 4A, while there is an apparent decrease of emission toward source VLA 4B that we think is probably not real but an artifact of continuum oversubtraction, due to the non-additivity of optically thick intensities. As discussed in Section 4.3.2, the dust emission toward VLA 4B es very compact and intense, so it likely traces dust emission with a very

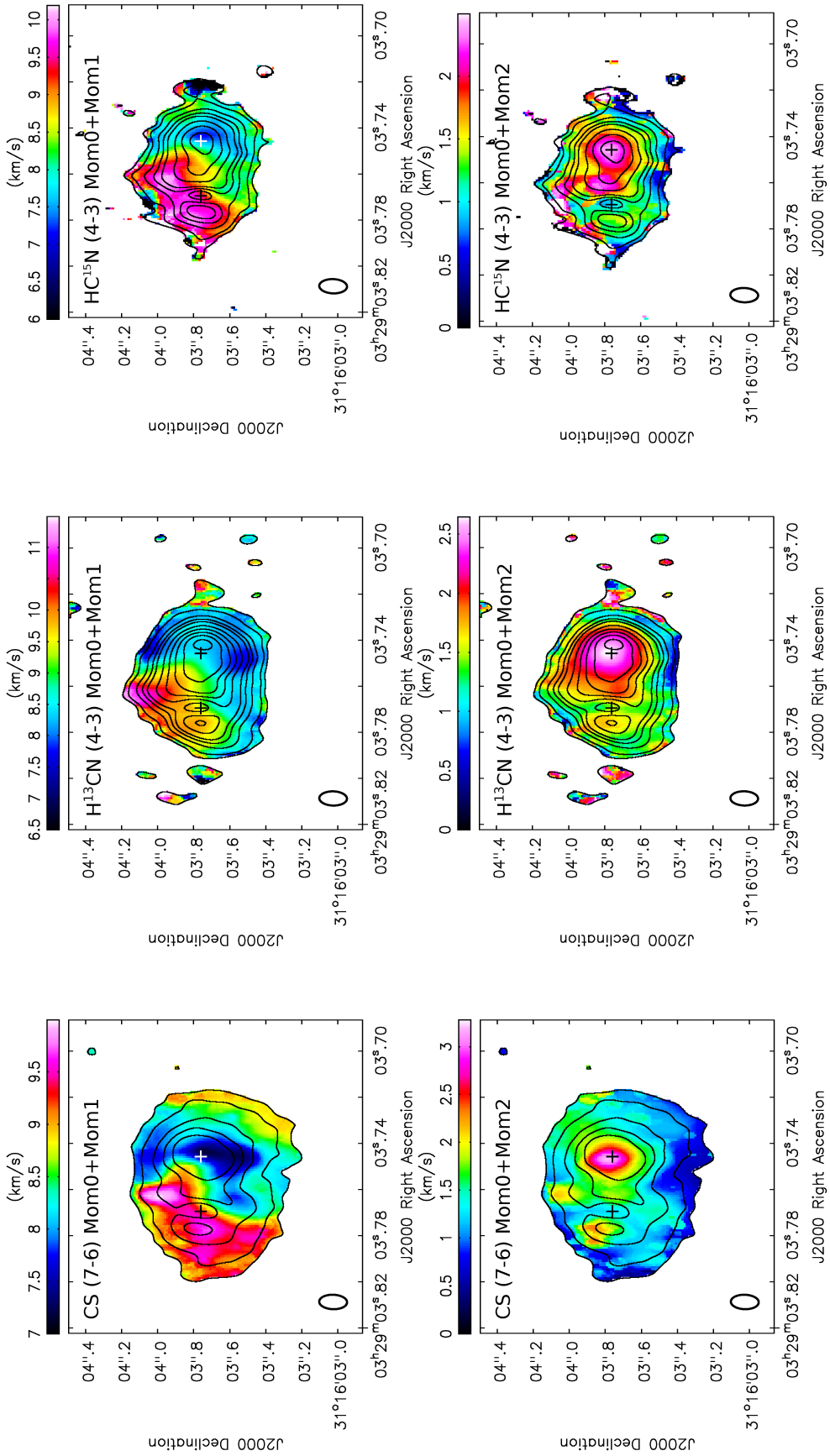

Figure 4.11 Continuum-subtracted velocity-integrated emission (zeroth-order moment; contours), intensity-weighted mean velocity (first-order moment; color scale in top panels) and velocity dispersion (second-order moment; color scale in bottom panels) of the CS (7-6), $H^{13}CN$ (4-3), and $HC^{15}N$ (4-3) molecular lines observed with ALMA toward SVS 13. Contours are -3, 3, 5, 10, 15, 20, 30, 40, 50, 60, and 70 times 25 mJy beam^{-1} km s^{-1} (CS), and 10 mJy beam^{-1} km s^{-1} ($H^{13}CN$ and $HC^{15}N$). Synthesized beam (indicated in the bottom left corner of the maps) is $0\farcs15 \times 0\farcs08$, P.A. $= -2°$. The positions of VLA 4A (western) and VLA 4B (eastern) are marked with plus signs.

high optical depth, so the emission is saturated making it difficult for the line emission to emerge over the continuum.

The integrated intensity maps presented in Figure 4.11 (in contours) show a roughly elliptical molecular emission ($\sim 1\farcs0 \times 0\farcs8$ or ~ 300 au $\times$ 240 au in size for CS, and slightly smaller, $\sim 0\farcs8 \times 0\farcs6$ or ~ 240 au $\times$ 180 au for the HCN isotopologues), with the major axis roughly E-W. If the real structure is assumed to be roughly circular, the observed ellipticity implies an inclination angle of the disk (angle of the disk axis and the line-of-sight, where 0° corresponds to face-on) of $\sim 40°$.

The first-order moment maps (Fig. 4.11 top panels) show a clear velocity gradient roughly in the SW-NE direction, with blue-shifted velocities toward the NW side. Actually, the maps show a kind of "yin-yang"-shaped velocity distribution that we attribute to the simultaneous presence of both infall and rotation with comparable velocities (see Fig. 4.12). Given that the southern lobe of the outflow associated with SVS 13 is blue-shifted, and assuming that the circumbinary emission is mainly distributed in a disk-like structure close to the equatorial plane (i.e., we are observing the circumbinary disk from "below") or, in other words, in such a way that its northern edge is the one closest to the observer. The observed velocity gradient implies a counter-clockwise rotation as seen from the observer. This direction of the circumbinary disk rotation is in agreement with that inferred from the observed orbital proper motions (Section 4.3.1.1) and the dust spirals in the 0.9 mm continuum emission (see Figs. 4.7, 4.9). Given the orientation of the disk-like structure, the presence of infall motions would produce additional red-shifted emission in its northern part and blue-shifted emission in its southern part, resulting in the observed "yin-yang"-shaped velocity distribution (see Fig. 4.12). However, given that the northern lobe of the bipolar outflow is red-shifted and the southern one is blue-shifted, a contribution from the outflow cannot be discarded.

The second-order moment maps (Fig. 4.11 bottom panels) show a large increase in velocity dispersion toward VLA 4A, which is likely indicative of strong turbulent and/or infall/accretion motions onto this source. The second-order moment increases from a typical value of 1.2 km s^{-1} in the circumbinary structure up to ~ 3.2 km s^{-1} toward source VLA 4A. Velocities of the order of ~ 2 km s^{-1} at scales of ~ 10 au (the beam radius) would imply a mass of the order of 0.04 $M_\odot$ if they are gravitationally bound. Therefore, we expect the mass of the VLA 4A protostar to be of this order.

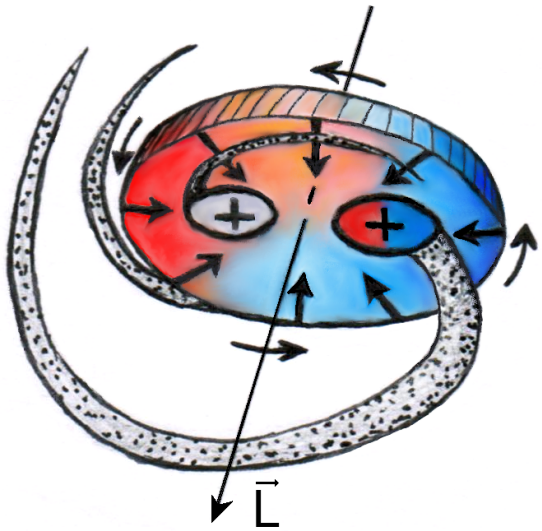

Figure 4.12 Sketch of the proposed geometrical and kinematical configuration of the SVS 13 protobinary system and its circumbinary material.

Toward VLA 4B there is only a modest increase in the velocity dispersion. This suggests that VLA 4A could be the main accretion center, as the position of the origin of the main spiral arm also suggests (see Section 4.3.2.1). However, it is unclear whether the apparent decrease in the second-order moment toward VLA 4B is real, with the turbulence and/or accretion being smaller toward this source, or it is an artifact due to an oversubtraction of the continuum that reduces artificially the observed line emission toward this position.

4.3.4.2 Detection of Molecular Transitions

Figure 4.13 shows the full 2.8 GHz spectral band, obtained over a region with the size of the beam ($0\farcs16 \times 0\farcs08$, P.A. = $0°$) toward source VLA 4A (blue) and toward source VLA 4B (red), as well as toward the circumbinary material in a position between the two protostars (black). In general, lines are strongest toward the central position, and stronger toward VLA 4A than toward VLA 4B. On the other hand, lines are broader toward VLA 4A than toward other positions of the molecular structure, as was already inferred from the second-order moment images shown in Figure 4.11. We took spectra in several positions of the circumbinary structure and found that lines are broader and more intense toward the western

part of the disk than toward the eastern, and that are narrower and more intense toward the southern part than the northern. Additionally, the intensity of the lines decreases as we move farther from the center of the disk. The profiles of several strong lines frequently present absorption features near the peak, suggesting that they are optically thick; this is particularly evident toward VLA 4A. Lines are weaker toward VLA 4B, but their intensity could be affected by an oversubtraction of the continuum which is particularly intense (and likely optically thick) at the stellar position.

To identify the detected transitions we compared the spectra with synthetic ones modeled in CASSIS[1] applying the LTE radiative transfer equations to a homogeneous column of gas along the line of sight, where the distribution of the population of all the rotational energy levels for a given molecule is described by a single excitation temperature, also known as rotational temperature. To obtain an initial guess of the expected intensities of the different transitions, in our model we considered T_{ex} = 100 K based on previous works (Belloche et al. 2020b), a source size of $0\farcs16$ (the region where the spectrum was taken), and, in general, an FWHM of 2 km s^{-1}, and changed manually the species column density relative to H_2 and the FWHM to match the observed spectrum. We note that our goal in this procedure was the identification of the lines, not to derive parameters from the model. In a first round, we used the species in the "Lowmass hot corino" and "ISM" filters of CASSIS. We only included in our model transitions with upper level energies ($E_{\rm up}$) below 500 K. To identify the remaining unknown lines after this first stage, we included in the model any species with transitions close to the unidentified lines and with upper level energies up to 700 K.

Our proposed identifications are listed in Table 4.3. We report 180 transitions of 19 species, as well as 28 unidentified lines. We note that in some cases (marked as NRM in Table 4.3) the intensity of the lines is not well reproduced by the model, which could be due to departures from LTE or other effects such as optical depth or gradients.

Complex Organic Molecules (COMs, molecules with six or more atoms with at least one carbon atom, Herbst & van Dishoeck 2009) are usually detected in association with the so-called Hot Molecular Cores (HMC), which are hot and

[1]CASSIS has been developed by IRAP-UPS/CNRS.

dense regions that characterize one of the first stages in the formation of massive stars (Osorio et al. 1999). However, in a few cases, these complex molecules have been also detected in association with low-mass protostars, and are called "hot corinos".

Hot corinos are small, dense regions very close to their host protostar with temperatures higher than the water ice desorption temperature of ~ 100 K, and are considered the low-mass counterparts of HMCs. COMs are the trademark of hot corinos. COMs have been detected previously toward SVS 13 with poorer angular resolution (from 0.″3 to few arcseconds) observations that do not allow to resolve well the emission of the two components (López-Sepulcre et al. 2015; Lefèvre et al. 2017; De Simone et al. 2017; Belloche et al. 2020b). Since in these observations the peak emission of the detected COMs was found close to the compact source VLA 4A, Lefèvre et al. (2017) proposed that this component of the binary was the hot corino. With our higher angular resolution observations (0.″16), we are able to detect COMs associated with both components of the binary, VLA 4A and VLA 4B, as well as in the circumstellar material (Table 4.3).

We confirm the previous detection of acetaldehyde (Belloche et al. 2020b), ethanol (Belloche et al. 2020b), formamide (López-Sepulcre et al. 2015), ethylene glycol, methanol, and methyl formate (Lefèvre et al. 2017; Belloche et al. 2020b). We additionally report the detection of acetone, ethyl cyanide, ethylene oxide, methyl cyanide, deuterated methanol, and deuterated methyl cyanide. In general, these COMs emit in an extended region that appears to be associated with circumbinary gas. In a few transitions (marked 4A in Table 4.3), the emitting region is restricted to a small region surrounding VLA 4A (e.g., Fig. 4.14). Interestingly, deuterated acetaldehyde is only detected toward the position between the two protostars (marked as CB in Table 4.3).

We find that, in general, the molecules detected toward VLA 4A are also present toward VLA 4B. The weaker transitions are not detected toward VLA 4B, and a few transitions are only detected toward VLA 4A. This suggests that the chemistry in VLA 4A could be much richer than in VLA 4B, as previous studies with lower angular resolution also suggest (e.g., Lefèvre et al. 2017). As noted above, the velocity dispersion toward VLA 4A is much larger than toward VLA 4B; also VLA 4A appears to be the origin of the main spiral arm. All these facts together suggest that a higher kinematical and heating activity is taking place in VLA 4A.

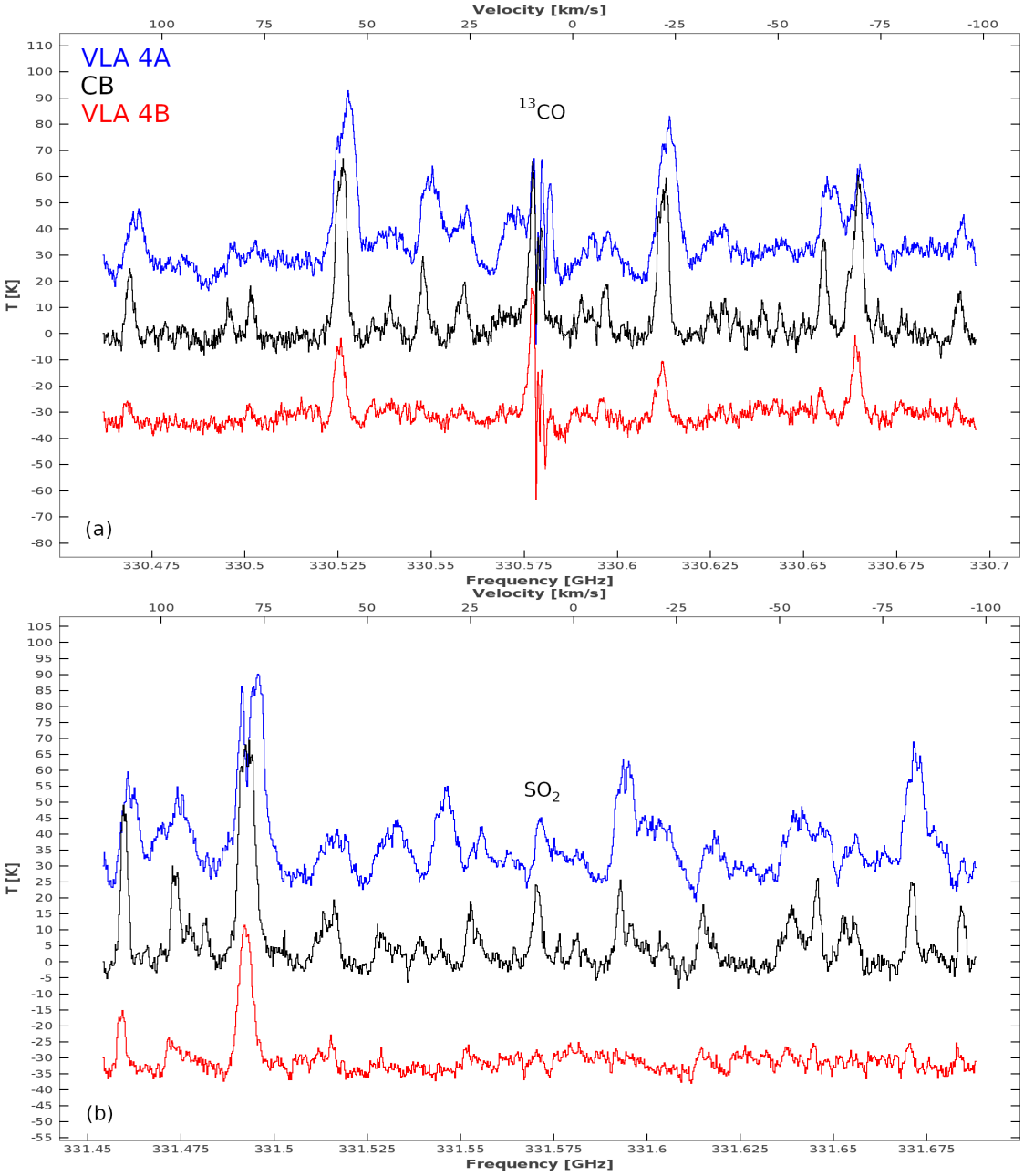

Figure 4.13 Spectra taken in beam-size (0.″16 × 0.″08, P.A.=0°) regions toward VLA 4A (blue), VLA 4B (red), and the geometric center of the components (black). VLA 4A and VLA 4B spectra are offset by 30 K and −30 K, respectively, for illustrative purposes. The bottom x-axis shows the observed frequency, and the top x-axis shows the velocity referred to the frequency of ^{13}CO (3-2) (a), SO_2 (11-12) (b), CS (7-6) (c), HC^{15}N (4-3) (d), H^{13}CN (4-3) (e), and ^{12}CO (3-2) (f). Continued in the next page.

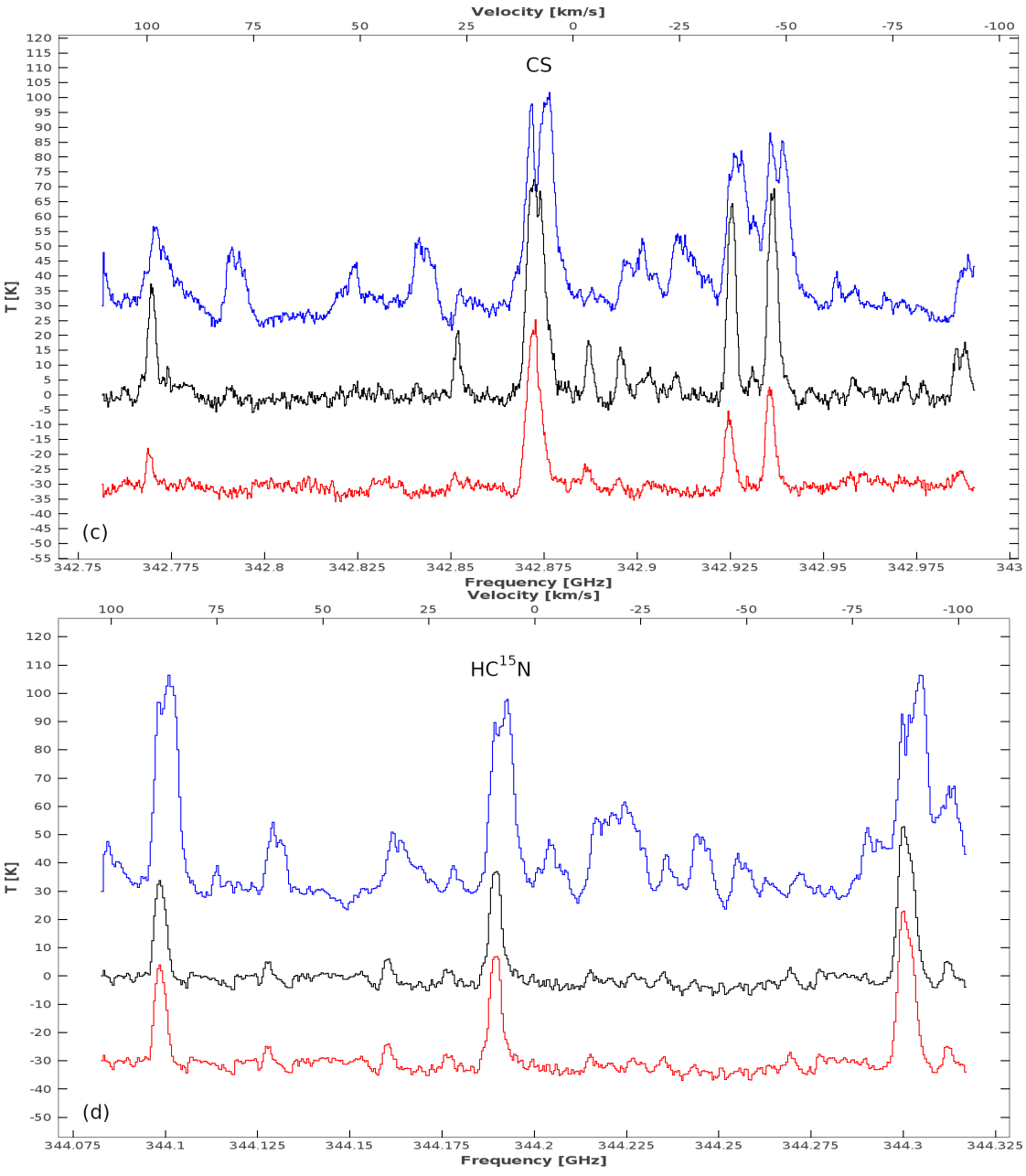

Figure 4.13 Continued in the next page.

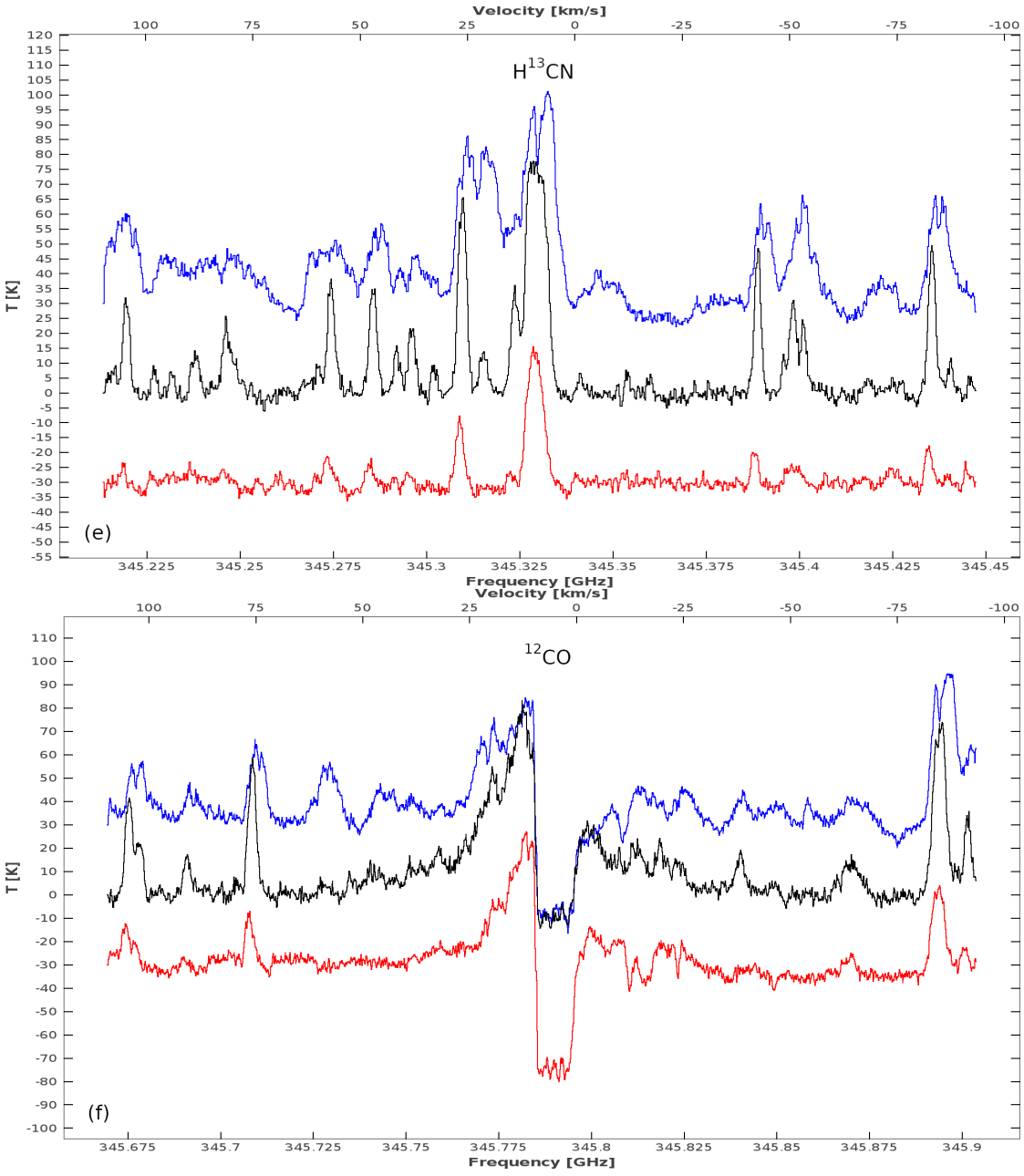

Figure 4.13 Final.

Table 4.3 Molecular Transitions Detected toward SVS 13[a]

Species	Formula	Quantum Numbers	Rest Frequency[b] (MHz)	E_u/k (K)	A_{ul} (s^{-1})	Notes[c]
Acetaldehyde	CH_3CHO, vt=0	5 3 2 2 - 4 2 2 2	330566.705	34.26	1.15E-4	NRM
		17 1 16 3 - 16 1 15 3	330580.420	352.489	1.25E-3	
		17 1 16 2 - 16 1 15 2	331602.178	146.645	1.25E-3	
		17 1 16 0 - 16 1 15 0	331680.380	146.6	1.25E-3	
	CH_3CDO, vt=0,1	17 2 15 0 - 16 2 14 0	331490.785	149.161	1.28E-3	CB
Acetone	CH_3COCH_3, v=0	17 15 3 1 - 16 14 2 1	330506.310	138.132	1.28E-3	
		17 15 2 1 - 16 14 3 1	330512.291	138.132	1.28E-3	B
		17 15 3 1 - 16 14 3 2	330549.327	138.023	1.28E-3	
		15 8 7 0 - 14 7 8 1	331525.975	95.682	1.30E-4	B
		17 17 1 0 - 16 16 0 0	342780.035	147.049	1.85E-3	
		17 17 0 0 - 16 16 1 0	342780.036	147.049	1.85E-3	
		41 3 39 0 - 41 2 40 1	342836.464	447.674	1.53E-4	B, DI
		41 2 39 0 - 41 1 40 1	342836.464	447.674	1.53E-4	B, DI
		18 12 6 1 - 17 11 7 1	342836.912	141.302	4.35E-4	B, DI
		18 12 6 0 - 17 11 7 0	342864.593	141.23	4.41E-4	LSNR
		18 12 6 0 - 17 11 7 1	342896.394	141.271	4.35E-4	B
		18 15 4 0 - 17 14 3 0	345256.037	150.827	1.29E-3	B
		18 15 3 0 - 17 14 4 0	345305.365	150.828	1.29E-3	
		24 12 12 1 - 23 13 11 1	345875.586	235.239	7.51E-4	B, LSNR
		24 12 12 1 - 23 13 11 2	345877.896	235.239	7.52E-4	B, LSNR
Butadiynyl	$^{13}CCCCH$	36 36.5 37 36.5 - 35 35.5 36 35.5	330637.439	293.629	1.57E-4	B
		36 36.5 37 37.5 - 35 35.5 36 36.5	330637.439	293.628	1.57E-4	B
		36 36.5 36 36.5 - 35 35.5 35 35.5	330638.331	293.618	1.57E-4	B
		36 36.5 36 35.5 - 35 35.5 35 34.5	330638.355	293.618	1.57E-4	B
		36 35.5 36 35.5 - 35 34.5 35 34.5	330672.730	293.685	1.57E-4	B
		36 35.5 36 36.5 - 35 34.5 35 35.5	330672.754	293.685	1.57E-4	B
		36 35.5 35 34.5 - 35 34.5 34 33.5	330673.647	293.692	1.57E-4	B
		36 35.5 35 35.5 - 35 34.5 34 34.5	330673.647	293.693	1.57E-4	B
Carbon Monoxide	CO, v=0	3 - 2	345795.990	33.192	2.50E-6	
	^{13}CO	3 - 2	330587.965	31.732	2.19E-6	
Carbon Monosulfide	CS, v=0-4	7 0 - 6 0	342882.850	65.828	8.40E-4	
Ethanol	C_2H_5OH, v=0	19 4 16 0 - 18 4 15 0	330478.629	234.672	3.23E-4	
		14 5 9 1 - 14 4 11 0	330599.812	179.62	1.04E-4	B
		20 0 20 2 - 19 1 19 2	330621.123	169.18	3.82E-4	
		9 6 3 0 - 8 5 3 1	331469.617	138.161	1.61E-4	
		9 6 4 0 - 8 5 4 1	331469.664	138.161	1.61E-4	B

Table 4.3 Molecular Transitions Detected toward SVS 13[a]

Species	Formula	Quantum Numbers	Rest Frequency[b] (MHz)	E_u/k (K)	A_{ul} (s^{-1})	Notes[c]
		11 5 7 1 - 11 4 7 0	331648.876	147.183	1.02E-4	B
		11 3 8 2 - 10 2 9 2	331655.211	66.945	1.26E-4	
		21 1 21 0 - 20 1 20 0	345229.285	241.552	3.71E-4	B
		21 1 21 1 - 20 1 20 1	345295.355	246.22	3.67E-4	
		22 3 19 1 - 21 4 17 0	345311.658	286.007	7.58E-5	
		21 0 21 0 - 20 0 20 0	345333.442	241.539	3.72E-4	
		21 0 21 1 - 20 0 20 1	345408.165	246.207	3.67E-4	B
Ethyl Cyanide	C_2H_5CN, v=0	37 12 25 - 36 12 24	331484.515	462.06	2.77E-3	B
		37 12 26 - 36 12 25	331484.515	462.06	2.77E-3	B
		37 11 26 - 36 11 25	331487.287	436.589	2.83E-3	
		37 11 27 - 36 11 26	331487.287	436.589	2.83E-3	
		37 10 28 - 36 10 27	331523.317	413.325	2.88E-3	B
		37 10 27 - 36 10 26	331523.317	413.325	2.88E-3	B
		37 14 23 - 36 14 22	331549.416	519.581	2.66E-3	CB, LSNR
		37 14 24 - 36 14 23	331549.416	519.581	2.66E-3	CB, LSNR
		37 9 29 - 36 9 28	331605.594	392.28	2.92E-3	B
		37 9 28 - 36 9 27	331605.594	392.28	2.92E-3	B
		37 15 22 - 36 15 21	331608.406	551.61	2.59E-3	B
		37 15 23 - 36 15 22	331608.406	551.61	2.59E-3	B
		37 2 35 - 36 2 34	331662.287	310.75	3.08E-3	
		10 6 5 - 9 5 4	344278.941	63.667	2.03E-4	
		10 6 4 - 9 5 5	344278.941	63.667	2.03E-4	
Ethylene Glycol	aGg'-$(CH_2OH)_2$	22 6 17 0 - 21 5 17 1	330510.922	142.638	3.93E-5	B
		18 8 10 0 - 17 7 10 1	330539.249	115.544	2.45E-5	B
		18 8 11 0 - 17 7 11 1	330544.758	115.544	2.44E-5	B
		33 18 15 0 - 32 18 14 1	331479.210	434.667	6.27E-4	4A, B
		33 18 16 0 - 32 18 15 1	331479.210	434.667	6.27E-4	4A, B
		35 3 33 0 - 34 3 32 1	331553.542	304.273	8.86E-4	4A, B
		35 2 33 0 - 34 2 32 1	331554.797	304.273	8.86E-4	4A, B
		33 17 16 0 - 32 17 15 1	331608.371	417.526	6.56E-4	B
		33 17 17 0 - 32 17 16 1	331608.371	417.526	6.56E-4	B
		34 4 31 1 - 33 4 30 0	342800.519	297.127	9.61E-4	4A, NRM
		34 3 31 1 - 33 3 30 0	342850.907	297.124	9.81E-4	4A, NRM
		22 5 17 0 - 21 4 18 0	342899.671	138.24	4.26E-5	B
		34 13 22 0 - 33 13 21 1	342920.095	375.646	8.43E-4	4A, B
		34 13 21 0 - 33 13 20 1	342920.100	375.646	8.43E-4	4A, B
		20 4 16 1 - 19 2 17 0	342941.447	113.509	8.79E-6	DI, LSNR

Table 4.3 Molecular Transitions Detected toward SVS 13[a]

Species	Formula	Quantum Numbers	Rest Frequency[b] (MHz)	E_u/k (K)	A_{ul} (s^{-1})	Notes[c]
		34 5 30 1 - 33 4 29 1	344137.936	305.126	2.42E-4	B
		33 18 15 1 - 32 18 14 0	344226.046	434.972	7.02E-4	B
		33 18 16 1 - 32 18 15 0	344226.046	434.972	7.02E-4	B
		20 17 3 1 - 20 16 5 0	344228.068	245.387	8.84E-6	B
		20 17 4 1 - 20 16 4 0	344228.068	245.387	8.84E-6	B
		33 19 14 1 - 32 19 13 0	344231.354	453.099	6.68E-4	B
		33 19 15 1 - 32 19 14 0	344231.354	453.099	6.68E-4	B
		33 17 16 1 - 32 17 15 0	344253.269	417.828	7.35E-4	4A
		33 17 17 1 - 32 17 16 0	344253.269	417.828	7.35E-4	4A
		33 20 13 1 - 32 20 12 0	344264.330	472.207	6.33E-4	4A
		33 20 14 1 - 32 20 13 0	344264.330	472.207	6.33E-4	4A
		33 16 17 1 - 32 16 16 0	344319.573	401.672	7.65E-4	B
		33 16 18 1 - 32 16 17 0	344319.573	401.672	7.65E-4	B
		33 21 12 1 - 32 21 11 0	344321.301	492.291	5.95E-4	B
		33 21 13 1 - 32 21 12 0	344321.301	492.291	5.95E-4	B
		33 12 22 1 - 32 12 21 0	345224.705	347.051	8.75E-4	4A, B
		33 12 21 1 - 32 12 20 0	345224.778	347.051	8.75E-4	4A, B
		21 7 15 0 - 20 6 14 0	345266.087	137.904	8.68E-5	4A, B
		35 4 31 0 - 34 4 30 1	345278.673	321.646	8.99E-4	B
		33 11 23 1 - 32 11 22 0	345737.011	335.95	9.00E-4	4A, B
		33 11 22 1 - 32 11 21 0	345738.443	335.95	9.01E-4	4A, B
		34 9 26 0 - 33 9 25 1	345812.719	333.572	9.36E-4	B
		34 8 27 0 - 33 8 26 1	345832.886	325.787	5.43E-4	
Ethylene Oxide	c-C_2H_4O	9 5 5 - 8 4 4	345688.322	90.408	3.37E-4	B
Formaldehyde	$H_2C^{18}O$	5 0 5 - 4 0 4	345881.039	49.871	1.19E-3	B
	p-D_2CO	6 1 6 - 5 1 5	330674.347	53.025	1.02E-3	B
Formamide	$HC(O)NH_2$, v=0	16 3 14 - 16 2 15	331685.873	165.588	7.87E-5	4A, B, DI
		16 1 15 - 15 1 14	345325.391	145.155	3.02E-3	
Hydrogen Cyanide	$HC^{15}N$, v=0	4 - 3	344200.109	41.298	1.88E-3	B
	$H^{13}CN$, v=0	4 - 3	345339.769	41.435	1.90E-3	B
Methanol	CH_3OH, vt=0-2	11 1 10 0 - 11 0 11 0	331502.319	169.008	3.93E-4	NRM
		18 2 17 1 - 17 3 15 1	344109.039	419.401	6.80E-5	B
		10 2 9 5 - 11 3 9 5	344312.267	491.913	1.77E-4	B
		16 1 15 0 - 15 2 14 0	345903.916	332.651	1.04E-4	
	$CH_3{}^{18}OH$, v=0-2	13 0 13 0 - 12 1 12 0	331482.670	202.281	1.99E-4	B
	$^{13}CH_3OH$, vt=0,1	7 2 5 0 - 6 2 4 0	330535.222	85.799	1.44E-4	B
		7 -2 6 0 - 6 -2 5 0	330535.890	89.448	1.46E-4	B

Table 4.3 Molecular Transitions Detected toward SVS 13[a]

Species	Formula	Quantum Numbers	Rest Frequency[b] (MHz)	E_u/k (K)	A_{ul} (s^{-1})	Notes[c]
	CH_2DOH	5 3 2 1 - 6 2 5 0	330606.339	77.042	7.70E-6	
		9 0 9 1 - 8 2 6 0	330686.419	109.536	4.06E-7	DI
		15 7 9 1 - 16 6 10 1	331647.951	458.992	9.48E-6	B, LSNR
		15 7 8 1 - 16 6 11 1	331647.959	458.992	9.48E-6	B, LSNR
		17 2 16 0 - 17 1 17 0	342935.645	342.828	1.67E-4	
		20 2 18 1 - 19 3 16 2	344138.882	478.684	7.97E-5	B
		8 2 7 2 - 7 3 5 0	345284.157	112.579	1.88E-6	B
		16 2 14 0 - 15 3 13 0	345398.904	310.213	5.83E-5	
		23 4 19 1 - 23 3 21 2	345701.510	662.813	1.34E-4	
		3 2 1 1 - 2 1 2 1	345718.718	39.435	4.23E-5	B, NRM
		19 1 19 1 - 18 2 17 2	345820.793	418.03	2.94E-5	B
		22 4 19 1 - 22 3 19 2	345850.485	613.622	1.29E-4	
Methyl Cyanide	$CH_3{}^{13}CN$, v=0	18 6 - 17 6	330679.886	407.876	2.80E-3	
	CH_2DCN	20 1 20 - 19 1 19	345685.380	179.63	3.60E-3	B
Methyl Formate	CH_3OCHO v=0	27 13 15 4 - 26 13 14 4	330602.640	522.121	4.24E-4	B
		27 11 16 5 - 26 11 15 5	330634.841	490.367	4.59E-4	
		28 3 25 2 - 27 4 24 1	330641.527	247.741	5.56E-5	
		28 3 25 0 - 27 4 24 0	330653.474	247.738	5.56E-5	
		27 12 16 3 - 26 12 15 3	330701.651	505.429	4.43E-4	
		27 12 15 3 - 26 12 14 3	330701.651	505.429	4.43E-4	
		28 3 25 0 - 27 3 24 0	331469.465	247.739	5.36E-4	B
		27 10 17 5 - 26 10 16 5	331483.804	476.502	4.78E-4	B
		27 22 5 2 - 26 22 4 2	331539.684	543.597	1.88E-4	DI, NRM
		27 21 6 0 - 26 21 5 0	331564.665	515.157	2.21E-4	
		27 21 7 0 - 26 21 6 0	331564.665	515.157	2.21E-4	
		27 21 6 2 - 26 21 5 2	331586.163	515.149	2.21E-4	LSNR
		27 21 7 1 - 26 21 6 1	331589.894	515.146	2.21E-4	LSNR
		27 20 7 0 - 26 20 6 0	331625.030	488.026	2.52E-4	
		27 20 8 0 - 26 20 7 0	331625.030	488.026	2.52E-4	
		27 20 8 1 - 26 20 7 1	331647.933	488.017	2.52E-4	B
		27 20 7 2 - 26 20 6 2	331648.683	488.018	2.52E-4	B
		28 10 18 5 - 27 10 17 5	344108.640	493.017	5.42E-4	B, NRM
		28 18 10 0 - 27 18 9 0	344170.930	454.246	3.66E-4	
		28 18 11 0 - 27 18 10 0	344170.930	454.246	3.66E-4	
		28 18 10 2 - 27 18 9 2	344187.246	454.239	3.66E-4	
		28 18 11 1 - 27 18 10 1	344197.339	454.238	3.66E-4	B
		23 13 10 2 - 23 12 11 2	344206.436	274.953	4.27E-5	B

Table 4.3 Molecular Transitions Detected toward SVS 13[a]

Species	Formula	Quantum Numbers	Rest Frequency[b] (MHz)	E_u/k (K)	A_{ul} (s^{-1})	Notes[c]
		23 13 11 1 - 23 12 12 1	344210.812	274.944	4.27E-5	B
		23 13 10 0 - 23 12 11 0	344237.391	274.954	4.27E-5	
		23 13 11 0 - 23 12 12 0	344237.414	274.954	4.27E-5	
		28 11 18 4 - 27 11 17 4	344300.259	506.713	5.27E-4	
		28 17 11 0 - 27 17 10 0	344322.992	431.091	3.94E-4	B
		28 17 12 0 - 27 17 11 0	344322.992	431.091	3.94E-4	B
		18 13 5 2 - 18 12 6 2	345230.296	212.973	3.22E-5	B
		18 13 6 1 - 18 12 7 1	345241.935	212.959	3.22E-5	
		28 10 19 4 - 27 10 18 4	345248.210	492.904	5.48E-4	
		18 13 5 0 - 18 12 6 0	345281.320	212.973	3.22E-5	B
		18 13 6 0 - 18 12 7 0	345281.320	212.973	3.22E-5	B
		17 13 4 2 - 17 12 5 2	345351.333	202.36	2.89E-5	
		17 13 5 1 - 17 12 6 1	345364.235	202.345	2.89E-5	
		17 13 4 0 - 17 12 5 0	345405.869	202.36	2.89E-5	B
		17 13 5 0 - 17 12 6 0	345405.869	202.36	2.89E-5	B
		16 13 3 2 - 16 12 4 2	345451.103	192.34	2.51E-5	B, LSNR
		13 13 0 0 - 13 12 1 0	345714.339	165.831	8.37E-6	B, LSNR
		13 13 1 0 - 13 12 2 0	345714.339	165.831	8.37E-6	B, LSNR
		9 9 0 0 - 8 8 1 0	345718.662	80.32	9.86E-5	B
		9 9 1 0 - 8 8 0 0	345718.662	80.32	9.86E-5	B
		28 6 23 4 - 27 6 22 4	345828.557	451.764	5.99E-4	B
		9 9 0 3 - 8 8 1 3	345908.676	268.174	1.00E-4	B
		9 9 1 3 - 8 8 0 3	345908.676	268.174	1.00E-4	B
Nitrogen Sulfide	NS	8 1 1 8.5-7 1 -1 7.5	345823.288	70.795	7.36E-4	B
		8 1 1 7.5-7 1 -1 6.5	345823.288	70.797	7.23E-4	B
		8 1 1 6.5-7 1 -1 5.5	345824.130	70.799	7.21E-4	B
Sulfur Dioxide	SO_2, v=0	11 6 6 - 12 5 7	331580.244	148.954	4.35E-5	
		13 2 12 - 12 1 11	345338.538	92.984	2.38E-4	B
	$^{34}SO_2$	21 2 20 - 21 1 21	330667.565	218.583	1.45E-4	LSNR
		10 4 6 - 10 3 7	344245.346	88.384	2.96E-4	
		9 4 6 - 9 3 7	345285.620	79.203	2.88E-4	B
Sulfur Monoxide	SO, v=0	8 8 - 7 7	344310.612	87.482	5.19E-4	B
Thioformaldehyde	H_2CS	10 0 10 - 9 0 9	342946.424	90.592	6.08E-4	
	$H_2{}^{13}CS$	10 2 8 - 9 2 7	330544.304	140.012	5.23E-4	B

Table 4.3 Molecular Transitions Detected toward SVS 13[a]

Species	Formula	Quantum Numbers	Rest Frequency[b] (MHz)	E_u/k (K)	A_{ul} (s^{-1})	Notes[c]
Unknown-1	···	···	330505.17±0.11	···	···	B
Unknown-2	···	···	330557.57±0.04	···	···	
Unknown-3	···	···	330568.63±0.05	···	···	B
Unknown-4	···	···	330622.88±0.03	···	···	B
Unknown-5	···	···	330648.70±0.06	···	···	
Unknown-6	···	···	330664.981±0.022	···	···	B
Unknown-7	···	···	331562.19±0.06	···	···	B
Unknown-8	···	···	331694.12±0.06	···	···	CB
Unknown-9	···	···	342861.84±0.04	···	···	B
Unknown-10	···	···	342905.73±0.06	···	···	
Unknown-11	···	···	342995.74±0.06	···	···	B
Unknown-12	···	···	342998.23±0.05	···	···	
Unknown-13	···	···	344123.73±0.04	···	···	
Unknown-14	···	···	344280.87±0.07	···	···	B
Unknown-15	···	···	345302.08±0.13	···	···	
Unknown-16	···	···	345319.641±0.020	···	···	
Unknown-17	···	···	345411.12±0.06	···	···	B
Unknown-18	···	···	345445.62±0.02	···	···	
Unknown-19	···	···	345700.72±0.09	···	···	B
Unknown-20	···	···	345911.608±0.025	···	···	
Unknown-21	···	···	342832.15±0.13	···	···	4A, B
Unknown-22	···	···	342905.45±0.07	···	···	4A, B
Unknown-23	···	···	342909.61±0.06	···	···	4A, B
Unknown-24	···	···	342913.49±0.10	···	···	4A, B
Unknown-25	···	···	342962.08±0.08	···	···	4A, B
Unknown-26	···	···	344213.75±0.22	···	···	4A, B
Unknown-27	···	···	345354.36±0.14	···	···	4A, B
Unknown-28	···	···	345430.74±0.17	···	···	4A, B, W

[a] From spectra obtained in beam-size ($0\farcs16 \times 0\farcs08$, P.A. = 0°) regions toward VLA 4A, VLA 4B, and the geometric center of the components.

[b] For identified transitions, this is the laboratory frequency reported in the catalogs used (JPL, CDMS, VASTEL). For unidentified transitions, this is derived from a Gaussian fit to the line and we report the formal error of the fit. In general, we used for the fit the spectrum taken toward the geometric center of the components (systemic velocity of 8.75 km s^{-1}). In the cases where the unidentified line is detected only toward VLA 4A, we used for the fit the spectrum taken toward this component (systemic velocity of 7.3 km s^{-1}). When the unidentified line is blended with known lines, the same FWHM was used for all during the fit. We only report intense ($> 10\sigma$) unidentified lines.

[c] 4A: detected only toward VLA 4A; CB: detected only in the circumbinary material, toward the geometric center of the components; B: blended with a line at a different rest frequency; DI: doubtful identification; LSNR: low ($< 5\sigma$) signal-to-noise ratio; NRM: not well reproduced by the LTE model; W: wide, there is probably a blending of several lines.

Alternatively, the lack of detection of several molecular transitions toward VLA 4B could reflect the fact that the continuum emission peak toward VLA 4B has a very high optical depth that makes difficult the observation of line emission at this position. Recently, De Simone et al. (2020) have suggested that some reported differences in the COM detections toward binary protostars that have been attributed to differences in the chemical activity of the two binary components, could, in fact, be due to a high dust opacity that would hide the molecular lines. This effect could be taking place for some molecular transitions in the SVS 13 binary. However, the high sensitivity of our observations allow us to confirm that COMs are present in both component of the SVS 13 binary and, therefore, that both components are "bona fide" hot corinos.

4.3.4.3 Circumstellar Molecular Gas

We interpreted the presence of compact 0.9 mm continuum emission directly associated with VLA 4A and VLA 4B as tracing circumstellar disks of dust with sizes of $\sim$ 20 au associated with these objects (see Fig. 4.8 and discussion in Section 4.3.2). On the other hand, the maps presented in Figure 4.11 and discussed in Section 4.3.4.1 show that both the integrated intensity (zero-order moment) and the velocity dispersion (second-order moment) of the observed molecular emission clearly peak toward VLA 4A and (less clearly, likely because of the high optical depth of the dust) tend to increase in the proximity of VLA 4B. This suggests that the two protostars are also associated with circumstellar molecular emission.

This association of molecular gas at circumstellar scales is nicely illustrated by some transitions of the ethylene glycol molecule which are only detected toward VLA 4A, as Figure 4.14 shows. The top panels in Figure 4.14 show the integrated emission of different transitions of ethylene glycol which is clearly associated with VLA 4A at circumstellar scales. These panels also show the presence of a clear velocity gradient in the E-W direction which is consistently detected in all these transitions (note that the righter-most panels include two blended transitions). The bottom panels in Figure 4.14 show position-velocity cuts along a P.A. = 90° to better unveil the structure of this gradient, which is suggestive of rotation motions associated with VLA 4A. Figure 4.15 further illustrates the distribution of the blue- and red-shifted emission, integrated over two separate velocity ranges, of the transition displayed in the left panel of Figure 4.14.

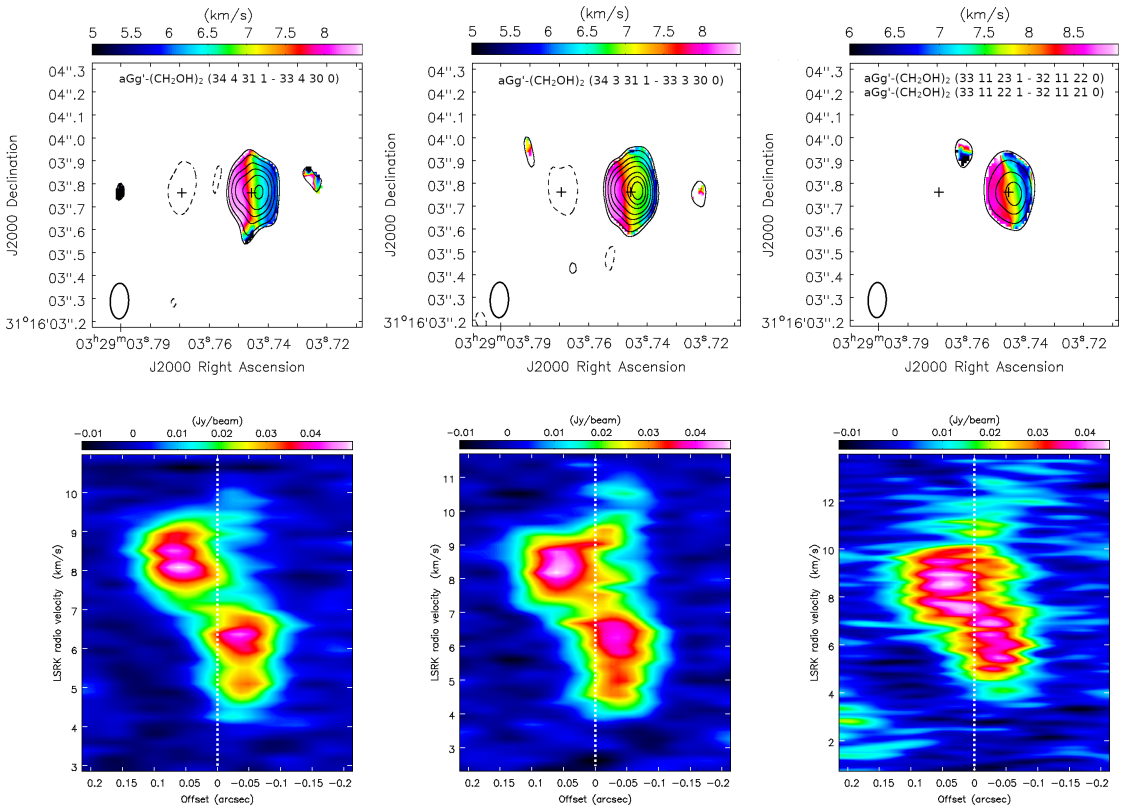

Figure 4.14 Continuum-subtracted velocity-integrated emission (zeroth-order moment; contours) and intensity-weighted mean velocity (first-order moment; color scale in top panels) of the ethylene glycol (aGg'-$(CH_2OH)_2$ conformer) lines directly associated with component VLA 4A of SVS 13 that have been detected with ALMA. Contours are −3, 3, 5, 9, 13, 18, 25, 30, and 35 times 4.5 mJy beam^{-1} km s^{-1} (left and middle top panels), and 15 mJy beam^{-1} km s^{-1} (right top panel). Synthesized beam (indicated in the bottom left corner of the maps) is $0\farcs15 \times 0\farcs08$, P.A. $= -2°$. The positions of VLA 4A (western) and VLA 4B (eastern) are marked with plus signs. The E-W velocity gradients are clearly observed. The lower panels show the corresponding position-velocity diagrams along the E-W direction centered on the position of VLA 4A. Offsets are in Right Ascension coordinates relative to VLA 4A. Transitions are indicated in the upper panels. Note that the righter-most panels include the emission of two blended transitions.

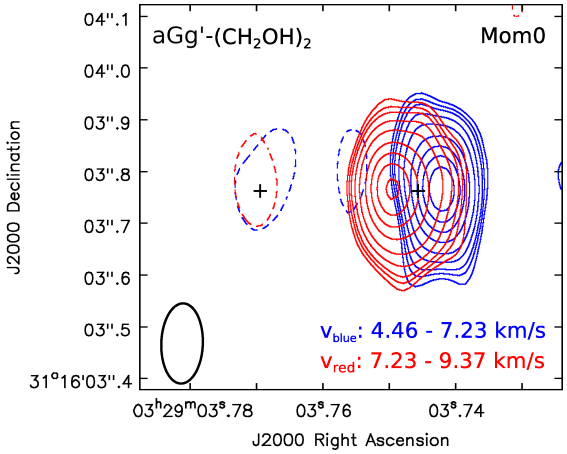

Figure 4.15 Continuum-subtracted emission of the ethylene glycol —transition (34 4 31 1 - 33 4 30 0) of the aGg'-$(CH_2OH)_2$ conformer; left panel of Fig. 4.14— associated with the component VLA 4A of SVS 13. The emission has been integrated over two velocity ranges, from 4.46 to 7.23 km s^{-1} (blue contours) and from 7.23 to 9.37 km s^{-1} (red contours), to illustrate the two velocity components observed toward VLA 4A. Contours are −3, 3, 4, 5, 7, 10, 15, 20, 25, 30, and 35 times 2.5 mJy $beam^{-1}$ km s^{-1}. The positions of VLA 4A (western) and VLA 4B (eastern) are marked with plus signs. The synthesized beam is indicated in the bottom left corner.

4.3.5 Physical and Chemical Parameters of the SVS 13 System and its Close Environment

4.3.5.1 Temperature and Molecular Column Densities

We can use the detected molecular transitions to estimate the kinetic temperature by inferring the excitation temperature of the rotational levels, also known as the rotational temperature, $T_{\rm rot}$. For this, we used CASSIS to build rotational diagrams to derive the temperature and the column density, assuming optically thin lines and LTE. In this case, the upper-level column density

$$N_u = \frac{8\pi k\nu^2}{hc^3 A_{ul}} \int T_{\rm mb}\, dV \tag{4.1}$$

and the rotational temperature $T_{\rm rot}$ are related as

$$\ln \frac{N_u}{g_u} = \ln N_{\rm mol} - \ln Q\,(T_{\rm rot}) - \frac{E_u}{kT_{\rm rot}}, \tag{4.2}$$

where k is the Boltzmann's constant, h is the Planck's constant, c is the speed of light, ν is the frequency of the transition and A_{ul} its Einstein coefficient for spontaneous emission, g_u is the statistical weight of the upper level and E_u its energy, $N_{\rm mol}$ is the total column density of the molecule, $Q(T_{\rm rot})$ is the partition function for $T_{\rm rot}$, and $\int T_{\rm mb}\, dV$ is the integrated main beam brightness temperature of the line, which is derived from a Gaussian fit to the observed molecular line.

We use only molecular lines that have been positively identified and well reproduced by the LTE model, with energies that span over a relatively large range, and that are non-blended, or, in case they are blended, we were able to isolate them by a multi-component Gaussian fitting taking into account all the blended lines involved. These selection criteria allow us to populate the diagrams only for a few molecules (CH_3OCHO, CH_2DOH, and aGg'-$(CH_2OH)_2$); in the case of aGg'-$(CH_2OH)_2$ this is possible only toward VLA 4A.

In Figure 4.16 we show the rotational diagrams toward the positions of VLA 4A, VLA 4B, and toward the geometric center of the system (CB, that we adopt as representative of the circumbinary disk). In Table 4.4 we report the rotational temperatures and column densities derived from these diagrams. From CH_3OCHO and CH_2DOH we obtain similar temperatures of $\sim$ 140 K toward both VLA 4A and the central position CB. From ethylene glycol (aGg'-$(CH_2OH)_2$), a molecule emitting in a small region around VLA 4A, we find a slightly higher value, $T_{\rm rot} \simeq 145$ K, toward this position. Therefore, we conclude that there are no substantial differences in rotational temperature between these two positions. On the other hand, our two temperature measurements toward VLA 4B give values of 90$\pm$6 and 160$\pm$39 K; since the observed molecular emission toward this position could be more affected by dust opacity effects (see Section 4.3.4.2), we consider these values of $T_{\rm rot}$ as less reliable, and we adopt 140 K as a representative value of the kinetic temperature for all the positions, including VLA 4B. Indeed, the peak brightness temperature towards VLA 4B in our highest angular resolution continuum map (Fig. 4.8) is $\sim$ 140 K, strongly suggesting optically thick dust emission with this kinetic temperature.

Belloche et al. (2020b), from a large number of molecular transitions with data at lower frequencies and poorer angular resolution that did not separate the binary, obtained a wide range of rotational temperatures, from $\sim$ 30 K to $\sim$ 350 K. However, when considering only the values with signal-to-noise ratio higher than 3.5σ their temperatures range from $\sim$ 100 - 200 K, which are in better agreement with ours. For the two molecules we have in common (CH_3OCHO

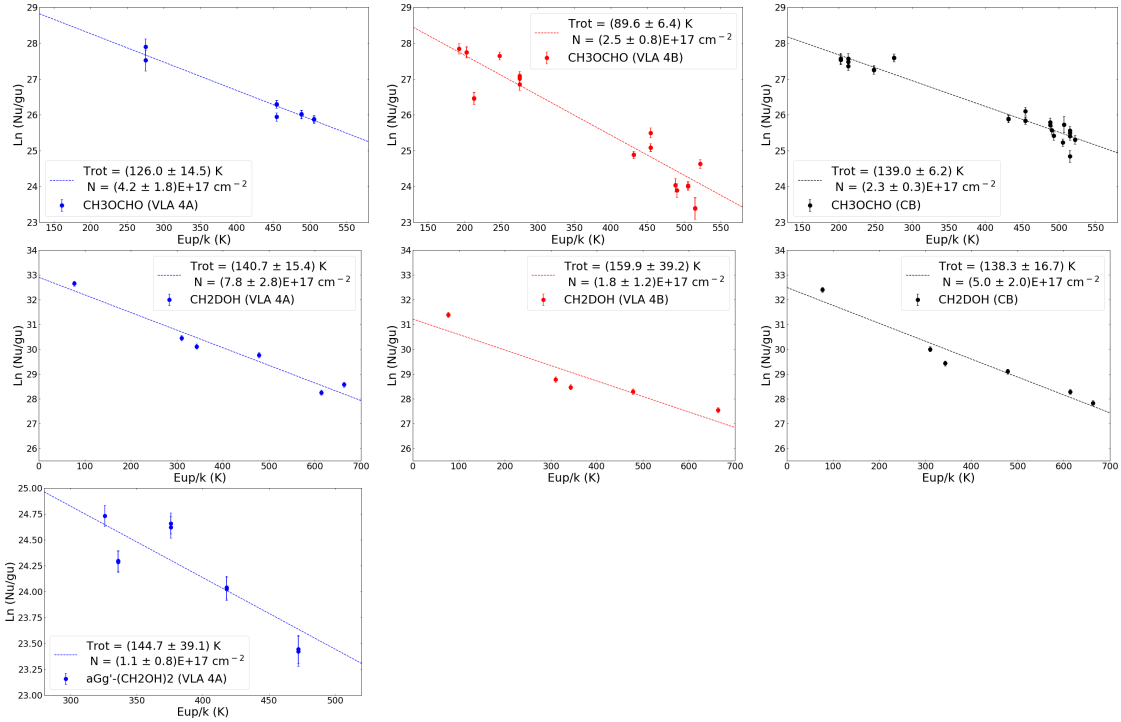

Figure 4.16 Rotational diagrams for methyl formate (CH_3OCHO), deuterated methanol (CH_2DOH) and ethylene glycol (aGg'-$(CH_2OH)_2$), for VLA 4A (blue), VLA 4B (red), and the circumbinary disk (black), using spectra taken in beam-size regions toward each component and toward the geometric center of the system (shown in Fig. 4.13). We only include in the plot lines that have been positively identified and well reproduced by the LTE model, that are non-blended, or, in case they are blended, that we were able to isolate by a multi-component Gaussian fit. In the case of aGg'-$(CH_2OH)_2$ this is possible only toward VLA 4A.

and aGg'-$(CH_2OH)_2$) the temperatures obtained by Belloche et al. (2020b) are $\sim$ 100 K, which are somewhat lower than our values.

The molecular column density of CH_3OCHO obtained by these authors is 2.1×10^{17} cm^{-2}, which is a factor ~ 2 lower than the value we find toward VLA 4A, but similar to the column density we find in the rest of the source (Table 4.4). For aGg'-$(CH_2OH)_2$, which we only detect toward the position of VLA 4A, Belloche et al. (2020b) found a column density of 1.3×10^{16} cm^{-2}, which is about one order of magnitude lower than the value we obtained. We attribute these discrepancies to the non-uniform distribution of this molecular emission, as revealed by our higher angular resolution data, which is smeared within the larger beam of the Belloche et al. (2020b) observations, resulting in lower averaged values. We point out that the rotational diagrams presented in Belloche et al. (2020b) have an error in the labeling of the y-axis units (Belloche et al. 2020a). Our diagrams are consistent

Table 4.4 Rotational Temperatures and Molecular Column Densities

Molecule	VLA 4A			VLA 4B			CB[a]		
	$T_{\rm rot}$[b] (K)	$N_{\rm mol}$[b] ($\rm cm^{-2}$)	$X_{\rm mol}$[c]	$T_{\rm rot}$[b] (K)	$N_{\rm mol}$[b] ($\rm cm^{-2}$)	$X_{\rm mol}$[c]	$T_{\rm rot}$[b] (K)	$N_{\rm mol}$[b] ($\rm cm^{-2}$)	$X_{\rm mol}$[c]
CH_3OCHO	127(14)	$4.1(1.6)\times10^{17}$	5.6×10^{-8}	90(6)	$2.5(0.8)\times10^{17}$	2.3×10^{-8}	139(6)	$2.3(0.3)\times10^{17}$	1.3×10^{-7}
CH_2DOH	141(15)	$7.8(2.8)\times10^{17}$	1.1×10^{-7}	160(39)	$1.8(1.2)\times10^{17}$	1.6×10^{-8}	138(17)	$5.0(2.0)\times10^{17}$	2.7×10^{-7}
aGg'-$(CH_2OH)_2$	145(39)	$1.1(0.8)\times10^{17}$	1.5×10^{-8}	...	...	...	...	...	...
$^{13}CH_3OH$	...	...	...	...	...	...	...	8×10^{16}	4.4×10^{-8}
$CH_3{}^{18}OH$	...	...	...	...	...	...	...	3×10^{16}	1.7×10^{-8}
CH_3OH	...	...	...	...	...	...	...	$(0.6\text{-}1.7)\times10^{19}$	$(3.3\text{-}9.4)\times10^{-6}$
H_2	...	7.4×10^{24}	1	...	1.1×10^{25}	1	...	1.8×10^{24}	1

[a] Central position, between VLA 4A and VLA 4B, taken as representative of the circumbinary material.

[b] Rotational temperature and molecular column density obtained from the rotational diagram fits shown in Fig. 4.16, for CH_3OCHO, CH_2DOH, and aGg'-$(CH_2OH)_2$. The values into parentheses are the formal errors of the fits. For $^{13}CH_3OH$ and $CH_3{}^{18}OH$, molecular column densities are obtained from the observed spectra assuming $T_{\rm rot}$ = 140 K. The CH_3OH column densities are obtained from those of its isotopologues, $^{13}CH_3OH$ (lower value) and $CH_3{}^{18}OH$ (higher value), assuming $^{12}C/^{13}C = 77$ and $^{16}O/^{18}O = 560$. The H_2 column density is calculated from the dust emission, assuming optically thin emission, a dust temperature of 140 K, and a gas-to-dust ratio of 100. See text for further details.

[c] Molecular abundance relative to H_2.

with those after the proper correction is performed. The rotational temperatures obtained from these diagrams, and the column densities reported by these authors, which were obtained from radiative transfer models, are not affected by the error.

We detected four transitions of the main isotopologue of methanol (CH_3OH). However, these transitions appear to be optically thick and the lines are saturated, so we cannot derive reliable values of the molecular column density directly from these data. Fortunately, we detected the isotopologues $^{13}CH_3OH$ and $CH_3{}^{18}OH$, which are optically thinner, and are therefore more suitable for deriving column densities. However, the number of detected transitions of these isotopologues is insufficient to construct rotational diagrams for a temperature and column density fitting. So, we have adopted a temperature of 140 K to obtain the column densities that provide the best fit to the observed spectra, assuming optically thin emission and LTE. Finally, we have calculated the methanol column density assuming $^{12}C/^{13}C = 77$ and $^{16}O/^{18}O = 560$ (Wilson & Rood 1994).

In Table 4.4 we report the values found toward the center of the circumbinary disk (CB), a position in between VLA 4A and VLA 4B (the analysis toward the positions of the protostars is more challenging since the lines are wider and difficult to separate from other lines). The methanol column density is $(0.6 - 1.7)\times10^{19}$ $\rm cm^{-2}$ towards CB, and drops to $(0.8 - 2.8)\times10^{18}$ $\rm cm^{-2}$, and to $(2.3 - 4.5)\times10^{18}$ $\rm cm^{-2}$, for positions $0\farcs2$ offset to the north (close to spiral S3) and the south (close to spiral

S1) of CB, respectively. In all these estimates, the lower value is obtained from the $^{13}CH_3OH$ isotopologue and the higher value is obtained from $CH_3{}^{18}OH$. If the isotopic ratios were as assumed and the emission of both isotopologues was optically thin, we would expect the $^{13}CH_3OH$ column density to be a factor $560/77 \simeq 7$ higher than the $CH_3{}^{18}OH$, resulting in the same derived methanol column density in both cases. However, the ratio of isotopologue column densities obtained is ~ 3, smaller than expected, indicating that either the $^{13}CH_3OH$ emission is optically thick or that the isotopic ratios are somewhat different than assumed. Since this ratio is similar towards positions away from the center (where the column density has decreased and the emission is expected to become optically thinner), the discrepancy does not seem to be due to opacity effects. Therefore, we conclude that the ^{13}C isotope is probably somewhat more abundant and/or the ^{18}O less abundant than we have assumed. Thus, we will adopt intermediate values for the methanol column densities, resulting $\sim 1 \times 10^{19}$ cm^{-2} toward CB.

Belloche et al. (2020b) found a lower value of 2×10^{18} cm^{-2} for the methanol column density in SVS 13. As discussed above, we attribute this discrepancy to the larger beam of those observations. On the other hand, our derived values would imply a deuteration fraction of 0.05, similar to values found in other low-mass protostars (Taquet et al. 2019).

We also derive the H_2 beam-averaged column densities from the dust emission, assuming optically thin emission, a dust temperature of 140 K (from the rotational diagrams), a gas-to-dust ratio of 100 (Bohlin et al. 1978), and a dust opacity $\kappa_\nu(0.9\ \mathrm{mm}) = 1.65\ \mathrm{cm}^2\ \mathrm{g}^{-1}$ (per unit mass of dust). The value of $\kappa_\nu(0.9$ mm) was obtained by interpolating the values at 0.7 mm and 1 mm from Ossenkopf & Henning (1994) and should be adequate for protostellar objects where the dust grain growing is still incipient. These dust opacities have been obtained by including thin ice mantles in an MRN model (Mathis, Rumpl & Nordsieck 1977), consisting of a mixture of spherical silicate and graphite grains with separated power-law particle size distributions. Since we assumed optically thin emission, the values derived for the H_2 column densities are lower limits in this respect; however, the presence of temperature gradients, uncertainties in the dust opacity and in the gas-to-dust ratio can be important and difficult to estimate. Therefore these results should be taken with caution. We find a 50% higher H_2 column density toward VLA 4B than toward VLA 4A, while there is a decrease by a factor of ~ 5 toward the central position (CB) between the two protostars, and by a factor of ~ 12 - 14 when moving $0\farcs2$ to the north or to the south of this central position. Using these

estimated column densities, in Table 4.4 we also show the abundances relative to H_2 of the discussed molecules.

4.3.5.2 Masses from Dust

Once we have an estimate of the temperature, we can derive masses from the observed 0.9 mm continuum emission, which traces thermal dust emission (since the expected free-free contribution at this short wavelength is negligible). Assuming optically thin emission from an isothermal source, the observed flux density is directly related to the total mass of emitting material as:

$$M = \frac{S_\nu D^2}{\kappa_\nu B_\nu(T_{\rm dust})}, \tag{4.3}$$

where D is the distance to the source, S_ν is the flux density, κ_ν is the dust opacity at the observed frequency ν, $B_\nu(T_{\rm dust})$ is the Planck function, and $T_{\rm dust}$ is the dust temperature that we will assume equal to $T_{\rm rot}$. If the dust emission is not optically thin, then this mass will be a lower limit. As in the previous Section, we adopt a dust opacity $\kappa_\nu(0.9\ {\rm mm}) = 1.65\ {\rm cm^2\ g^{-1}}$ and assume a gas-to-dust ratio of 100.

Given the uncertainties involved and the fact that we do not observe large variations of rotational temperature from one position to another, we will assume a single value of the dust temperature for all the positions. Using eq. (4.3), the flux densities in Table 4.2, and a dust temperature of $\sim$ 140 K (from the rotational diagrams presented in Section 4.3.5.1), we calculate the total (dust+gas) masses of the disks. We obtain $M_{\rm CS}(4{\rm A}) \simeq 0.005\ M_\odot$, $M_{\rm CS}(4{\rm B}) \simeq 0.006\ M_\odot$, and $M_{\rm CB} \simeq 0.06\ M_\odot$, for the circumstellar disks associated with VLA 4A, VLA 4B, and the circumbinary, respectively.

These values of the masses could be underestimated if the dust emission is not optically thin enough. To test this possibility we have calculated the dust mass of the circumbinary material using lower frequency data from the literature (Table 4.2) obtaining higher values of the mass by a factor of a $\sim$ 3. Therefore, we estimate that our masses derived from dust are underestimated by a factor of a few.

4.3.5.3 Dynamical Masses

An additional way to obtain the masses is from the measured velocities, using dynamical equations. For a gravitationally bound system of two objects in orbital motion, the orbital period is given by:

$$\left(\frac{P}{\mathrm{yr}}\right) = \left(\frac{a}{\mathrm{au}}\right)^{3/2} \left(\frac{M_{\mathrm{tot}}}{M_{\odot}}\right)^{-1/2}, \tag{4.4}$$

where M_{tot} is the total mass of the system and a is the separation between the two components.

Equivalently,

$$\left(\frac{M_{\mathrm{tot}}}{M_{\odot}}\right) = 1.12 \times 10^{-3} \left(\frac{a}{\mathrm{au}}\right) \left(\frac{V_{\mathrm{rel}}}{\mathrm{km\ s^{-1}}}\right)^{2}, \tag{4.5}$$

where V_{rel} is the relative velocity between the two objects.

From the observed proper motions of the VLA 4A and VLA 4B protostars, and using eq. (4.5), we can estimate the stellar masses. First, we obtain the 3D relative velocity by adding quadratically the observed proper motions in RA (0.6 km s^{-1}) and Dec (2.3 km s^{-1}), with the relative radial velocity (2.2 km s^{-1}) inferred from the molecular lines detected toward the positions of VLA 4A and VLA 4B (Section 4.3.4.2), resulting in V_{rel} = 3.2 km s^{-1}. Then, taking into account that the separation is a = 90 au, from eq. (4.5) we obtain a total mass of the system of 1.0 $M_{\odot}$.

In principle, from the observed gradients in the first-order moment maps (Fig. 4.11) one could obtain a dynamical estimate of the total mass (stars+disks). However, the likely high optical depth of the brighter molecular transitions, the complex structure of the source, and the expected presence of infall motions that would require detailed modeling to infer reliable values of the mass, prevent us from attempting this calculation.

Nevertheless, we can discuss the implications of the observed velocity gradient toward VLA 4A from the ethylene glycol data (Figs. 4.14 and 4.15). The position-velocity diagrams in the lower panels of Figure 4.14 show the presence of a clear velocity gradient in the E-W direction which is consistently detected in all these transitions (note that the righter-most panels include two blended transitions). This gradient is suggestive of rotation motions associated with VLA 4A. As can be seen in this figure and in Figure 4.15, there are two sharply differentiated velocity components that we interpret may be tracing either the receding (eastern) and approaching (western) sides of a circumstellar rotating disk around VLA 4A. Alternatively, the two velocity components could be tracing molecular gas associated with two different objects orbiting one around each other.

If it is assumed that the observed gradients originate from a rotating disk around the VLA 4A protostar, we infer a disk radius of $\sim 0\farcs05$ ($\sim$ 15 au) and a rotation velocity of $\sim$ 1.5 km s^{-1} (component along the line-of-sight). Assuming an inclination angle of about 45°, as suggested by the elongation of the molecular emission (see Section 4.3.4.1) and the ratio of proper motions to radial velocity (see above), we obtain a deprojected rotation velocity of 2.1 km s^{-1}, resulting in a stellar mass of 0.07 $M_\odot$ for VLA 4A. This value would imply that the primary would be VLA 4B with a stellar mass of 0.93 $M_\odot$.

However, since the characteristic curvature of the Keplerian profiles is not clearly seen, we consider the possibility that the observed gradient toward VLA 4A corresponds to two orbiting objects. In this case, their relative line-of-sight velocity would be $\sim$ 3 km s^{-1} and the separation 30 au, resulting in a total mass of 0.6 $M_\odot$ for VLA 4A, assuming an inclination angle of the orbital plane of this system of 45°, coplanar to that of the main binary. Under this hypothesis, VLA 4A would be, in its turn a binary, and the resulting mass of VLA 4B would be 0.4 $M_\odot$. Furthermore, the presence of dust toward VLA 4A and the position-velocity diagrams suggest that each of the two subcomponents of VLA 4A could be associated, in its turn, with an angularly unresolved ($\lesssim 0\farcs1$ in size) disk with a total velocity range of its associated emission of $\sim$ 2 - 3 km s^{-1}, implying individual stellar masses of the subcomponents of about 0.05 - 0.1 $M_\odot$, depending on the assumed inclination angles. The total mass implied by this calculation $\sim$ 0.1 - 0.2 $M_\odot$, is significantly smaller than the value of 0.6 $M_\odot$ inferred from their orbital motion. Therefore, given the uncertainties involved and that there are not strong arguments to favor any of the two possibilities, we consider that the current data are insufficient to draw a robust conclusion regarding whether VLA 4A is a single star surrounded by a rotating disk of dust or two stars, each associated with its own rotating disk.

4.4 Summary and Conclusions

We carried out a comprehensive study of the protobinary system associated with the SVS 13 star in the region of NGC 1333. We have clarified the properties and physical structure at a very small scale thanks to the high-angular resolution and sensitive VLA and ALMA observations. However, a number of important questions are still remaining. Here we summarize our main conclusions and remaining uncertainties:

1. We confirm that SVS 13 is a multiple protostellar system with at least two embedded protostars, known as VLA 4A and VLA 4B, being associated with free-free emission. Up to four stellar objects, one of them a visible star, could be present within a region < 100 au.

2. At least two circumstellar disks of dust and gas, and one circumbinary/circum-multiple disk with prominent spiral arms, that appears to be in the earliest stages of formation, are associated with this protostellar system.

3. Dust emission appears more intense and compact toward VLA 4B, while VLA 4A seems to be associated with a larger amount of dust and with stronger molecular transitions.

4. Molecular transitions typical of hot corinos are detected toward both VLA 4A and VLA 4B. We are able to estimate rotational temperatures and molecular column densities, indicating hot temperatures and rich chemistry.

5. Orbital proper motions have been inferred from high-resolution data taken over 30 years. However, most of the positions are obtained from free-free emission that can be affected by episodic ejections of ionized material. Since the emission at 7 mm and shorter wavelengths is strong enough, accurate results can be obtained with future VLA and ALMA observations based on the dust emission.

6. Proper motions, spiral arms, and radial velocity gradients in both circumstellar and circumbinary disks have been observed. All of them indicate rotation in the same direction, and there is a hint that there is a connection with larger structures in the surrounding environment.

7. From the observed dust emission and the kinematical information, we estimate the orientation of the system, the stellar masses, and the mass of their associated disks. Estimated stellar masses are of the order of 0.5 $M_{\odot}$ and disk masses of the order of 0.1 $M_{\odot}$, but uncertainties are large.

8. In summary, SVS 13 seems to be an excellent test-bed to test numerical simulations of the earliest stages in the formation of binary and multiple systems.

Chapter 5

Summary and Conclusions

In this work we present and discuss new, sensitive, high-angular resolution VLA and ALMA data at cm and mm wavelengths toward two regions of active, non-isolated star formation: A region centered on the two bright far-infrared sources FIR 3 (HOPS 370) and FIR 4 (HOPS 108), in the OMC-2/3 region of the Orion Molecular Cloud, and a region centered on the binary system associated with the star SVS 13, in the NGC 1333 star-forming region. The main aim of our work is to better understand how the standard paradigm of isolated star formation is modified in a realistic scenario with multiple stars forming simultaneously. In the OMC 2/3 region we focus our study on the deeply embedded cluster of protostars traced by their cm continuum emission to infer their nature and interactions. For SVS 13 system we analyze the dust, and the ionized and molecular gas from its close environment to study the first stages in the formation of the stellar binary, and the circumstellar and the circumbinary disks.

Our main conclusions can be summarized as follows:

1. We discovered a powerful radio jet associated with the intermediate-mass HOPS 370 protostar in OMC-2. The radio jet shows a highly collimated bipolar thermal (free-free) core (VLA 11), at scales of ∼200-300 au from the protostar, and a non-thermal lobe, at distances of 7500-12500 au to the south-west. The non-thermal knots of the radio jet move away from the protostar at velocities of ∼40-100 km/s in a region of strong shocks, suggesting that their non-thermal emission is likely synchrotron emission from relativistic electrons accelerated in these shocks.

2. The Class 0 protostar HOPS 108 is identified as a compact radio source independent and kinematically separated from the radio emission of the knots

of the HOPS 370 radio jet. Its position along the path of the HOPS 370 jet, coincident with different shock tracers, suggests a scenario where the formation of HOPS 108 has been triggered by the interaction of the HOPS 370 jet with the surrounding medium. This is one of the best candidates for triggered star formation ever identified. However, the possibility of a very high stellar proper motion is intriguing.

3. Overall, we detect and characterize the properties of 57 radio sources in a region of 1.5 pc in diameter, comprising the southernmost part of the OMC-3 region and the whole OMC-2 region. We find that 41 (72%) out of these 57 radio sources are associated with the OMC-2/3 star-forming region. For 36 of them, we positively identify their nature as young stellar objects in different evolutionary stages, from Class 0 to Class III.

4. Our high-resolution detection of free-free emission complements previous high-resolution detections of thermal dust emission, attributed to circumstellar disks, allowing us to establish a more complete picture of potential jet/disk systems in the OMC-2/3 region. Outstanding cases, in addition to HOPS 370 (VLA 11), are Source 1, Source 11, and Source 42, where we image well-collimated radio jets, perpendicular to their elongated circumstellar disks.

5. We investigate the multiplicity of our OMC-2/3 sample of radio sources in a range of projected distances between 154 and 3000 au. We detect at radio wavelengths components of 11 possible binary systems, two possible triple systems, three possible quadruple systems, and one possible quintuple system, for a total of 17 potential multiple systems, where additional known objects at other wavelengths have been included.

6. We verify the empirical correlation between radio and bolometric luminosities, which is assumed to link the processes of accretion and outflow in very young stellar objects, for all but four of the 31 HOPS far-IR sources located within our field of view. For three of the four sources that are radio-underluminous (HOPS 64, 108, and 369) we suggest that external heating from nearby shocks could have an important contribution to the bolometric luminosity; for the other source (HOPS 56) the ionization mechanism seems to be less efficient than expected.

7. We confirm that SVS 13, in the NGC 1333 star-forming region, is a multiple protostellar system with at least two embedded protostars, known as VLA 4A and VLA 4B, being associated with free-free emission. Up to four different stellar objects, one of them a visible star, could be present within a region < 100 au.

8. At least two circumstellar disks of dust and gas, and one circumbinary/circum-multiple disk with prominent spiral arms, that appears to be in the earliest stages of formation, are associated with this protostellar system. Dust emission appears more intense and compact toward the eastern component, VLA 4B, while VLA 4A seems to be associated with a larger amount of dust and with stronger molecular transitions.

9. Molecular transitions typical of hot corinos are detected toward both VLA 4A and VLA 4B. From them, we are able to estimate rotational temperatures and molecular column densities, indicating hot temperatures and rich chemistry.

10. We have inferred orbital proper motions from high-resolution data of SVS 13 taken over 30 years. However, most of the positions are obtained from free-free emission that can be affected by episodic ejections of ionized material. Since the emission at 7 mm and shorter wavelengths is strong enough, we expect that more accurate results will be obtained with future VLA and ALMA observations based on the dust emission.

11. We have observed proper motions, spiral arms, and radial velocity gradients in both circumstellar and circumbinary disks of SVS 13. All of them indicate rotation in the same direction, with a hint of a connection with larger structures in the surrounding environment.

12. Although uncertainties are still large, from the observed dust emission and the kinematical information we can estimate the orientation of the SVS 13 system, the stellar masses, and the mass of their associated disks. Estimated stellar masses are of the order of 0.5 $M_{\odot}$ and disk masses of the order of 0.1 $M_{\odot}$.

5.1 Future work

In this thesis we make a proposal on what is the nature of most of the radio sources detected in our field of view of the OMC-2/3 region. Several follow-up observations can help to obtain more robust results. For example, the detection of optical and mid-IR forbidden line emission could help to confirm our proposed photo-evaporating disks; accurate proper motion measurements can help to distinguish between galactic and extragalactic sources; proper motion studies can also help to confirm that the proposed multiple systems are indeed gravitationally bound. Additional multi-epoch and multi-frequency radio observations could shed light on interesting cases, like the sources that appear as underluminous in the Anglada correlation between radio and bolometric luminosities, or the very young sources that present high radio variability.

An intriguing result is the apparent high proper motion velocity (of about 30 km s^{-1}) estimated for HOPS 108, the Class 0 protostar proposed as a triggered star-formation candidate. Although the current uncertainties are very large, given the difficulties in the measurements at centimeter wavelengths due to the proximity to the HOPS 370 jet lobe emission, future observations at shorter wavelengths over a long enough time baseline can provide accurate velocity measurements. This would allow us to ascertain whether HOPS 108 is compatible with a triggered star-formation scenario or whether it is a runaway star candidate.

Finally, we emphasize that our study of the OMC-2/3 region would serve as a starting point for future surveys of star-forming regions with upcoming powerful instruments such as the Next Generation VLA (ngVLA) and the Square Kilometre Array (SKA). In particular, our methodology to classify the nature of the radio sources, in combination with machine-learning techniques, could prove useful when dealing with the large number of sources expected in those surveys.

So far, only a few close (i.e., with separations between components of $\sim$100 au or less) protobinary/multiple systems, where the interaction between components is most important, have been identified. Among them, and after our work, SVS 13 has certainly become one of the best characterized in its physical and chemical properties. Despite all the remaining uncertainties, this makes it an excellent test-bed for numerical simulations of the earliest stages in the formation of binary and multiple systems. Our work is only a first step into revealing the complexities of this system that can still be better studied, even with the currently available instrumentation. For example, the existence of a third, or even a fourth, compo-

nent in the system can be further investigated. A confirmation of the coincidence, or independence, of the optical and radio (VLA 4B) components can be obtained when refined GAIA proper motions are available. Additional radio proper motions (from the dust emission observed with the VLA or ALMA) would provide the means to derive accurate orbital parameters of the system. The system can be studied with a still higher angular resolution with ALMA, which could clarify the presence of one or two objects associated with the western component, VLA 4A. Detection of complex organic molecules (COMs) at lower frequencies, where the dust emission toward VLA 4B would be lower, could also be attempted. Detection of circumstellar gas directly associated with VLA 4B would be a decisive step in the full dynamical characterization of the system. Additionally, our data provide the means to perform a future in-depth study of the rich chemistry toward this system and to investigate the nature of the spirals structures detected in the circumbinary disk in conjunction with additional molecular data.

Bibliography

Adams, F. C., Lada, C. J., & Shu, F. H. 1987, ApJ, 312, 788

Adams, F. C., & Shu, F. H. 1986, ApJ, 308, 836

Adams, J. D., Herter, T. L., Osorio, M., et al. 2012, ApJ, 749, L24

Alexander, R., Pascucci, I., Andrews, S., et al. 2014, Protostars and Planets VI, 475

ALMA Partnership, Brogan, C. L., Pérez, L. M., et al. 2015, ApJ, 808, L3

Alves, F. O., Caselli, P., Girart, J. M., et al. 2019, Science, 366, 90

André, P. 1996, Radio Emission from the Stars and the Sun, 273

André, P., Arzoumanian, D., Könyves, V., et al. 2019, A&A, 629, L4

André, P., Di Francesco, J., Ward-Thompson, D., et al. 2014, Protostars and Planets VI, 27

André, P., Men'shchikov, A., Bontemps, S., et al. 2010, A&A, 518, L102

André, P., Ward-Thompson, D., & Barsony, M. 1993, ApJ, 406, 122

Anglada, G. 1995, Revista Mexicana de Astronomia y Astrofisica Conference Series, 1, 67

Anglada, G. 1996, Radio Emission from the Stars and the Sun, 93, 3

Anglada, G., Estalella, R., Rodriguez, L. F., et al. 1991, A&A, 252, 639

Anglada, G., Rodriguez, L. F., Canto, J., et al. 1987, A&A, 186, 280

Anglada, G., Rodriguez, L. F., Canto, J., et al. 1992, ApJ, 395, 494

Anglada, G., Rodríguez, L. F., & Carrasco-Gonzalez, C. 2015, Advancing Astrophysics with the Square Kilometre Array (AASKA14), 121

Anglada, G., Rodríguez, L. F., & Carrasco-González, C. 2018, Astron Astrophys Rev, 26, 3

Anglada, G., Rodríguez, L. F., Osorio, M., et al. 2004, ApJ, 605, L137

Anglada, G., Rodríguez, L. F., & Torrelles, J. M. 2000, ApJ, 542, L123

Anglada, G., Villuendas, E., Estalella, R., et al. 1998, AJ, 116, 2953

Artymowicz, P., & Lubow, S. H. 1994, ApJ, 421, 651

Arzoumanian, D., André, P., Didelon, P., et al. 2011, A&A, 529, L6

Aspin, C. 2003, AJ, 125, 1480

Bacciotti, F. 2004, Ap&SS, 293, 37

Bachiller, R., Gueth, F., Guilloteau, S., et al. 2000, A&A, 362, L33

Bachiller, R., Guilloteau, S., Gueth, F., et al. 1998, A&A, 339, L49

Bally, J. 2016, ARA&A, 54, 491

Bally, J., Devine, D., & Reipurth, B. 1996, ApJ, 473, L49

Bally, J., Ginsburg, A., Arce, H., et al. 2017, ApJ, 837, 60

Bally, J., Langer, W. D., Stark, A. A., & Wilson, R. W. 1987, ApJ, 312, L45

Bally, J., & Zinnecker, H. 2005, AJ, 129, 2281

Barenfeld, S. A., Carpenter, J. M., Sargent, A. I., et al. 2019, ApJ, 878, 45

Bate, M. R. 1998, The Astrophysical Journal, 508, L95

Bate, M. R. 2000, MNRAS, 314, 33

Bate, M. R. 2004, Astrophysics and Space Science, 292, 297

Bate, M. R. 2012, MNRAS, 419, 3115

Bate, M. R. 2018, MNRAS, 475, 5618

Bate, M. R., & Bonnell, I. A. 1997, MNRAS, 285, 33

Bate, M. R., Bonnell, I. A., & Bromm, V. 2002, MNRAS, 336, 705

Bate, M. R. & Keto, E. R. 2015, MNRAS, 449, 2643

Belloche, A., Garrod, R. T., Müller, H. S. P., et al. 2020a, A&A, 637, C4

Belloche, A., Maury, A. J., Maret, S., et al. 2020b, A&A, 635, A198

Belloche, A., Parise, B., van der Tak, F. F. S., et al. 2006, A&A, 454, L51.

Beltrán, M. T., Estalella, R., Anglada, G., Rodríguez, L. F., & Torrelles, J. M. 2001, AJ, 121, 1556

Beuther, H., Schilke, P., Sridharan, T. K., et al. 2002, A&A, 383, 892

Blandford, R. D., & Payne, D. G. 1982, MNRAS, 199, 883

Blitz, L. 1993, Protostars and Planets III, 125

Bohlin, R. C., Savage, B. D., & Drake, J. F. 1978, ApJ, 224, 132

Bonnell, I. A. 1994, Monthly Notices of the Royal Astronomical Society, 269, 837

Bonnell, I. A., & Bate, M. R. 1994a, MNRAS, 269, L45

Bonnell, I. A., & Bate, M. R. 1994b, MNRAS, 271, 999

Boss, A. P. 1988, The Astrophysical Journal, 331, 370

Bourke, T. L., Crapsi, A., Myers, P. C., et al. 2005, ApJ, 633, L129

Bouwman, J., Lawson, W. A., Dominik, C., et al. 2006, ApJ, 653, L57

Briggs, D. S. 1995, Bulletin of the American Astronomical Society, 27, 112.02

Carrasco-González, C., Anglada, G., Rodríguez, L. F., et al. 2008a, ApJ, 676, 1073

Carrasco-González, C., Anglada, G., Rodríguez, L. F., et al. 2008b, AJ, 136, 2238

Carrasco-González, C., Henning, T., Chandler, C. J., et al. 2016, ApJ, 821, L16

Carrasco-González, C., Osorio, M., Anglada, G., et al. 2012, ApJ, 746, 71.

Carrasco-González, C., Rodríguez, L. F., Anglada, G., et al. 2009, ApJ, 693, L86

Carrasco-González, C., Rodríguez, L. F., Anglada, G., et al. 2010, Science, 330, 1209

Carrasco-González, C., Rodríguez, L. F., Anglada, G., et al. 2013, European Physical Journal Web of Conferences, 61, 03003

Cheetham, A. C., Kraus, A. L., Ireland, M. J., et al. 2015, ApJ, 813, 83

Chen, X., Arce, H. G., Zhang, Q., et al. 2010, ApJ, 715, 1344

Chini, R., Reipurth, B., Ward-Thompson, D., et al. 1997, ApJ, 474, L135

Cieza, L. A., Padgett, D. L., Allen, L. E., et al. 2009, ApJ, 696, L84

Condon, J. J. 1984, ApJ, 287, 461.

Conway, J. E., Cornwell, T. J., & Wilkinson, P. N. 1990, MNRAS, 246, 490

Crimier, N., Ceccarelli, C., Lefloch, B., & Faure, A. 2009, A&A, 506, 1229

Curiel, S., Canto, J., & Rodriguez, L. F. 1987, RMxAA, 14, 595

Curiel, S., Rodríguez, L. F., Cantó, J., et al. 1989, Astrophysical Letters and Communications, 27, 299

Daemgen, S., Correia, S., & Petr-Gotzens, M. G. 2012, A&A, 540, A46

Daemgen, S., Elliot Meyer, R., Jayawardhana, R., et al. 2016, A&A, 586, A12

Dai, F., Facchini, S., Clarke, C. J., et al. 2015, MNRAS, 449, 1996

D'Alessio, P. 1996, Ph.D. Thesis

Da Rio, N., Robberto, M., Hillenbrand, L. A., Henning, T., & Stassun, K. G. 2012, ApJ, 748, 14

Da Rio, N., Robberto, M., Soderblom, D. R., et al. 2009, ApJS, 183, 261

De Simone, M., Ceccarelli, C., Codella, C., et al. 2020, ApJ, 896, L3

De Simone, M., Codella, C., Testi, L., et al. 2017, A&A, 599, A121

Dong, R., Zhu, Z., Rafikov, R. R., et al. 2015, ApJ, 809, L5

Drury, L. O. 1991, MNRAS, 251, 340

Duarte-Cabral, A., Dobbs, C. L., Peretto, N., & Fuller, G. A. 2011, A&A, 528, A50

Duchêne, G., Bouvier, J., Bontemps, S., et al. 2004, A&A, 427, 651

Duchêne, G., & Kraus, A. 2013, ARA&A, 51, 269

Dzib, S. A., Loinard, L., Rodríguez, L. F., et al. 2017, ApJ, 834, 139

Eisloeffel, J., Guenther, E., Hessman, F. V., et al. 1991, ApJ, 383, L19

Estalella, R., & Anglada, G., *Introducción a la Física del Medio Interestelar*, Textos Docents, 50. Edicions UB, Barcelona, 2008 (ISBN: 978-84-475-3253-7)

Estalella, R., Anglada, G., Díaz-Rodríguez, A. K., et al. 2019, A&A, 626, A84

Fischer, W. J., Megeath, S. T., Ali, B., et al. 2010, A&A, 518, L122

Fischer, W. J., Megeath, S. T., Furlan, E., et al. 2017, ApJ, 840, 69

Fisher, R. T. 2004, ApJ, 600, 769

Font, A. S., McCarthy, I. G., Johnstone, D., et al. 2004, ApJ, 607, 890

Forbrich, J., Rivilla, V. M., Menten, K. M., et al. 2016, ApJ, 822, 93

Frank, A., Ray, T. P., Cabrit, S., et al. 2014, Protostars and Planets VI, 451

Fűrész, G., Hartmann, L. W., Megeath, S. T., Szentgyorgyi, A. H., & Handen, E. T. 2008, ApJ, 676, 1109-1122

Furlan, E., Fischer, W. J., Ali, B., et al. 2016, ApJS, 224, 5

Furlan, E., Megeath, S. T., Osorio, M., et al. 2014, ApJ, 786, 26

Gaia Collaboration, Brown, A. G. A., Vallenari, A., et al. 2018, A&A, 616, A1

Garay, G., Brooks, K. J., Mardones, D., et al. 2003, ApJ, 587, 739

Garay, G., Ramirez, S., Rodriguez, L. F., et al. 1996, ApJ, 459, 193

Gerin, M., Pety, J., Fuente, A., et al. 2015, A&A, 577, L2

Getman, K. V., Broos, P. S., Kuhn, M. A., et al. 2017, ApJS, 229, 28

Ghez, A. M., Neugebauer, G., & Matthews, K. 1993, AJ, 106, 2005

Girart, J. M., Estalella, R., Viti, S., et al. 2001, ApJ, 562, L91

Goddi, C., Humphreys, E. M. L., Greenhill, L. J., Chandler, C. J., & Matthews, L. D. 2011, ApJ, 728, 15

Gómez, L., Rodríguez, L. F., Loinard, L., et al. 2008, ApJ, 685, 333-343

González-García, B., Manoj, P., Watson, D. M., et al. 2016, A&A, 596, A26

Goodwin, S. P., Whitworth, A. P., & Ward-Thompson, D. 2004, A&A, 414, 633

Graves, S. F., Richer, J. S., Buckle, J. V., et al. 2010, MNRAS, 409, 1412

Großschedl, J. E., Alves, J., Meingast, S., et al. 2018, A&A, 619, A106

Habel, N., et al. 2020, submitted to Astronomy and Astrophysics

Hacar, A., Tafalla, M., Forbrich, J., et al. 2018, A&A, 610, A77

Hennemann, M., Motte, F., Schneider, N., et al. 2012, A&A, 543, L3

Herbst, E., & van Dishoeck, E. F. 2009, ARA&A, 47, 427

Hernández-Gómez, A., Loinard, L., Chandler, C. J., et al. 2019, ApJ, 875, 94

Heyer, M., & Dame, T. M. 2015, ARA&A, 53, 583

Hill, T., Motte, F., Didelon, P., et al. 2011, A&A, 533, A94

Hillenbrand, L. A. 1997, AJ, 113, 1733

Hillenbrand, L. A., Hoffer, A. S., & Herczeg, G. J. 2013, AJ, 146, 85

Hoare, M. G. 2006, ApJ, 649, 856

Hodapp, K. W. & Chini, R. 2014, ApJ, 794, 169

Huang, J., Andrews, S. M., Pérez, L. M., et al. 2018, ApJ, 869, L43

Hut, P., & Bahcall, J. N. 1983, ApJ, 268, 319

Isella, A., Guidi, G., Testi, L., et al. 2016, Phys. Rev. Lett., 117, 251101.

Jensen, E. L. N., & Akeson, R. 2014, Nature, 511, 567

Jensen, E. L. N., Mathieu, R. D., Donar, A. X., et al. 2004, ApJ, 600, 789

Mayen-Gijon, J. M., 2015, Ph.D. Thesis, University of Granada, Granada, Spain

Mayen-Gijon, J. M., Anglada, G., Osorio, M., et al. 2014, MNRAS, 437, 3766

Kainulainen, J., Stutz, A. M., Stanke, T., et al. 2017, A&A, 600, A141

Karnath, N., Megeath, S. T., Tobin, J. J., et al. 2020, ApJ, 890, 129

Kim, G., Lee, C. W., Maheswar, G., et al. 2019, ApJS, 240, 18

Kim, M. K., Hirota, T., Honma, M., et al. 2008, PASJ, 60, 991

Köhler, R., Petr-Gotzens, M. G., McCaughrean, M. J., et al. 2006, A&A, 458, 461

Koresko, C. D. 2000, ApJ, 531, L147

Kounkel, M., Covey, K., Suárez, G., et al. 2018, AJ, 156, 84

Kounkel, M., Hartmann, L., Loinard, L., et al. 2014, ApJ, 790, 49

Kounkel, M., Hartmann, L., Loinard, L., et al. 2017, ApJ, 834, 142

Kounkel, M., Megeath, S. T., Poteet, C. A., Fischer, W. J., & Hartmann, L. 2016, ApJ, 821, 52

Kratter, K., & Lodato, G. 2016, ARA&A, 54, 271

Kratter, K. M., Matzner, C. D., Krumholz, M. R., et al. 2010, ApJ, 708, 1585

Kraus, A. L., Ireland, M. J., Hillenbrand, L. A., et al. 2012, ApJ, 745, 19

Kurtovic, N. T., Pérez, L. M., Benisty, M., et al. 2018, ApJ, 869, L44

Lacy, M., Baum, S. A., Chandler, C. J., et al. 2019, arXiv e-prints, arXiv:1907.01981

Lada, C. J., & Lada, E. A. 2003, ARA&A, 41, 57

Lada, C. J., & Wilking, B. A. 1984, ApJ, 287, 610

Larson, R. B. 1969, MNRAS, 145, 271

Larson, R. B. 1972, MNRAS, 157, 121

Larson, R. B. 2003, Reports on Progress in Physics, 66, 1651

Lefèvre, C., Cabrit, S., Maury, A. J., et al. 2017, A&A, 604, L1

Leinert, C., Zinnecker, H., Weitzel, N., et al. 1993, A&A, 278, 129

Li, Z.-Y., & Nakamura, F. 2006, ApJ, 640, L187

Lim, J. & Takakuwa, S. 2006, ApJ, 653, 425

Lis, D. C., Serabyn, E., Keene, J., et al. 1998, ApJ, 509, 299

Lodato, G. & Rice, W. K. M. 2005, MNRAS, 358, 1489

Loinard, L., Chandler, C. J., Rodríguez, L. F., et al. 2007, ApJ, 670, 1353

Long, F., Pinilla, P., Herczeg, G. J., et al. 2018, ApJ, 869, 17

Looney, L. W., Mundy, L. G., & Welch, W. J. 2000, ApJ, 529, 477

López-Sepulcre, A., Jaber, A. A., Mendoza, E., et al. 2015, MNRAS, 449, 2438

López-Sepulcre, A., Taquet, V., Sánchez-Monge, Á., et al. 2013, A&A, 556, A62

Lugo, J., Lizano, S., & Garay, G. 2004, ApJ, 614, 807

Macías, E., Anglada, G., Osorio, M., et al. 2016, ApJ, 829, 1

Macías, E., Espaillat, C. C., Ribas, Á., et al. 2018, ApJ, 865, 37

Manoj, P., Watson, D. M., Neufeld, D. A., et al. 2013, ApJ, 763, 83

Marti, J., Rodriguez, L. F., & Reipurth, B. 1993, ApJ, 416, 208

Masqué, J. M., Rodríguez, L. F., Araudo, A., et al. 2015, ApJ, 814, 44

Mathis, J. S., Rumpl, W., & Nordsieck, K. H. 1977, ApJ, 217, 425

Matsumoto, T. & Hanawa, T. 2003, ApJ, 595, 913

Matzner, C. D., & McKee, C. F. 2000, ApJ, 545, 364

Maureira, M. J., Arce, H. G., Dunham, M. M., et al. 2020a, MNRAS, 499, 4394

Maureira, M. J., Pineda, J. E., Segura-Cox, D. M., et al. 2020b, ApJ, 897, 59

Maury, A. J., André, P., Testi, L., et al. 2019, A&A, 621, A76

McKee, C. F., & Ostriker, E. C. 2007, ARA&A, 45, 565

Megeath, S. T., Gutermuth, R., Muzerolle, J., et al. 2012, AJ, 144, 192

Megeath, S. T., Gutermuth, R., Muzerolle, J., et al. 2016, AJ, 151, 5

Menten, K. M., Reid, M. J., Forbrich, J., & Brunthaler, A. 2007, A&A, 474, 515

Mezger, P. G., Chini, R., Kreysa, E., Wink, J. E., & Salter, C. J. 1988, A&A, 191, 44

Mezger, P. G., Wink, J. E., & Zylka, R. 1990, A&A, 228, 95

Montesinos, M., Perez, S., Casassus, S., et al. 2016, ApJ, 823, L8

Muto, T., Grady, C. A., Hashimoto, J., et al. 2012, ApJ, 748, L22

Myers, P. C. 2009, ApJ, 700, 1609

Nakamura, F., & Li, Z.-Y. 2007, ApJ, 662, 395

Nakamura, F., Oyamada, S., Okumura, S., et al. 2019, PASJ, 32

Navarete, F., Damineli, A., Barbosa, C. L., et al. 2015, MNRAS, 450, 4364

Neuhaeuser, R., Wolk, S. J., Torres, G., et al. 1998, A&A, 334, 873

Nielbock, M., Chini, R., Müller, S. A. H. 2003, A&A, 408, 245

Ochi, Y., Sugimoto, K., & Hanawa, T. 2005, ApJ, 623, 922

O'Dea, C. P. 1998, PASP, 110, 493

Offner, S. S. R., Clark, P. C., Hennebelle, P., et al. 2014, Protostars and Planets VI, 53

Offner, S. S. R., Kratter, K. M., Matzner, C. D., et al. 2010, ApJ, 725, 1485

Ogilvie, G. I. & Lubow, S. H. 2002, MNRAS, 330, 950

Ortiz-León, G. N., Loinard, L., Dzib, S. A., et al. 2018, ApJ, 865, 73

Ortiz-León, G. N., Loinard, L., Mioduszewski, A. J., et al. 2015, ApJ, 805, 9

Osorio, M., Anglada, G., Carrasco-González, C., et al. 2014, ApJ, 791, L36

Osorio, M., Díaz-Rodríguez, A. K., Anglada, G., et al. 2017, ApJ, 840, 36

Osorio, M., Lizano, S., & D'Alessio, P. 1999, ApJ, 525, 808

Osorio, M., Macías, E., Anglada, G., et al. 2016, ApJ, 825, L10

Ossenkopf, V., & Henning, T. 1994, A&A, 291, 943

Ouyed, R., & Pudritz, R. E. 1997a, ApJ, 482, 712

Ouyed, R., & Pudritz, R. E. 1997b, ApJ, 484, 794

Padoan, P., Juvela, M., Goodman, A. A., et al. 2001, ApJ, 553, 227

Padoan, P. & Nordlund, Å. 1999, ApJ, 526, 279

Palau, A., Zapata, L. A., Rodríguez, L. F., et al. 2014, MNRAS, 444, 833

Papaloizou, J. & Pringle, J. E. 1977, MNRAS, 181, 441.

Penston, M. V., Hunter, J. K., & Oneill, A. 1975, MNRAS, 171, 219

Pérez, L. M., Carpenter, J. M., Andrews, S. M., et al. 2016, Science, 353, 1519

Peterson, D. E., & Megeath, S. T. 2008, Handbook of Star Forming Regions, Volume I, 4, 590

Phuong, N. T., Dutrey, A., Di Folco, E., et al. 2020, A&A, 635, L9

Polychroni, D., Schisano, E., Elia, D., et al. 2013, ApJ, 777, L33

Pudritz, R. E., & Norman, C. A. 1983, ApJ, 274, 677

Pudritz, R. E., & Norman, C. A. 1986, ApJ, 301, 571

Pudritz, R. E., Ouyed, R., Fendt, C., et al. 2007, Protostars and Planets V, 277

Raghavan, D., McAlister, H. A., Henry, T. J., et al. 2010, ApJS, 190, 1

Reid, M. J., Schneps, M. H., Moran, J. M., et al. 1988, ApJ, 330, 809

Reipurth, B., & Mikkola, S. 2012, Nature, 492, 221

Reipurth, B., Rodríguez, L. F., Anglada, G., & Bally, J. 2004, AJ, 127, 1736

Reipurth, B., Rodríguez, L. F., & Chini, R. 1999, AJ, 118, 983

Reipurth, B., & Zinnecker, H. 1993, A&A, 278, 81

Remijan, A., Biggs, A., Cortes, P., Dent, B., Di Francesco, J., Fomalont, E., Hales, A., Kameno, S., Mason, B., Philips, N., Saini, K., Stoehr, F., Vila Vilaro, B., Villard, E. 2020, ALMA Technical Handbook, ALMA Doc. 8.3, ver. 1.0

Reynolds, S. P. 1986, ApJ, 304, 713

Rodríguez, L. F., Anglada, G., & Curiel, S. 1999, ApJS, 125, 427

Rodríguez, L. F., D'Alessio, P., Wilner, D. J., et al. 1998, Nature, 395, 355

Rodríguez, L. F., Dzib, S. A., Loinard, L., et al. 2017, ApJ, 834, 140

Rodríguez, L. F., Garay, G., Brooks, K. J., & Mardones, D. 2005, ApJ, 626, 953

Rodríguez, L. F., Marti, J., Canto, J., Moran, J. M., & Curiel, S. 1993, RMxAA, 25, 23

Rodríguez, L. F., Yam, J. O., Carrasco-González, C., et al. 2016, AJ, 152, 101.

Rodríguez, L. F., Zapata, L. A., Dzib, S. A., et al. 2014, ApJ, 793, L21.

Rodríguez-Kamenetzky, A., Carrasco-González, C., Araudo, A., et al. 2016, ApJ, 818, 27

Rosero, V., Hofner, P., Kurtz, S., et al. 2019, arXiv e-prints, arXiv:1905.12089

Rudolph, A. L., Bachiller, R., Rieu, N. Q., et al. 2001, ApJ, 558, 204

Saigo, K., & Hanawa, T. 1998, ApJ, 493, 342

Samus', N. N., Kazarovets, E. V., Durlevich, O. V., Kireeva, N. N., & Pastukhova, E. N. 2017, Astronomy Reports, 61, 80

Sandell, G., & Knee, L. B. G. 2001, ApJ, 546, L49

Scholz, A., Wood, K., Wilner, D., et al. 2010, MNRAS, 409, 1557

Shimajiri, Y., Takahashi, S., Takakuwa, S., Saito, M., & Kawabe, R. 2008, ApJ, 683, 255-266

Shimajiri, Y., Takahashi, S., Takakuwa, S., Saito, M., & Kawabe, R. 2009, PASJ, 61, 1055

Shu, F. H. 1977, ApJ, 214, 488

Shu, F. H., Adams, F. C., & Lizano, S. 1987, ARA&A, 25, 23

Shu, F. H., Najita, J. R., Shang, H., et al. 2000, Protostars and Planets IV, 789

Skrutskie, M. F., Cutri, R. M., Stiening, R., et al. 2006, AJ, 131, 1163

Stamatellos, D., & Whitworth, A. P. 2009, MNRAS, 392, 413

Stanke, T., McCaughrean, M. J., & Zinnecker, H. 2002, A&A, 392, 239

Stanke, T., Stutz, A. M., Tobin, J. J., et al. 2010, A&A, 518, L94

Stapelfeldt, K. R., Krist, J. E., Ménard, F., et al. 1998, ApJ, 502, L65

Strassmeier, K. G. 2009, A&A Rev., 17, 251

Strom, S. E., Vrba, F. J., & Strom, K. M. 1976, AJ, 81, 314

Stutz, A. M. 2018, MNRAS, 473, 4890

Stutz, A. M., & Gould, A. 2016, A&A, 590, A2

Stutz, A. M. & Kainulainen, J. 2015, A&A, 577, L6

Stutz, A. M., Tobin, J. J., Stanke, T., et al. 2013, ApJ, 767, 36

Takahashi, S., Ho, P. T. P., Teixeira, P. S., et al. 2013, ApJ, 763, 57

Takahashi, S., Saito, M., Ohashi, N., et al. 2008, ApJ, 688, 344-361

Takakuwa, S., Saigo, K., Matsumoto, T., et al. 2017, ApJ, 837, 86

Taquet, V., Bianchi, E., Codella, C., et al. 2019, A&A, 632, A19

Teixeira, P. S., Takahashi, S., Zapata, L. A., et al. 2016, A&A, 587, A47

Terebey, S., Shu, F. H., & Cassen, P. 1984, ApJ, 286, 529

Testi, L., Birnstiel, T., Ricci, L., et al. 2014, Protostars and Planets VI, 339

Thompson, R. I. 1984, ApJ, 283, 165

Tobin, J. J., Hartmann, L., Furesz, G., Mateo, M., & Megeath, S. T. 2009, ApJ, 697, 1103-1118

Tobin, J. J., Kratter, K. M., Persson, M. V., et al. 2016a, Nature, 538, 483

Tobin, J. J., Looney, L. W., Li, Z.-Y., et al. 2016b, ApJ, 818, 73

Tobin, J. J., Looney, L. W., Li, Z.-Y., et al. 2018, ApJ, 867, 43

Tobin, J. J., Megeath, S. T., van't Hoff, M., et al. 2019, ApJ, 886, 6

Tobin, J. J., Sheehan, P. D., Megeath, S. T., et al. 2020, ApJ, 890, 130

Tobin, J. J., Stutz, A. M., Manoj, P., et al. 2016c, ApJ, 831, 36

Tobin, J. J., Stutz, A. M., Megeath, S. T., et al. 2015, ApJ, 798, 128

Torrelles, J. M., Gomez, J. F., Rodriguez, L. F., et al. 1996, ApJ, 457, L107

Tsujimoto, M., Koyama, K., Kobayashi, N., et al. 2003a, AJ, 125, 1537

Tsujimoto, M., Koyama, K., Tsuboi, Y., Goto, M., & Kobayashi, N. 2002, ApJ, 566, 974

Tsujimoto, M., Koyama, K., Tsuboi, Y., Goto, M., & Kobayashi, N. 2003b, ApJ, 585, 602

Tychoniec, Ł., Tobin, J. J., Karska, A., et al. 2018, ApJS, 238, 19

Vaytet, N., Audit, E., Chabrier, G., et al. 2012, Astronomy and Astrophysics, 543, A60

Vaytet, N., & Haugbølle, T. 2017, A&A, 598, A116

Wakelam, V., Smith, I. W. M., Herbst, E., et al. 2010, Space Sci. Rev., 156, 13

Williams, J. P., Blitz, L., & McKee, C. F. 2000, Protostars and Planets IV, 97

Williams, J. P., Plambeck, R. L., & Heyer, M. H. 2003, ApJ, 591, 1025

Wilson, T. L. & Rood, R. 1994, ARA&A, 32, 191

Wilson, B. A., Dame, T. M., Masheder, M. R. W., et al. 2005, A&A, 430, 523

Xu, S., Ji, S., & Lazarian, A. 2019, arXiv e-prints, arXiv:1905.06341

Yokogawa, S., Kitamura, Y., Momose, M., & Kawabe, R. 2003, ApJ, 595, 266

Yu, K. C., Bally, J., & Devine, D. 1997, ApJ, 485, L45

Zapata, L. A., Rodríguez, L. F., Fernández-López, M., et al. 2020, ApJ, 896, 132

Zapata, L. A., Schmid-Burgk, J., Ho, P. T. P., Rodríguez, L. F., & Menten, K. M. 2009, ApJ, 704, L45